Chemical kinetics tabulation for pollutants prediction in internal combustion engines

Diana Elena Tudorache

Ecole Centrale Paris

THESE

présentée par

Diana Elena TUDORACHE

pour l'obtention du

GRADE de DOCTEUR

Formation doctorale : Energétique

Laboratoire d'accueil : Laboratoire d'Énergétique Moléculaire et Macroscopique, Combustion (EM2C) du CNRS et de l'ECP

Tabulation de la cinétique chimique pour la prédiction des polluants dans les moteurs à combustion interne

Soutenance prévue Février 2013

Jury :	M.	Angelberger	C	Rapporteur
	M.	Guibert	P.	Rapporteur
	M.	Darabiha	N.	Directeur de thèse
	M.	Fiorina	B.	Examinateur
	Mme.	Honnet	S.	Examinateur
	Mme.	Rousselle	C.	Examinateur
	M.	Thobois	L.	Examinateur

Ecole Centrale des Arts et Manufactures
Grand Établissement sous tutelle
du Ministère de l'Éducation Nationale
Grande Voie des Vignes
92295 Châtenay-Malabry Cedex
Tél : 33 (1) 41 13 10 00
Télex : 634 991 F EC PARIS

Laboratoire d'Énergétique Moléculaire et Macroscopique, Combustion (E.M2.C.)
UPR 288, CNRS et Ecole Centrale Paris
Tél : 33 (1) 41 13 10 31
Fax : 33 (1) 47 02 80 35

2013

Abstract

Today hydrocarbon fuel combustion covers most of energy needs in transportation. Due to environmental concerns and regulations, automotive manufacturers aim at acquiring knowledge of physical and chemical phenomena inside the combustion chamber to understand and control pollutant emissions such as carbon monoxide (CO), unburned hydrocarbons (HC) and nitrogen oxides (NOx).
Despite the outstanding performances in the domain of high performance intensive numerical calculation, the numerical simulations of the combustion chambers of the internal combustion engines (ICE) do not allow a detailed description of the chemical processes. Indeed, the kinetic models for the reference fuels contain hundreds of species.
The present study aims to improve the turbulent combustion models based on Large Eddy Simulation approach by developing an efficient cost-cutting tabulation method to fit chemistry in engine combustion modeling.
A particular attention is paid to the capacity of the tabulation method to reproduce the pollutant species formation during the compression stroke, the reaction phase, and the power stroke of an ICE. This method assumes that IC engine chemistry can be mapped by a collection of 0-D reactor computation data, using for coordinates: the progress variable, the mixture fraction, the energy and the density.
In a first step, the chemical prediction capability of this technique is validated on an auto-igniting variable volume simulation. The Tabulated Thermo Chemistry (TTC) method recently proposed by Vicquelin *et al.* [85] was initially developed to couple the chemical kinetics with compressible Navier-Stokes solvers for low Mach number flows. In this work, the TTC method was adapted in the framework of variable pressure combustion. A TTC version dedicated to engine combustion is thus coupled in the unsteady compressible LES code AVBP [1]. The method of coupling was successfully tested both on simplified configurations and on a Rapid Compression Machine [41].

Actuellement, la combustion des hydrocarbures couvre la majorité des besoins pour le transport. Les responsabilités et les réglementations environnementales font que les constructeurs automobiles visent à acquérir des connaissances approfondies sur les phénomènes physico-chimiques des chambres de combustion des moteurs pour la compréhension et le contrôle des émissions polluantes tels que le monoxyde de carbone (CO), les hydrocarbures imbrûlés (HC) et les oxydes d'azote (NOx).
En dépit des performances remarquables dans le domaine du calcul numérique intensif de trés haute performance, les simulations numériques des chambres de combustion des moteurs à combustion interne ne permettent pas encore une description détaillée des processus chimiques. En effet, les modèles cinétiques pour les combustibles de référence contiennent des centaines d'espèces.
L'objectif de ces travaux est d'améliorer les modèles de combustion turbulente basés sur la Simulation aux Grandes Echelles (Large Eddy Simulation, LES) en développant une méthode de tabulation de la cinétique chimique représentative de la combustion dans un cycle moteur.
Une attention toute particulière est portée sur la capacité de la méthode de tabulation à reproduire la formation des espèces polluantes lors des phases de compression, d'auto-allumage et de détente d'un moteur à combustion interne.
Cette méthode suppose que la chimie dans une chambre de combustion interne peut être approchée par une tabulation des résultats issus de calculs de réacteurs 0-D en volume constant, les quatre coordonnées de la table étant: la variable de progrès, la fraction de mélange, l'énergie et la masse volumique. La capacité prédictive de la technique de tabulation a été testée par des simulations d'auto-allumage en volume variable.
La méthode de tabulation "Tabulated Thermo Chemistry" (TTC) proposée récemment par Vicquelin *et al.* [85] a été initialement développée pour coupler la cinétique chimique à des solveurs Navier-Stokes compressibles dans des situations d'écoulement à faible nombre de Mach. Dans ce travail, la méthode TTC a été adaptée pour la combustion à pression variable. Une version TTC dédiée à la combustion dans les moteurs est donc implantée dans le code instationnaire LES compressible AVBP [1]. La méthode de couplage a été testée avec succès tant sur des configurations simplifiées que sur une Machine à Compression Rapide [41].

Contents

Abstract **iii**

General introduction **1**

I Chemical kinetics tabulation **7**

1 Chemical kinetics tabulation techniques **9**
1.1 Introduction 9
1.2 Kinetics of chemical reactions 10
1.3 Reduction methodologies 13
1.4 Coupling tabulated chemistry with compressible solvers . . 32

2 Chemistry tabulation for ICE applications **35**
2.1 Introduction 36
2.2 Primary reference fuel 36
2.3 Chemical kinetic mechanism 39
2.4 Verifying ignition delay predictions of the 89-species skeletal mechanism for n-heptane 41
2.5 The thermo-chemical table generation methodology 45
2.6 Thermo-chemical table discretization benchmark for auto-ignition delay prediction 50
2.7 Variable volume validations 63

II Coupling a non-adiabatic chemical table with a LES compressible solver 71

3 Coupling a chemical table with the AVBP compressible CFD solver 73
3.1 Introduction . . . 73
3.2 Equations for reactive flows using tabulated techniques . . 75
3.3 Coupling the AVBP LES compressible solver with non-adiabatic tables . . . 85

4 Tests validations 91
4.1 Introduction . . . 92
4.2 Implementation validation: study of compressible effects . 93
4.3 Modeling validations: auto-ignition delays . . . 115

5 Rapid Compression Machine 123
5.1 Introduction . . . 123
5.2 Geometrical configuration of RCM . . . 125
5.3 Boundary conditions with tabulated chemistry: the impact of isothermal wall on ignition . . . 132
5.4 *LES* results analysis . . . 136

References 177

A N-heptane kinetical mechanisme 179

B Linear acoustic equations 185

C 1-D characteristic wave 187
C.1 From conservative variables to non-conservative variables . 187
C.2 Characteristic wave decomposition . . . 190

General introduction

Introduction and state-of-the-art

Internal Combustion Engines (ICE) are devices able to convert the chemical energy contained in the fuel to mechanical power. After combustion, the work is transferred between the burned products and the piston. Furthermore the power is transmitted through a connecting rod and a crank mechanism to the drive shaft. The reciprocating piston motion is shown in Fig. 1 [44], for a four-cycle operating system as it is used in the majority of today's car engines.

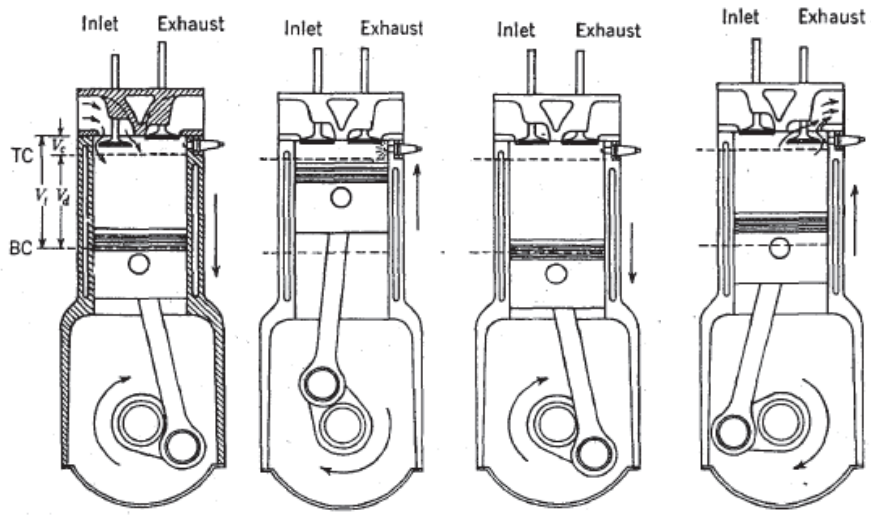

(a) Intake (b) Compression (c) Expansion (d) Exhaust

Figure 1 : *The four-stroke operating cycles of ICE [44]. TC: top-dead center; BC: bottom-dead center, V_c : clearance volume, V_t : total volume, V_d : displaced volume*

In the intake stroke Fig. 1(a) the cylinder is filled with fresh fuel/air mixture by the pistons motion between the top-dead center (TDC or TC) crank position to the bottom-dead center (BDC or BC) crank position. Afterwards, during the compression stroke Fig. 1(b), the mixture is compressed and when the piston is close to the TDC, the combustion takes place. In the power stroke, Fig. 1(c), the high-pressure burned gases push the piston towards the BDC and the crankshaft converts the reciprocating motion into rotatory motion. The burned gases are evacuated from the chamber during the exhaust stroke, Fig. 1(d), allowing for another cycle to start.

The engine efficiency is the relationship between the total energy contained in the fuel and the restored mechanical energy. It is important to optimize the engine efficiency in order to avoid the loss of energy, particularly in the context of sustainable development.

An automobile engine offers today, under optimum operation conditions, a maximum efficiency of approximatively 36% for a gasoline engine and of approximatively 42% for a Diesel engine. Thus, the engines are able to convert only a third of the available energy to useful energy to advance the vehicle, and the remaining energy is mainly dissipated as heat loss in the atmosphere.

The emission-control requirements have changed the way internal combustion engines are designed and operated. The engine outputs, nitrogen oxides (NOx), unburned hydrocarbon (HC), carbon monoxide (CO) and particulate matter (PM) are regulated. Since 2005, the European standards impose reduction of 70 % of NOx with respect to the new $Euro$ 6 norm that will be in force in 2014, as shown in Fig. 2. This should be achieved without any increase in the CO or HC emissions.

Automotive manufacturers aim to develop cleaner internal combustion engines with significant reduction in fuel consumption and simultaneously pollutant emissions. Alternative types of internal combustion engines, such as homogeneous charge compression-ignition $HCCI$ engines, were proposed in order to join characteristics as lower emissions associated with spark ignition engines SI or high efficiency as in compressed ignition engines CI.

The numerical simulations are an essential tool to advance automotive technologies in terms of optimization of the combustion chamber.

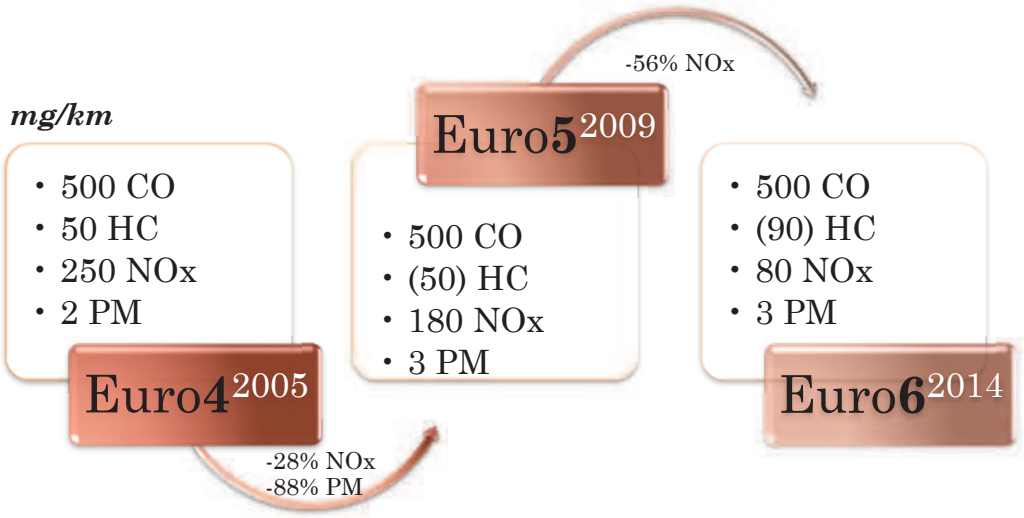

Figure 2 : *European emission standards define the acceptable limits for exhaust emissions of Diesel vehicles*

By means of numerical simulations, knowledge is acquired on the auto-ignition and chemical flame structure and new technological innovations in engine design are developed in order to reduce fuel consumption and to protect the environment.
Various modes of combustion appear in internal combustion engine [14]. The beginning of combustion in CI or Diesel engines or in a single engine cycle simulator (e.g. in a Rapid Compression Machines RCM) is controlled by an auto-ignition regime in which a premixed charge of air and fuel at a given equivalence ratio has the minimum temperature and pressure to ignite. In SI or gasoline engine the air-fuel mixture is ignited by a spark from a spark plug. In this case if the auto-ignition regime occurs it will be the undesirable phenomenon called knock, that has a destructive effect on SI engine. The knock consists in the onset of auto-ignition in the unburned fuel-air mixture ahead of the propagating flame and limits the increase in compression ratio and yields a broad range of fuels non operational in gasoline engines [49].
After ignition either by reaching a minimum mixture energy or a minimum ignition energy by a source, two modes of combustion can be distinguished

following the level of mixing of fuel, air and residual gas in the cylinder.
A first combustion mode is a premixed propagation flame that arises after ignition in a gasoline engine or in a rapid compression machine because the air and fuel are usually mixed together in the intake system before entering the cylinder using a carburetor or fuel injection system.
The second combustion mode is the non-premixed flame that can be found in Diesel engines where the fuel is injected into the engine cylinders leading to an imperfect mixing in the system. Molecular mixing brings reactants in contact within thin reaction zones and will control the combustion.
To understand these combustion modes, the interaction between the flow dynamics and the chemical phenomena which take place during fuel combustion is required. The most accurate chemical description available is the detailed chemistry approach that can provide information on the chemical polluting species. A description of chemistry requires to take into account several hundreds of species and thousands of reactions. Nevertheless, such complex mechanism takes an excessive computing time for the numerical simulations as one balance equation is resolved for each species.
In practice, for the majority of the chemical kinetic combustion models existing today, chemistry is reduced to one or several reaction. This leads to a lack of information on the chemical composition.
Tabulated-chemistry method proposes to create a database from elementary configurations of combustion obtained using detailed chemistry. This table will include all needed information on chemistry, allowing a precise description of chemistry and also a substantial profit in computational resources. The tabulated-chemistry approaches rely on a progress variable whose role is to follow the evolution of the chemical species along trajectories in the composition spaces.
The tabulated-chemistry approach preserves the main chemistry characteristics under industrial computational time restrictions. Since 1990's this approach was successfully used for the chemistry of hydrocarbons, initially for laminar reactive flows [28, 33, 34, 38, 65, 82, 83] and then coupled with turbulent combustion models. As an example the 3-Zones Extended Coherent Flame Model $EMCF3Z$ [14] approach or statistical models [34] were successfully used in ICE turbulent reactive flows mod-

eling [15, 48, 59, 67] by using a Reynolds Average Navier-Stokes ($RANS$) approach.
Large Eddy Simulation (LES) is now available for industrial application. Enaux and al. [29] performed a cycle-to-cycle LES simulation of a spark ignition engine, including the intake and the exhaust plenum. The drawback of this simulation is the use of a two-step chemistry for the propane fuel considered.
In the present PhD work, our main goal will be to implement the engine-adapted tabulated-chemistry methodology to a variable volume LES of reactive flow. For that, the technique is coupled with the $AVBP$ LES compressible solver [1] following the Tabulated Thermo Chemistry (TTC) formalism, proposed by Vicquelin *et al.* in [85]. The tabulated chemistry model will be tested on an unsteady combustion configuration with variable volume.

Organisation

This work is organized as follows.

The *first chapter* will highlight the need of the use of detailed chemistry in order to predict auto-ignition process and pollutants emission. Then an overall view of the reduction techniques for the detailed chemical kinetics that can be used in ICE's applications is given. The classical chemical reduction methodologies such as quasi-steady state approximation $QSSA$ for some intermediate species and radicals and partial equilibrium assumption PEA for particular reactions will be introduced. Then a mathematical formalism, called Intrinsic Low Dimensional Manifold $ILDM$, that is able to find the best reduction of a detailed chemical kinetic mechanism will be discussed. This approach cannot be directly used for ICE reference fuels but it is behind the Flame Prolongation of $ILDM$ (FPI) [38] or similarly Flamelet Generated Manifolds (FGM) [83] that is afterwards described in more detail as it is further-on used in this work. Information about Tabulated Kinetics for Auto-ignition (TKI) [20] is given, being a model largely used for the prediction of a auto-ignition delay in ICE.

The *second chapter* introduces a FPI approach for chemistry tabulation method adapted to internal combustion engine simulations from the onset of auto-ignition up to the end of the expansion stroke. The choice of the primary reference fuel and of the corresponding chemical kinetic mechanism will be argued for an accurate ignition delay prediction. Then the tabulation methodology, including the choice of the controlling variables, in the engine context is presented. In order to obtain low-size thermo-chemical tables, the discretization requirements benchmarks will be defined for each retained dimension. The chapter is ended by $0-D$ variable volume computations.

The *third chapter* is devoted to the coupling of the engine-adapted thermo-chemical table with a fully compressible Large Eddy Simulation solver. In the first part of the chapter the coupling between the Navier-Stokes equations with tabulated chemistry will be addressed, underlying the unclosed terms that are recovered from the thermo-chemical table. Then the equations are written in the Favre formalism used in LES technique.

The *fourth chapter* presents the coupling validation tests that support the accurate connection between the engine-adapted thermo-chemical table and a compressible LES solver. The compressible behavior of the code is analyzed when acoustic or entropic waves cross the computational domain. The second class of tests are constant vo-lume and variable volume homogenous computations that aim at validating the discretization benchmark of the thermo-chemical table.

The *fifth chapter* presents a simulation performed with the tabulated chemistry approach on a 3-D rapid compression machine. The capacity of the approach to account for thermal stratification inside the domain and for thermal heat losses will be highlighted.

The manuscript will be ended with final conclusions and prospects.

Part I

Chemical kinetics tabulation

Chapter 1

Chemical kinetics tabulation techniques

The main motivation of the present chapter is to highlight the importance of the use of detailed chemical kinetics in computational simulations of ICEs for an accurate prediction of the auto-ignition delays and pollutants emissions. The second objective is to review the main techniques that allow to incorporate realistic fuels in ICE computations. The tabulation technique is afterwards outlined, being well adapted to large-scale simulations, demanding low CPU time and having an accurate chemical species and auto-ignition delay feedback.

1.1 Introduction

In the last decades, the main target in combustion research has been to decrease the pollutant emissions. Indeed, this process, besides heat, generates unwanted products, with direct impact on human health and on the environment, such as carbon monoxide, nitrogen oxides or unburned hydrocarbons. Due to an increased awareness of the ecological impact of these pollutants, restrictive emission regulations are imposed to the car industry.

The engine manufactures need to acquire comprehensive knowledge of the physical and chemical phenomena taking place inside combustion chambers. As the interest is focused on the auto-ignition delays and pollutants chemistry, the computational simulation of ICE requires complete chemical kinetic description.

1.2 Kinetics of chemical reactions

The particularity of a reacting flow is the reorganization that takes place between its molecular constituents. If the initial molecules knock against each other or to a solid object, then they are close enough to enable the valence electrons to rearrange and this allows the transformation into new chemical species. Notice that the probability for a molecule to find itself in the cross section of two other colliding molecules is extremely low. Consequently, a sequence of only two or three body elementary reactions will take place until the maximum entropy is reached, and the global reaction products are formed.
An example of n-heptane-air kinetic mechanism is given in Appendix A. The scheme comprises initiation, chain branching and termination sets of elementary reactions.
Auto-ignition process is controlled by the production of the initial radicals. Therefore, only the detailed chemistry can provide knowledge on the auto-ignition delays characteristics and pollutants formation.
Two examples illustrate the strong influence of the chemical pathway on the auto-ignition phenomenon.

- $H_2 - O_2$ pressure-auto-ignition temperature Z-shaped curve, see Fig. 1.1 from [55], cannot be explained without the intricacies of the chemical kinetics.

  Indeed, at low pressure the reaction is driven by a direct chain branching reaction:
  $\dot{H} + O_2 \rightarrow \dot{O} + H\dot{O}$

  When increasing the pressure, the frequency of the collision is increased and a propagative reaction transforms the hydrogen radicals in a more stable hydroperoxyde radical slowing down the overall reaction rate:

$\dot{H} + O_2 + M^* \rightarrow HO\dot{O} + M^*$

With further increase in pressure, the hydroperoxyde radical is destroyed:
$HO\dot{O} + H_2 \rightarrow H_2O_2 + \dot{H}$
A degenerate branching chain will finally trigger the reaction:
$H_2O_2 + M^* \rightarrow 2H\dot{O} + M^*$

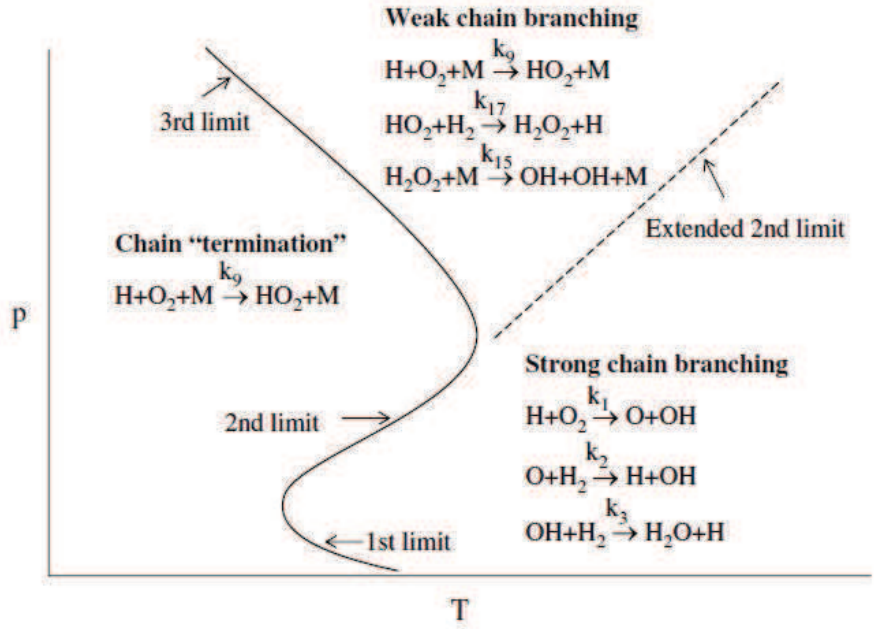

Figure 1.1 : *Schematic of the three auto-ignition limits of H_2/air mixture [55]*

- $C_xH_y - O2$ pressure-auto-ignition temperature often show a more complex shape, giving rise to a cool flame which is a partial oxidation phenomenon and a main flame. The detailed kinetics show different preferential reaction pathways for the two regimes, see also chapter 2.

Thus the combustion process is a complex succession of consecutive and competitive elementary reactions, englobed in the kinetic mechanism expressed in an abstract form by the equation 1.1.

$$\sum_{k=1}^{N_{sp}} \nu_{k,i}^{'} \chi_k \rightleftharpoons \sum_{k=1}^{N_{sp}} \nu_{k,i}^{''} \chi_k \qquad i = 1, ..., N_r \tag{1.1}$$

where $\nu_{k,i} = \nu_{k,i}^{''} - \nu_{k,i}^{'}$ is the stoichiometric coefficient for one of the k^{th} chemical species χ_k, interacting in the i^{th} reaction of the N_r reactions mechanism.
In order to describe the chemical processes to some specified level of accuracy, the kinetic model for a particular reaction should contain a large number of species N_{sp} and elementary reactions N_r. The species are non-monotonic and non-linearly coupled throughout the kinetic mechanism 1.1 and render their simulation computationally stiff [55].
To understand the fundamental elementary step chemistry means to have access to the total source therm $\dot{\omega}_k$ of each species χ_k:

$$\dot{\omega}_k = W_k \sum_{i=1}^{N_r} \nu_{k,i} r_i \tag{1.2}$$

where $\nu_{k,i}$ is the stoichiometric coefficient which counts the number of species χ_k involved in a specific reaction i of a rate r_i.
The reaction rate reads:

$$r_i = k_{fi} \prod_{k=1}^{N_{sp}} [\chi_k]^{\nu_{k,i}^{'}} \; - \; k_{ri} \prod_{k=1}^{N_{sp}} [\chi_k]^{\nu_{k,i}^{''}} \tag{1.3}$$

Obviously, each species concentration $[\chi_k]$ will directly impact on the reaction rate according to its own stoichiometric coefficient.
The forward k_{fi} and the reverse k_{ri} reaction rate coefficients stand for the probability that the two or three bodies collide and that they have enough energy to be transformed to other entities. The energy needed for an elementary reaction to take place is called activation energy E_a.
The dependency of the chemical reaction dynamics on the frequency of the collision between molecules, radicals and walls is expressed by the preexponential factors A and β and their total energetic contribution in the process is usually expressed by the modified Arrhenius equation:

$$r_f = AT^{\beta} e^{-\frac{E_a}{RT}} \tag{1.4}$$

Note that the reverse rate is more easily and more precisely obtained from the forward rate and the equilibrium constant K_{eq} by means of thermodynamic properties.

$$r_r = \frac{K_{eq}(p,T)}{k_f} \tag{1.5}$$

Considering a complete kinetic mechanism, one is able to track precisely the species time evolution by solving the conservation equations for each chemical species in the kinetic mechanism along with the classical Navier-Stokes equation for a non-reactive flow. Typically for auto-ignition at constant pressure, for instance, one should resolve N_{sp} coupled equations of the form:

$$\frac{\partial \rho Y_k}{\partial t} = \dot{\omega}_k, \qquad k = 1, ..., N_{sp} \tag{1.6}$$

1.3 Reduction methodologies

For a ICE primary reference fuel, the kinetic mechanism is typically composed of hundreds of species and thousands of elementary reactions making them impossible to be processed within reasonable time in a 3-D reactive flow configuration (see Appendix A for example).
The CPU expense is due to the high number of species balance equation to be solved and to the stiffness of the chemical reaction terms. Some additional time is spent for the chemical rates evaluation and for the inter-process communications for high performance computations but they are asymptotically inexpensive being linear functions of the number of species [55].
Therefore, alternative strategies need to be used in order to perform 3-D engine simulations with the today limitation of the computational power. In this chapter, different models that have been proposed to take into account the complexity of the combustion chemical kinetics, will be discussed. The first approach proposed was to do a chemical analysis reduction. Then, in the $90's$, the Intrinsic Low Dimensional Manifold ($ILDM$)

method was developed to mathematically identify the slow scales of the reactive system. To overcome the $ILDM$ limitations in low temperature regions, tabulation methodologies, identifying the manifolds by elementary configurations of the reactive system, were largely used afterward.

1.3.1 Chemical analysis reduction

The aim is to lump the detailed chemical-kinetics as to become a manageable size kinetics by eliminating unimportant species and reactions. In the chemical approach ad-hoc approximations are introduced , usually:

- **quasi-steady state approximation $QSSA$ for some intermediate species and radicals**. The non-trivial task is to identify species which react on very short time scales and therefore instantaneously equilibrate with respect to slower species. The QSS species concentration will be accessed from an algebraic expression by setting the net rate of production to zero [45].
- **partial equilibrium assumption PEA for particular reactions**, assumed to have equal forward and reverse reaction rates $|k_{forward}| = |k_{reverse}|$. Consequently, the rate in the direction of this specific reaction vectors is forced to vanish.

Although the resulting scheme becomes far more compact, the lumped rate parameters derived in this way are numerically to avoid as they are nonlinear functions of the original rate parameters.
In addition, the range of the thermo-chemical parameters validity (pressure, temperature, equivalence ratio) is very limited and the assumption may be improper outside this domain. In addition, it is difficult to apply to complex reaction sequences, such as the development of the first stage of the two stage ignition occurring in the alkane's low temperature regime.
Being aware of the approach shortcoming, one must admit its benefits: a speed-up factor up to 500 when compared to the full schemes for n-heptan [45] and the possibility to identify the main reaction pathways and rate controlling steps.
The QSSA and PEA reduction benchmark for CH_4 can be found in [45].

1.3.2 Intrinsic Low Dimensional Manifold $ILDM$

The idea behind the paper of Mass and Pope [56] is to find a general mathematical procedure for simplifying chemical kinetics without requiring an expert knowledge of chemistry, especially knowing which species are in a QSS or which reactions are in a PE.

A time scale analysis of the processes governing a gas-phase chemical reaction leads to the conclusion that the chemical reaction scatters a wide range of time scales from 10^{-9} to 10^{2} s, whereas the physics (flow, molecular transport, turbulence) will take place during a smaller range of 10^{-5} to 10^{-2} s.

The system dynamics with a wide range of time scales have the intrinsic property of convecting to an attractive invariant manifold [56]. If the fast scales, which are those responsible for the equilibration processes (PEA and QSSA) are neglected, then the degrees of freedom (number of variables of the system) for the state of the system are reduced. The purpose is to identify the slow manifold by neglecting the fast time scales. A mathematical formalism allows the separation of the fast and slow time scales (see figure 1.2) and consequently finds the attractive hypersurface in the composition space. The method is based on an eigenvector-eigenvalues analysis of the Jacobian matrix of the governing equation system.

Under homogeneous, isobaric and adiabatic hypothesis the reacting system state is described by the set of ordinary differential:

$$\frac{d\phi}{dt} = F(\phi),\ \phi(t=0) = \phi^0 \tag{1.7}$$

where $F(\phi)$ is the reaction rate vector. For testing the stability of the dynamic system, the response to a perturbation with respect to a reference composition ϕ^0 is studied.

$$\frac{d(\phi - \phi^0)}{dt} = F(\phi^0) + \frac{\partial F}{\partial \phi}(\phi - \phi^0) \tag{1.8}$$

with $J = \frac{\partial F}{\partial \phi}$ the Jacobian matrix, diagonalizable around ϕ^0. The system can be written in a diagonalized form:

$$\frac{d\phi'}{dt} = F'(\phi^{0'}) + \Lambda(\phi' - \phi^{0'}) \tag{1.9}$$

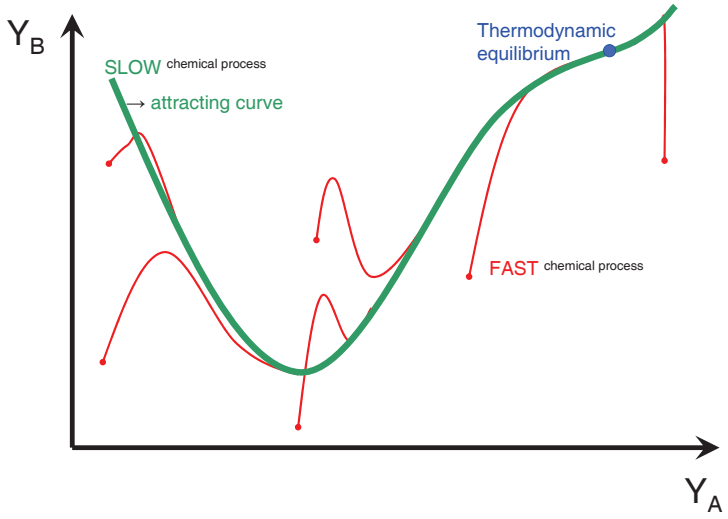

Figure 1.2 : *ILDM fast and slow time scales representation of a reacting mixture in the mass fraction space (Y_A, Y_B); the rapid chemical processes (red lines) relax to the 1-D low dimensional manifold (greed line) that leads to the thermodynamic equilibrium (blue dot) [38].*

where Λ is the diagonalized matrix composed of the eigenvalues λ_i, which are in fact the characteristic chemical time scales inverses.

$$\tau_i = \frac{1}{\|\lambda_i\|} \tag{1.10}$$

The eigenvalue can give the following information about the system:

- if $\|\lambda_i\| < 0$, then the magnitude of the perturbation will decrease, the system will fast relax to the equilibrium; the great majority of the eigenvalues have this attractive behavior;
- if $\|\lambda_i\| = 0$, then the perturbation remains unchanged, the eigenvectors can be expressed as linear combination of the element vectors, these are the invariants of the chemical system.
- if $\|\lambda_i\| < 0$, then the perturbation increases, the system continue to evolve, fortunately only very few eigenvalues have this behavior.

Mass and Pope were able to identify a subspace of the composition space where the system is "in equilibrium" with respect to its smallest eigenvector, consequently to its fastest time scales. Thus a subspace in which all movements correspond to slow time scales, called *low dimensional manifold*, is found and can be used to simplify the description of complicated chemical kinetics.

In the high temperature regions a two or three-dimensional manifold is established by a fast relaxation process. For low temperature regions, as the chemical time scales are of the same order of magnitude, more variables are necessary in order to define an $ILDM$ [17]. This restricts the use of this mathematical reduction technique for higher hydrocarbon mechanisms as it can not represent the variations in auto-ignition delay over the wide range of temperatures found in an IC engine.

Even if, the use of the $ILDM$ approach for the simulation of ICEs remains a critical issue, it gave a mathematical proof to the tabulated chemistry in function of a reduced number of variables.

1.3.3 Tabulated Chemistry from combustion elements

The chemistry characteristics are essential for the reactive flow simulations. Despite the existence of computer systems approaching the teraflops-region, numerical simulation of reactive mixtures for such industrial configurations can not follow the continuous evolution of the large number of chemical species. As mentioned above, the $ILDM$ tabulation method cannot cover low temperature reaction zones because of very small time scales.
Early studies of Peters [68] and then Bradley et al. [10] proposed to identify the chemical subspace by elementary configurations of the reactive flow. Based on this strategy, the tabulated chemistry approach proposes to respond to a particular physico-chemical phenomenon by using adapted tables build-up from representative combustion elements:

- If the leading phenomenon is the flame propagation throughout a premixed or partially-premixed mixture, then a collection of 1-D premixed flames is to be used for the database construction. This particular tabulated-chemistry approach is called Flame Prolongation of Intrinsic Low-Dimensional Manifolds (FPI) or Flamelet Generated Manifold (FGM).

- If the diffusion across iso-mixture fractions is important, the chemical trajectories are correctly reproduced by diffusion flames.

- If the accurate prediction of the auto-ignition is mandatory, like in Diesel engines, then the thermo-chemical table gathers 0-D reactors computations that cover the conditions swept by the piston.

- If various phenomena are describing the reactive flow as auto-ignition, laminar or turbulent premixed flame kernel [86], diffusion flames [77], then complex flames should be used to build the thermo-chemical tables.

Subsequently, the tabulated chemistry will be discussed in terms of table's coordinates, the generation or the coupling to a compressible flow. This section also aims to draw attention to the auto-ignition phenomenon under a tabulated chemistry approach.
Exhaustive description of the tabulated chemistry approach is given by Fiorina in [32].

1.3.3.1 Flame Prolongation of Intrinsic low dimensional manifold (FPI) or Flame Generated Manifold (FGM)

The chemistry tabulation techniques as FPI [6,34,36,38,58,59] or FGM [7, 61,64,82] seem to be a very advantageous approach as they allow tracking the chemical species evolution at a low CPU time.
The aim of the two similar approaches FPI and FGM is to describe the mixture's chemical evolution from fresh gases to burned products by a single progress variable. A transport equation is solved for the progress variable associated with the recovery of the mass fractions or the reaction rates from a look-up table. Relating the chemical quantities to the progress variable avoids solving expensive differential equations for each chemical species.
The premixed and partially-premixed regions in a complex geometry configuration can be approximated by a collection of 1-D laminar premixed flames computed using detailed chemistry [38]:

$$\rho\frac{\partial Y_k}{\partial t} + \rho u\frac{\partial Y_k}{\partial x} = -\frac{\partial}{\partial x}(\rho Y_k V_k) + \dot{\omega}_k, \qquad k = 1, ..., N_{sp} \tag{1.11}$$

where ρ is the mass density, Y_k the k^{th} species mass fraction, u is the velocity vector of the gas mixture, V_k is the diffusion velocity of the k species and $\dot{\omega}_k$ is the k^{th} species reaction rate.

$$\rho C_p\frac{\partial T}{\partial t} + \rho u C_p\frac{\partial T}{\partial x} = \frac{\partial}{\partial x}(\lambda\frac{\partial T}{\partial x}) + \sum_{k=1}^{N_{sp}} h_k\dot{\omega}_k \tag{1.12}$$

where T is the temperature, λ is the conduction coefficient and h_k the k^{th} species enthalpy.
A thermo-chemical table is built by solving a set of equations 1.11 and 1.12 for all the thermodynamic parameters (initial temperature, pressure) characterizing a premixed flame in an industrial configuration.
Then, during the simulation, the detailed chemistry is replaced by a single progress variable transport equation 1.13 describing all the possible chemical trajectories of the reacting flow.

$$\frac{\partial \rho Y_c}{\partial t} + \nabla(\rho\ \vec{u}\ Y_c) = \nabla(\rho\ D\ \nabla Y_c) + \dot{\omega}_{Y_c} \tag{1.13}$$

Unclosed terms, like the progress variable source term is obtained by reading inside the table $\dot{\omega}_{Y_c} = \dot{\omega}_{Y_c}^{FPI}$.
Under FPI approach a single progress variable is chosen to describe the chemical system.
To describe the dynamics of all intermediate chemical species, the progress variable is defined as a linear combination of a few chemical species [38], eq. 1.14. The choice of the species and their coefficients is critical to accuratey cover the entire chemical evolution and to avoid a refined discretization of the table in the progress variable direction.

$$Y_c = \sum_{l=1}^{N} \alpha_l Y_l \tag{1.14}$$

where α_l is the l^{th} species coefficient, $N \leqslant N_{sp}$ number of chosen species, Y_l a chosen species for the progress variable definition.
For hydrocarbon combustion, a possible definition is based on the carbon monoxide and carbon dioxide mass fraction [33]. For auto-ignition, the fuel mass fraction is also considered in order to cover the low-temperature region [28]:

$$Y_c = Y_{CO} + Y_{CO_2} - Y_{Fuel} \tag{1.15}$$

Typically a normalization is performed so that $c = 0$ in the fresh gases and $c = 1$ in fully burnt ones. The normalization allows a statistical independency between the progress variables and other variables like the mixture fraction bringing simplifications in probability density function approaches used in turbulent combustion modeling [35].

$$Y_c = \frac{Y_{CO} + Y_{CO_2} - Y_{Fuel}}{Y_{CO}^{eq} + Y_{CO_2}^{eq} - Y_{Fuel}^{eq}} \tag{1.16}$$

where Y^{eq} stands for the equilibrium state of the species.
Initially capable of reproducing laminar flames [38], the FPI approach was coupled with the presumed probability density function (PDF) to perform modeling of premixed turbulent combustion [35].

In applications with chemical composition heterogeneities, a quantity called mixture fraction Z is conveniently defined in order to locally describe the fuel-air mixing [72]. The mixture fraction allows to examine the flame structure inside the mixing region. At each given position and time, a correspondence between the mixture fraction and the equivalence ratio can be established. For example if nitrogen is considered a chemically inactive species, the relation between the mixture fraction Z and the equivalence ratio ϕ is the following:

$$Z(\phi) = \frac{\phi(1 - Y_{N_2})}{s + (1 - Y_{N_2})\phi} \tag{1.17}$$

where s is the stoichiometric fuel/air mass ratio and Y_{N_2} is the nitrogen mass fraction in the oxidizer stream.

A premixed flamelet approach was proposed by Gicquel [38]. In order to take into account the local composition variations the thermo-chemical tables are built for a given range of equivalence ratios using a set of 1-D laminar premixed flames.

The mixture fraction at a given position and time is obtained by solving the following transport equation:

$$\frac{\partial \rho Z}{\partial t} + \nabla(\rho\ \vec{u}\ Z) = \nabla(\rho\ D\ \nabla Z) \tag{1.18}$$

This technique was used to model a premixed turbulent flame diluted by hot products at a different equivalence ratio. As premixed character of the reactive layer is not altered, the chemistry can be tabulated by premixed flamelets [35]. It had been proved [31] that the FPI premixed flamelet approach can be accurately applied to partially-premixed flames if the fuel-oxidizer mixture equivalence ratio takes values within the flammability limit. For rich fuel-oxidizer streams, diffusion across iso-mixture fractious are important. Chemical trajectories deviate from the premixed flamelet manifold. In regions where the chemistry is slower, mainly when the equivalence ratios are outside the flammability limits, the fluxes through isomixture fraction may compete and dominate the flame response. In rich premixed flame in a counter-flow configuration against air, Fiorina et al. [31] proposed to use an index approach to identify between premixed burning layers that are dominated by the chemical reaction and diffusive burning layers that are sensitive to the strain rate imposed to the flame.

1.3.3.2 Diffusion flames

The premixed flamelet tabulation misses a basic properties of rich partially premixed and diffusion flames [34], the mass diffusion through iso-equivalence ratios surfaces. The diffusion regions in complex geometry configurations should be perceived like a group of laminar diffusion flames [59]. The time needed to generate one of the diffusion flamelets using a reduced 59 species mechanism [80] is one week [59]. For engine applications, thousands of flamelets are required to cover the temperature, pressure and equivalence ratio changes and consequently CPU time limits the use of this approach.

1.3.3.3 Auto-ignition

1.3.3.3.1 Tabulated Kinetics for Ignition

To acquire knowledge and thus in order to be able to control the ignition occurrence in internal combustion engines, auto-ignition models need to be integrated in the 3-D CFD codes.
A manner to locally detect the ignition (as a function of the temperature T, the pressure p, the equivalence ratio ϕ and of the fraction of dilution gases EGR) is to transport [53] an intermediate species $\tilde{Y_I}$ that will locally detect the moment when the condition of auto-ignition are reached. For example, under the assumption of a linear production of the intermediate species in a homogeneous flow, the appearance of the precursor is dictated by the equation 1.19.

$$\frac{d\tilde{Y_I}}{dt} = \frac{1}{\tau_{HT}} \tag{1.19}$$

This equation says that the critical precursor value, usually unity, which triggers the chemical oxidation reaction of the fuel is obtained from the knowledge of the auto-ignition delay τ_{HT}. General expression can be found in literature with more realistic non-linear production of the precursor [53] and also with convection and diffusion behaviour [54] but the concept remains the same.
In a homogeneous mixture for a constant pressure or volume process, the auto-ignition delay τ_{HT} is obtained by integrating the equation 1.19 bet-

ween the initial time t=0 when $\tilde{Y_I} = 0$ and the ignition time t_{ignit} when $\tilde{Y_I} = 1$, shown in the Fig. 1.3(a).
In a Homogeneous Charge Compression Ignition ($HCCI$) engine or in a Rapid Compression Machine (RCM), the fuel and the intake air are mixed and then compressed and heated. Thus the temperature of the reactive mixture is continuously increasing and the auto-ignition delay $\tau_{HT}(t)$ is progressively reduced during compression, in broad outline in figure 1.3(c) and leading to a non-linear production of the fictitious intermediate species, shown in the diagram 1.3(b).
For Diesel or HCCI engines empirical expressions for the auto-ignition delay time were proposed conditioned by the properties of the fresh gases [21, 53, 76]. As an example, the relationship developed in [76] and presented in equation 1.20 for the ignition delay time entails the air density ρ, the air temperature T and the molar concentration of fuel $Fuel$, and oxygen, O_2.

$$\tau_{HT} = A(O_2)^{\alpha}(Fuel)^{\beta}(\rho)^{\gamma}e^{\frac{T_a}{T}} \tag{1.20}$$

Figure 1.4 is a plot of the ignition delay times and of the precursor for an engine operating on compression ignition of homogeneous mixture of Diesel fuel and air for a compression ratio of 8:1 and 50% EGR rate and using the analytical relation 1.20.
Although the analytical relations are numerically advantageous, the constants A, α, β, γ and the activation temperature T_a depend on engine configuration and operating conditions, radically restricting their use.
An alternative is to use the Tabulated Kinetics for Ignition (TKI) [20] model which proposes to calculate the local delay times by interpolation inside an ignition delay database created a priori. Each delay time in the database is calculated by constant pressure homogeneous reactors performed for all pressures, fresh gases temperatures, equivalence ratios and EGR possibly encountered in an engine. Thus by using TKI model the tabulated delays are given by complex chemistry calculations. In order to cover the cold flame regime with the TKI model, the tabulation of the low temperature ignition delays τ_{LT} was initiated in [20] following the same procedure as the one presented above for the high temperature delays τ_{HT} and considering that 10% of the heat is released HR_{LT} during

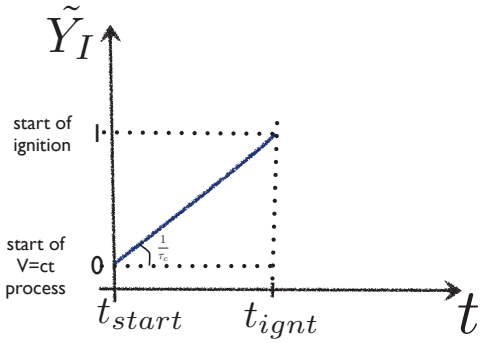

(a) Constant volume $\tilde{Y}_I$

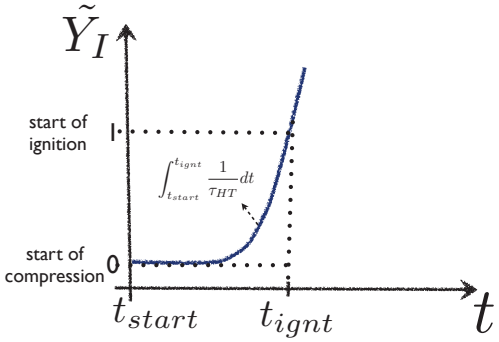

(b) Variable volume $\tilde{Y}_I$

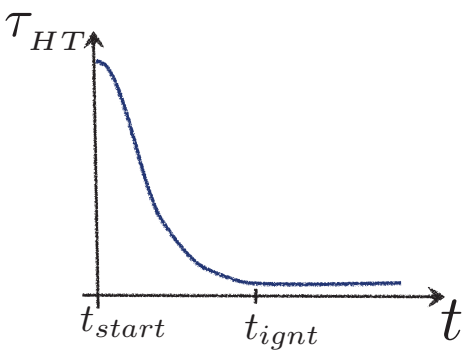

(c) Variable volume τ_{HT}

Figure 1.3 : *Temporal evolution of a fictitious intermediate species mass fraction and of the main ignition delay times*

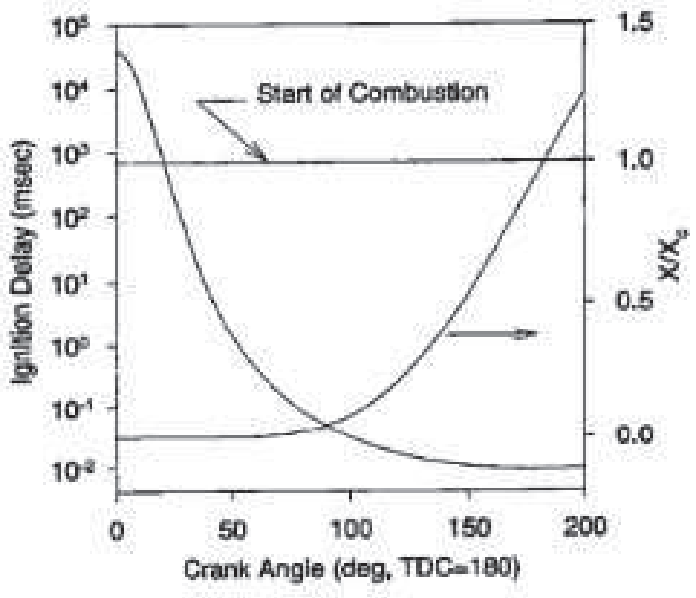

Figure 1.4 : *Temporal evolution of the main ignition delay times for a 8:1 CR and* 50% *EGR HCCI engines [76].*

the occurrence of a cool flame [20] or can be also tabulated by using complex chemistry calculations [15].
After the precursor $\tilde{Y}_I$ reaches the unity value, the fuel decomposition is activated under a characteristic consumption time τ_c.

$$\frac{d\tilde{Y_F}}{dt} = -\frac{1}{\tau_c} \tag{1.21}$$

In broad outline in figure 1.5 gives the evolution of the fuel mass fraction in a variable volume homogeneous 0-D reactor under the TKI approach. The TKI model was used for SI engines both RANS and LES [54] and also CI engines, mainly RANS. It was conceived and mainly used in the framework of Extended Coherent Flame Model 3-Zones $ECFM3Z$ or the LES version $ECFM - LES$ combustion models [54] and allowed prediction of auto-ignition in Diesel and gasoline engines.
A further development of the model [15] was proposed to replace the high

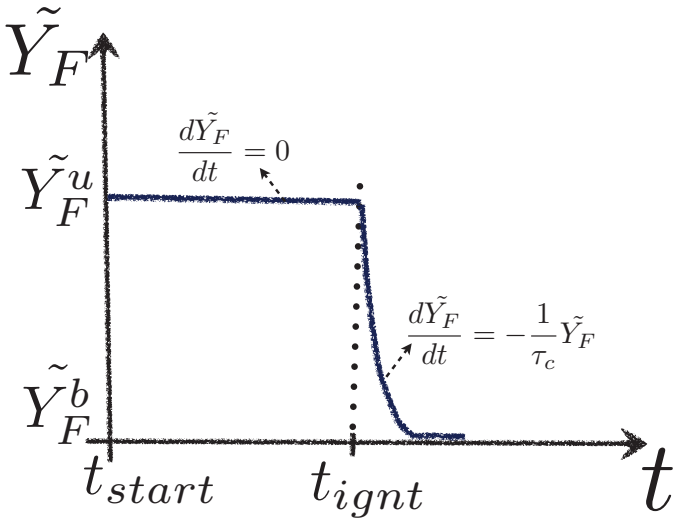

Figure 1.5 : *Temporal evolution of the fuel mass fraction*

temperature ignition delays by the tabulation of the progress variable production rates $\tilde{\dot{\omega}}_c$ as a function of the thermodynamic conditions (T, p, ϕ, EGR) and discrete values of the progress variable $\tilde{c}$. Thus the model evolves towards the more accurate chemical models presented in the following section.

1.3.3.3.2 0-D reactors tabulation

Auto-ignition regions in complex geometry configuration are not mapped by a flame but by a collection of auto-ignition of 0-D homogeneous reactors but using the same methodology.

$$\rho \frac{dY_k}{dt} = \dot{\omega}_k, \qquad k = 1, ..., N_{sp} \tag{1.22}$$

The chemical databases based on premixed or diffusion flames cannot recall the auto-ignition since they do not take into account this phenomenon. The idea to choose 0-D homogeneous reactor in the auto-ignition case seems coherent [28]. However for ICE applications specific difficulties appear and are discussed in the following.

An adiabatic closed system is represented by the mass conservation of each species, equation 1.22 together with the conservation of the total energy. For the development of the thermo-chemical table, one can argue wether the progress variable should evolve either at constant density and internal energy (ρ, e) and thus solving the equation 1.23a or at constant pressure and enthalpy (p, h) and thus using the equation 1.23b for the 0-D reactor computations.

$$C_v \frac{dT}{dt} = -\frac{1}{\rho} \sum_{k=1}^{N_{sp}} e_k \dot{\omega_k} \tag{1.23a}$$

$$C_p \frac{dT}{dt} = -\frac{1}{\rho} \sum_{k=1}^{N_{sp}} h_k \dot{\omega_k} \tag{1.23b}$$

The choice is obvious in the case of stationary combustors at constant pressure then 0-D constant pressure reactors are used by solving the equation 1.23b and if the auto-ignition would take place at constant volume and then 0-D constant volume reactors are suitable by solving equation 1.23a. However, for engine configuration, neither the pressure nor the volume are constant. Indeed when writing the total energy conservation for an adiabatic, closed system undergoing a volume change in the internal energy form, equation 1.24a, the temporal density evolution role is underlined $\frac{d\rho}{dt}$ and in the enthalpy form, equation 1.24b, the temporal pressure evolution role is underlined $\frac{dp}{dt}$.

$$C_v \frac{dT}{dt} = -\frac{1}{\rho} \sum_{k=1}^{N_{sp}} e_k \dot{\omega_k} + \frac{p}{\rho} \frac{d\rho}{dt} \tag{1.24a}$$

$$C_p \frac{dT}{dt} = -\frac{1}{\rho} \sum_{k=1}^{N_{sp}} h_k \dot{\omega_k} + \frac{1}{\rho} \frac{dp}{dt} \tag{1.24b}$$

Embouazza [28] found that the combustion inside an engine depends more on the pressure evolution than on the density evolution. This behavior is shown in figure 1.6 from [28] which compares the reaction rate of the

progress variable as a function of the progress variable calculated by a detailed chemical kinetics, with a tabulated chemistry approach with a constant volume table, and a constant pressure table. Therefore, it is more accurate to use thermo-chemical tables that assemble $0-D$ constant volume reactor, equation 1.23a which supposes that the density change has a minor influence on the chemistry kinetics and promotes the pressure impact on the chemical kinetics.

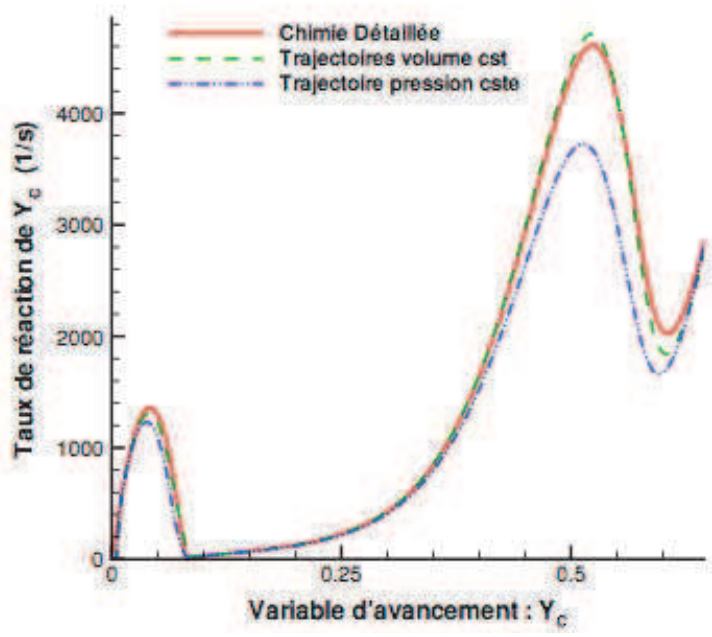

Figure 1.6 : *Evolution of the reaction rate in function of the progress variable: detailed chemistry in full line, tabulated chemistry with constant volume table in dashed line, tabulated chemistry with constant pressure table in dot-dashed liner [28]*

For this reason, Embouazza concluded in [28] that the chemistry manifold for engine applications should be build from $0-D$ constant volume reactors and parametrized by internal energy, density and progress variable (e, ρ, Y_c).
Colin et al. [67] used the tabulated chemistry with constant volume method-

ology initiated by Embouazza [28] for ICE applications but parametrized the table by the input pressure p, temperature T, equivalence ratio ϕ and dilution EGR. This gave prominence to a limitation of the FPI [48] for moving configurations. In fact, the 0-D reactors can go beyond the physical reality in some regions of the expansion stroke.
This was highlighted by Colin et al. [67] in a simplified configuration where the combustion takes place instantaneously at TDC and under the assumption of an isentropic compression and expansion. The input table temperature T^{FPI} is given at any moment by the conservation of the total energy at constant volume and thus at the end of the expansion T_f^{FPI} is given by the relation 1.25 [48]:

$$T_f^{FPI} - T_0 = (T_{com} - T_{ig})(\frac{T_0}{T_{ig}} - 1) \tag{1.25}$$

where T_0 is the initial temperature, T_{ig} is the temperature at TDC before ignition, T_{comb} is the temperature after combustion.
Therefore, as $T_0 \ll T_{ig}$ the input temperature at the end of the expansion T_f^{FPI} is lower than the initial temperature T_0 and can become negative.
A possible way to overcome this limitation is the Variable Volume Tabulated Homogeneous Chemistry ($VVTHC$) approach, recently proposed in [48]. The idea is to compute modified constant volume $0-D$ reactors for the thermo-chemical table:

- before progress variable has reached a value Y_{c0} which occurs at time t_0, the volume of the reactor is kept constant 1.23a
- after progress variable has reached a value Y_{c0}, a linear variation in time of the volume is imposed and thus tabulating the term $\frac{d\rho}{dt}$ of variable volume reactor equation 1.24a for a broad variation of expansions defined by a constant $\dot{V}$.

Finally the $VVTHC$ approach is parametrized by $(P, T, \phi, EGR, Y_c, Y_{c0}, \dot{V})$ and has been combined with the $ECFM3Z$ combustion model. The drawback of this method is that it still needs mass fraction balance equation for the main species [67].

1.3.3.4 Complex flames

1.3.3.4.1 Approximated Diffusion Flame (ADF)

Michel et al. [59] proposed an Approximated Diffusion Flame (ADF) model for reproducing the auto-ignition of heterogeneous mixtures in Diesel engines.

In this model, the tabulation is built from perfectly-stirred reactor calculations instead of laminar diffusion flames calculation. It is obvious that the diffusive effects on the chemical kinetics are lost and have to be introduced a posteriori.

To do so, a diffusive term is added to the progress variable transport equation 1.26.

$$\frac{\partial \rho Y_c}{\partial t} = \dot{\omega}_{Y_c} + \chi \frac{\partial^2 Y_c}{\partial Z^2} \tag{1.26}$$

The equation 1.26 is solved for all ranges of equivalence ratio and integrated in order to obtain a corrected progress variable that is coupled between all mixture fractions. This manipulation allows for the progress variable at a given mixture to depend on the progress variable at all other mixture fractions.

This approach accurately reproduces the cool and the main flame delays for low-strained flames and underestimates the cool and the main flame delay for higher strain rate flames mainly because the differential species diffusion is not taken into account. An improvement is proposed by the authors [59] based on a delay criterium, making of the ADF approach a promising tool for predicting auto-ignition and chemical composition of heterogeneous mixtures like the one found in Diesel engine.

1.3.3.4.2 Multidimensional Flamelet Manifolds (MFM)

The Multidimensional Flamelet Manifolds (MFM) model recently proposed in [63] brings new perspective to the modeling of hybrid (premixed and diffusion) combustion regimes. By making the hypothesis that the species depends only on an advance variable and on the mixture fraction $Y_k(Z, c)$ the evolution of the system is rewritten in the composition space and then equation to be solved is 1.27.

$$\frac{\partial Y_k}{\partial c}\dot{\omega}_c = \chi_Z \frac{\partial^2 Y_k}{\partial Z^2} + \chi_c \frac{\partial^2 Y_k}{\partial c^2} + 2\chi_{Z,c} \frac{\partial^2 Y_k}{\partial Z \partial c} + \dot{\omega}_k \tag{1.27}$$

The main characteristics of a tabulated chemistry approach is that the local variation of species composition and the reaction evolution can be captured from elementary combustion configurations and kept in a database for the range of physical parameters which characterize one specific application. A classification of the tabulated chemistry approaches in terms of the combustion mode for which it was conceived was presented in this section. In the following, the coupling of the tabulated approach with the flow will be discussed.

1.4 Coupling tabulated chemistry with compressible solvers

A challenging task is to couple the thermo-chemical table with compressible solvers. Depending on the particularity of the 3-D engine code mainly, two strategies enable the use of the tabulated chemistry approach:

- only transport equation for the density, momentum, energy and progress variable are solved; species mass fraction are then available by interpolation inside the thermo-chemical database and do not need to be transported by the solver.

  In this case, the only reaction rate that is needed in the table is that of the progress variable $\dot{\omega}_c$. As for the temperature, if the thermo-chemical table had been built at variable pressure, then it would be straightforward deduced from an energy equation.

  For a low Mach flow, an isobaric thermo-chemical table can also be used, but a temperature correction needs to be applied to take into account the compressible effects, as proposed by Vicquelin *et al.* [85]. This option needs highly refined table and was mainly used in compressible DNS solvers for simulating premixed flames [8].

  In the present work we propose to couple a non-adiabatic table with an LES compressible solver. It will be applied to a rapid compression machine simulation in chapter 5.

- along with the transport equation for the density, momentum, energy and progress variable, main species transport equation still need to be solved. In this case, the temperature is reconstructed from the transported species mass fraction and energy. In this case two approaches were proposed [58]:

  - the reaction rate RR formulation for which the species reaction rates $\dot{\omega}_i$ are directly read from a look-up table;
  - the species mass fraction MF formulation for which the species mass fraction Y_i along with the reaction rate for the progress variable $\dot{\omega}_c$ are tabulated; the species source terms $\dot{\omega}_i$ are reconstructed to relax the transported mass fractions towards the mass fraction values stored in the look-up table.

The two approaches were compared in [58] and it was advocated to use the MF formulation rather than the ill-posed RR formulation. The MM tabulation formalism was coupled with a compressible *RANS* code in [67] and successfully applied to a direct injection Diesel engine.

Chapter 2

Chemistry tabulation for ICE applications

This chapter describes a tabulated chemistry approach adapted to Diesel, Homogeneous Charge Compression Ignition (HCCI), Partial Homogeneous Charge Compression Ignition (PHCCI) or Rapid Compression Machine (RCM) combustion. The first part discusses the choice of the surrogate fuel. Thereafter, a skeletal mechanism suitable for ICE conditions is chosen as a compromise between a low computational time for the chemical table generation and an accurate ignition delay prediction. In order to describe the chemical evolution of an auto-igniting homogeneous mixture submitted to a continuous volume change, a 3-D subspace is necessary, having as coordinates: the progress variable and two thermodynamical state variables. Both for physical and technical reasons the energy and the density have been preferred in this work. The thermochemical table building methodology will be presented and the table's coordinates discretization benchmark will be defined. The tabulated chemistry strategy is validated by 0-D variable volume simulations.

2.1 Introduction

In order to describe chemical processes in ICEs with a high level of accuracy, the kinetic model for a relevant practical fuel should contain hundreds of species and thousands of reactions. For reasons exposed later on, a 89-species, 387-reactions skeletal kinetic mechanism was employed. In spite of $TFLOPS$ performance in the parallel supercomputer arena, 3-D simulations of ICE with such a complete chemistry description remain out of reach. As CPU-time requirements are extremely stringent, tabulated chemistry techniques have been developed to describe turbulent combustion regimes [23, 28, 35, 36, 38, 56, 62, 64]. Under this approach, the thermo-chemical quantities are expressed as a function of a reduced set of n variables. If n is sufficiently small compared to the number of the chemical species N_{sp} involved in the reaction scheme, this hypothesis will drastically reduce the number of balance equations to be solved, hence simplifying turbulent combustion modeling. The aim of the present work is to develop a chemistry tabulation method valid simultaneously in the compression stroke, the reaction phase and the power stroke of an ICE. First, the database construction is briefly presented and afterwards, a solution to take into account the low energy regions of the power stroke is proposed.
During the computation, the thermo-chemical table is stored on the local memory of each processor. The table's size becomes a significant issue, therefore the minimum and the maximum range and the discretization of each coordinate need to be optimized. For validation, variable volume homogeneous auto-ignition simulations are presented, by employing both a detailed reaction mechanism and a tabulated chemistry approach.

2.2 Primary reference fuel

To overcome uncertainties associated with the wide range of organic chemical compounds constituents of the Diesel fuel, highlighted in Fig. 2.1 [70], Primary Reference Fuels (PFR) are used in multi-dimensional CFD models for simulating engine combustion. Unlike for gasoline engines, in Diesel engines when the temperature and the pressure in the cylinder reach appropriate levels, auto-ignition occurs without use of any spark.

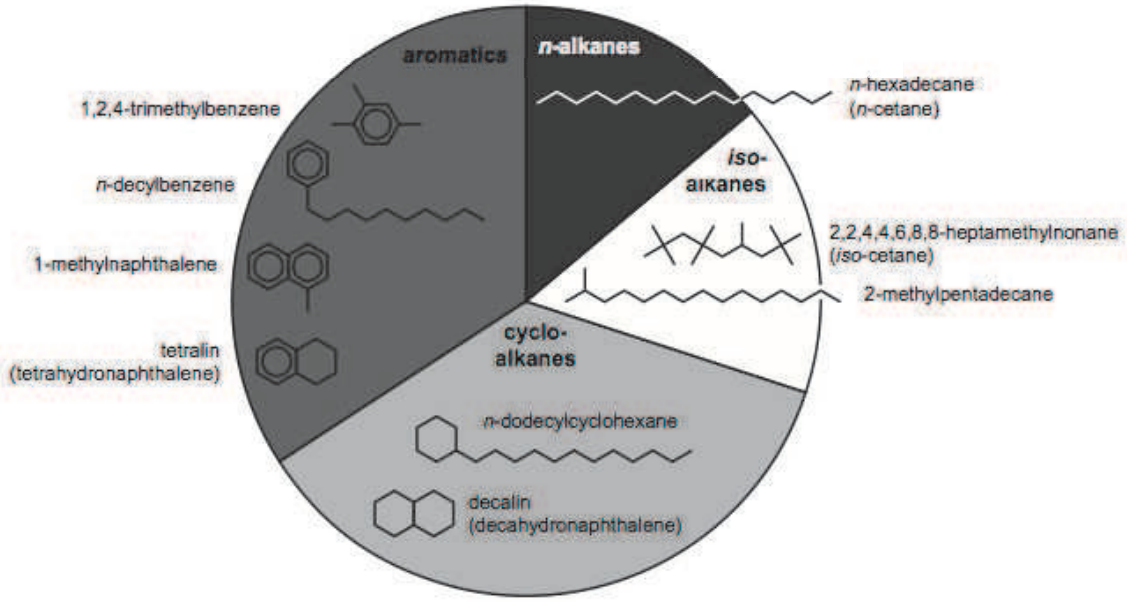

Figure 2.1 : *Relative amounts of various chemical classes in Diesel fuel [70]*

The time span between the moment when the mixture has reached the ignition conditions and the sudden acceleration of reaction rate is referred to as auto-ignition delay.
Normal heptane ($n - C_7H_{16}$) is a commonly-used surrogate component to stand in for Diesel fuels [70]. The choice of this specific n-alkane is supported by the following arguments:

- the ability to properly predict the auto-ignition delay,
- the cetane numbers are approximately 56 for n-heptane and Diesel fuel,
- the good reproduction of the cool flame regime.

The oxidation reactions of $n - C_7H_{16}$ start by a hydrogen atom abstraction from the carbonated fuel, see figure 2.2. Due to thermodynamical considerations the hydrogen extraction is very likely performed either by the hydroxyl radical $\dot{O}H$ or by the hydroperoxyl radical $\dot{H}O_2$, and less probable by the oxygen molecule O_2 because this initiation reaction is highly endothermic.
Then, the alkyl radicals sink by choosing preferential kinetic path depending on the energy that the system is able to spend in order to activate a specific pivotal reaction. This behavior can be observed for hydrocarbons

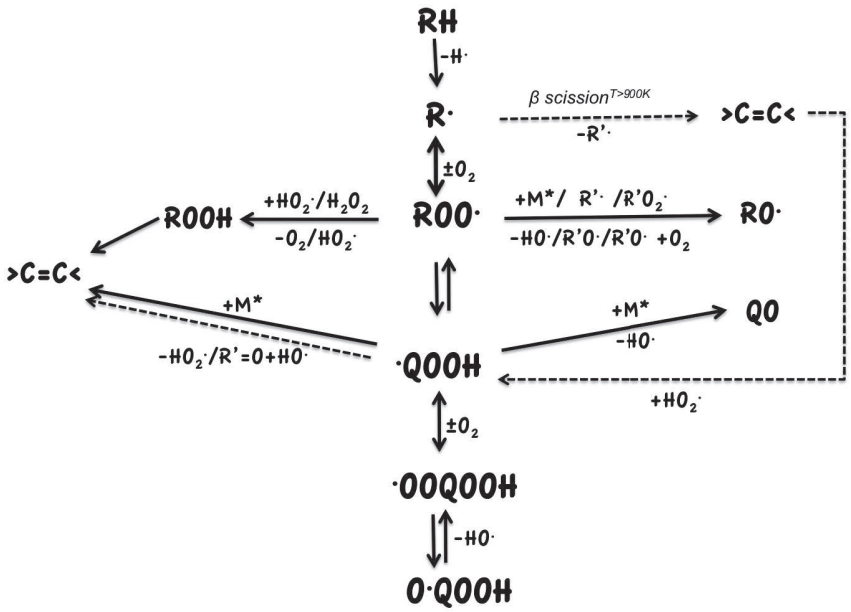

Figure 2.2 : *$n-C_7H_{16}$ primary oxidation reactions (full line: low temperature reaction path, dashed line: high temperature reaction path)*

which have above a certain number of carbon atoms, e.g. for n-heptane or iso-octane:

- At high temperatures, the activation energy barrier of the β-scission of the alkyl radicals is overcome and the more reactive smaller olefines are formed and easily lead to products (follow the dashed line path in the Fig. 2.2).

- At low/intermediate temperatures, i.e. below 900 K for $n-C_7H_{16}$, the oxidation has a different kinetic path behavior. Indeed, the β-scission of alkyl radicals is energetically disabled. The condition for the reaction to take place is that the alkyl radicals undergo two further O_2 additions [18], forming a very unstable radical, the hydroperoxy alkyleperoxy $\dot{O}OQOOH$ that breaks up to products (follow the horizontal full line in the Fig. 2.2). In the time evolution of an auto-igniting $n-C_xH_{2x+2}|_{x\geqslant 7}-air$ mixture at relatively low temperatures this may appear as a double step phenomenon, called cool flame and main flame, respectively.

- At the transition between the two temperature regions a Negative Temperature Coefficient NTC regime appears, where ignition delay time increases when increasing initial temperature.

Notice also that the main auto-ignition is dictated by a chain branching reaction, associated with the leading H_2O_2 molecule. Being relatively stable at low temperature, the hydroperoxyde H_2O_2 accumulates as the process develops. Once the temperature rises, the oxygen bound $O-O$ breaks producing the very reactive hydroxyl radicals $\dot{O}H$ that mark the main ignition, by rapidly consuming the fuel by a propagative reaction.

2.3 Chemical kinetic mechanism

The kinetic mechanisms should be able to accurately reproduce the chemical process for the particular application for which it has been developed i.e. to provide a comprehensive representation of in-cylinder Diesel combustion. As the table cannot outperform the prediction of the starting kinetic mechanism, special precautions are to be made when selecting the mechanism for the thermo-chemical table generation.
For this purpose a comparative assessment of a wide range of mechanism for n-heptane primary reference fuel will be performed in this study. The objective is to choose a mechanism valid at engine conditions, i.e. at pressure above the atmospheric pressure covering both low-temperature and high-temperature oxidations. Obviously, for efficiency in terms of table generation time, a low species number mechanism would be better. In the frame of this work, a comparative assessment of five n-heptane kinetic mechanisms with 274, 256, 188, 89 and 53 species is done. As observed by Law et al. [55], there is an almost linear correlation between the number of species and the number of reactions with a factor of 5, given roughly the number of reactions of the above mechanisms. The exact values are summarized in Table 2.1. The mechanisms have been selected between a broad range of mechanisms available in the literature on the criterium of including both aforementioned regimes: high and low/intermediate temperatures.
All the mechanisms chosen, except $KUCRS$, represent a reduced version of the more detailed Curran's mechanism with 561 species and 2539 elementary reactions, made available by Lawrence-Livermore National Labs

Mechanism	Species	Reactions	Ref
Golovitchev 53	53	281	[80]
KUCRS 274	274	919	[60]
LLNL 256	256	1369	[57]
LLNL 188	188	939	[89]
LLNL 89	89	387	[89]

Table 2.1 : *Characteristics of the examined n-heptane kinetic mechanisms*

($LLNL$) [18]. The $LLNL$ 256 and 188 species skeletal mechanisms were derived with a two-stage directed relation graph (DRD) [89]. The 256-species skeletal mechanism covers the range of equivalence ratios from 0.1 to 2.0, for temperatures between 600 K and 1800 K, and for pressures from 0.5 atm to 60 atm. By applying a DRG-aided sensitivity analysis ($DRGASA$) a 88-species skeletal mechanism was obtained [18]. All these skeletal mechanisms were demonstrated to mimic correctly the performances of the detailed mechanism under $HCCI$ conditions.
The Golovitchev mechanism is based on the major reaction paths and sensitivity analysis which allow to eliminate the reactions with small contributions [80]. It has been validated for relatively high pressures $p = 13.5$ to 41 bar and equivalence ratios ranging from 0.5 to 3. Golovitchev mechanism was primarily developed and applied on auto-ignition modeling [80] and [59].
In addition, a Knowledge-basing Utilities for Complex Reaction Systems ($KUCRS$) mechanism with 274 species was also considered. $KUCRS$ mechanism was created by using the utility software library specialized for the development of gas-phase chemical kinetic models of combustion reaction systems [60].
All chosen mechanisms were originally developed and validated for both low and high temperatures. They exhibit the characteristic NTC regime as illustrated by figure 2.3(a). The semi-detailed $LLNL$ mechanisms give similar results, but they are in discrepancy with the $KUCRS$ and Golovitchev mechanisms which give faster delay times.
The difference between kinetic mechanisms is a common issue in the specialized literature and generally antagonistic results are obtained when compared with different experimental sources: shock tubes, plug flow re-

actors, jet stirred flow reactors or rapid compression machines. Founti et al [51] tested various n-heptane mechanisms, by performing delay time validation and temperature and species mass concentration validation. The conclusion (see Table 3, page 3201 in [51]) was favorable to Curran's $LLNL$ 561 species mechanism, which gives a good agreement for all tests and for all experiments performed. This limited the selection to the semi-detailed mechanism obtained from the detailed $LLNL$ 561 species. As shown in Fig. 2.3(b), the 256 and 188 mechanisms are at least 5 times more CPU expensive than the 89-species LLNL mechanism with a similar ignition delay prediction. Therefore the 89-species LLNL mechanism is a good compromise for the thermo-chemical table generation used for the rapid compression machine study in chapter 5.
Remark that, although the thermo-chemical table generation methodology is regardless of the mechanism, the choice of the kinetics mechanism is critical for the quality of the inclosed thermo-chemical information with respect to a given application.

2.4 Verifying ignition delay predictions of the 89-species skeletal mechanism for n-heptane

This section focuses on the testing and validation of the ignition delay prediction of the chosen 89-species skeletal mechanism over a wide range of engine conditions.
A comparison of the measured main ignition delay times performed in shock-tube by Ciezki [13] with 0-D isochoric simulations was done.
The auto-ignition delays appear to be affected by pressure, temperature, fuel nature and mixture composition [21]. Shock-tube experiments are suited to measure ICE ignition times below 15 ms as they do not feature a slow temperature heat-up [43].
Ciezki [13] analyzed ignition delay times for undiluted n-heptane/air mixtures in the temperature range from 660 K through 1350 K, equivalence ratios of 0.5 to 2 with air as oxidizer and pressures of 6.5 to 42 bar. Ignition delay calculations are performed by using the $REGATH$ package developed at the EM2C laboratory, by the Numerical Combustion Group, based on the CHEMKIN [50] formalism. An idealized closed homogeneous

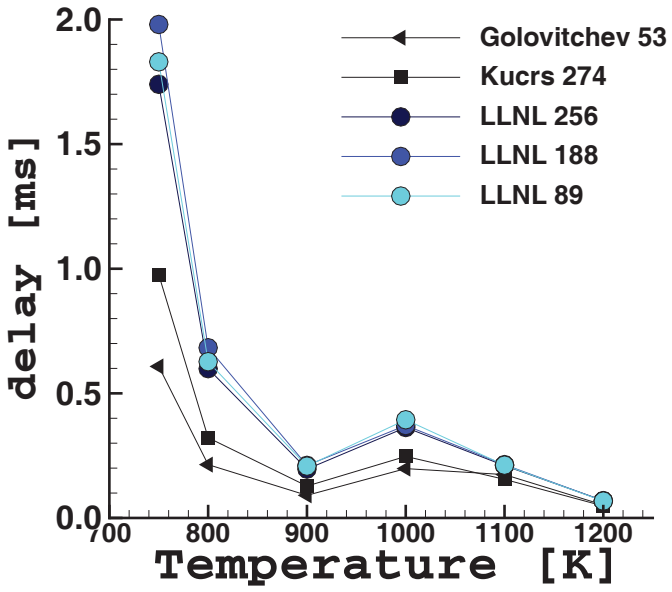

(a) Delay time

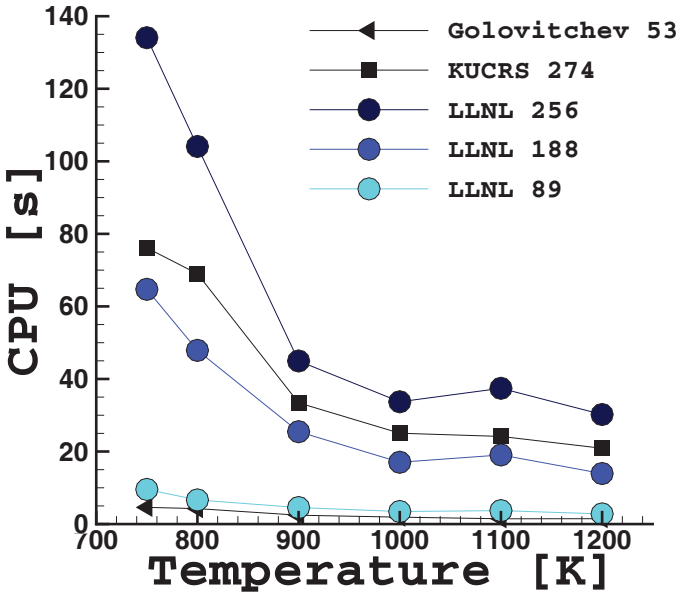

(b) CPU time

Figure 2.3 : *Auto-ignition at constant volume for different chemical kinetics mechanisms: a)Delay time, b)CPU time*

reactor model with a n-heptane 89-species skeletal mechanism was used. The same test was performed by Curran [18] for the detailed $LLNL$ 561-species mechanism, allowing a cross comparison with the main reference mechanism behavior.

Figure 2.4 shows a plot of ignition time versus 1000/temperature, for various pressures and equivalence ratios. Figure 2.4(a) shows current computations with the n-heptane 89-species skeletal mechanism against Ciezki's shock-tube experiments [13]. The figure 2.4(b) shows Curran's computations [18] with the n-heptane 561-species mechanism against the same experiments.
The whole range of temperatures was swiped with temperature increments of 25 K. This covers ignition times over about four orders of magnitude. The main ignition time criterium was based on a limit fuel concentration. Although there are alternative criteria for the determination of ignition times, under the here investigated conditions, similar values were obtained when compared with a temperature inflection point criterium. Some trends in the influence of each parameter on the ignition delay are:

- *The influence of the mixture initial temperature.* Being the time required for the total radical concentration to reach a critical value, the auto-ignition delay is expected to be inversely proportional to the rate of the branching elementary reactions. This signifies that the auto-ignition delay decreases by increasing initial temperature. On the contrary, in the NTC region, due to the competition between the chain-termination and the chain branching reactions, the evolution will be reversed. The comparison with the experimental data shows that the model generates consistent trends. The NTC region, the differential characteristics between low and high octane number fuels, is correctly predicted by both detailed and semi-detailed mechanisms.

- *The influence of the mixture initial pressure.* The increase of pressure restrains the temperature interval where the NTC region exhibits. The shape of the left curves of 2.4(a) and 2.4(b) is almost identical and in agreement with the experimental data. Thus the

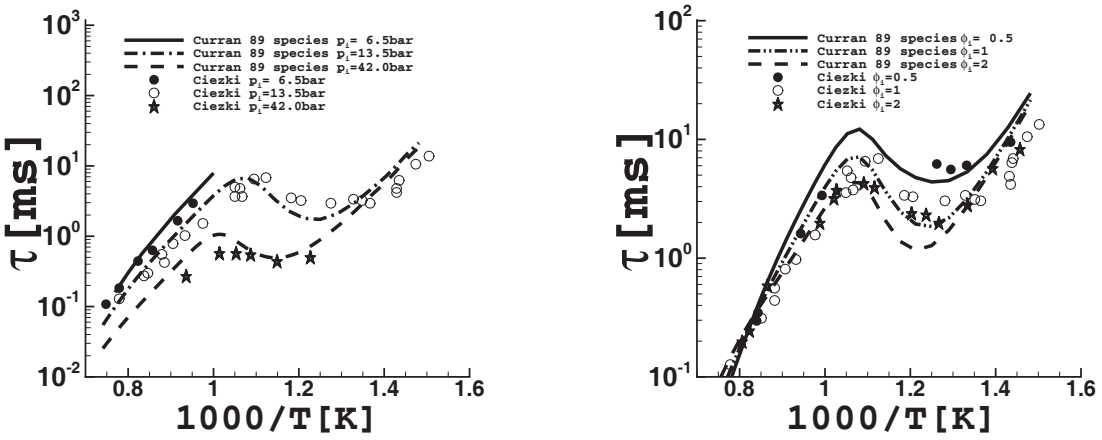

(a) Current work using skeletal n-heptane Curran Mechanism

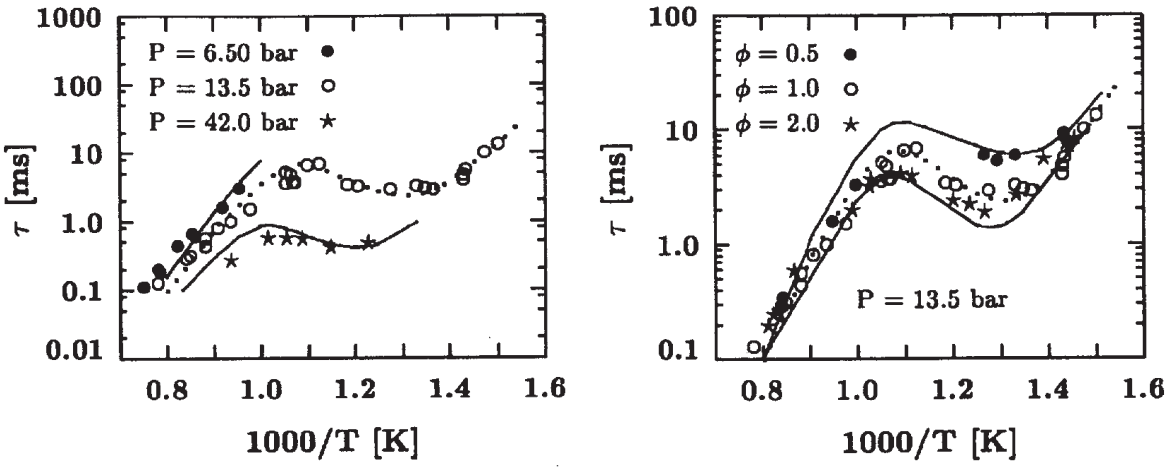

(b) Detailed n-heptane Curran Mechanism [18]

Figure 2.4 : *Auto-ignition delays under engine relevant conditions obtained by Curran's mechanism: a) Current work using skeletal n-heptane mechanism, b) Curran's computations using detailed mechanism [18]*

skeletal mechanism is suitable for high pressure engine conditions.

- *The influence of the mixture equivalence ratio.* The impact of the equivalence ratio is most pronounced in the NTC regime. For the range of temperature considered, below 1350 K, the decrease of

the equivalence ratio yields higher ignition delay times and a less pronounced NTC behavior. The dependency on the equivalence ratio is well represented by the simulation for lean and stoichiometric mixtures. The values slightly disagree for rich mixtures. Particularly, the 89-species skeletal mechanism indicates a more pronounced NTC behavior compared to the experimental results as it was originally developed and validated for lean mixtures.

In conclusion, the ignition delay of lean n-heptane mixtures at high and low/ intermediate temperatures and high pressures can be accurately modeled with the 89-species skeletal mechanism [89] and will be used for the thermo-chemical table generation for internal combustion engine applications.

2.5 The thermo-chemical table generation methodology

In this section the thermo-chemical table building methodology for ICE applications will be introduced. The tabulated thermo-chemistry approach assumes that ICE chemistry can be mapped by a collection of 0-D reactor computations. In order to describe the chemical evolution of an auto-igniting homogeneous mixture submitted to a continuous volume change, a 3-D subspace is necessary, having as coordinates: the progress variable and two thermodynamical state variables.
For n-heptane oxidation, the following definition of the progress variable (Eq. 2.1) enables to tackle initial fuel decomposition, the cool flame and the main flame as suggested by [28]:

$$Y_c = Y_{CO_2} + Y_{CO} - Y_{C_7H_{16}} \tag{2.1}$$

The normalized progress variable reads:

$$c^* = \frac{Y_{CO_2} + Y_{CO} - Y_{C_7H_{16}} + Y^0_{C_7H_{16}}}{Y^{eq}_{CO_2} + Y^{eq}_{CO} - Y^{eq}_{C_7H_{16}} + Y^0_{C_7H_{16}}} \tag{2.2}$$

where Y^{eq} and Y^0 correspond to the equilibrium and initial mass fractions respectively.

The associated progress variable reaction rate is defined as:

$$\dot{\omega}_{Y_c} = \dot{\omega}_{CO_2} + \dot{\omega}_{CO} - \dot{\omega}_{C_7H_{16}} \tag{2.3}$$

Because of work exchanges during the piston displacement, the configuration of the engine causes changes in the energy (chemical plus sensible):

$$e = \int_{T_0}^{T} C_v dT - \frac{RT_0}{W} + \sum_{k=1}^{N_{sp}} \triangle h^0_{f,k} Y_k \tag{2.4}$$

Similarly, as the system is closed during the ignition cycle of ICE, the density ρ varies with time because of the combustion chamber volume changes. The choice of these thermodynamical state variables ρ and e as coordinates of the thermo-chemical database is argued in section 1.3.3.1. Density and energy ranges covered by realistic engine computations are $[\rho^-, \rho^+]$ and $[e^-, e^+]$, ρ^- and ρ^+ are respectively the minimal and maximal densities, e^- and e^+ are the minimal and maximal energies encountered during the compression and power strokes, respectively. To build up the database, a set of 0-D reactors at constant volume and constant energy is computed and then thermo-chemical parameters are tabulated as a function of specified normalized coordinates (ρ^*, e^*, c^*) varying between 0 and 1 [28, 47]. However, constant volume calculations cannot cover the entire range of energy. Indeed, a minimal energy e_{ai} exists, below which auto-ignition will not occur under realistic delay time. This point was also mentioned by Colin et al. [47] who found that the energies during the power stroke of an engine would become too low to be tabulated using a constant volume reactor.

We aim at illustrating the fact that constant volume 0-D reactors can not cover the entire behavior of a variable volume computation. For this purpose, we plotted in Fig. 2.5 the temperature evolution during a variable volume computation (in full line). On the same plot is shown the input temperature T_0 of a database (in dashed line) calculated by resolving the internal energy $e(T_0, Y_{k0})$, see equation 2.4, in each point of the variable volume computation. In order to obtain the temperature, the input composition Y_{k_0} is used as the real composition Y_k is not available during the table generation.

The following situations are identified:

region a: the compression phase before the reaction occurs; the composition does not change drastically from the initial composition $Y_{ka} \approx Y_{k0}, k = 1, N_{sp}$, thus an input temperature T_{a0} parameter can be obtained by resolving equation 2.4 and it will be close to the variable volume computation temperature $T_{a0} \approx T_a$

region b: the reaction occurs either at the end of compression or start of the power stroke; the composition changes drastically from the initial composition $Y_{kb} \neq Y_{k0}, k = 1, N_{sp}$, an input temperature T_{a0} parameter can be obtained by resolving equation 2.4 but the value is lower than the variable volume computation temperature $T_{b0} \neq T_b$ because the chemical energy is overestimated $\sum_{k=1}^{N_{sp}} \triangle h^0_{f,k} Y_{kb} < \sum_{k=1}^{N_{sp}} \triangle h^0_{f,k} Y_{k0}$

region c: the reaction occurred and the internal energy decreases continuously due to the descending motion of piston in the power stroke; the composition is close to equilibrium at the given thermodynamical condition (e_c, ρ_c), ${Y_{kc}}^{eq} \approx Y_{kc} \neq Y_{k0}, k = 1, N_{sp}$, an input temperature T_{c0} parameter still can be defined by resolving equation 2.4 also is very different from the variable volume computation temperature $T_{c0} \neq T_c$

region d: the reaction occurred; the internal energy reached the limit e_{ai} where the constant volume computations do not ignite under a realistic time considered in this work as 50 s; the composition is close to equilibrium at the given thermodynamical condition (e_d, ρ_d), ${Y_{kd}}^{eq} \approx Y_{kd} \neq Y_{k0}, k = 1, N_{sp}$; the input temperature T_{d0} parameter has unphysical low value (even negative value).

If the evolution during the region a, b and c can be tabulated from constant volume computations (examples are given in the low part of the Fig. 2.5), they cannot cover the low part of the power stroke, region d.

A methodology to tabulate the chemistry over the whole range of energy $[e^-,\ e^+]$ is proposed. A thermo-chemical table made of 0-D constant volume reactors is first computed over the range $[\rho^-,\ \rho^+]$ and $[e_{ai},\ e^+]$ by solving the following set of equations:

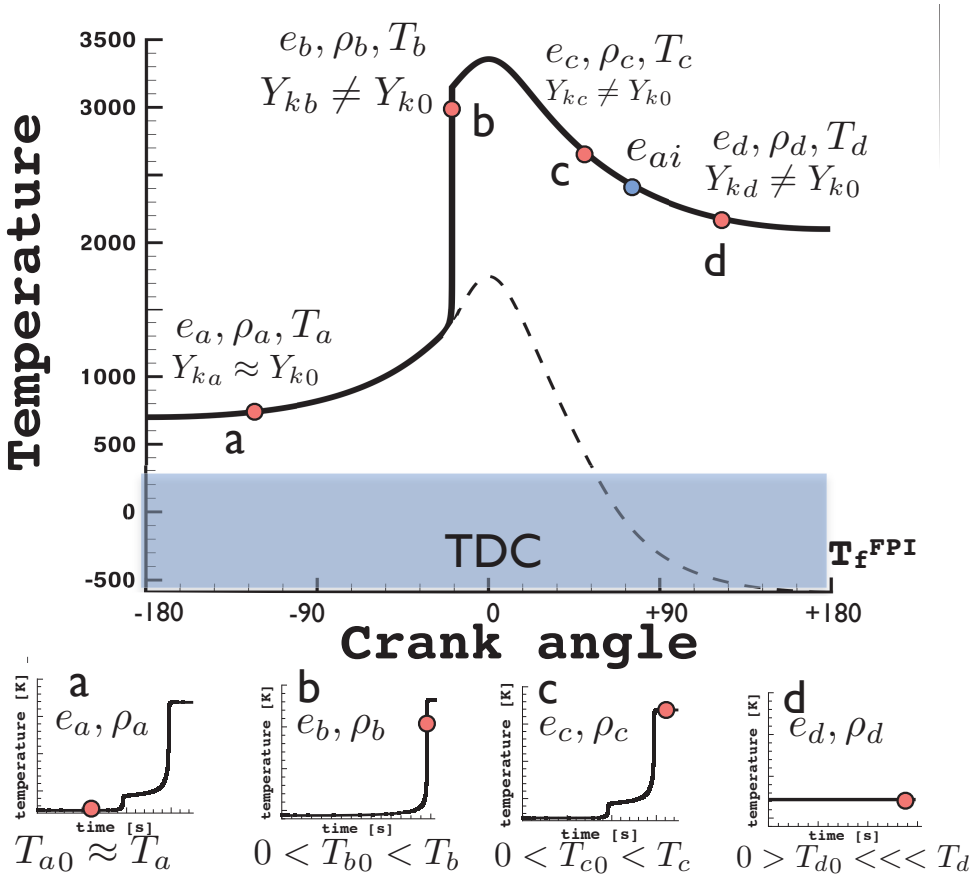

Figure 2.5 : *Temporal evolution of the temperature in an engine (full line) of the input temperature of the thermo-chemical table (dashed line); examples of 0-D constant volume reactor used for the thermo-chemical table.*

$$\begin{cases} \rho \dfrac{dY_k}{dt} = \dot{\omega}_k, k = 1, ..., N_{sp} \\ \dfrac{de}{dt} = 0 \end{cases} \tag{2.5}$$

The grey region of the Fig. 2.6 represents the 2-D projection on the normalized (c, e) subspace. As the carbon chemistry characteristic time is very fast ($\sim 10^{-9}s$) compared to the piston motion (1 degree of crank angle is covered in $\sim 10^{-4}s$ at 1500 rpm) the composition state is in practice very close to thermodynamic equilibrium during the power stroke.

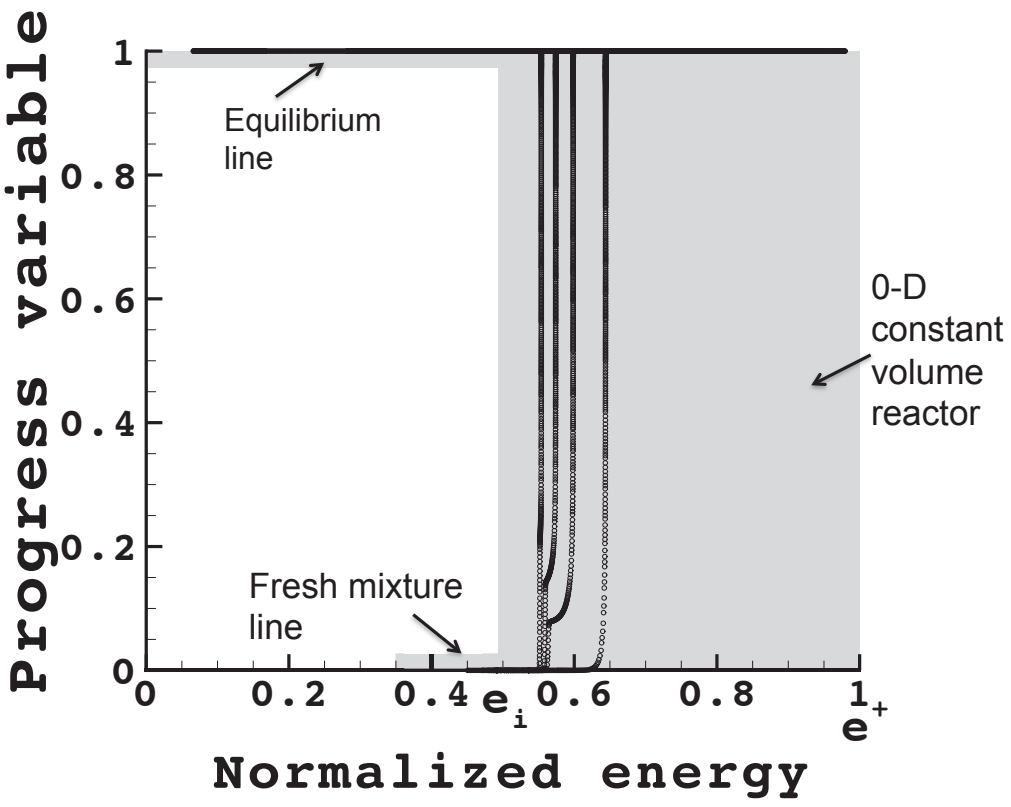

Figure 2.6 : *Grey region: 2-D projection in (c, e) subspace of the thermochemical . Symbols: trajectories accessed by 0-D variable volume computations.*

Therefore it can be assumed that the gas state below e_{ai} is either the fresh mixture or the equilibrium. In fact, intermediate states ($0 < c < 1$) are never accessed for $e < e_{ai}$ in realistic engines. These limits are represented by the bold horizontal grey lines defined by $c = 1$ and $c = 0$. Trajectories in (c, e) subspace followed by variable volume computations are plotted in Fig. 2.6. It shows that for $e < e_{ai}$, the domain between $0 < c < 1$ is never accessed by the variable volume chemical trajectories.

2.6 Thermo-chemical table discretization benchmark for auto-ignition delay prediction

In order to reduce the thermo-chemical table size, an optimization of the coordinates discretization step is required. The discretization requirements of each of the database coordinates will be defined with respect to an accurate estimation of the delay time and of the temperature and the carbon monoxide CO species mass fraction evolution.

2.6.1 Energy discretization step

As the database was conceived for a discrete set of energy points, an error $\epsilon_\psi(\Delta e)$ is introduced for a thermo-chemical variable ψ calculated by interpolation in the table, as depicted in Fig.2.7.

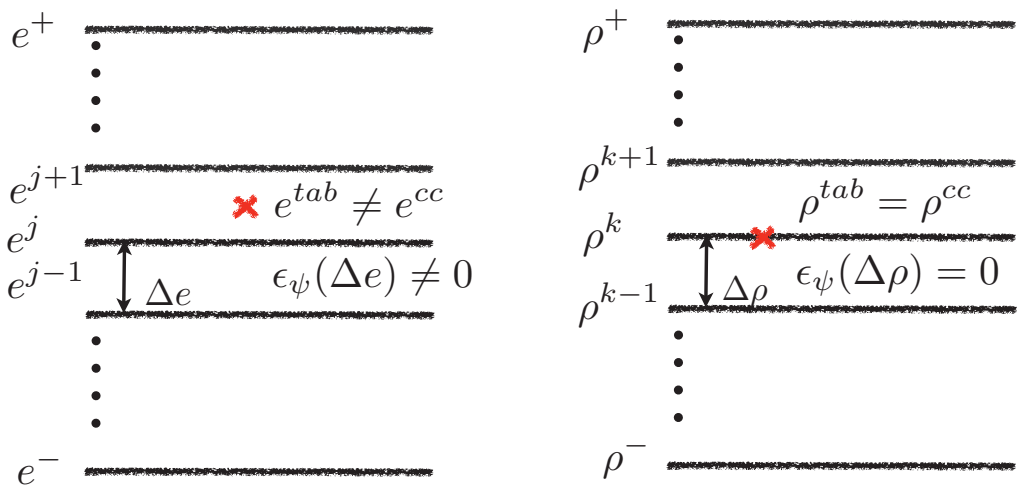

Figure 2.7 : *Interpolation error on a thermo-chemical variable ψ within the range of a discrete set of known energy points (e^{cc}, ρ^{cc} -complex chemistry energy,density; e^{tab}, ρ^{tab} - tabulated chemistry energy, density; $\epsilon_\psi(\Delta e)$, $\epsilon_\psi(\Delta\rho)$ - interpolation error induced by the energy, density discretization related the thermo-chemical variable ψ)*

The foremost feature of the table is to have low linear interpolation errors $\epsilon_\psi(\Delta e)$ so as to not create gaps in the ignition-delay estimation. The

objective is to find the discretization step in the energy coordinate Δe that will guarantee enough low interpolation errors. In order to not interfere with the errors due to the interpolation in the density space, a discrete value of density is considered $\rho^k = \rho^{tab} = \rho^{cc}$. Likewise, a low discretization step in the progress variable coordinate was generally used.

To estimate the optimum energy step Δe, thermo-chemical tables with increasing energy discretization steps were build. The tables were conceived for a lean 79% CO_2 and N_2 diluted mixture. The energy steps, constant during each table generation (20 thermo-chemical databases in total), are given in Table 2.2 together with the corresponding initial temperature steps ΔT. Two cases were considered: a high initial temperature case where only the main ignition occurs and a low initial temperature case where both cool and main flame appear.

Δe $[kJ/kg]$	ΔT $[K]$ **for** $\rho = 4.5$ kg/m^3	ΔT $[K]$ **for** $\rho = 5.73$ kg/m^3
11	10	11
22	21	22
33	31	33
44	42	45
55	52	56
66	62	68
77	73	79
88	84	91
99	94	102
110	105	114

Table 2.2 : *Energy and initial temperature steps in the thermo-chemical tables for high initial temperature case ($\rho = 4.5$ kg/m^3) and low initial temperature case ($\rho = 5.73$ kg/m^3)*

The different energy step discretization Δe tables were tested on constant volume computations performed with an initial energy situated inbetween two discrete known energy points of the table $[e^j, e^{j+1}]$ and a density corresponding to a discrete value in the database , see Fig. 2.7. Simulations were performed by using the $REGATH$ $0-D$ code to solve the system of equations 2.6 in idealized homogeneous reactor conditions

with the 89-species skeletal mechanism. For the tabulated chemistry approach, a specific solver was developed for the system of equations 2.7.

Chemical kinetic mechanism

$$\begin{cases} \dfrac{d\rho}{dt} = 0 \\ \rho\dfrac{dY_k}{dt} = \dot{\omega}_k, k = 1, ..., N_{sp} \\ \dfrac{de}{dt} = 0 \end{cases} \quad (2.6)$$

Tabulated chemistry approach

$$\begin{cases} \dfrac{d\rho}{dt} = 0 \\ \rho\dfrac{dY_c}{dt} = \dot{\omega}_{Y_c}^{tab} \\ \dfrac{de}{dt} = 0 \end{cases} \quad (2.7)$$

The progress variable reaction rate $\dot{\omega}_{Y_c}^{tab}$ in eq. 2.7 is found by linear interpolation in the database.Therefore it will be affected by the error that is introduced due to the energy discretization step $\epsilon_{\dot{\omega}_{Y_c}}(\Delta e)$.
Figure 2.8 shows the temporal evolution of the temperature and of the CO mass fraction using tabulated chemistry with different thermo-chemical table discretization in terms of energy steps (or the corresponding temperature steps given in Table 2.2.)
On the same figure, the detailed chemistry results are given in full line.
This highlights the importance of the table discretization in terms of energy for an accurate prediction of the auto-ignition delay:

- The main ignition delay, see Fig. 2.8(a), is very sensitive to energy discretization, thus errors in the energy values created by the 1^{st} order interpolation in the table impact the auto-ignition delay estimation.

- It seems that the pre-ignition delay times, see Fig. 2.8(b), are less sensitive to the precision in energy than the main ignition delays. This is consistent to the fact that in Curran's 561-species mechanism, the activation energy for the O_2 additions to the alkyl radicals is taken equal to zero [18]. This explains the low temperature pathway independency on the errors on temperature value due to interpolation in the thermo-chemical table.

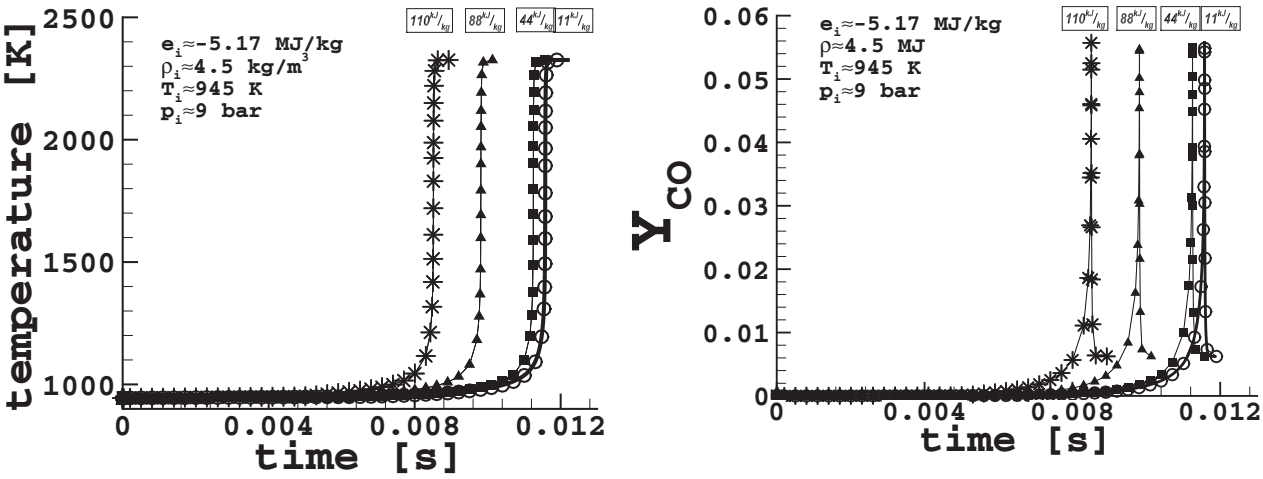

(a) Single-stage ignition chemistry: temperature (left figure) and *CO* mass fraction (right figure) temporal evolution

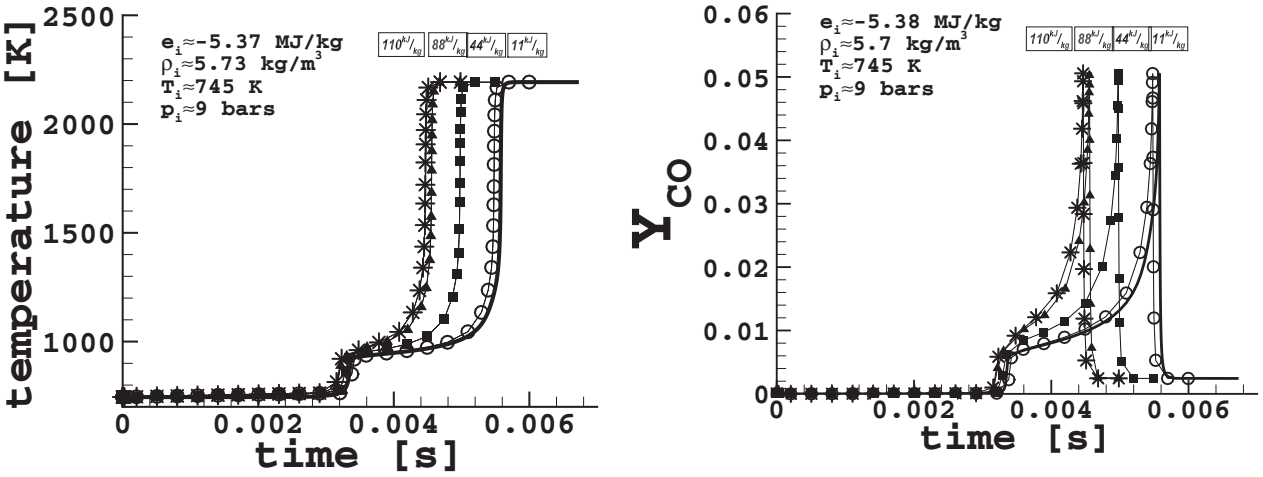

(b) Two-stage ignition chemistry: temperature (left figure) and *CO* mass fraction (right figure) temporal evolution

Figure 2.8 : *Table discretization in the energy (temperature) coordinate: 11 KJ/kg step, 44KJ/kg step, 88KJ/kg step, 110 KJ/kg step*

An overview of the performances of each thermo-chemical table is given in Fig. 2.9. At high temperature, beyond a certain energy discretization step, around 80 kJ/kg, the error on the ignition delay increases very rapidly. For a NTC regime flame, the main ignition-delay error increases

almost linear with the energy discretization step. For a delay time estimation error below 5% between the estimated tabulated delay and the detailed chemistry delay, the discretization in temperature should be below 20 J.

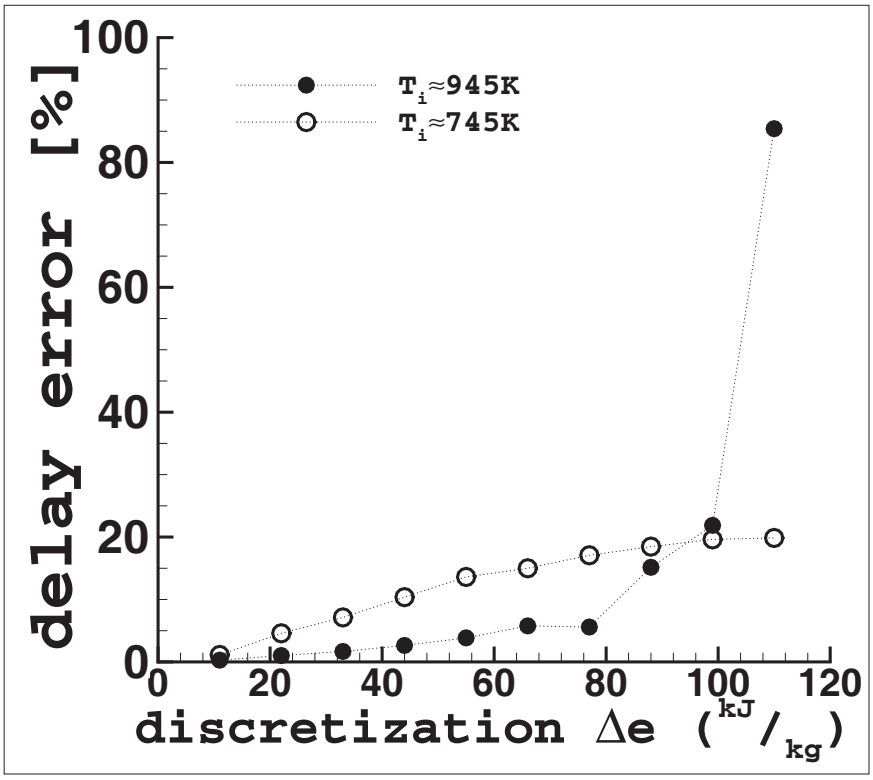

Figure 2.9 : *Auto-ignition delay error as a function of the energy discretization of the thermo-chemical table: filled circle-the main ignition delay of a high temperature flame; empty circle-the main ignition delay of a NTC regime flame*

2.6.2 Density discretization step

The objective of this section is to identify the density discretization step required for the thermo-chemical table. Twelve thermo-chemical tables with various values in density step from 0.76 kg/m^3 to 2.83 kg/m^3 were considered in this study, see Table 2.3.

$\Delta\rho$	Δp **for** $T_i = 939,67$	Δp **for** $T_i = 738,84$
0.76 kg/m^3	0.95 bar	0.75 bar
0.94 kg/m^3	1.90 bar	1.50 bar
1.41 kg/m^3	2.85 bar	2.25 bar
1.89 kg/m^3	3.80 bar	3.00 bar
2.36 kg/m^3	4.75 bar	3.75 bar
2.83 kg/m^3	10.45 bar	8.25 bar

Table 2.3 : *Density and pressure steps in the thermo-chemical tables for high initial temperature case ($T_i = 939,67$) and low initial temperature case ($T_i = 738,84$)*

In order to eliminate errors due to energy discretization, the energy for which the constant volume computations were performed was a discrete value of the database as depicted in Fig. 2.10. The density was situated in-between two discrete values of the thermo-chemical table, therefore the thermo-chemical variables are subject to linear interpolation errors in the density space. In order to minimize possible errors due to the progress variable interpolation, a low discretization step in the progress variable coordinate was generally used.
Constant volume computations were performed by solving the equations 2.6 and 2.7.
Figure 2.11 shows the temporal evolution of the temperature and of the CO mass fraction using tabulated chemistry with different thermo-chemical table discretizations in terms of density (symbols in figures) and compared with the detailed chemistry approach (line in figures).
As previously, two cases were considered: a high initial temperature case 2.11(a) where only the main ignition occurs and a low initial temperature case 2.11(b) where both cool and main flame appear .
The figures show a weak dependance of the delay estimation on the den-

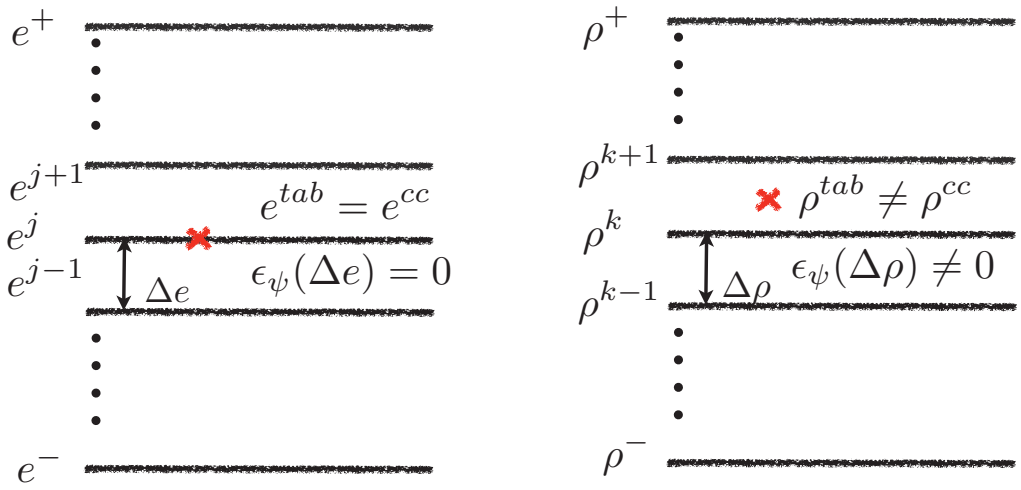

Figure 2.10 : *Interpolation error on a thermo-chemical variable ψ within the range of a discrete set of known density points (e^{cc}, ρ^{cc} -complex chemistry energy, density; e^{tab}, ρ^{tab} - tabulated chemistry energy/density; $\epsilon_\psi(\Delta e)$, $\epsilon_\psi(\Delta\rho)$ - interpolation error induced by the energy, density discretization related the thermo-chemical variable ψ)*

sity discretization which could be expected as the auto-ignition delay is expressed by an empirical relationship proposed by [21] of the form:

$$\tau = Kp^{-n}e^{\frac{B}{T}} \tag{2.8}$$

where K is a constant found to be dependent on the nature of the mixture and on the equivalence ratio, $B > 0$ is a constant independent of the equivalence ratio and n takes values of order one. The linear dependency of the auto-ignition delay with pressure gives a reason for the good auto-ignition delays prediction independent of the thermo-chemical table discretization in terms of pressure.
Figure 2.12 shows that the density discretization is not a key parameter in terms of delay estimation, and the errors are minor when compared with those of the energy Fig. 2.9.

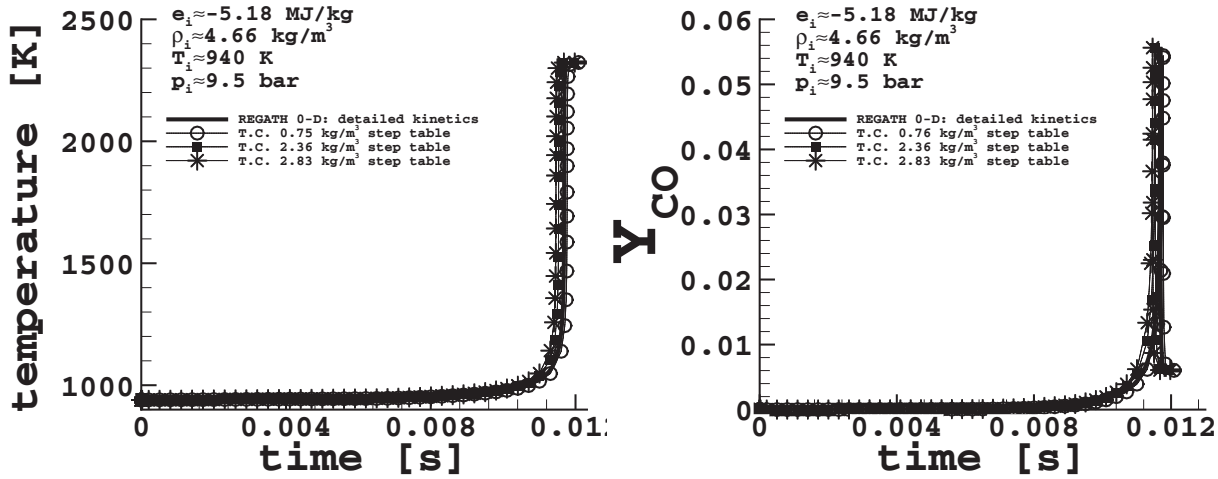

(a) Single-stage ignition chemistry: temperature (left figure) and CO mass fraction (right figure) temporal evolution

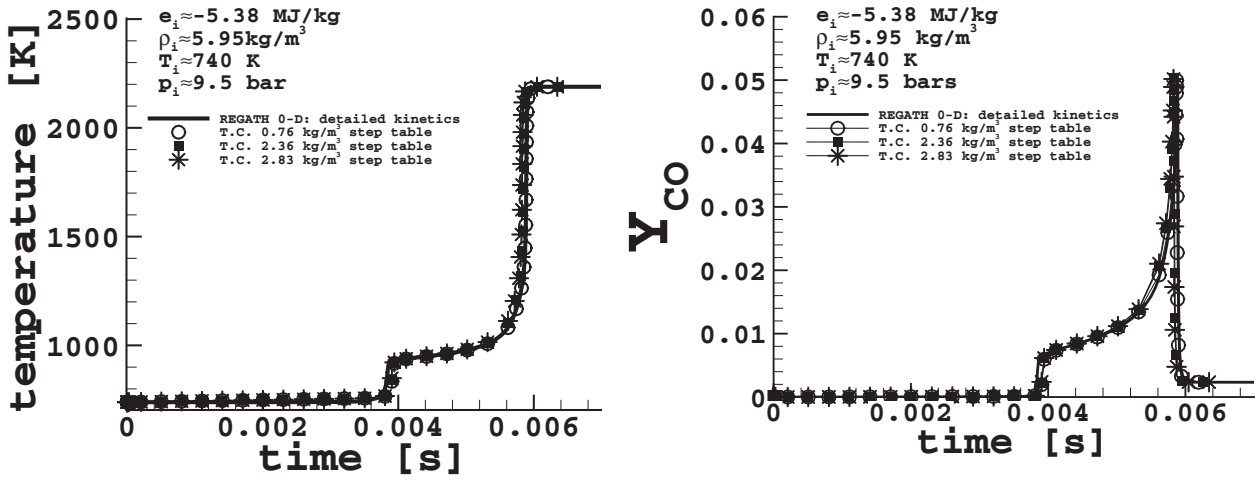

(b) Two-stage ignition chemistry: temperature (left figure) and CO mass fraction (right figure) temporal evolution

Figure 2.11 : *Table discretization in the density coordinate*

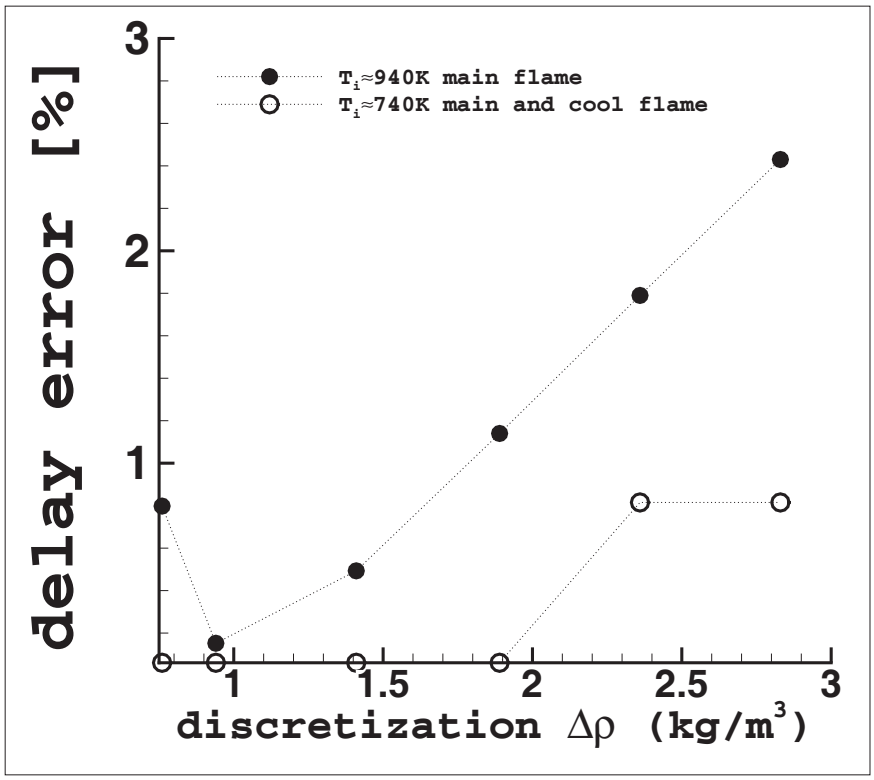

Figure 2.12 : *Auto-ignition delay error as a function of the density discretization of the thermo-chemical table*

2.6.3 Progress variable discretization step

In this part, the progress variable discretization step is assessed.
To avoid spending a lot of points in the low part of the progress variable, the progress variable rate is considered constant before a critical value of the progress variable $Y_c < \xi$ is reached.
Under the above assumption the progress variable evolution will be:

$$\begin{cases} 0 \geqslant Y_c < \xi : \textit{a linear evolution of } Y_c \textit{ during the physical time } t_\xi(e,\rho) \\ \quad Y_c \geqslant \xi : \textit{evolution of } Y_c \textit{ given by the complex chemical process} \end{cases} \tag{2.9}$$

The critical value of the progress variable ξ is obtained by using the

reaction rate conservation:

$$\begin{cases} 0 \leqslant Y_c < \xi : \dot{\omega}_{Y_c} = \dot{\omega}_\xi = \dfrac{\xi}{t_\xi(e,\rho)} \\ Y_c \geqslant \xi : \dot{\omega}_{Y_c} = \dot{\omega}^{tab}_{Y_c}(e,\rho,Y_c) \end{cases} \tag{2.10}$$

where $t_\xi(e,\rho)$ is the physical time for the progress variable to reach the value $Y_c = \xi$.

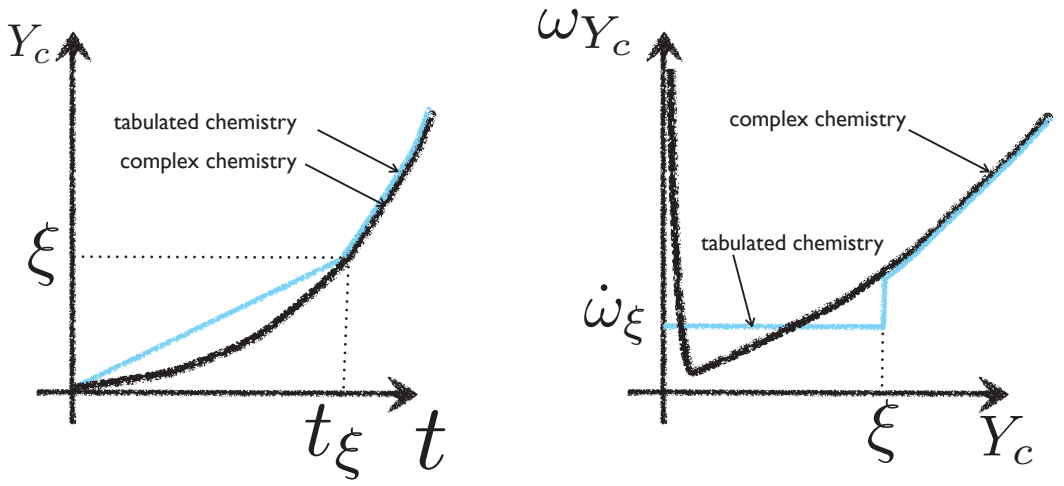

(a) (b)

Figure 2.13 : *Comparaison of tabulated chemistry with complex chemistry: a) Temporal evolution of the progress variable, b) Evolution of the progress variable rate with the progress variable*

The normalized progress variable at the time $t_\xi(e,\rho)$ is:

$$c^*_\xi = \frac{\xi - Y_c^-}{Y_c^+ - Y_c^-} \tag{2.11}$$

where Y_c^+ is the progress variable value at equilibrium and Y_c^- is the progress variable value in the initial mixture.
Four tables with different discretizations in the progress variable coordinate were built and are presented in Table 2.4.
Constant volume computations were performed using both complex chemistry approach and tabulated chemistry approach associated with the various progress variable discretization step databases. For all the computations the initial energy e_i and density ρ_i are discrete values of the

c^* **points**	c^* **step**	c^*_ξ (1^{st} 5 points)
26	0,04	0,2
51	0,02	0,1
101	0,01	0,05
151	0,00(6)	0,0(3)

Table 2.4 : *Characteristics of the examined thermo-chemical tables*

database, see Fig. 2.14 and thus there are no interpolation errors induced by the energy $\epsilon_\psi(\Delta e)$ and density discretization $\epsilon_\psi(\Delta\rho)$ steps.

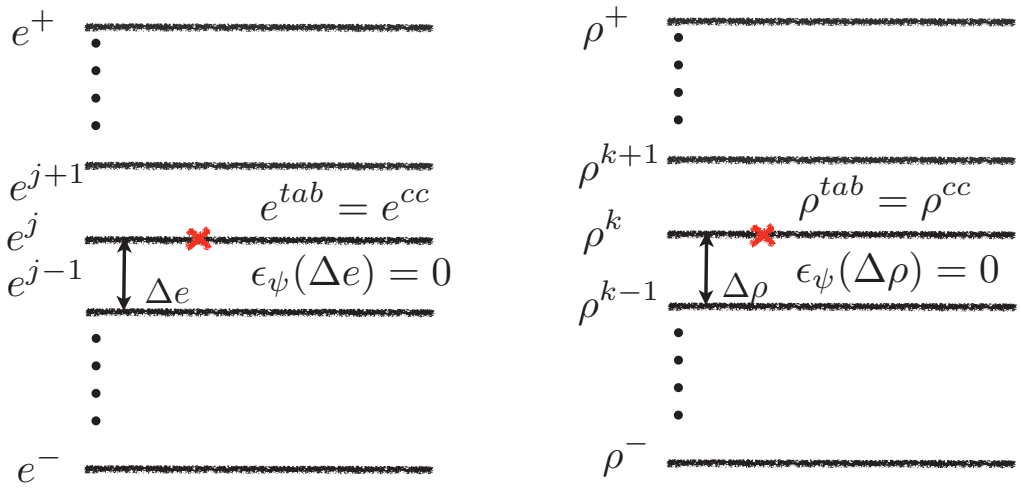

Figure 2.14 : *Interpolation error on a thermo-chemical variable ψ within the range of a discrete set of known progress variable points (e^{cc}, ρ^{cc} -complex chemistry energy, density; e^{tab}, ρ^{tab} - tabulated chemistry energy, density; $\epsilon_\psi(\Delta e)$, $\epsilon_\psi(\Delta\rho)$ - interpolation error induced by the energy, density discretization related the thermo-chemical variable ψ)*

Figure 2.15 shows a comparison between the tabulated and the detailed chemistry approaches.
The following conclusions can be drawn concerning the critical progress variable c^*_ξ. For the auto-ignition delay higher than 5 ms presented in Fig. 2.15 the value $c^*_\xi = 0.2$ is too high and skips some information concerning the cool flame. Therefore, for the auto-ignition delays range in

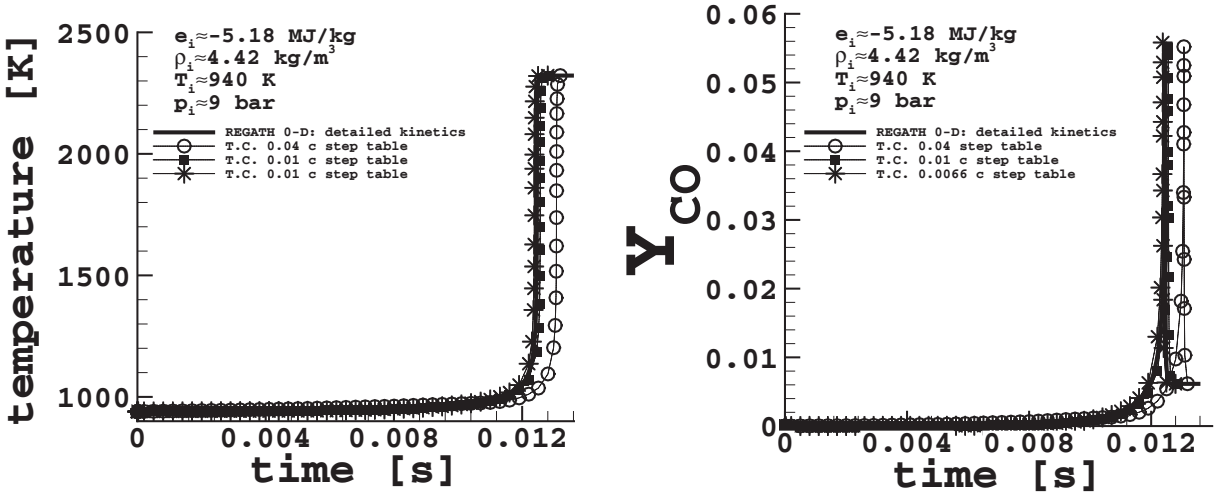

(a) Single-stage ignition chemistry: temperature (left figure) and *CO* mass fraction (right figure) temporal evolution

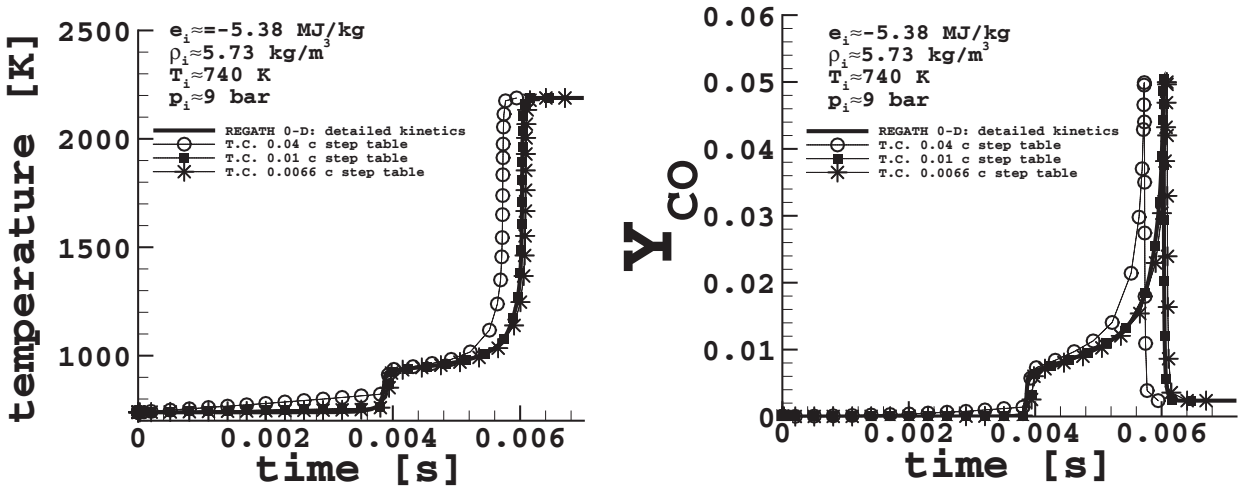

(b) Two-stage ignition chemistry: temperature (left figure) and *CO* mass fraction (right figure) temporal evolution

Figure 2.15 : *Table discretization in the progress variable coordinate*

ICE a lower value $c_\xi^* = 0.05$ was chosen.
A progress variable discretization of 0.01 and a $c_\xi^* = 0.05$ is adapted for *ICE* applications, as sustained by the Fig. 2.16

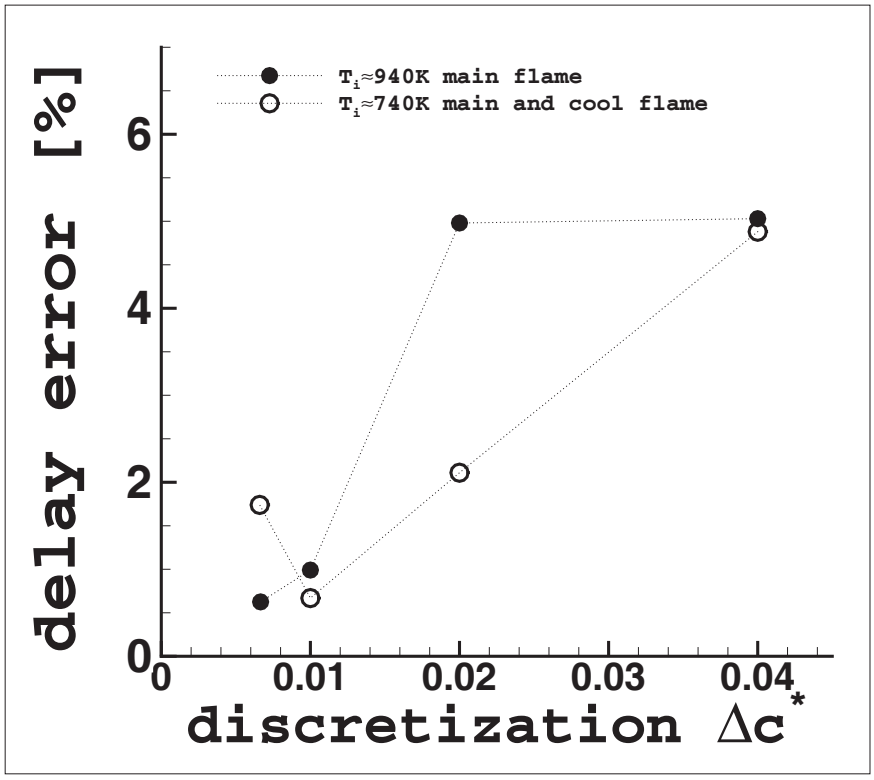

Figure 2.16 : *Auto-ignition delay error as a function of the progress variable discretization of the thermo-chemical table*

For the auto-ignition delay estimation, the progress variable and energy discretization have the biggest impact and the density discretization has a minor effect.

2.7 Variable volume validations

The thermo-chemical tables limits in terms of density ρ^-, ρ^+ and energy e^-, e^+ should be chosen in order to cover the entire range of conditions of the simulation. A minimum table size is needed for parallelized codes therefore an optimized discretization step for the table coordinates has been determined in the previous section.
To verify the methodology of the table generation and the discretization benchmark for its coordinate, computations of 0-D variable-volume engines were performed by solving the following set of equations:

$$\begin{cases} \rho = \rho(t) \\ \rho\dfrac{dY_k}{dt} = \dot{\omega}_k, k = 1, ..., N_{sp} \\ \dfrac{de}{dt} = \dfrac{P}{\rho}\dfrac{d\rho}{dt} \end{cases} \tag{2.12}$$

The tabulated-chemistry calculations are based on the following set of equations by using the pressure and the reaction rate values stored in a thermo-chemical table that responds to the discretization benchmarks defined in the previous section and by choosing adequate density and energy limits.

$$\begin{cases} \rho = \rho(t) \\ \rho\dfrac{dY_c}{dt} = \dot{\omega}_c \\ \dfrac{de}{dt} = \dfrac{P}{\rho}\dfrac{d\rho}{dt} \end{cases} \tag{2.13}$$

The main characteristic of the thermo-chemical table presented in this chapter is that, as the energy is a coordinate of the database, the thermo-chemical variables values can be directly obtained from the table with no other assumptions.
The density $\rho(t)$ is given for an engine with the following characteristics: bore = 85 mm, stroke = 88 mm, rpm = 1500.
The 0-D variable volume validations were made for the n-heptane-air mixtures and are presented in Table 2.5.

Equivalence ratio	Dilution	Mechanism	Initial conditions
stoichiometric (1.0)	-	Golovitchev	$p_i = 1\ bar$
lean (0.8)	79% CO_2, N_2	Curran	$T_i = 300\ K, 400\ K, 500\ K$

Table 2.5 : *Characteristics of the 0-D variable volume computations*

2.7.1 Stoichiometric n-heptane-air mixture

The calculations have been performed for n-heptane/air at stoichiometric conditions using Golovitchev's mechanism [80] with 53 species and 281 reactions.
Solutions of this set of equations are compared to the detailed chemistry computations in Fig. 2.17. Time evolution of temperature, pressure, CO_2 and CO mass fractions are plotted for different initial temperatures. For all variables and configurations, the tabulated chemistry solution (symbols) is in very good agreement with the detailed chemistry reference solution (lines) in all the domain confirming the validity of density and energy limits of the database (ρ^*, e^*, c^*).

2.7.2 Lean n-heptane-air mixture

A thermo-chemical table responding to the previous discretization benchmarks, namely an energy step of $\Delta e = 25\ J$ corresponding to a temperature step of $\Delta T \approx 20K$, a density step $\Delta\ \rho = 0.7kg/m^3$ thus $\Delta p \approx 2bar$ and a progress variable step $\Delta c^* = 0.01$ was built for a lean 79% CO_2 and N_2 diluted mixture. The 0-D reactor calculations have been performed with the n-heptane/air Curran's mechanism [89] with 89 species and 387 reactions that was validated previously for lean mixtures.
This thermo-chemical table was conceived in order to match the experimental conditions needs of the rapid compression machine (RCM) [42] of which the simulations will be presented in the chapter 5.
A comparison of $0-D$ variable volume computations with detailed chemistry (lines) and the tabulated chemistry solution (symbols) is shown in Figs. 2.18 and 2.19.
The Fig. 2.18(a) shows the lean, diluted $n-C_7H_{16}$ / air mixture thermo-chemical table with temperature contour and also the path that the $0-D$

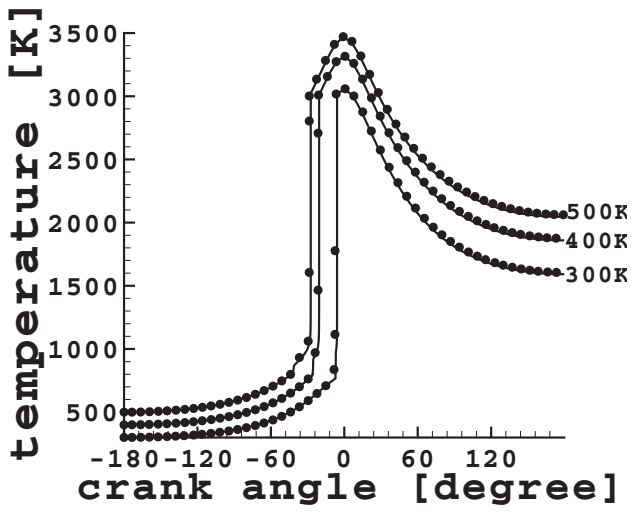

(a) Temperature

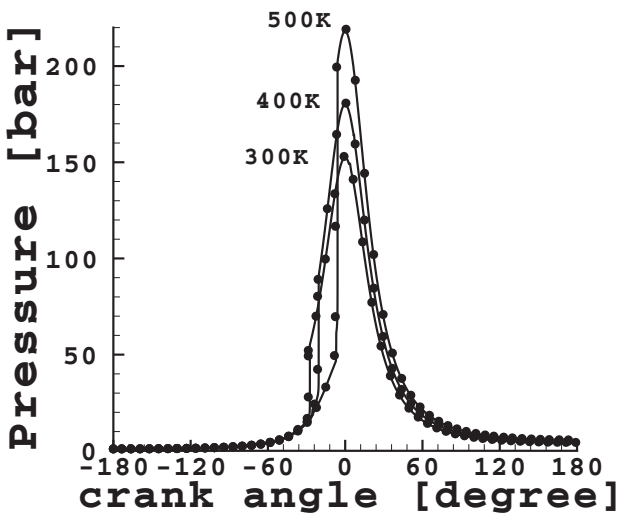

(b) Pressure

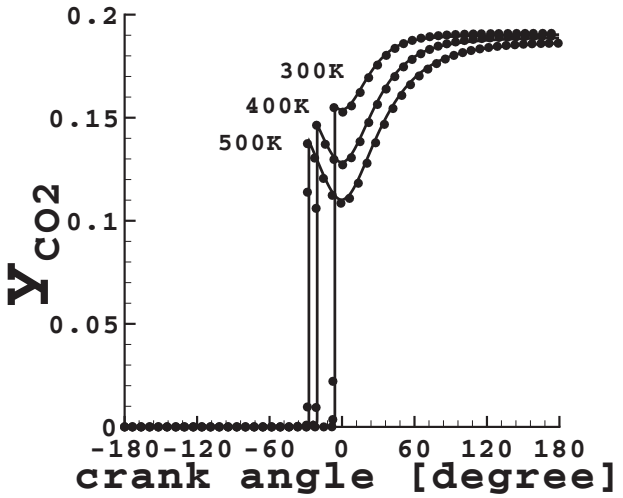

(c) CO_2

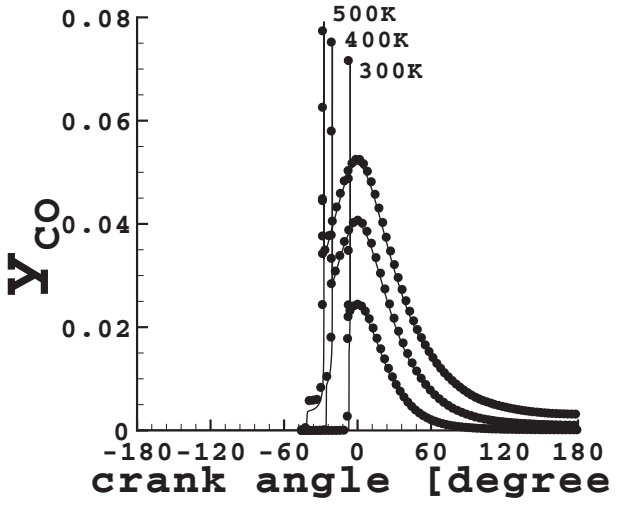

(d) CO

Figure 2.17 : *0-D variable-volume computations for various initial temperature in stoichiometric conditions. Tabulated chemistry (symbols) is compared to detailed chemistry (line) in terms of temporal evolution of temperature, pressure, CO_2 and CO mass fractions*

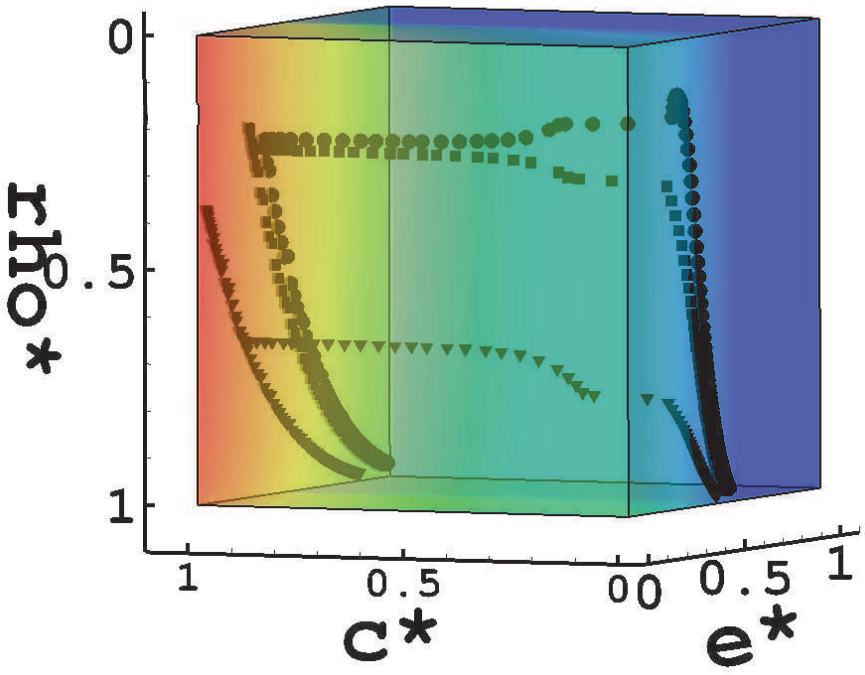

(a) Thermo-chemical table with temperature contour

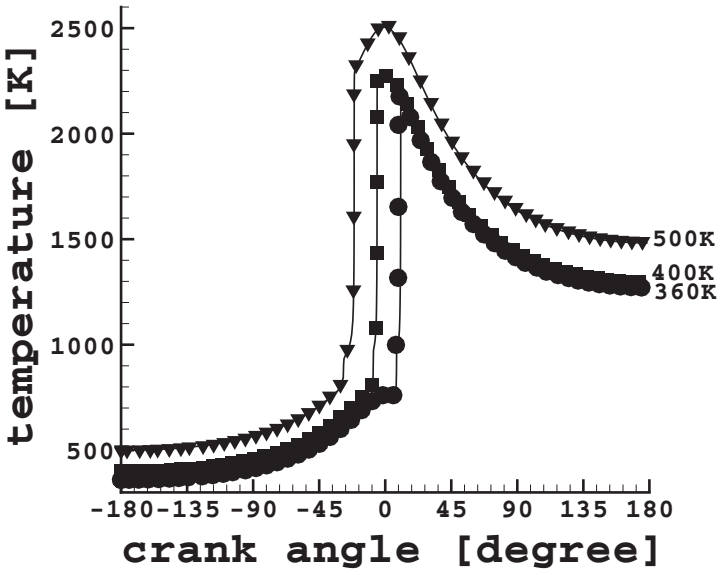

(b) Temperature

Figure 2.18 : *The temperature read in a non-adiabatic table*

variable volume computations from Fig. 2.18(b) cross in order to read the temperature value. Note that, in the tabulated approach the system of

equations 2.13 is solved given the values for the database coordinates.
The thermo-chemical table gives access to the major and minor species presented in the mechanism, e.g. CO_2 Fig. 2.19(b) , CO Fig. 2.19(c) and H_2O_2 Fig. 2.19(d) mass fractions with a perfect agreement with the detailed chemistry approach. In an ICE, the hydroperoxyde H_2O_2 is crucial for a good main-auto-ignition delay prediction.
The (ρ^*, e^*, c^*) tabulated-chemistry is therefore able to predict the main behavior of the combustion process in an ICE engine at a reduced CPU time. The calculations shown above take around 5 minutes under the detailed chemistry approach with an adaptive time step code and only 30 seconds for the tabulated chemistry approach among which 20 seconds are needed to read the 43 Mb thermo-chemical table.

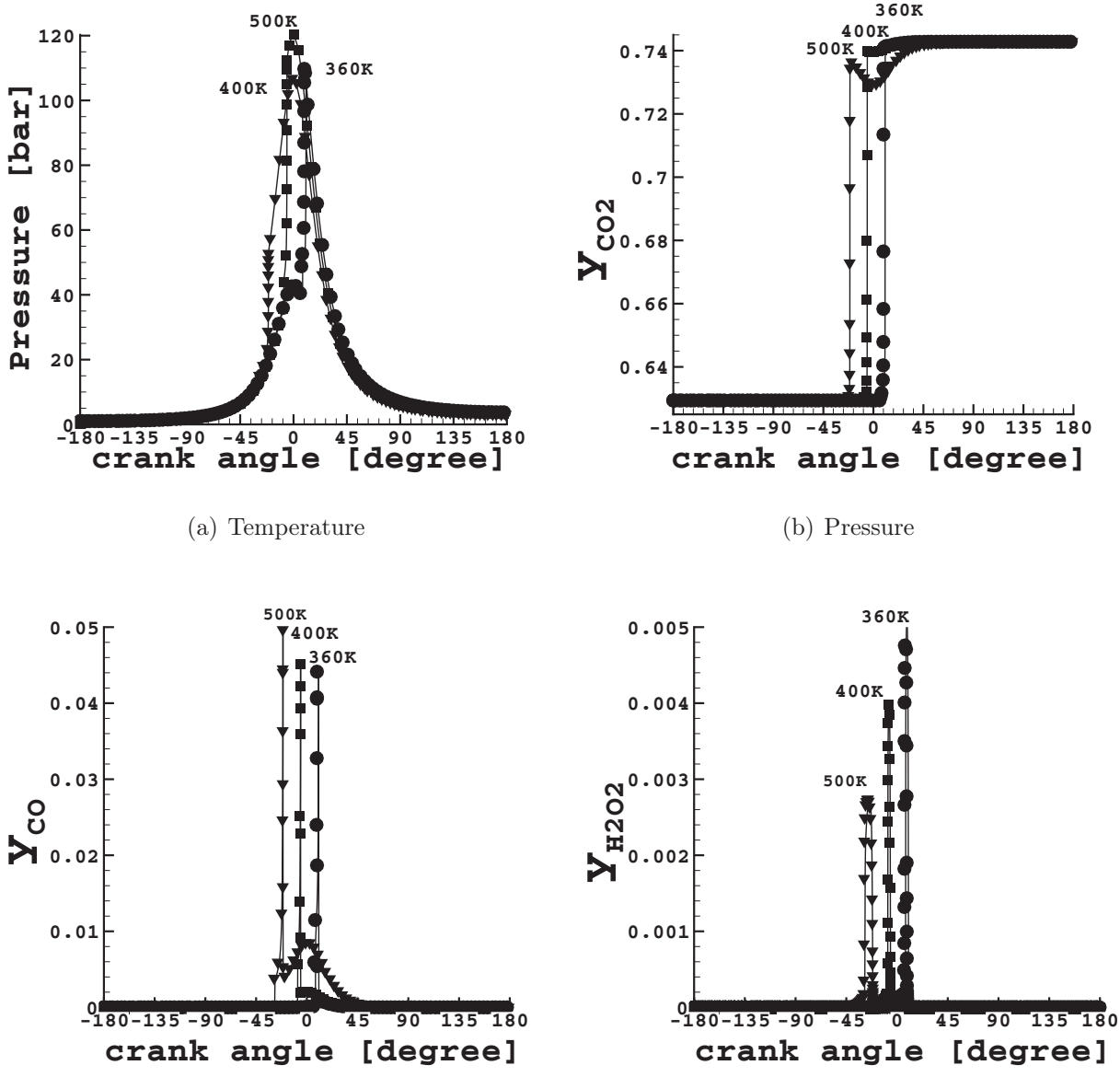

(a) Temperature

(b) Pressure

(c) CO_2

(d) CO

Figure 2.19 : *0-D variable-volume computations for various initial temperature conditions in a lean $\phi = 0.8$, 79% CO_2 and N_2 diluted mixture . Tabulated chemistry (symbols) is compared to detailed chemistry (line) in terms of temporal evolution of pressure, CO_2, CO and H_2O_2 mass fractions*

In this chapter a 3-D thermo-chemical table (ρ^*, e^*, c^*) that is suited to premixed flames with thermal heterogeneities that may occur in $HCCI$ engine, $PHCCI$ engine and RCM was conceived. The approach can be extended to partially premixed flames by additional coordinates, namely the equivalence ratio standing for the composition heterogeneities. The benchmark discretization for each coordinate (ρ^*, e^*, c^*) of the table was addressed. In the case where more dimensions are added to the table and the memory space of the table becomes penalizing for implementation on massively parallel computers the self-similar proprieties of the tabulated chemistry can be used. Ribert et al. [73] evidenced the self-behavior of laminar premixed flames when they are written in a Hawarth-Dorodnitzyn reduced spatial coordinate. Thus a general reaction rate or species mass fraction profile is identified and scaling rule will retrieve the dependency on each flame parameter equivalence ratio, pressure, temperature [73] and even dilution by burned gases [87]. This approach is also available for table generated from auto-igniting homogeneous reactor [74].

Part II

Coupling a non-adiabatic chemical table with a LES compressible solver

Chapter 3

Coupling a chemical table with the AVBP compressible CFD solver

In this chapter the large-eddy simulation LES technique is discussed in a non-adiabatic tabulated chemistry context. First, the coupling of the Navier-Stokes equations with tabulated techniques will be addressed, underlying the changes that the equations undergo with the tabulated chemistry approach and the thermo-chemical variables that should be recovered in the database. Then, under the LES approach, the filtering of the equations will be discussed. These filtered equations govern only the evolution of the large scale motions and thus subgrid scale models are required in order to carry the effect of the small scale. A brief overview of the models for the correlation between the fluctuations and the filtered reaction rate that are compatible with tabulated techniques will be given.

3.1 Introduction

The increase of computational power allows to use *LES* compressible solvers in engine configurations nevertheless lacking in chemistry descrip-

tion [26,29,40,75,84]. The simulations remain too expensive with detailed chemistry which explains the interest of coupling the tabulated chemistry models with the Navier- Stokes equations.

Generally, perturbations due to compressible effects are not considered during the database generation. As the transported energy value e will not coincide with the energy e^{tab} for which the table was conceived, further assumptions are required in order to accommodate the tabulated thermochemical variables in compressible solvers. Viquelin et al. [85] developed a new strategy which enables the coupling of tabulated chemistry in compressible solvers for constant pressure applications. The formalism, called Tabulated Thermochemistry for Compressible flows (TTC), assumes that the constant volume heat capacity C_v^{tab}, read from the table, is constant within weak acoustic perturbations. Under this assumption, knowing the local energy e, the local temperature will be approximated from the tabulated temperature T^{tab} as follows: $T = T^{tab} + \frac{e-e^{tab}}{C_v^{tab}}$.

The formalism was coupled with the $AVBP$ solver [1], conceived to simulate unsteady turbulent and compressible reactive flows using LES techniques, and henceforth labeled $AVBP - TTC$ to mark the use of the tabulated thermo-chemistry.

For highly compressible configurations, like ICEs, isobaric tables are no longer suitable and, as explained in the previous chapter, the energy should be considered as database coordinate in order to capture the strong pressure effects. The created table presented in the chapter 2 has been implemented in the $AVBP - TTC$ version.

In the first part of this chapter, the conservation equations for the conservative variables ρ, ρu_j, ρY_c, ρE are formulated, underlying the differences in the equations related to the tabulated chemistry framework and pointing out the thermo-chemical variables that are directly estimated from the look-up table $\psi^{tab}(\rho^*,e^*,c^*)$, where ρ^* is the normalized density, e^* is the normalized energy and c^* is the normalized progress variable. Then, the equations are expressed under LES numerical solving technique.

3.2 Equations for reactive flows using tabulated techniques

3.2.1 Conservation equations

3.2.1.1 Mass conservation law - Equation of continuity

The mass conservation law for a compressible flow without mass sources or sinks reads:

$$\frac{\partial \rho}{\partial t} + \frac{\partial \rho u_j}{\partial x_j} = 0 \tag{3.1}$$

where ρ is the mixture's total mass density and u_j the bulk mass-averaged velocity.

3.2.1.2 Momentum conservation law

Generally, two types of forces act on a fluid, short ranged (i.e. surface stress forces) and long ranged (i.e. body forces). They are embodied in the equation of momentum as follows:

$$\frac{\partial \rho u_i}{\partial t} + \frac{\partial \rho u_i u_j}{\partial x_j} = -\frac{\partial (p\delta_{ij} - \tau_{ij})}{\partial x_j} + \rho f_i, \qquad i = 1, 2, 3 \tag{3.2}$$

Here, it is assumed that there are no body forces $f_i = 0$.

Both for the chemical kinetic mechanism approach and for tabulated chemistry approach, the mathematical expression of the momentum conservation law remains the same expressed by the equation 3.2. In the following section 3.2.2, the way to address the thermodynamic and the transport variables under complex chemistry and tabulated chemistry approach will be given.

3.2.1.3 Species versus progress variable conservation law

In this section the main characteristic of the tabulated techniques is depicted. The species mass fraction conservation equation will be discussed. Then, it will be shown how these equations are restricted to the conservation equation for the progress variable.

The k^{th} species mass conservation law ρ_k in a N_{sp} multicomponent system is given by:

$$\frac{\partial \rho Y_k}{\partial t} + \frac{\partial \rho Y_k u_j}{\partial x_j} = -\frac{\partial J_j^k}{\partial x_j} + \dot{\omega}_k, \qquad k = 1, ..., N_{sp} \tag{3.3}$$

where the vector quantity $J_j^k = \rho Y_k U_j^k$ denotes the diffusion mass flux of species k. Various chemical species do not move along at the same velocity, they can travel faster or slower than the mean mass velocity (i.e. H_2 diffuses faster than CO_2). Consequently, the velocity of the k^{th} species u_j^k is different from the local bulk mass-average velocity $u_j = \sum_{k=1}^{N} Y_k u_j^k$. The gap between them, namely the average motion of a given species with respect to the local bulk mass-average velocity, is called diffusion mass velocity: $U_j^k = u_j^k - u_j$.
In the tabulated thermo-chemistry approach, the progress variable Y_c is defined as one of the chemical species or a linear combination $\sum_{k=1}^{N_c} \alpha_k Y_k$ of a few N_c species Y_k [1] belonging to the reaction mechanism, e.g. for n-heptane by equation 2.1. The subsequent conservation equation for the progress variable obtained from (3.3) is:

$$\frac{\partial \rho Y_c}{\partial t} + \frac{\partial \rho Y_c u_j}{\partial x_j} = -\frac{\partial J_j^{Y_c}}{\partial x_j} + \dot{\omega}_{Yc} \tag{3.4}$$

where the quantity $J_j^{Y_c} = \rho Y_c U_j^{Y_c}$ denotes the diffusion mass flux of the progress variable.
Only a transport equation is solved for the progress variable 3.4 instead of the conservative equations 3.3 for all chemical species in the reaction mechanism allowing for considerable computational time savings.

3.2.1.4 Energy conservation law

For the energy equation, several options are available: the enthalpy, the total enthalpy, the internal energy or the total energy formulation. The latest is used in $AVBP - TTC$ code and is presented in the current section.

[1] The chosen species should have a monotone evolution and be able to follow the reaction path

The total energy reads:

$$E = \sum_{i=1}^{3} \frac{u_i^2}{2} + e \tag{3.5}$$

where e is the internal energy with the sensible and the chemical energy contributions:

$$e = \int_{T_0}^{T} C_v(T')dT' - \frac{rT_0}{W} + \sum_{k=1}^{N_{sp}} \Delta h_{f,k}^0 Y_k \tag{3.6}$$

where $\Delta h_{f,k}^0 Y_k$ is the formation enthalpy of the species k.
The conservation of the total energy is:

$$\frac{\partial \rho E}{\partial t} + \frac{\partial \rho E u_j}{\partial x_j} = -\frac{\partial u_i(p\delta_{ij} - \tau_{ij})}{\partial x_j} - \frac{\partial q_j}{\partial x_j} \tag{3.7}$$

The first term of the right-hand side represents energy production due to pressure variations and viscous effects, the second one stands for the heat flux q_j.

3.2.2 Thermodynamical variables

Under the ideal gas behavior assumption, the static pressure p is computed from the equation of state $p = \rho\ r\ T$. Mayer's relation for an ideal gas says that the mixture gas constant r is related to the mean mass heat capacities at constant pressure and constant volume: $r = C_p - C_v$. The total pressure is computed as follows:

$$p = \rho\ (C_p - C_v)\ T \tag{3.8}$$

In standard AVBP, the mixture thermodynamics can be calculated through the relations 3.9 and 3.10 and the temperature by inversion of the sensible energy 3.11.
The majority of the thermo-chemical tables found in literature [22, 34, 36, 52, 59, 83] are adiabatic. In the tabulated chemistry approach presented in chapter 2, the internal energy is a database coordinate, so the thermo-chemical table is non-adiabatic. For this thermo-chemical table

the thermodynamic variables and the temperature can be directly read in the database with no other assumptions [85].

AVBP chemical kinetic mechanism

⋆ *before iterating:*

$Cv_k(T)$, $Cp_k(T)$, $e_{s,k}(T)$
read from an input file
$\Delta T = 100\ K$

⋆ *for each iteration:*

$$Cv = \sum_{k=1}^{N_{sp}} Cv_k Y_k \tag{3.9}$$

$$Cp = \sum_{k=1}^{N_{sp}} Cp_k Y_k \tag{3.10}$$

$$T:\ inversion\ of\ e_s = \sum_{k=1}^{N_{sp}} e_{s,k} Y_k \tag{3.11}$$

AVBP-TTC tabulated chemistry

⋆ *before iterating:*

Cv^{tab}, Cp^{tab}, T^{tab}
read from thermo-chemical table
ΔT given by the table discretization

⋆ *for each iteration:*

$$Cv = Cv^{tab}(\rho^*, e^*, c^*) \tag{3.12}$$

$$Cp = Cp^{tab}(\rho^*, e^*, c^*) \tag{3.13}$$

$$T = T^{tab}(\rho^*, e^*, c^*) \tag{3.14}$$

3.2.3 The viscosity

The mixture viscous stress tensor τ_{ij}, is modeled identical to the stress tensor for a single-component Newtonian fluid.

$$\tau_{ij} = \mu\left(\frac{\partial \boldsymbol{u_j}}{\partial x_i} + \frac{\partial \boldsymbol{u_i}}{\partial x_j} - \frac{2}{3}\delta_{ij}\frac{\partial \boldsymbol{u_l}}{\partial x_l}\right) \tag{3.15}$$

where δ_{ij} is the Kronecker operator: $\delta_{ij} = \begin{cases} 1 & for\ i = j \\ 0 & for\ i \neq j \end{cases}$ and

μ is the dynamic viscosity of the mixture, addressed as follows:

AVBP chemical kinetic mechanism

⋆ *before iterating:*

c_1, c_2, T^{ref}
read from an input file

⋆ *for each iteration:*

$$\mu = c_1(\frac{T}{T^{ref}})^{c_2} \tag{3.16}$$

$$\mu = c_1 \frac{T^{3/2}}{T + c_2} \frac{T^{ref} + c_2}{T^{ref\,3/2}} \tag{3.17}$$

AVBP-TTC tabulated chemistry

⋆ *before iterating:*

μ^{tab}
read from thermo-chemical table
with ΔT given by the table discretization

⋆ *for each iteration:*

$$\mu = \mu^{tab}(\rho^*, e^*, c^*) \tag{3.18}$$

For saving CPU-time, in the complex chemistry formulation, the average mixture viscosity may be assumed independent of the composition of the mixture and only the temperature dependence is considered through standard models as Sutherland [79], equation 3.16 or Power equation 3.17 law $\mu(c_1, c_2, T^{ref}, T^{tab})$. For accurate results, the model constants c_1 and c_2 should be found by fitting them to the viscosity of comparable mixture. As for the thermodynamical variables C_p, C_v and T, the transport variable μ can be directly read in the thermo-chemical table, equation 3.18.

3.2.4 The diffusivity

Multi-component descriptions for the diffusivity is predictable with high accuracy by the molecular kinetic theory [39]. However, to reduce the computation cost in CFD, the convenient Hirschfelder and Curtiss approximation [19] is preferred:

$$U_j^k Y_k = -D_k \frac{W_k}{W} \frac{\partial X_k}{\partial x_j} + Y_k \sum_{l=1}^{N} \frac{W_l}{W} D_l \frac{\partial X_l}{\partial x_j} \tag{3.19}$$

The second term represents a correction velocity that ensures the null sum of the diffusive species fluxes $\sum_{k=1}^{N} U_j^k Y_k = 0$ as implied by the total mass conservation.

The k^{th} species mixture diffusion coefficient D_k is expressed as proposed by Bird [9] by the relation:

$$D_k = \frac{1 - Y_k}{\sum_{k \neq l} \frac{X_k}{D_{l,k}}} \tag{3.20}$$

where $D_{l,k}$ is the binary diffusion coefficient for the k^{th} and l^{th} species.
If the number of species is larger than $\simeq 100$, which is usually the case for realistic fuels, the computational time for diffusion becomes higher than that for the chemical reaction [55].
Neglecting the molar mass gradients and making the hypothesis of a constant species diffusion coefficient $D = D_k$, the expression 3.2.4 leads to Fick's law of diffusion, that will be used in this work.

$$U_j^k Y_k = -D \frac{\partial Y_k}{\partial x_j} \tag{3.21}$$

It asserts that the mass diffusion effect of species k is driven by the mass fraction gradient in the direction of decreasing Y_k.
The species diffusivity can be recovered from the momentum diffusivity.

$$D = \frac{\mu}{\rho Sc} \tag{3.22}$$

In the tabulated thermo-chemistry approach, Fick's law for the progress variable diffusion lead to:

$$U_j^{Y_c} = -D_{Yc} \frac{\partial \boldsymbol{Y_c}}{\partial x_j} \tag{3.23}$$

where D_{Yc} is the progress variable diffusion coefficient expressed as:

$$D_{Yc} = \frac{\mu}{\boldsymbol{\rho} Sc} \tag{3.24}$$

In this paper, the Schmidt number Sc was set to 0.75.
As to summarize:

AVBP chemical kinetic mechanism

⋆ *for each iteration:*

$$D = \frac{\mu}{\rho Sc} \tag{3.25}$$

AVBP-TTC tabulated chemistry

⋆ *for each iteration:*

$$D = \frac{\mu^{tab}}{\rho Sc} \tag{3.26}$$

3.2.5 The reaction rate

The reaction rate $\dot{\omega}_k$ for the k^{th} species can be calculated by summation of all elementary reactions in which the k^{th} species is involved, weighted by its stoichiometric coefficient (see eq. 1.2).
The reaction rate of the progress variable $\dot{\omega}_{Y_c} = \dot{\omega}^{tab}_{Y_c}(\rho^*,e^*,c^*)$ will be an information recovered directly from the chemical database by a 1^{st} order interpolation.

AVBP chemical kinetic mechanism

$$\dot{\omega}_k = W_k \sum_{i=1}^{N_r} \nu_{k,i} r_i \tag{3.27}$$

AVBP-TTC tabulated chemistry

$$\dot{\omega}_{Y_c} = \dot{\omega}^{tab}_{Y_c}(\rho^*,e^*,c^*) \tag{3.28}$$

3.2.6 The conductivity

The heat flux q_j is modeled as:

$$q_j = -\lambda \frac{\partial T}{\partial x_j} + \sum_{k=1}^{N_{sp}} J_j^k h_k \tag{3.29}$$

The heat flux through species diffusion, the second term of the right-hand side of the equation (3.29), implies species mass fraction derivatives that are not available during the tabulated chemistry computation. For this reason, the following form is preferred for the heat flux vector :

$$q_j = -\frac{\lambda}{C_p} \frac{\partial h}{\partial x_j} \tag{3.30}$$

where the mixture enthalpy (sensible plus chemical) is defined as:

$$h = \int_{T_0}^{T} C_p(T')dT' + \sum_{k=1}^{N_{sp}} h_{f,k}^0 Y_k \tag{3.31}$$

Remark that, either formulation of the heat fluxes (3.29) or (3.30) becomes the same for unity species Lewis number $\frac{\lambda}{\rho C_p D} = 1$ as proved by the following sequence of equations :

$$\begin{aligned}
\frac{\lambda}{C_p}\frac{\partial h}{\partial x_j} &= \frac{\lambda}{C_p}\frac{\partial}{\partial x_j}\sum_{k=1}^{N_{sp}} h_k Y_k \\
&= \frac{\lambda}{C_p}\sum_{k=1}^{N_{sp}}\left(\frac{\partial h_k}{\partial x_j}Y_k + \frac{\partial Y_k}{\partial x_j}h_k\right) \\
&= \frac{\lambda}{C_p}\sum_{k=1}^{N_{sp}}\left(C_{pk}Y_k\frac{\partial T}{\partial x_j} + \frac{\partial Y_k}{\partial x_j}h_k\right) \\
&= \lambda\frac{\partial T}{\partial x_j} + \rho D\sum_{k=1}^{N_{sp}}\frac{\partial Y_k}{\partial x_j}h_k
\end{aligned} \tag{3.32}$$

The heat conduction coefficient λ is obtained by supposing a constant Prandtl number Pr in standard AVBP or by linear interpolation in the table in $AVBP - TTC$.

AVBP chemical kinetic mechanism

⋆ *before iterating:*

Pr
read from an input file

⋆ *for each iteration:*

$$\lambda = \frac{\mu C_p}{Pr} \tag{3.33}$$

AVBP-TTC tabulated chemistry

⋆ *before iterating:*

λ^{tab}
read from thermo-chemical table
with ΔT given by the table discretization

⋆ *for each iteration:*

$$\lambda = \lambda^{tab}(\rho^*, e^*, c^*) \tag{3.34}$$

To summarize, the transport equations are:

AVBP chemical kinetic mechanism

⋆ *transported equations:*

$$\frac{\partial \rho}{\partial t} + \frac{\partial \rho u_j}{\partial x_j} = 0 \tag{3.35a}$$

$$\frac{\partial \rho u_i}{\partial t} + \frac{\partial \rho u_i u_j}{\partial x_j} = -\frac{\partial p \delta_{ij}}{\partial x_j} + \frac{\partial \tau_{ij}}{\partial x_j}, \qquad i = 1, 2, 3 \tag{3.35b}$$

$$\frac{\partial \rho Y_k}{\partial t} + \frac{\partial \rho Y_k u_j}{\partial x_j} = \frac{\partial}{\partial x_j}\left(\frac{\mu}{Sc}\frac{\partial Y_k}{\partial x_j}\right) + \dot{\omega}_k, \qquad k = 1, ..., N_{sp} \tag{3.35c}$$

$$\frac{\partial \rho E}{\partial t} + \frac{\partial \rho E u_j}{\partial x_j} = -\frac{\partial u_i p \delta_{ij}}{\partial x_j} + \frac{\partial u_i \tau_{ij}}{\partial x_j} + \frac{\partial}{\partial x_j}\left(\frac{\mu}{Pr}\frac{\partial h}{\partial x_j}\right) \tag{3.35d}$$

⋆ *before iterating:*

c_1, c_2, T^{ref}, Sc, Pr read from an input file
$C_{v,k}(T)$, $C_{p,k}(T)$, $e_{s,k}(T)$ read from an input file with a step $\Delta T = 100\ K$

⋆ *for each iteration:*

$$C_v = \sum_{k=1}^{N_{sp}} C_{v,k} Y_k \tag{3.36a}$$

$$C_p = \sum_{k=1}^{N_{sp}} C_{p,k} Y_k \tag{3.36b}$$

$$T: \ inversion\ of\ e_s = \sum_{k=1}^{N_{sp}} e_{s,k} Y_k \tag{3.36c}$$

$$\mu = c_1 \frac{T^{3/2}}{T + c_2} \frac{T^{ref} + c_2}{{T^{ref}}^{3/2}} \quad or \quad \mu = c_1 (\frac{T}{T^{ref}})^{c_2} \tag{3.36d}$$

$$D = \frac{\mu}{\rho Sc} \tag{3.36e}$$

$$\lambda = \frac{\mu C_p}{Pr} \tag{3.36f}$$

$$\dot{\omega}_k = W_k \sum_{i=1}^{N_r} \nu_{k,i} r_i \tag{3.37}$$

AVBP-TTC tabulated chemistry approach

⋆ *transported equations:*

$$\frac{\partial \rho}{\partial t} + \frac{\partial \rho u_j}{\partial x_j} = 0 \tag{3.38a}$$

$$\frac{\partial \rho u_i}{\partial t} + \frac{\partial \rho u_i u_j}{\partial x_j} = -\frac{\partial p \delta_{ij}}{\partial x_j} + \frac{\partial \tau_{ij}}{\partial x_j}, \qquad i = 1,2,3 \tag{3.38b}$$

$$\frac{\partial \rho Y_c}{\partial t} + \frac{\partial \rho Y_c u_j}{\partial x_j} = \frac{\partial}{\partial x_j}\left(\frac{\mu}{Sc}\frac{\partial Y_c}{\partial x_j}\right) + \dot{\omega}_{Y_c} \tag{3.38c}$$

$$\frac{\partial \rho E}{\partial t} + \frac{\partial \rho E u_j}{\partial x_j} = -\frac{\partial u_i p \delta_{ij}}{\partial x_j} + \frac{\partial u_i \tau_{ij}}{\partial x_j} + \frac{\partial}{\partial x_j}\left(\frac{\lambda}{Cp}\frac{\partial h}{\partial x_j}\right) \tag{3.38d}$$

⋆ *before iterating:*

C_v^{tab}, C_p^{tab}, T^{tab}, μ^{tab} , λ^{tab}
read from the thermo-chemical table with a step ΔT given by the table discretization

⋆ *for each iteration:*

$$C_v = C_v^{tab}(\rho^*, e^*, c^*) \tag{3.39a}$$

$$C_p = C_p^{tab}(\rho^*, e^*, c^*) \tag{3.39b}$$

$$T = T^{tab}(\rho^*, e^*, c^*) \tag{3.39c}$$

$$\mu = \mu^{tab}(\rho^*, e^*, c^*) \tag{3.39d}$$

$$D = \frac{\mu^{tab}(\rho^*, e^*, c^*)}{\rho Sc} \tag{3.39e}$$

$$\lambda = \lambda^{tab}(\rho^*, e^*, c^*) \tag{3.39f}$$

$$\dot{\omega}_{Y_c} = \dot{\omega}_{Y_c}^{tab}(\rho^*, e^*, c^*) \tag{3.40}$$

3.3 Coupling the AVBP LES compressible solver with non-adiabatic tables

As no analytical solution for turbulent flows in geometries of engineering interest is available for the system (3.38), the equations are discretized and solved numerically. In this paper, the Large Eddy Simulation (LES) technique will be used, as Direct Numerical Simulation (DNS) which proposes to solve all turbulence scales, is far out of reach for ICE configurations. Renynolds Averaged Navier-Stokes ($RANS$) equations on the other hand propose a temporal average over the ensemble of realization and gives the principal trends of the flow.
In LES approach, the large energy containing scales are resolved where smallest are modeled. When coupled with an accurate description of combustion chemistry, LES is an attractive tool to predict pollutant emissions in Internal Combustion Engines.
The differential equations for the large scale structures are obtained by applying a low-pass filter G[2] on the Navier-Stokes equations.
The variables ψ are filtered in the domain D using the following definition:

$$\overline{\psi}(x) = \int_D \psi(x')G(x, x'; \overline{\Delta})dx' \tag{3.41}$$

where $\overline{\Delta}$ is the filter width. For inhomogeneous turbulent flows the minimum size of the eddies that needs to be resolved is not the same in all regions of the flow. Therefore, the computational grid size varies and consequently the implicit filters are non-uniform in space.
When applying the filter operations to the governing equations for compressible flows (3.38), new terms $\overline{\rho\psi}$ appear and it is convenient to use Favre-filtered variables defined as:

$$\tilde{\psi} = \frac{\overline{\rho\psi}}{\overline{\rho}} \tag{3.42}$$

Like in Reynolds formalism $\psi = \overline{\psi} + \psi'$, in Favre formalism each variable can undergo a decomposition into mean and fluctuating parts $\psi = \tilde{\psi} + \psi''$

[2]In the spectral space, the filter passes low-frequency signals but attenuates signals with frequencies higher than the cut-off frequency and in physical space the filter makes a weighted average in a given volume.

and obviously they will be different from the previous ones: $\tilde{\psi} \neq \overline{\psi}$, $\psi'' \neq \psi'$.

3.3.1 Filtered mass conservation law

The Favre filtering avoids subgrid scale SGS terms in the mass conservation equation:

$$\frac{\partial \overline{\rho}}{\partial t} + \frac{\partial \overline{\rho}\tilde{u}_j}{\partial x_j} = 0 \tag{3.43}$$

3.3.2 Filtered momentum conservation law

Favre-filtered equations of momentum can be written in the form:

$$\frac{\partial \overline{\rho}\tilde{u}_i}{\partial t} + \frac{\partial \overline{\rho}\tilde{u}_i\tilde{u}_j}{\partial x_j} = -\frac{\partial \overline{p}\delta_{ij}}{\partial x_j} + \frac{\partial \overline{\tau_{ij}}}{\partial x_j} + \frac{\partial \overline{\tau_{ij}}^{sgs}}{\partial x_j} \qquad i = 1,2,3 \tag{3.44}$$

Usually, the enclosure due to the non-linearity of the viscous stress tensor is neglected. If done so, the filtered stress tensor can be approximated by the relation:

$$\overline{\tau_{ij}} \approx \overline{\rho}\nu(\frac{\partial \tilde{u}_j}{\partial x_i} + \frac{\partial \tilde{u}_i}{\partial x_j} - \frac{2}{3}\delta_{ij}\frac{\partial \tilde{u}_l}{\partial x_l}) \tag{3.45}$$

The Reynolds tensor $\overline{\tau_{ij}}^{sgs} = -\overline{\rho}\widetilde{u_i''u_j''} = -\overline{\rho}(\widetilde{u_i u_j} - \tilde{u}_i\tilde{u}_j)$ is the term that must account for the energy dissipation from the resolved through the unresolved scales. Essentially the Reynolds tensor describes the drain yield during the energy cascade of turbulence. Consequently, most of the SGS models proposed in literature are eddy-viscosity models and differ only in the estimation of the eddies viscosity.

$$\overline{\tau_{ij}}^{sgs} = \overline{\rho}\nu_t\left(\frac{\partial \tilde{u}_j}{\partial x_i} + \frac{\partial \tilde{u}_i}{\partial x_j} - \frac{2}{3}\delta_{ij}\frac{\partial \tilde{u}_l}{\partial x_l}\right) \tag{3.46}$$

This relation shows that the subgrid stress tensor can be deduced from the large-scale strain-rate tensor that is resolved on an LES mesh and will be scaled by a subgrid-scale turbulent viscosity ν_t factor. The general idea

behind the algebraical models for the SGS turbulent viscosity is, that the energy transfer occurs instantaneously and entirely as all small eddies are considered to be in equilibrium. The general equation of the SGS turbulent viscosity ν_t can be written as:

$$\nu_t = C v_t \overline{\Delta} \tag{3.47}$$

where C is a model constant to be adapted to the physical conditions, v_t is a velocity scale and $\overline{\Delta}$ denotes the filter length.
Different approaches exist for the velocity scale but generally it will be a function of the resolved strain rate tensor.
In AVBP code, several algebraic models are available like Smagorinsky (classical, filtered or dynamic) [24, 37, 78] or WALE [25], which fits the model constants and proposes equations for the velocity scale in order to better adapt to the simulation conditions.
A subgrid-scale energy transport equation can also be solved in order to obtain a better velocity scale estimation, but the computational time is penalized.
For more informations concerning the subgrid-scale models, refer to [69].

3.3.3 Filtered progress variable conservation law

Under the LES formalism, the progress variable conservation equation becomes:

$$\frac{\partial \overline{\rho} \tilde{Y}_c}{\partial t} + \frac{\partial \overline{\rho} \tilde{Y}_c \tilde{u}_j}{\partial x_j} = -\frac{\partial \overline{J_j^{Y_c}}}{\partial x_j} - \frac{\partial \overline{J_j^{Y_c}}^{sgs}}{\partial x_j} + \overline{\dot{\omega}}_{Y_c} \tag{3.48}$$

Neglecting the correlations between the progress variable's molecular diffusivity and the progress variable's gradient fluctuations and also considering that the filtering and derivative operations commute, the filtered diffusive progress variable flux is approximated by the following relation:

$$\overline{J_j^{Y_c}} \approx -\overline{\rho} \frac{\nu}{Sc_{Y_c}} \frac{\partial \tilde{Y}_c}{\partial x_j} \tag{3.49}$$

The SGS progress variable diffusive flux $\overline{J_j^{Y_c}}^{sgs} = -\overline{\rho}\widetilde{Y_c'' u_j''} = -\overline{\rho}(\widetilde{Y_c u_j} - \tilde{Y}_c \tilde{u}_j)$ is usually modeled as a gradient law:

$$\overline{J_j^{Y_c}}^{sgs} = -\overline{\rho} \frac{\nu_t}{Sc_{Y_c}^t} \frac{\partial \tilde{Y}_c}{\partial x_j} \tag{3.50}$$

The species will be driven between the large and the small scales with a turbulent Schmidt number $Sc^t_{Y_c} = 0.6$.
The modeling of $\overline{\dot{\omega}}_{Y_c}$ is challenging as it depends on SGS flame turbulence interactions. A wide range of modeling strategies has been developed for that purpose in LES with tabulated chemistry (e.g. Thickened Flame model for LES ($TFLES$) [16] or the Filtered Flame Formulation for LES ($F-TACLES$) [5, 27]). In this preliminary work, we will focus on combustion regimes that exhibit low gradients of temperature and species. Indeed, in chapter 5, the auto-ignition phenomenon in a quasi-homogeneous mixture will be studied. We will assume that interactions between chemistry and turbulence are resolved at the LES filter size scale. Therefore, the filtered reaction rate of the progress variable is approximated by:

$$\overline{\dot{\omega}}_{Y_c} \approx \dot{\omega}^{tab}_{Y_c}(\tilde{Y_c}). \tag{3.51}$$

3.3.4 Filtered energy conservation law

The total energy equation under the LES approach is written:

$$\frac{\partial \overline{\rho}\tilde{E}}{\partial t} + \frac{\partial \overline{\rho}\tilde{E}\tilde{u_j}}{\partial x_j} = -\frac{\partial \overline{u_i p \delta_{ij}}}{\partial x_j} + \frac{\partial \overline{u_i \tau_{ij}}}{\partial x_j} - \frac{\partial \overline{q_j}}{\partial x_j} - \frac{\partial \overline{q_j}^{sgs}}{\partial x_j} \tag{3.52}$$

Higher order correlations between the different variables of the viscous stress tensor are assumed negligible:

$$\overline{u_i p \delta_{ij}} + \overline{u_i \tau_{ij}} \approx \tilde{u_i}\overline{p}\delta_{ij} + \overline{\rho}\nu(\frac{\partial \tilde{u_j}}{\partial x_i} + \frac{\partial \tilde{u_i}}{\partial x_j} - \frac{2}{3}\delta_{ij}\frac{\partial \tilde{u_l}}{\partial x_l}) \tag{3.53}$$

The filtered heat flux is:

$$\overline{q_j} = -\overline{\rho}\frac{\nu}{Pr}\frac{\partial \tilde{h}}{\partial x_j} \tag{3.54}$$

The SGS heat flux vector $\overline{q_j}^{sgs} = -\overline{\rho}\widetilde{E''u''_j} = -\overline{\rho}(\widetilde{Eu_j} - \tilde{E}\tilde{u_j})$ is usually modeled as a gradient law:

$$\overline{q_j}^{sgs} = -\overline{\rho}\frac{\nu_t}{Pr^t}\frac{\partial \tilde{h}}{\partial x_j} \tag{3.55}$$

The heat transfer between the large and the small scales is calculated under a turbulent Prandtl number $Pr^t = 0.9$. So, the turbulent Lewis number will be $Le_t = 0.66$

Using all these models, the system of reactive Navier-Stokes equations to be solved becomes:

$$\frac{\partial \overline{\rho}}{\partial t} + \frac{\partial \overline{\rho}\tilde{u_j}}{\partial x_j} = 0 \tag{3.56a}$$

$$\frac{\partial \overline{\rho}\tilde{u_i}}{\partial t} + \frac{\partial \overline{\rho}\tilde{u_i}\tilde{u_j}}{\partial x_j} = -\frac{\partial \overline{p}\delta_{ij}}{\partial x_j} + \frac{\partial}{\partial x_j}(\mu+\mu_t)\left(\frac{\partial \tilde{u_j}}{\partial x_i} + \frac{\partial \tilde{u_i}}{\partial x_j} - \frac{2}{3}\delta_{ij}\frac{\partial \tilde{u_l}}{\partial x_l}\right) \quad , i = 1,2,3 \tag{3.56b}$$

$$\frac{\partial \overline{\rho}\tilde{Y_c}}{\partial t} + \frac{\partial \overline{\rho}\tilde{Y_c}\tilde{u_j}}{\partial x_j} = \frac{\partial}{\partial x_j}\left[\left(\frac{\mu}{Sc_{Y_c}} + \frac{\mu_t}{Sc^t_{Y_c}}\right)\frac{\partial \tilde{Y_c}}{\partial x_j}\right] + \dot{\omega}^{tab}_{Y_c}(\tilde{Y_c}) \tag{3.56c}$$

$$\begin{aligned}\frac{\partial \overline{\rho}\tilde{E}}{\partial t} + \frac{\partial \overline{\rho}\tilde{E}\tilde{u_j}}{\partial x_j} = &-\frac{\partial \tilde{u_i}\overline{p}\delta_{ij}}{\partial x_j} + \frac{\partial}{\partial x_j}\tilde{u_i}(\mu+\mu_t)\left(\frac{\partial \tilde{\boldsymbol{u_j}}}{\partial x_i} + \frac{\partial \tilde{u_i}}{\partial x_j} - \frac{2}{3}\delta_{ij}\frac{\partial \tilde{u_l}}{\partial x_l}\right) \\ &+ \frac{\partial}{\partial x_j}\left[\left(\frac{\mu}{Pr} + \frac{\mu_t}{Pr^t}\right)\frac{\partial h}{\partial x_j}\right]\end{aligned} \tag{3.56d}$$

Chapter 4

Tests validations

In this chapter the consistency of the coupling between the thermo-chemical table and the CFD solver will be ensured through analysis of the compressible effects and of the auto-ignition delay predictions. The first objective is to investigate the propagation of a $1-D$ *longitudinal acoustic wave through a one-component gaseous medium with periodical boundary conditions. The variations in pressure are addressed either by means of complex chemistry or by tabulated chemistry approach. The second test consists in simulating an entropic wave carried by the mean velocity field through a multi-component n-heptane-air mixture, using tabulated chemistry approach. The table discretization requirements are put forward under the constraint of not introducing significant parasite acoustic waves when the thermo-chemical database is used. Then, 0-D constant volume simulations were performed to check the accuracy of the ignition delay estimation. For the last test, the chemical prediction capability of this technique is validated in a homogeneous HCCI configuration by performing simulations under variable volume.*

4.1 Introduction

In chapter 2, a new approach to address chemical species and auto-ignition delays in engine combustion was carried out through a tabulated chemistry method characterized by three controlling variables, the normalized energy, density and progress variable (ρ^*,e^*,c^*). As exhaustively discussed in chapter 3, this tabulated chemistry approach has particularities that allow the coupling with a compressible *LES* solver.
The objective of this chapter is to validate the coupling through a collection of various test cases summarized in Table 4.1

Case	Reactivity	Approach	Component
Acoustic wave	non-reactive	chemical kinetics tabulated chemistry	single
Entropic wave	reactive non-reactive	tabulated chemistry	multi
Auto-ignition	reactive	chemical kinetics tabulated chemistry	multi

Table 4.1 : *Coupling validation test cases*

Under compressible effects considerations, a consistent coupling is required. Therefore linear acoustics equations which possess analytical solutions are used to ensure a proper description of the convective and the acoustic phenomena.
Then, the auto-ignition delay simulations are validated by performing constant volume computations pertinent to internal combustion engine operating conditions, including pressure and temperature. The last test validates the behavior of the thermo-chemical table in a variable volume configuration.

4.2 Implementation validation: study of compressible effects

The 1-D Euler system of equations for a multi-component flow is expressed by eqs. 4.1 when a chemical kinetic mechanism is considered and by eqs. 4.2 when a tabulated chemistry approach describes the chemical evolution of the system.

Chemical kinetic mechanism

$$\frac{\partial \rho}{\partial t} + \frac{\partial \rho u}{\partial x} = 0 \tag{4.1a}$$

$$\frac{\partial \rho u}{\partial t} + \frac{\partial \rho u^2}{\partial x} = -\frac{\partial p}{\partial x} \tag{4.1b}$$

$$\frac{\partial \rho E}{\partial t} + \frac{\partial \rho u E}{\partial x} = -\frac{\partial up}{\partial x} \tag{4.1c}$$

$$\frac{\partial \rho Y_k}{\partial t} + \frac{\partial \rho u Y_k}{\partial x} = 0, k = 1, ..., N_{sp} \tag{4.1d}$$

Tabulated chemistry approach

$$\frac{\partial \rho}{\partial t} + \frac{\partial \rho u}{\partial x} = 0 \tag{4.2a}$$

$$\frac{\partial \rho u}{\partial t} + \frac{\partial \rho u^2}{\partial x} = -\frac{\partial p}{\partial x} \tag{4.2b}$$

$$\frac{\partial \rho E}{\partial t} + \frac{\partial \rho u E}{\partial x} = -\frac{\partial up}{\partial x} \tag{4.2c}$$

$$\frac{\partial \rho \psi_l}{\partial t} + \frac{\partial \rho u \psi_l}{\partial x} = 0, l = 1, ..., N \tag{4.2d}$$

where Y_k stands for the mass fraction of species evolving in the chemical kinetic mechanism, explicitly used in the solver and ψ_l stands for the reduced variables when the chemistry is indirectly considered through tabulation chemistry approach. Two of the controlling variables, namely the energy and the density are transported. Therefore only an additional equation for the progress variable ψ_l is needed for the system to be complete.

As shown in the appendix C, the eigenvectors of the *Jacobian* matrix of the non-viscous fluxes in the primitive variables formulation enable to express the characteristic wave variations $\partial\overrightarrow{W}$ in terms of primitive variables $\partial\overrightarrow{V}$, appendix C eq. C.25. The eigenvalues of the same matrix fill the main diagonal of the diagonal matrix and allow for the system of equations, see eq. (4.1) or (4.2) to be rewritten in terms of characteristic waves. This highlights, in *1-D* configuration, the existence of the following characteristic waves:

- $\partial w_s = \partial\rho - \frac{1}{c^2}\partial p$ an entropic wave traveling at an eigenvalue u

- $\partial w_+ = \partial u + \frac{1}{\rho c}\partial p$ an acoustic wave traveling at an eigenvalue $u + c$
- $\partial w_- = -\partial u + \frac{1}{\rho c}\partial p$ an acoustic wave traveling at an eigenvalue $u - c$
- $\partial w_{s_{Y_k}} = \partial Y_k$ chemical species entropic waves traveling at an eigenvalue u or
- $\partial w_{s_{\psi_l}} = \partial \psi_l$ reduced variable entropic waves traveling at an eigenvalue u

In the following, a gaseous medium will be perturbed either by an acoustic or an entropic wave. In both cases, a gaussian wave perturbation will be considered and superimposed onto a mean flow in a *1-D* domain aligned with the x-axis of coordinates.

$$\partial\overrightarrow{W}(x) = \mathcal{A}\, e^{-\frac{(x-x_0)^2}{\sigma^2}}\mathbb{1} \tag{4.3}$$

where $\mathbb{1} = \begin{pmatrix}1 & \dots & 1\end{pmatrix}^T$ is a $N+3$ column matrix for multi-component case and a 4 column matrix for tabulated chemistry approach. $\mathcal{A}$ is the wave amplitude, x_0 is the mean location of the peak, σ is the variance which will measure the width of the gaussian distribution.
In order to acoustically (∂w_+, ∂w_-) or entropically (∂w_s) disturb the flow, the chosen gaussian wave $\partial\overrightarrow{W}$ is transmitted as initial solution to the solver. In compressible codes, like $AVBP$, the $\overline{\overline{R_U}}$ matrix, that enables the passage from the characteristic wave $\partial\overrightarrow{W}$ to the actually transported conservative variables $\partial\overrightarrow{U}$, is then required. For additional information concerning the creation of a disturbance in a compressible solver under the chemical kinetics formalism and under the tabulated chemistry approach proposed in this paper refer to the appendix C.

4.2.1 Non-reactive acoustic waves

In the current section, the behavior of acoustic wave traveling at the speed $u + c$ will be evaluated. To add precisely this acoustic disturbance of velocity $u + c$, the entropic wave variation must vanish $\partial w_s = 0$ and also the acoustic wave traveling at the speed $u - c$ has to cancel $\partial w_- = 0$. In order to compare the two versions of the code i.e. chemical kinetics and tabulated chemistry, a one-component N_2 flow is considered. The wave's spatio-temporal evolution is given by the system 4.1 or 4.2.

It is clear that in this particular case no chemical reaction is to be expected and as a result the progress variable is identical to zero $c^* = 0$ everywhere. Under these restrictions as long as the perturbation remains relatively small, as established in appendix B, the evolution of the $u + c$ acoustic wave is adequately described by the relation (B.10a).

$$\partial p_+ = c^2 \partial \rho_+ \qquad and \qquad \partial p_+ = \overline{\rho}\, c \partial u_+ \tag{4.4}$$

and consequently:

$$\partial w_+ = 2\partial u \quad or \quad \partial w_+ = \frac{2}{\rho c}\partial p \tag{4.5}$$

This means that, given a certain perturbation of amplitude $\mathcal{A}$ i.e. linked to the velocity ∂u, the perturbations to impose on pressure and density are known through relations (4.4) and can be added to the mean field. Then, the matrix $\overline{\overline{R_U}}$ will make the passage from the chosen acoustic wave ∂w_+ to the conservative variable transported in the code,
- in multi-component formulation:

$$\begin{pmatrix} \partial\rho \\ \partial\rho u \\ \partial\rho E \end{pmatrix} = \begin{pmatrix} 1 & \frac{\rho}{2c} & \frac{\rho}{2c} & 0 \\ u & \frac{\rho}{2c}(u+c) & \frac{\rho}{2c}(u-c) & 0 \\ e_c - \frac{\mathcal{X}}{\beta} & \frac{\rho}{2c}(e_c - \frac{\mathcal{X}}{\beta} + cu + \frac{c^2}{\beta}) & \frac{\rho}{2c}(e_c - \frac{\mathcal{X}}{\beta} - cu + \frac{c^2}{\beta}) & \frac{\rho}{\beta}\chi_{Y_{N_2}} \end{pmatrix} \begin{pmatrix} 0 \\ \partial w_+ \\ 0 \\ 0 \end{pmatrix} \tag{4.6}$$

- and in tabulated chemistry formulation:

$$\begin{pmatrix} \partial\rho \\ \partial\rho u \\ \partial\rho E \\ \partial c^* \end{pmatrix} = \begin{pmatrix} 1 & \frac{\rho}{2c} & \frac{\rho}{2c} & 0 \\ u & \frac{\rho}{2c}(u+c) & \frac{\rho}{2c}(u-c) & 0 \\ e_c - \frac{\mathcal{X}}{\beta} & \frac{\rho}{2c}(e_c - \frac{\mathcal{X}}{\beta} + cu + \frac{c^2}{\beta}) & \frac{\rho}{2c}(e_c - \frac{\mathcal{X}}{\beta} - cu + \frac{c^2}{\beta}) & -\frac{\rho}{\beta}\chi_{c^*} \\ c^* & \frac{\rho}{2c}c^* & \frac{\rho}{2c}c^* & \rho \end{pmatrix} \begin{pmatrix} 0 \\ \partial w_+ \\ 0 \\ 0 \end{pmatrix} \tag{4.7}$$

As underlined in section 3.2.2, the thermodynamical variables are addressed differently in $AVBP$ (complex chemistry) and $AVBP - TTC$ (tabulated chemistry). To validate the correct implementation of the tabulated chemistry ($\rho^*,\ e^*,\ c^*$) in AVBP, two cases were chosen to be tested:

- The 1^{st} case for which the heat capacities are constant throughout the imposed acoustic wave.
- The 2^{nd} case for which the heat capacities change their values at some position inside the acoustic wave.

The aim of the implementation validation is to assure that the waves (acoustic or entropic) are propagated in the same way by new solver version $AVBP - TTC$ and the departure solver $AVBP$. Therefore, the thermodynamical variables read in the database (ρ^*, e^*, c^*) are identical with those calculated with complex chemistry.

4.2.1.1 Constant heat capacity throughout the acoustic wave

$\mathcal{A}$. Problem set-up

Boundary conditions. The disturbance evolution and existence in the domain is related to its boundary conditions. Periodicity is assumed because it is the only situation where the problem can be closed exactly, as the computation domain is folded on itself. As no boundary conditions are required, their effect is separated and does not interfere with the current problem.

Thermo-chemical table description. For an accurate comparison between the two manner of considering chemistry in compressible solvers, the thermo-chemical table must contain the same information as the one employed when using a chemical kinetic mechanism. The purpose-build N_2 thermo-chemical table is conceived as to adapt to the particularities of the $AVBP$ multi-component formalism. Thus, a brief description of the procedure to address thermo-chemistry in the $AVBP$ code will be given in the following:

- *Solving the Euler system of equation (4.1).* The sensible mass enthalpy for each species is tabulated as function of temperature with a step of 100 K. This also gives access to the sensible mass energy as they are related through an analytical formula: $e_s = h_s + \frac{R}{W^{tab}}$. The constant pressure and the constant volume heat capacities are the slope of the enthalpy or sensible energy $C_p = \frac{\partial h_s}{\partial T}$, $C_v = \frac{\partial e_s}{\partial T}$,

consequently they are constant on each 100 K temperature interval. Making use of the fact that the temperatures varie continuously with the transported variable either enthalpy or energy, it can be obtained by linear interpolation. The pressure is given by the ideal gas law.

- *Solving the Euler system of equation (4.2).* Under tabulated chemistry approach, as the species are no longer transported, as proposed in chapter 3, the temperature T^{tab} is recovered from the thermo-chemical table. Using the tabulated heat capacities C_p^{tab}, C_v^{tab} and the ideal gas law, will give access to the pressure: $p = \boldsymbol{\rho}\ r^{tab}\ T^{tab}$.

Thus, for the Euler system of equation, only the temperature $T^{tab}(\rho^*, e^*, c^*)$ and the gas constant $r^{tab}(\rho^*, e^*, c^*)$ must be recovered from the table in order to closure the problem.
To assure that the thermo-chemical data enclosed in the purpose-build N_2 table mimics the multi-component behavior its coordinates are defined as follows:

1. The energy coordinate calculated by performing the integral $e_s^{tab} = \int_{T_-}^{T_+} C_v dT - \frac{RT_0}{W}$ using the convenient heat capacities, constant within each 100 K interval.

2. The progress variable coordinate is a dummy variable and keeps its initial value $c^* = 0$, corresponding to a fixed initial value $Y_{N_2} = 1$ for the mass fraction of the only chemical species in the medium. This indicates that, in a non-reactive system, the tabulated thermo-chemical variable moves in a $2-D$ subspace: $T^{tab}(\rho^*, e^*)$, $r^{tab}(\rho^*, e^*)$.

3. The density coordinate is also a dummy variable in this case. Indeed, the gas constant depends only on the chemical composition $r = \sum_{k=1}^{N_{sp}} \frac{RY_k}{W_k}$ which does not undergo any change in a cold mixture. In other words the value of the gas constant is fixed by the initial composition $r^{tab} = constant$. Furthermore, during the cold flow computation the constant volume heat capacity depends no longer on composition but only on temperature $C_v = \sum_{k=1}^{N_{sp}} C_{v,k}(T) Y_k$ thus the sensible energy $e = \int_{T_0}^{T} C_v dT - \frac{RT_0}{W}$ is only a function of temperature, and vice versa $T^{tab}(e^*)$.

Therefore, to study the evolution of a non-reactive acoustic wave, a $1-D$ thermo-chemical table which contains the temperature $T^{tab}(e^*)$ and the gas constant $r^{tab} = C_v^{tab}(e^*) - C_v^{tab}(e^*)$ is self-sufficient. For the current case the thermo-chemical database is presented in Table 4.2. For the chosen wave amplitude, the chosen extrema temperature of the table are $T^- = 320K$ and $T^+ = 360\ K$, corresponding to the values of energy $e^- \approx 237\ KJ/kg$ and respectively $e^+ \approx 267\ KJ/kg$.

Point	e^*	$T[K]$	$C_p[J/kg/K]$	$C_v[J/kg/K]$
1	0	320	1040,22	744,49
2	0.25	330	1040,22	744,49
3	0. 5	340	1040,22	744,49
4	0.75	350	1040,22	744,49
5	1	360	1040,22	744,49

Table 4.2 : *N_2 table with constant heat capacities*

Initial solution. The mean flow field and the gaussian acoustic wave in accordance with 4.3 of amplitude $\mathcal{A} = \frac{u'}{c}$ superimposed on it are given in Table 4.3.

$\overline{p}$	$10^5\ Pa$	p'	$52,7\ Pa$
$\overline{\rho}$	$0,9626\ kg/m^3$	ρ'	$3,4910^{-4}\ kg/m^3$
$\overline{T}$	$350\ K$	T'	$0.05\ K$
$\overline{u}$	$0\ m/s$	u'	$0.1382\ m/s$

Table 4.3 : *Initial solution when heat capacities are constant throughout the wave*

As the linear acoustic theory asserts, the fluctuations presented in Table 4.3 respect the relations B.10a and B.9a. In fact, it can be observed that for this acoustic wave moving at the speed $u + c$, the perturbations on u', p' and ρ' have the same sign. Figure 4.1 presents the comparison between the initial acoustic wave when it is imposed by applying:

- the relation 4.6: N_2 species being directly considered in the code; lines in the figures

- the relation 4.7: when the tabulated chemistry approach is used; symbols on the figures.

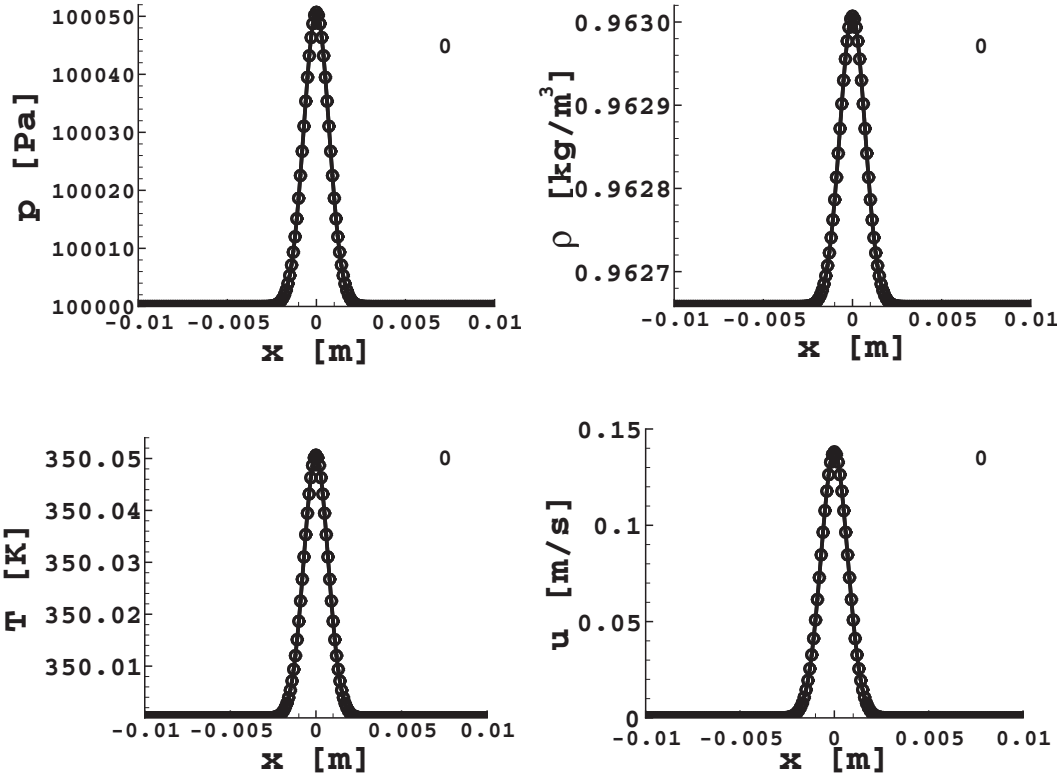

Figure 4.1 : *Non reactive acoustic wave disturbance at constant heat capacities : pressure, density, temperature and velocity fluctuations. Line: multi-component code; Symbols: tabulated chemistry code*

The similarity between the two curves is a first proof that a non-adiabatic table $T(e^*)$ is able to account for the acoustics of the system without further assumptions as done when the thermo-chemical tables are generated at constant pressure [85].

$\mathcal{B}$. Results

Time evolution of the acoustic wave is followed inside the periodic domain and presented in figures 4.2. The estimated physical time required for 1 lap time τ_{lap} is related to the domain length L and the sound speed c:

$\tau_{tour} = \frac{c}{L}$. Therefore, 15 laps calculations have been done over the total physical time of 0.785 ms.

The figures claim that after 1, 5 or even 15 laps (from left to right) inside the domain, the acoustic behavior is similar whether the chemical table (symbols) is used or not (line). The test case presented in this section evidences that a non-adiabatic thermo-chemical table is able to precisely reproduce a typical behavior of a compressible solver. In the same direction, a second non-adiabatic thermo-chemical table will be build as to trace a more realistic wave which changes the value of heat capacity.

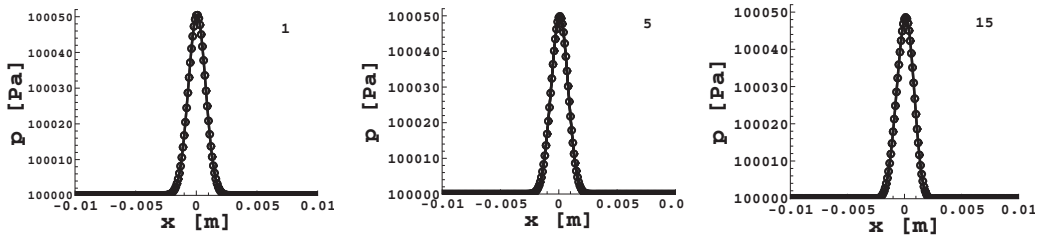

(a) Pressure

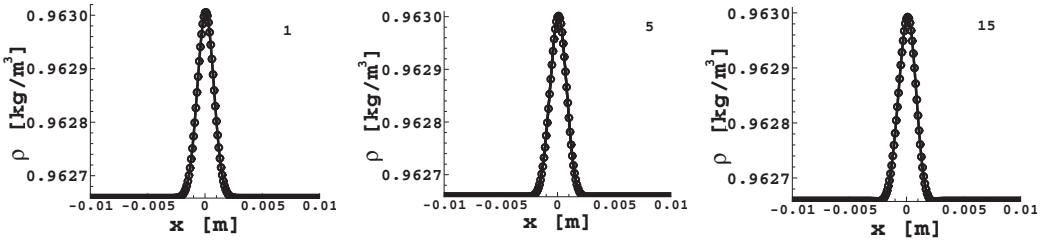

(b) Density

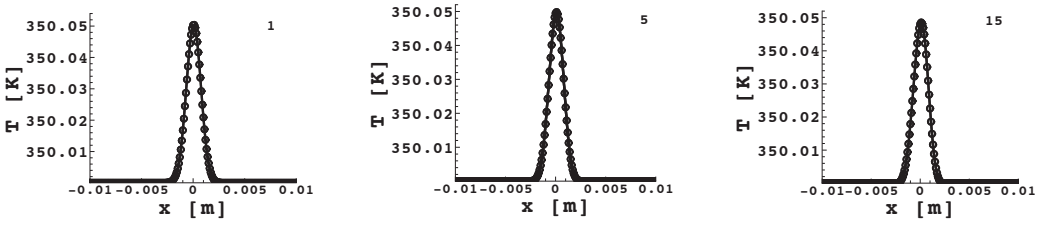

(c) Temperature

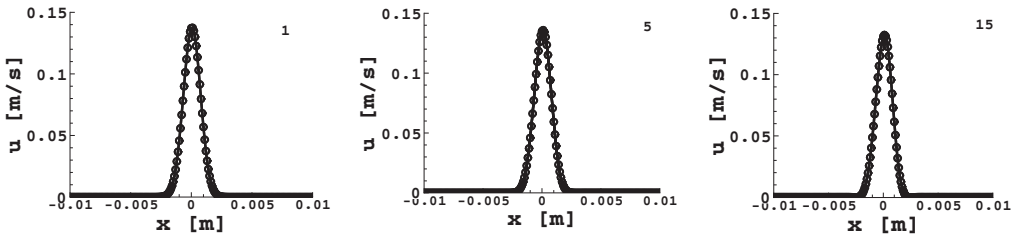

(d) Velocity

Figure 4.2 : *Non reactive acoustic wave propagation in a periodic domain, pressure, density, temperature and velocity evolution after* $1^{st}, 5^{th}, 15^{th}$ *laps (from left to right). Line: multi-component; Symbols: tabulated chemistry ,* $T_i = 350K$

4.2.1.2 Variable heat capacity throughout the acoustic wave

$\mathcal{A}$. Problem set-up

Boundary conditions. As in the previous section, periodicity is imposed at the boundary.

Thermo-chemical table description The thermo-chemical table features are identical to the ones presented for the previous case.
The temperature of the N_2 chemical table varies between $T^- = 280K$ and $T^+ = 320\ K$ with a step of $\Delta T = 10\ K$. For the chosen temperature interval the sensible energy varies from $e^- \approx 207\ KJ/kg$ to $e^+ \approx 237\ KJ/kg$. The information enclosed in the N_2 thermo-chemical with variable heat capacities is presented in Table 4.4.

Point	e^*	$T[K]$	$C_p[J/kg/K]$	$C_v[J/kg/K]$
1	0	280	1039,28	742,34
2	0.25	290	1039,28	742,34
3	0. 5	300	1040,22	744,49
4	0.75	310	1040,22	744,49
5	1	320	1040,22	744,49

Table 4.4 : *N_2 table with variable heat capacities*

Initial solution The mean flow field, on which a gaussian acoustic wave 4.3 of amplitude $\mathcal{A} = \frac{u'}{c}$ is superimposed, is given in Table 4.5 and plot in figure 4.3.

$\overline{p}$	$10^5\ Pa$	p'	$52,7\ Pa$
$\overline{\rho}$	$1,1236\ kg/m^3$	ρ'	$4,0710^{-4}s\ kg/m^3$
$\overline{T}$	$299,97\ K$	T'	$0,043\ K$
$\overline{u}$	$0\ m/s$	u'	$0,1279\ m/s$

Table 4.5 : *Initial solution when heat capacities vary throughout the wave*

Again, it can be observed that for this acoustic wave going at the speed $u + c$, the perturbations on u', p' and ρ' have the same sign. Figure 4.3

presents the comparison between the initial wave when it is imposed by applying:

- the relation 4.6: N_2 species being directly considered in the code; lines in the figures
- the relation 4.7, when the tabulated chemistry approach is used; symbols on the figures.

The similarity between the two curves prove the capacity of a non-adiabatic table $T(e^*)$ to account for the acoustics of the system without further assumptions [85].

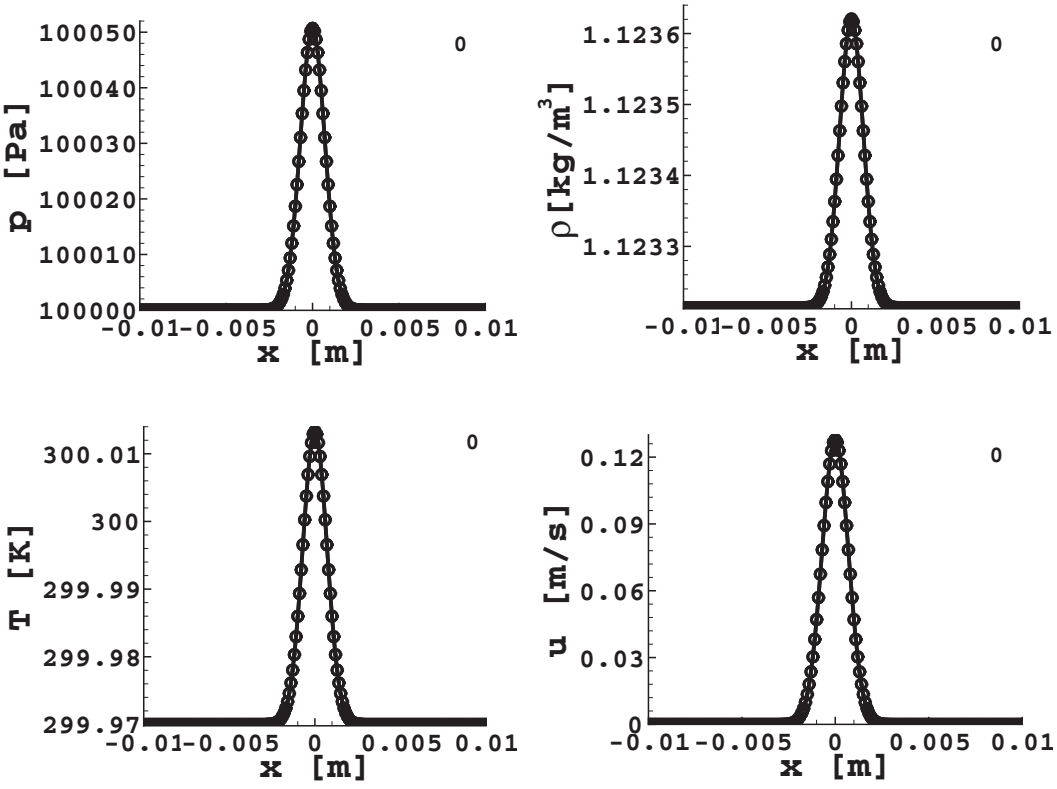

Figure 4.3 : *Non reactive acoustic wave disturbance at variable heat capacity: pressure, density, temperature and velocity fluctuations. Line: multicomponent; Symbols: tabulated chemistry*

$\mathcal{B}$. Results

Time evolution of the acoustic wave is followed inside the periodic domain and presented in figure 4.4 .

The figures claim that after 1, 5 or even 15 laps (from left to right) inside the domain, the acoustic behavior is similar whether the chemical table (symbols) is used or not (line).

In this section it was shown that the non-adiabatic thermo-chemical tables are able to tackle the energy fluctuations due to acoustic pressure perturbations. Accordingly, for a fully compressible code, the thermo-chemical variables can be directly read in the table.

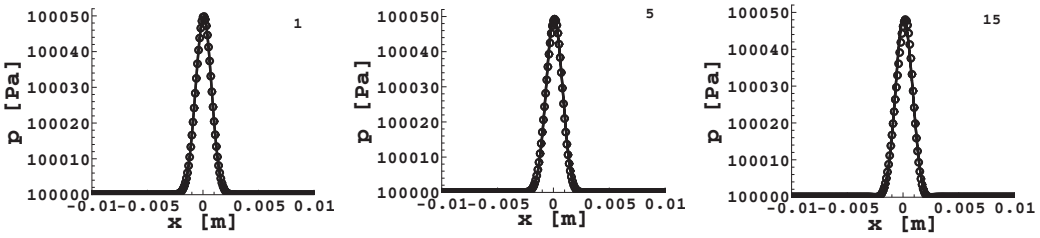

(a) Pressure

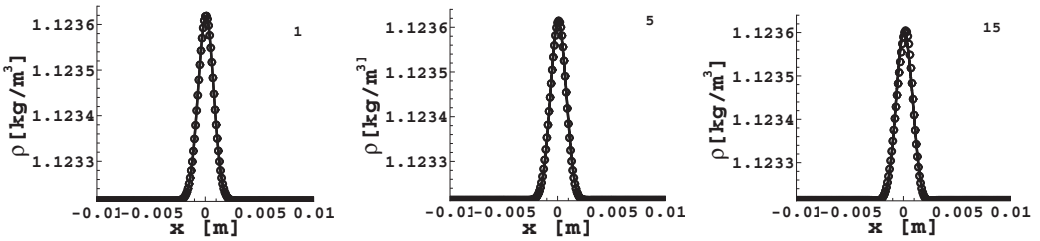

(b) Density

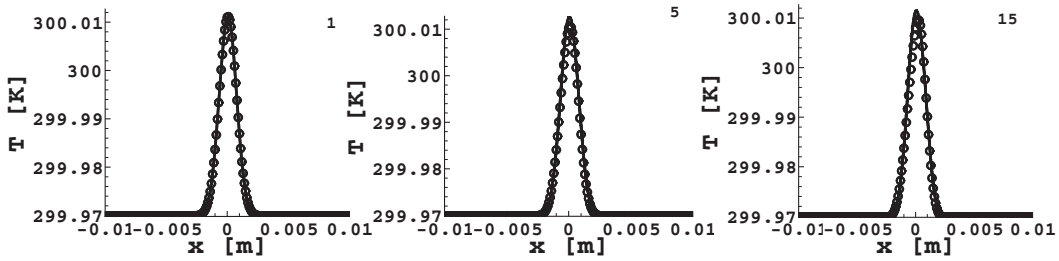

(c) Temperature

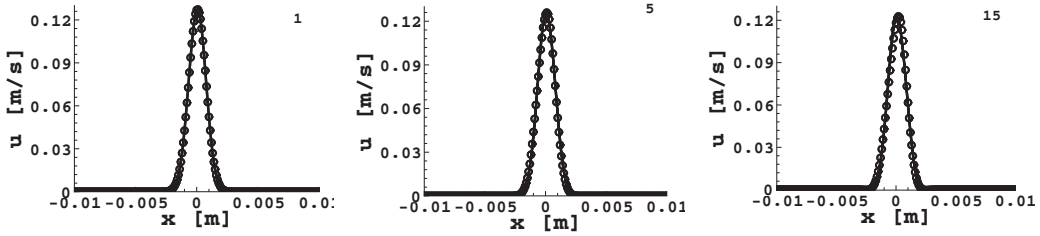

(d) Velocity

Figure 4.4 : *Non reactive acoustic wave propagation in a periodic domain, evolution after* $1^{st}, 5^{th}, 15^{th}$ *laps (from left to right). Line: multi-component; Symbols: tabulated chemistry ,* $T_i = 300K$

4.2.2 Non-reactive entropic waves

In the second test, the behavior of the entropic wave traveling from left to right at the speed u was evaluated. The purpose of this test is to evaluate the needed thermo-chemical table discretization when it is coupled with compressible solvers.
In order to add only a small entropic disturbance with a velocity u, the acoustic wave variations must vanish simultaneously $dw_+ = 0$ and $dw_- = 0$, achievable only if there are neither pressure nor velocity fluctuations. In this case there are entropic variations in the medium $dw_s \neq 0$, so:

$$\partial p_s = 0 \qquad and \qquad \partial u_s = 0 \qquad and \qquad \partial \rho_s \neq 0 \tag{4.8}$$

To impose an entropic wave as initial solution for a compressible solver, the following transformation is required (see appendix B and C):
- multi-component formulation:

$$\begin{pmatrix} \partial\rho \\ \partial\rho u \\ \partial\rho E \end{pmatrix} = \begin{pmatrix} 1 & \frac{\rho}{2c} & \frac{\rho}{2c} \\ u & \frac{\rho}{2c}(u+c) & \frac{\rho}{2c}(u-c) \\ e_c - \frac{\mathcal{X}}{\beta} & \frac{\rho}{2c}(e_c - \frac{\mathcal{X}}{\beta} + cu + \frac{c^2}{\beta}) & \frac{\rho}{2c}(e_c - \frac{\mathcal{X}}{\beta} - cu + \frac{c^2}{\beta}) \end{pmatrix} \begin{pmatrix} \partial w_s \\ 0 \\ 0 \end{pmatrix} \tag{4.9}$$

- tabulated chemistry formulation:

$$\begin{pmatrix} \partial\rho \\ \partial\rho u \\ \partial\rho E \\ \partial c^* \end{pmatrix} = \begin{pmatrix} 1 & \frac{\rho}{2c} & \frac{\rho}{2c} & 0 \\ u & \frac{\rho}{2c}(u+c) & \frac{\rho}{2c}(u-c) & 0 \\ e_c - \frac{\mathcal{X}}{\beta} & \frac{\rho}{2c}(e_c - \frac{\mathcal{X}}{\beta} + cu + \frac{c^2}{\beta}) & \frac{\rho}{2c}(e_c - \frac{\mathcal{X}}{\beta} - cu + \frac{c^2}{\beta}) & -\frac{\rho}{\beta}\chi_{c^*} \\ c^* & \frac{\rho}{2c}c^* & \frac{\rho}{2c}c^* & \rho \end{pmatrix} \begin{pmatrix} \partial w_s \\ 0 \\ 0 \\ 0 \end{pmatrix} \tag{4.10}$$

In this section a non reactive stoichiometric C_7H_{16}-air mixture will be disturbed by an entropic wave.

$\mathcal{A}$. Problem set-up

Boundary conditions For the same reasons mentioned in section 4.2.1, the evolution of the entropic wave will be pursued in a domain with periodic boundary conditions.

Thermo-chemical table description For this test case $n - C_7H_{16}$ tables are used. Refer to the chapter 2, for information about their coordinates variables and enclosed information. According to section 4.2.1, in a non-reactive mixture, the density ρ^* and the progress variable c^* are dummy variables. Hence only the discretization of the thermo-chemical table in terms of energy will be discussed.
For a non-reacting mixture, the energy and the temperature are in linear relationship with a slope equal to the mixture's constant volume heat capacity, see Fig. 4.5. Therefore, discretization in terms of energy Δe also means discretization in terms of temperature ΔT. Four thermo-chemical tables discretization will be discussed $\Delta T \approx 55K$, $\Delta T \approx 27K$, $\Delta T \approx 18K$ and $\Delta T \approx 5K$.

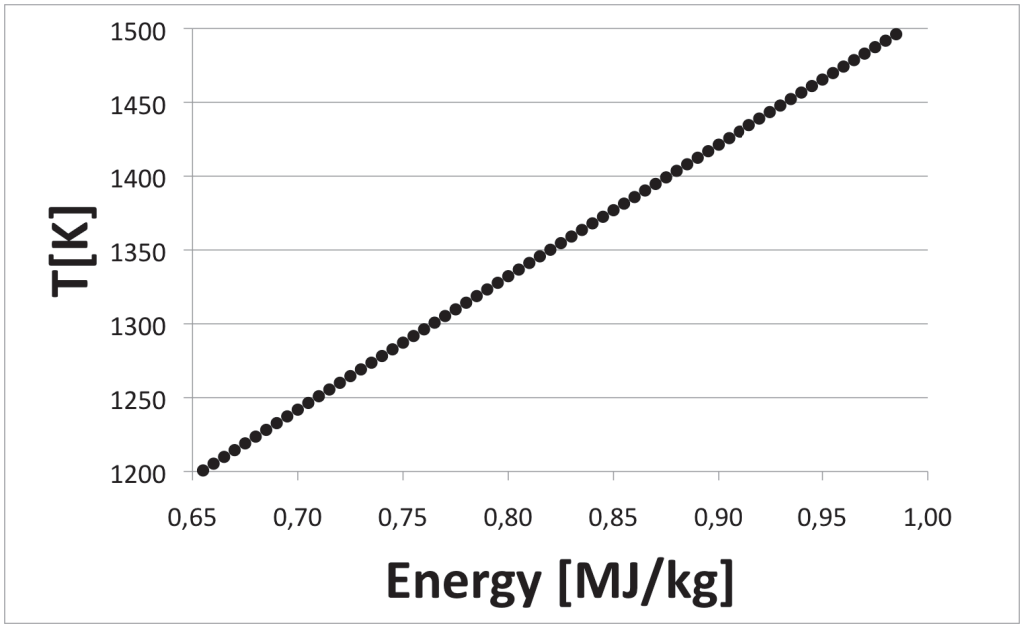

Figure 4.5 : *Relationship between the energy and the temperature for a non-reactive n-heptane-air mixture*

Initial solution
A parametric study of the influence of thermo-chemical table discretization on an entropic wave was performed. The same initial entropic wave (shown in figure 4.6) was imposed to a constant mean field for all thermo-

chemical tables tested.

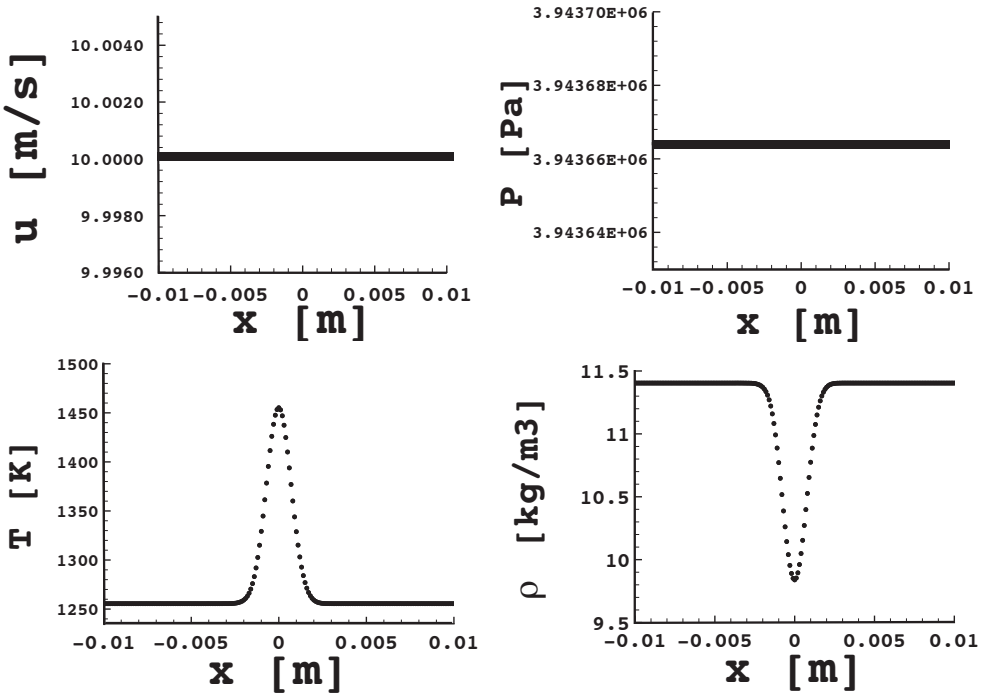

Figure 4.6 : *Non-reactive entropic wave: velocity, density, pressure, temperature*

As the focus is put on the effect of the table discretization, imposing the initial wave under 1^{st} order approximation assumption turns out to be insufficient or limited to very small fluctuations. To ensure that the contingent pressure fluctuations are related only to the table discretization, the entropy disturbance was set by means of an iterative search.
Given a fluctuation, i.e. imposed on the temperature ∂T, the corresponding density fluctuation is found with the use of the ideal gas law: $(\overline{\rho} + \partial\rho) = \frac{\overline{p}}{r(\overline{T}+\partial T)}$ by imposing the constant pressure $\overline{p}$ and considering the fact that r is constant for a non-reactive mixture. Then, the energy fluctuation due to temperature fluctuations are found by linear interpolation in the table.

$\mathcal{B}$. Results

First iteration overview

As shown in the figure 4.7, after the first iteration small acoustic perturbations are created in the domain, and they can be easily correlated to the discretization of the thermo-chemical database, presented as straight lines in the plots. Pressure scales of all figures are the same, yielding to the fact that coarser the table is, higher the pressure disturbance created by the linear interpolation in the database. Although the first iteration displays the dependency between the table discretization and acoustic perturbations created in the domain, they are too small to give knowledge about the thermo-chemical table discretization in relation with an accurate acoustic behavior. Thus, an analysis of the evolution in time of the perturbations was made.

Evolution in time

In figures 4.8 through 4.11, the evolution of the entropic perturbation is shown after 1^{st}, 5^{th}, 10^{th} and 15^{th} lap inside the domain.

The table discretization plays a minor role and creates very small parasite acoustic waves, that move inside the domain and interfere to each other. Even for the case when the largest table discretization temperature step of 55 K, the acoustic perturbation created does not exceed a relative error on pressure of $0,001\ {}^{0}/_{00}$. Thus, the table discretization with respect to ignition delay estimation will be of first concern.

The test cases presented in this section underline that the non-adiabatic tables are suitable for the coupling with compressible solvers.

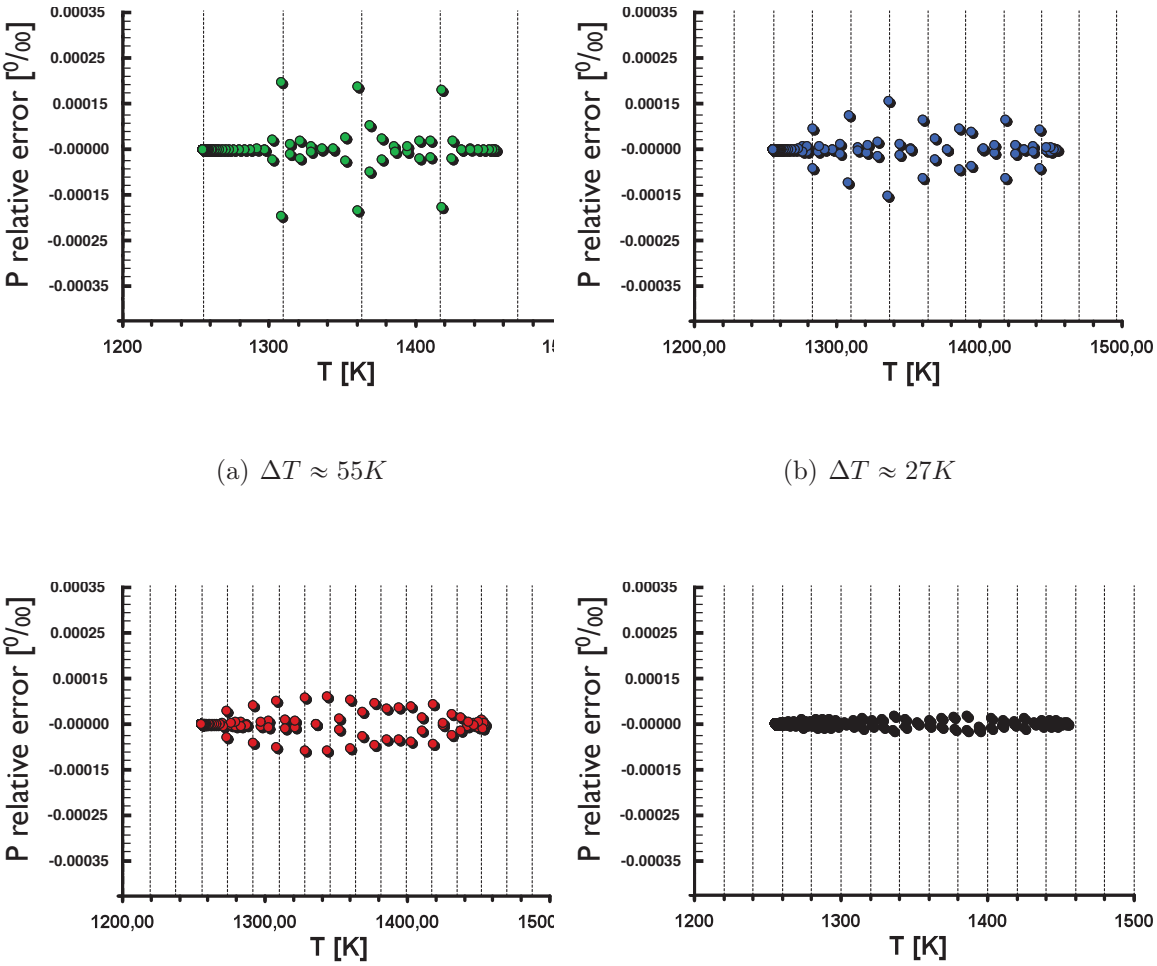

(a) $\Delta T \approx 55K$

(b) $\Delta T \approx 27K$

(c) $\Delta T \approx 18K$

(d) $\Delta T \approx 5K$

Figure 4.7 : *Non reactive entropic wave disturbance: pressure change after first iteration for various discretization of the thermo-chemical tables. Discontinuous lines are table values, corresponding do (a) $\Delta T \approx 55K$, (b) $\Delta T \approx 27K$, (c) $\Delta T \approx 18K$ and (d) $\Delta T \approx 5K$ discretization in temperature.*

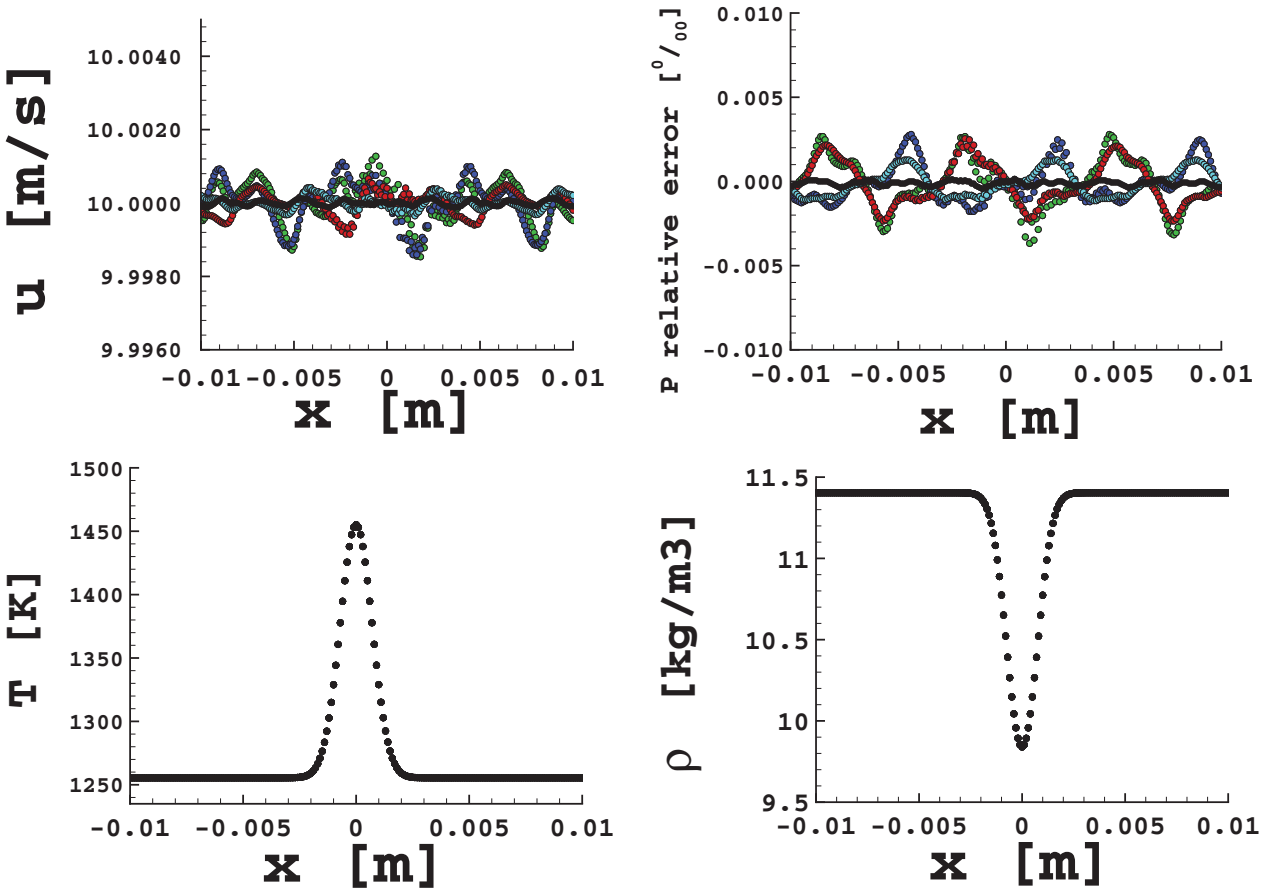

Figure 4.8 : *Non reactive entropic wave propagation in a periodic domain after* 1^{st} *lap time. The thermo-chemical table discretization given in terms of temperature is :* $\Delta T \approx 55K$ *(green),* $\Delta T \approx 27K$ *(blue),* $\Delta T \approx 18K$ *(red) and* $\Delta T \approx 5K$ *(black).*

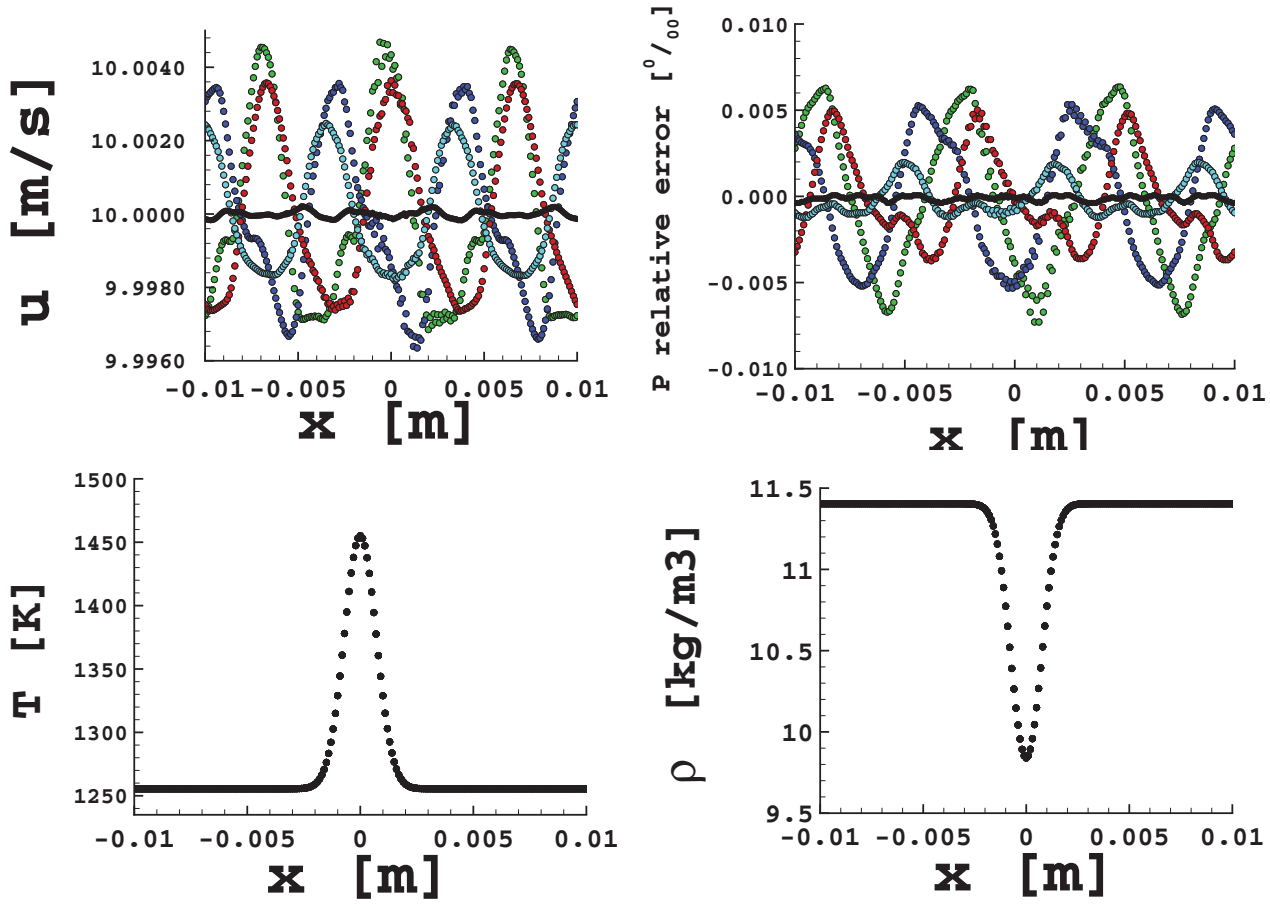

Figure 4.9 : *Non reactive entropic wave propagation in a periodic domain after 5^{th} lap time. The thermo-chemical table discretization given in terms of temperature is : $\Delta T \approx 55K$ (green), $\Delta T \approx 27K$ (blue), $\Delta T \approx 18K$ (red) and $\Delta T \approx 5K$ (black).*

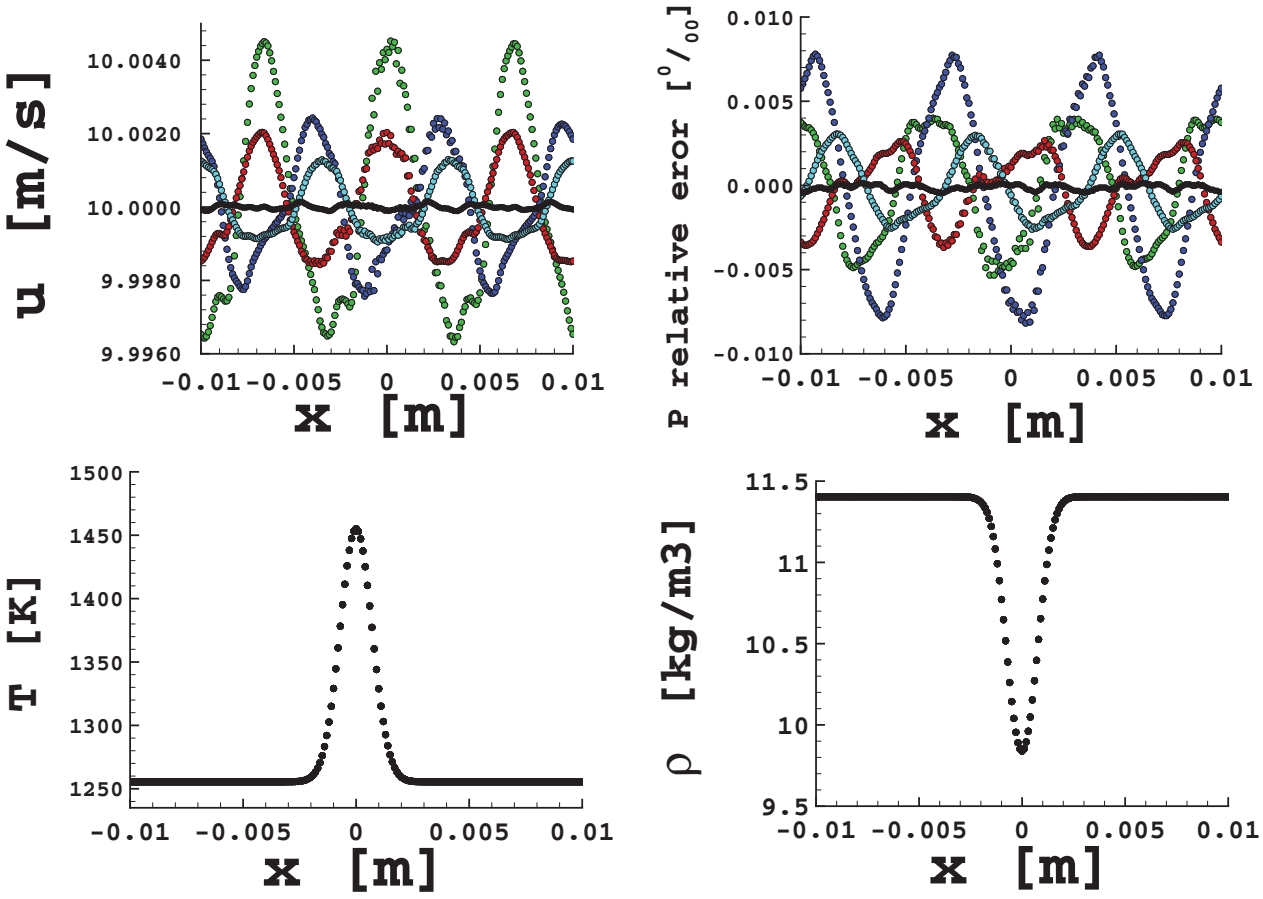

Figure 4.10 : *Non reactive entropic wave propagation in a periodic domain after* 10^{th} *lap time. The thermo-chemical table discretization given in terms of temperature is :* $\Delta T \approx 55K$ *(green),* $\Delta T \approx 27K$ *(blue),* $\Delta T \approx 18K$ *(red) and* $\Delta T \approx 5K$ *(black).*

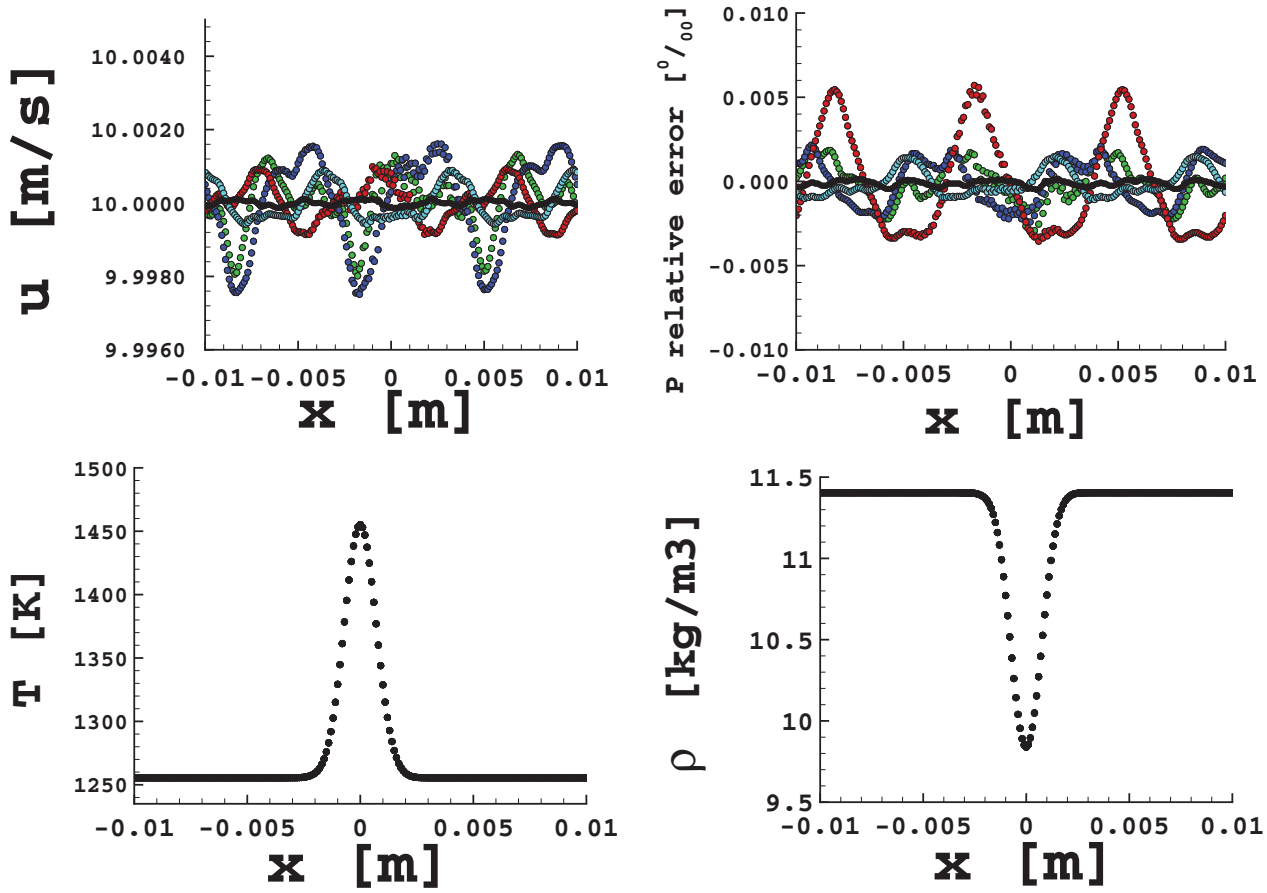

Figure 4.11 : *Non reactive entropic wave propagation in a periodic domain after* 15^{th} *lap time. The thermo-chemical table discretization given in terms of temperature is :* $\Delta T \approx 55K$ *(green),* $\Delta T \approx 27K$ *(blue),* $\Delta T \approx 18K$ *(red) and* $\Delta T \approx 5K$ *(black).*

4.3 Modeling validations: auto-ignition delays

4.3.1 Constant volume

As $AVBP$ is at least 2 dimensional solver, therefore the tabulated strategy was first tested on a $2-D$ constant volume computation. The $AVBP-TTC$ parameters are summarized in Table 4.6. The uniform 2-D mesh was created using the Hip tool [4].
To validate both the low temperature regime and the high temperature regime, two cases were chosen. Their temperature evolution is presented in the Figure 4.12. The AVBP TTC solution (symbols), see chapter 3, is compared with detailed kinetics calculations (line) for a low and a high temperature regime. The good agreement demonstrates the table's ability to account for variable pressure configurations.

4.3.2 0-D variable volume computations

In a four stroke cycle internal combustion engine, the piston has a reciprocating movement between the top dead center (TDC) and the bottom dead center (TDC) crank position. They are characterized by the minimum cylinder volume, called clearance volume V_c and the total or maximum cylinder volume V_t, respectively.
The difference between them is the volume swept out by the piston motion and it is called displaced volume V_d.

$$V_t = V_c + V_d \tag{4.11}$$

The ratio between the maximum and the minimum volume is the compression ratio r_c, typical CI engines value are 12 to 24.

$$r_c = \frac{V_c + V_d}{V_c} \tag{4.12}$$

The cylinder volume $V(\theta)$ at any crank angle position θ is

$$V(\theta) = V_c + \frac{\pi B^2}{4}(l + a - s(\theta)) \tag{4.13}$$

Grid and BC

Element type	**quads**
Total number of nodes	**44 (11*4)**
Total number of elements	**30**
Length L_x x L_y	**0.02 m x 0.02m**
x_{min} / y_{min}	2 10^{-3} m / 6.66 10^{-3} m
Boundary conditions	**slip, adiabatic walls**

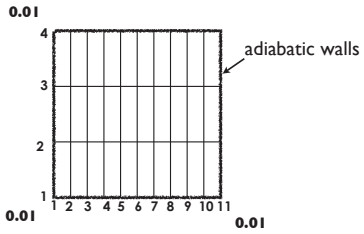

Flow Features

Governing equations	**unsteady Navier-Stokes**
Turbulence	**no** LES
Kinetics	**Tabulated chemistry**

Numerical parameters

Numerical scheme	**Lax Wendroff**
CFL	**0.01**
Artificial viscosity	**disabled**

Initial conditions

homogeneous mixture at	**low temperature**	**high temperature**
Energy	2 10^5 J/kg	4 10^5 J/kg
Density	2.58 10^5 kg/m^3	2.58 10^5 kg/m^3
Temperature	759 K	960 K
Pressure	5.4 bar	6.8 bar

Table 4.6 : *AVBP-TTC parameters for constant volume simulation*

where B is the cylinder bore, l is the connecting rod length, a is the crank radius and s is the distance between the crank axis and the piston pin axis, given by:

$$s(\theta) = acos\theta + \sqrt{l^2 - a^2 sin^2\theta} \tag{4.14}$$

The mean piston speed $\overline{S_p}$

$$\overline{S_p} = 2LN \tag{4.15}$$

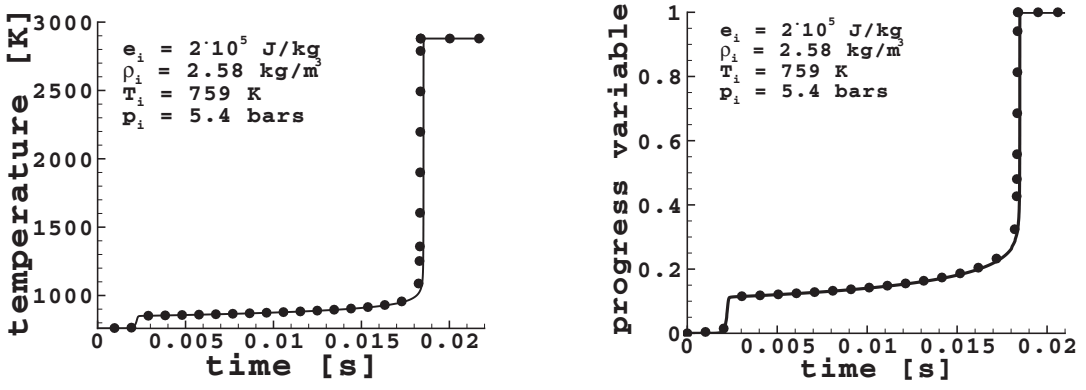

(a) Low temperature regime

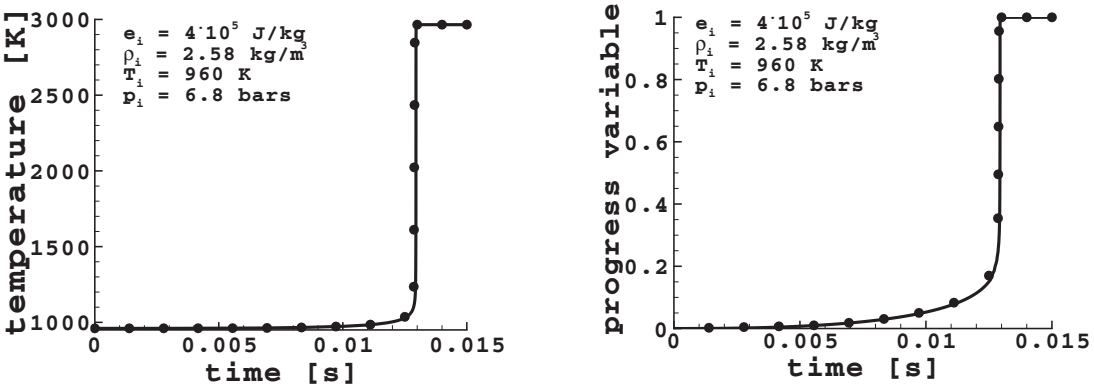

(b) High temperature regime

Figure 4.12 : *0D constant volume validation: evolution of temperature, pressure and progress variable; full line: detailed chemistry REGATH 0D code; symbols: tabulated chemistry AVBP TTC code*

where L is the piston stroke and N is the rotational speed of the crankshaft. The studied configuration is a CI single cylinder taken from a production type $PSA\ DW10B$ engine. The $AVBP-TTC$ parameters are summarized in Table 4.7.

The motion of piston is accounted for using an Arbitrary Eulerian Lagrangian (ALE) technique [1]. The grid points located on a moving

Engine parameters	
Total cylinder volume V_t	528 mL
Displaced volume V_d	506 mL
Bore x Stroke	8.5 cm **x** 8.8 cm
Connecting rod	14.5 cm
Compression ratio	24
Rotational speed	1500

Grid and BC	
Moving mesh management	**ALE**
Mesh type	**unstructured tetra**
Total number of intermediate meshes (1 cycle)	**16** (i.e. BDC mesh in figure)
Interpolate solution between meshes	2^{nd} **order** [81]
Total number of elements	**from 0.4 to 0.7 millions**
Boundary conditions	**noslip, adiabatic walls**

Flow Features	
Governing equations	**unsteady Navier-Stokes**
Turbulence	**standard Smagorinsky model**
Kinetics	**Tabulated chemistry**

Numerical parameters	
Numerical scheme	**Lax Wendroff**
CFL	**0.7**
Artificial viscosity	**based on Colin Sensor [1]**

Initial conditions at BDC	
Fuel **stoichiometric**	**n-heptane/air homogeneous mixture**
Temperature	350 K
Pressure	0.96 bar

Table 4.7 : *AVBP-TTC parameters for variable volume simulation*

boundary displace according to a predefined law (i.e. analytical law of the piston of an engine 4.13) and additional calculations are required for the internal grid points.
To use the same grid for the entire computation (from BDC to TDC) is not conceivable for two reasons:

- **numerical**: during the whole engine cycle, the motion of the piston induces distortion, contraction or dilatation of the computational mesh. As explained in section 3.3, errors in the LES filtered equations are due to the assumption that the filtering operator commutes with partial derivatives. For ICE applications, both space-dependent and time-dependent commutation errors are made due to the unstructured grids and respectively to the ALE method. However, their influence on the computation is found to be negligible when various intermediate meshes are used for moderate compression ratios and engine speed ($\leqslant$3000 rpm) [84].

- **computational costs**: if the same BDC mesh is used at TDC, it will be compressed and therefore too refined with respect to the spatial scales required by the physics [84] is used in some regions of the computation.

The moving mesh management in the $AVBP$ code is also discussed in the chapter 5.
Each engine compression or power stroke phase is split into 8 intermediate meshes with their key parameters given in Table 4.8. The acronym $DCH - P$ stands for the distance between the cylinder head and the piston at the top dead centre.
The computer-aided design CAD geometry and the unstructured mesh of the PSA $DW10B$ engine was build by using the $ANSA$ [2] computer-aided engineering CAE tool, widely used in the automotive industry.
The simulation starts at BDC with flow at rest in the whole geometry. The initial composition is assumed to be an homogeneous mixture of air and n-heptane at stoichiometry 350 K.
The thermo-chemical table used in this case was obtained with the 59-species Golovitchev mechanism.
Figure 4.13 shows the temperature evolution in a PSA $DW10B$ engine performed with the $AVBP - TTC$ code.

Phase	$DCH-P$ **+ stroke (cm)**	**Cells**
1 BDC	8.875	409020
2	7,408	386977
3	5.167	422566
4	3.021	471974
5	1.495	442087
6	0.646	492294
7	0.266	448260
8	0.128	668043
9 TDC	0.007468	

Table 4.8 : *PSA $DW10B$ meshing*

The first purpose of this test is to check the behavior of the code after the coupling in a moving mesh environment.
The second purpose is to validate the auto-ignition delay for a variable volume computation by using the $AVBP-TTC$ code and therefore a comparison with a $0-D$ detailed chemistry computation obtained by $REGATH$ $0-D$ code is done. Figure 4.13 shows that an accurate temperature evolution is obtained by using the tabulated chemistry approach both during the compression and the power stroke.

In this chapter the coupling between an engine-adapted thermo-chemical table and a compressible LES solver was validated in terms of acoustic behavior and ignition delay both in a constant and variable volume domain. The acoustic waves that were sent inside a periodical domain under tabulated chemistry approach follow the same evolution as they would in a detailed chemistry code. As for the entropic wave, they do not introduce significant pressure perturbation if the tabulated chemistry is used. Finally, the ignition delay estimation is accurate both for constant volume and variable volume calculations.

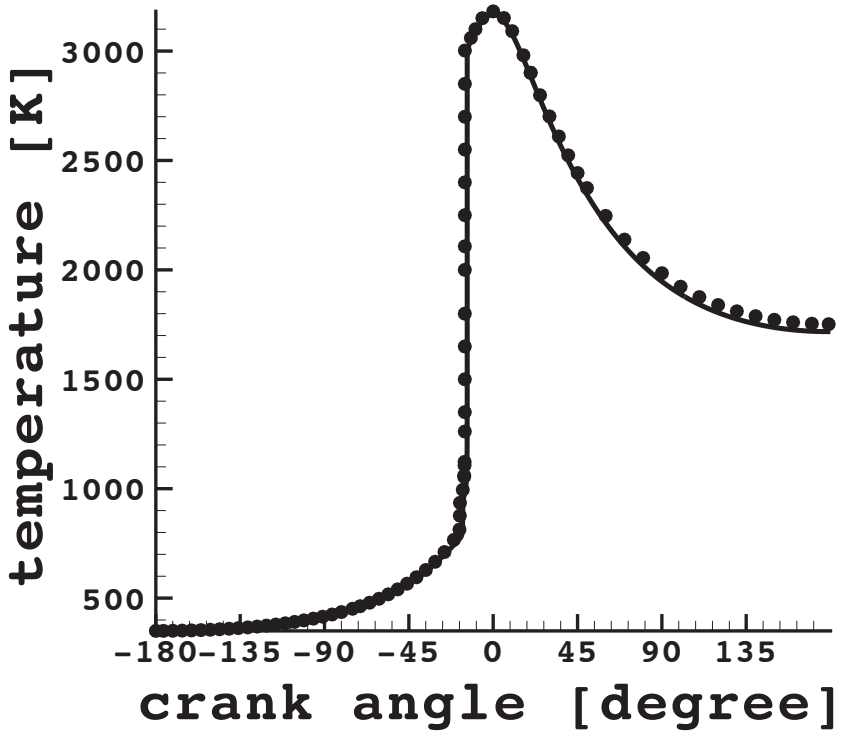

Figure 4.13 : *Variable volume validation: evolution of temperature (full line: detailed chemistry REGATH $0-D$ code; symbols: tabulated chemistry AVBP TTC code)*

Chapter 5

Rapid Compression Machine

In this chapter the influence of the thermal stratification on auto-ignition is studied by Large Eddy Simulation using tabulated chemistry for a better understanding of the combustion process in homogeneous charge compression ignition engines. The rapid compression machines are experimental facilities that reproduce the compression stroke of an automotive engine and consequently they are used for auto-ignition studies in an $HCCI$-like environment. Experimental techniques based on digital image analysis have been recently carried out on a rapid compression machine at the Université Pierre et Marie Currie ($UPMC$) and will be used for verifying and validating the numerical solutions obtained using the $AVBP$ compressible LES solver coupled with the thermo-chemical tables (ρ^*,e^*,c^*).

5.1 Introduction

Homogeneous Charge Compression Ignition ($HCCI$) engine is an alternative piston-engine combustion process that combines the advantageous features of both spark ignition (SI) and compression ignition (CI).
In the HCCI engine, the dilute intake charge, by being very lean or/and by using exhaust gas recirculation (EGR), is mixed prior to combustion.

The obtained homogeneous charge is heated by compression and will auto-ignite close to the top dead center (TDC).
Because the fuel and air are well mixed prior to combustion, the chemical reactions occur simultaneously throughout the volume rather than in a propagating flame front. This allows combustion to take place at lower temperatures and at lower dilutions level, so that the particle emissions are minimized and the conditions needed for significant NOx production usually are not reached. Another important attribute of HCCI engine is its high efficiency, consequence of the fact that the charge is mixed and compression ignites [30]. The combustion duration is therefore shorter, taking place in only a few crank angle degrees.
Although a high level of homogeneity is worthwhile under many situations, the creating of a partially non-homogeneous charge improves at limiting the large heat release occurring at high-load operations. Therefore, further improvements in HCCI development require to be able to distribute the heat release over several crank angle degrees. One possibility for this to be achieved is to promote thermal inhomogeneities [89], engender by the incomplete turbulent mixing between the gases wrapped inside the cylinder and the cold walls. Spatial temperature non-uniformities affect the combustion evolution phenomenology so that both volumetric and front-like combustion modes may be present in the system. Notice that, although it will not be discussed in this paper, charge inhomogeneities might be also introduced by incomplete mixing. As these methods involve stratification of the charge mixture, in terms of temperature or composition, the mode of operation is alternatively referred as Stratified Charge Compression Ignition $SCCI$.
To study this phenomenon in real engine configuration implies to isolate the influence of different parameters that control their behavior. Therefore different numerical and experimental techniques have emerged to overcome this limitation.
Information relevant to the modeling of $SCCI$ may be obtained by means of DNS in close constant volume at typical $SCCI$ engines conditions i.e. by superimposing random temperature field on the mean temperature field as done by [89]. Although turbulence is inherently three dimensional, due to computer power limitations, the DNS simulations are restricted to one or at most two dimensional ignition problems.

In order to provide knowledge about the influence of the temperature on the combustion modes in a HCCI or SCCI-like environment, experimental facilities as Rapid Compression Machine (RCM) had also been used. Unlike the conventional engines, in RCM the piston is stopped at the TDC without any rebound, so that the pressure and temperature can be hold for a larger duration at values typical to the TDC. This allows the detailed study of the ignition delay time as a function of the post-compression turbulence, providing possible control techniques of the ignition timing [42].
In this chapter, the large eddy simulations using $AVBP-TTC$ code will be applied to calculate a rapid compression machine as the one designed at the *Institut Jean le Rond d'Alembert* at the *Université Pierre et Marie Currie* ($UPMC$) [41]. In the first part, the geometrical configuration of the $UPMC$ rapid compression machine will be briefly discussed. Information about Computer-aided design (CAD) of the physical objects components of the RCM and about the unstructured grids used in the numerical simulation are given. A comparison is made between the two-dimentional velocity field measured by Particle Image Velocimetry (PIV) and calculated with the $AVBP-TTC$ compressible LES solver with tabulated chemistry. Knowing that the RCM has cold walls, as for the ignition kernels to be captured, the tabulated chemistry should be able to address heat losses. The thermo-chemical table (ρ^*,e^*,c^*) is adapted for modeling this type of applications throughout its energy coordinate. Finally, the reactive AVBP-TTC simulation of the RCM is discussed.

5.2 Geometrical configuration of RCM

5.2.1 Rapid Compression Machine CAD

A partial cross-section view of the $UPMC$ RCM is shown in Fig. 5.1, the details are given in [42].
Briefly, in RCM, as in $HCCI$ engines, the fuel and the air are mixed before entering the cylinder through the mixture inlet port (1). The machine holds a hydraulic system capable to move a single piston (2,3) inside a pre-compression chamber (4) and then throughout a convergent section (5) until the lowest cylinder head is reached. After this point,

the acquisition and control system are able to get information about the post-compression turbulence evolution in the combustion chamber (5) by PIV or visualize the combustion process by high speed camera images.

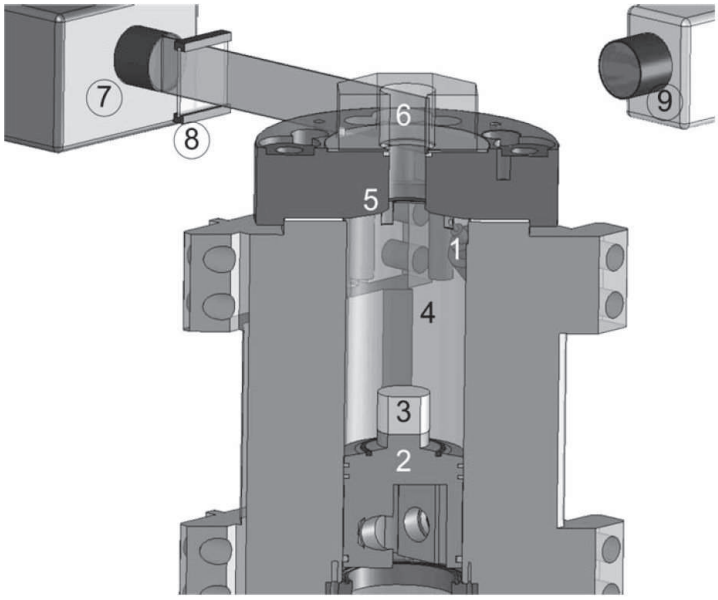

Figure 5.1 : *UPMC RCM components: 1 mixture inlet port; 2: piston body; 3: piston nose; 4: pre-compression chamber; 5: convergent section; 6: combustion chamber; 7: PIV laser head mounted with its laser sheet generation optics; 8: refining cylindrical lens; 9: PIV camera*

The design drawing are shown in Fig. 5.2. The entire RCM reactor has 1.06 L at BDC. When the piston reaches the TDC, the available volume is only 0.07 L. The chamber has a bore of 40 mm and a height of 42.40 mm.
The simulations were performed at full-scale and for the entire piston motion from BDC to TDC.

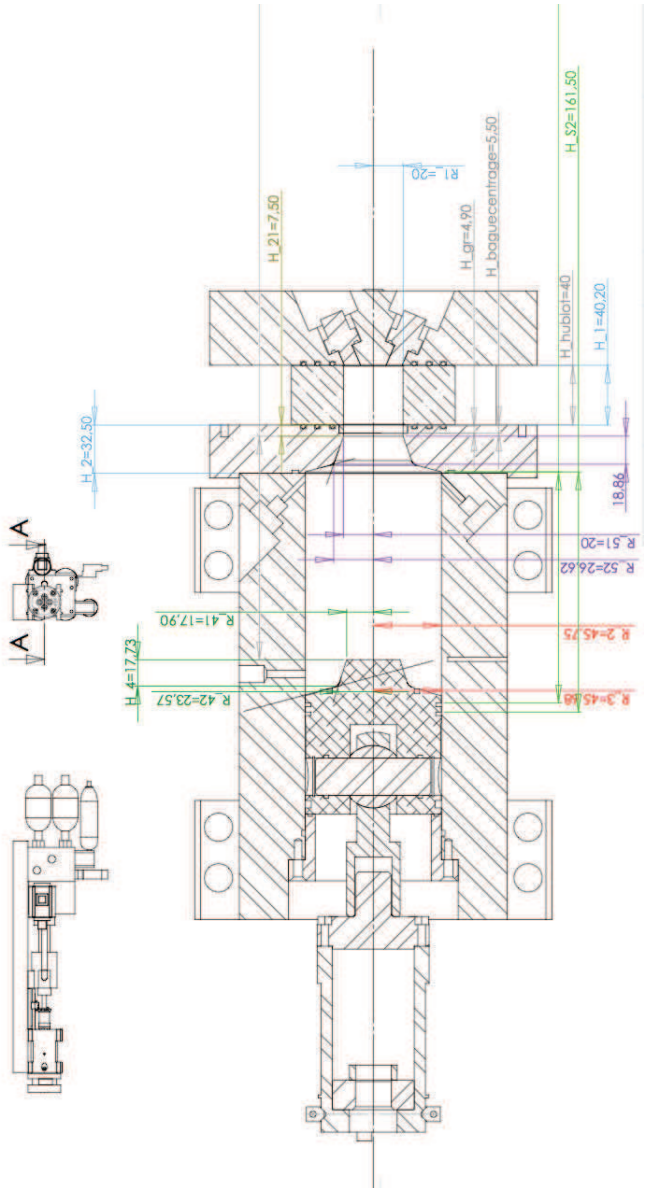

Figure 5.2 : *RCM design drawing*

The computer-aided design (CAD) geometry of the $UPMC$ RCM was build by using the $ANSA$ tool [2].
$AVBP$ being an unstructured solver, it is flexible for handling complicated geometry, thus unstructured grids were generated inside the CAD structures using the $CENTAUR$ software [3].

5.2.2 Moving mesh management

The Arbitrary Eulerian Lagrangian (ALE) technique [1] is used to move the grid system. In this approach, the grid points located on a moving boundary displace according to a predefined law. The internal grid points move at different velocities due to the piston shape. In $AVBP$, a Laplacian type solver calculates the percentage field of the internal grid points.

The ALE moving grid technique requires both the initial grid and the grid for the final mesh position, called the target grid, see Fig. 5.3.

As to prevent negative cells the target meshes were generated by using the Adaptive Moving Mesh AMM code provided by $CERFACS$ [1]. The AMM code is performing mesh smoothing (Laplacian smoothing, Optimisation-based smoothing) and remeshing operations (Local remeshing, Refinement, Coarsening, Swapping) in order to maintain the quality of the target deformed grid.

The target mesh must have the same connectivity as the initial mesh also it corresponds to a future physical time, therefore to a different piston position. Of course these two contradictory conditions, namely same connectivity with smaller cells in the compression stroke (or higher cells in the power stroke) can not be reached without locally grid skewness. Therefore, several times the connectivity of the mesh must be changed implying to interpolate the intermediate i phase solution on an adapted connectivity mesh and continue the compression throughout the next phase $i+1$.

The first mesh generated corresponds to the initial physical time, so the piston is situated at the BDC and has about 4 million tetrahedral cells for a total internal volume of the machine of $1.06L$, corresponding to an implicit LES filter size in the interval $0.22\ mm < V_{cell}^{1/3} < 1.56\ mm$. In the RCM the combustion chamber is mainly immobile but the mesh inside the pre-compression chamber and in the convergent section moves along with the piston.

The mesh was refined in the combustion chamber region $V_{cell}^{1/3} \approx 0.5\ mm$ and the values were kept as constant as possible along the computation in order to avoid transitions from the sub grid scale to the resolved scale. Between each mesh the solution was interpolated on a different connectivity mesh with optimized grids for the given piston position using *hip* tool [4].

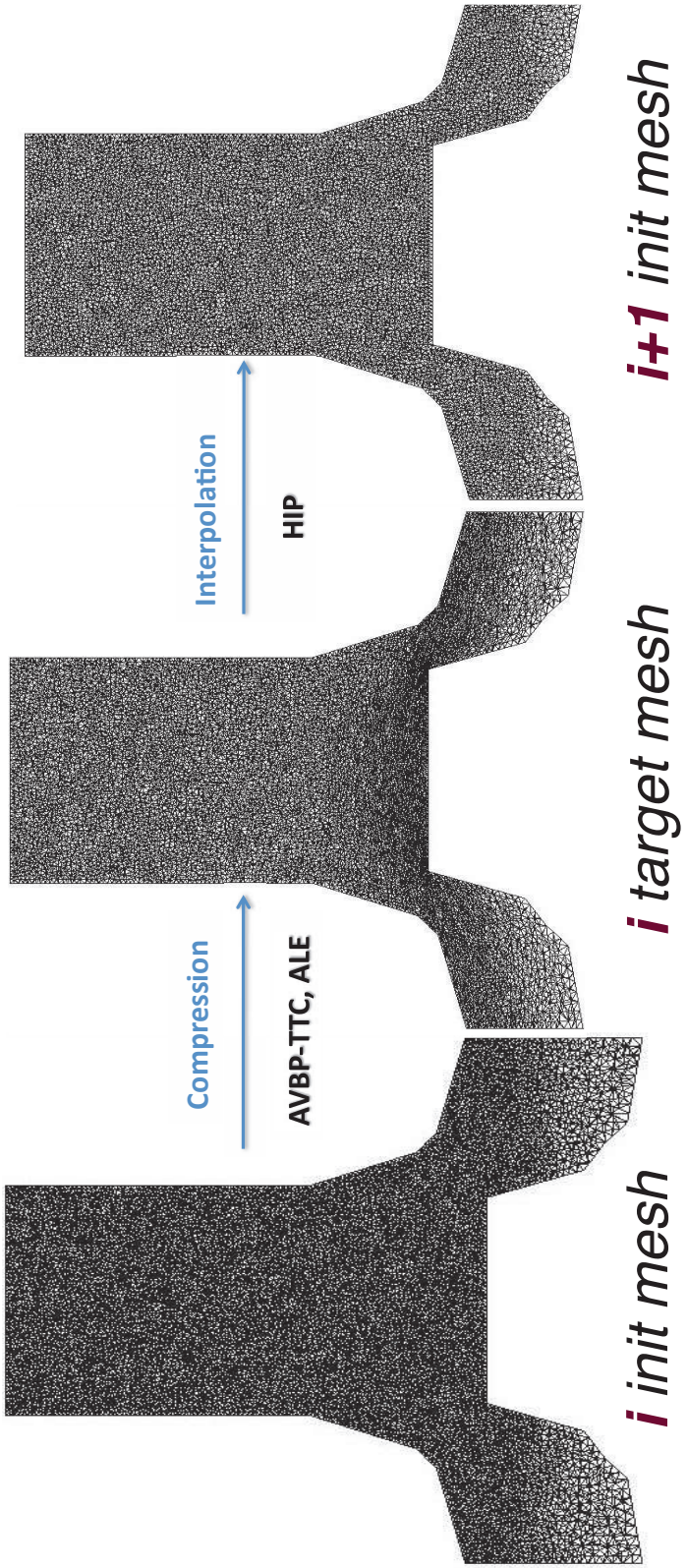

Figure 5.3 : *RCM mesh transformation during i to $i+1$ phase*

In order to avoid cell deformations of more than ≈ 20%, 15 intermediate tetrahedral meshes between 1.5 to 4 million cells and the corresponding target meshes were created in order to simulate the entire evolution of the *RCM* piston motion, see Table 5.1.

Phase	Total volume (L)	Mesh change time (ms)	Cells (millions)
1 *BDC*	1.06	0	3.9
2	1.02	4.8	4.1
3	0.93	7.2	4.0
4	0.81	9.9	3.9
5	0.69	12.6	3.8
6	0.55	15.1	3.8
7	0.43	17.4	3.7
8	0.33	19.5	5.5
9	0.25	21.3	3.1
10	0.18	23.0	2.8
11	0.15	24.4	2.4
12	0.12	25.7	1.9
13	0.10	26.8	1.6
14	0.09	27.7	1.5
15	0.08	28.4	3.3
16 *TDC*	0.077	31.5	

Table 5.1 : *RCM mesh information throughout the compression*

The evolution of the *RCM* volume corresponding to the experimental displacement of the piston is given in the figure 5.4. As an example, the initial mesh, corresponding to the *BDC*, two intermediate mesh and the final mesh, corresponding the *TDC* are also shown in the figure 5.4.
The *RCM* geometry and mesh information is summarized in Table 5.2.

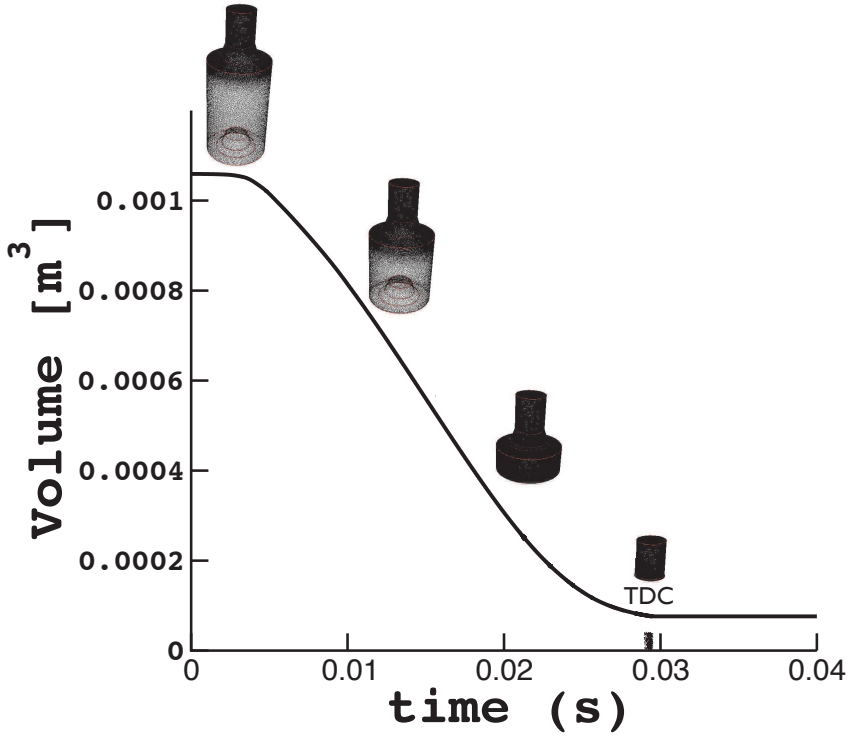

Figure 5.4 : *RCM piston displacement law*

RCM **parameters**	
BDC volume	1.06 *L*
TDC volume	0.07 *L*
Chamber Bore x Height	40 *cm* **x** 42.40 *cm*

Grid	
Moving mesh management	**ALE**
Mesh type	**unstructured tetra**
Total number of intermediate meshes	**15**
Interpolate solution between meshes	**hip** 1^{st} **order interpolation** [1]
Total number of elements	**from 1.5 to 5.5 millions**

Table 5.2 : *RCM Geometry and mesh parameters*

5.3 Boundary conditions with tabulated chemistry: the impact of isothermal wall on ignition

Internal combustion engines and rapid compression machines are usually water cooled, air cooled or cooled by natural convection and radiation [44]. Generally it can be considered that these industrial systems have isothermal walls. The heat transfer at the walls causes inhomogeneous temperature field and it will be shown later on it has a significant impact on the ignition process. To accurately describe an isothermal wall with a tabulated chemistry approach, it is necessary for the corresponding thermo-chemical table to have a coordinate able to account for the wall heat losses. By its energy coordinate, the thermo-chemical table developed during this work has the quality to address heat fluxes changes.
The boundary conditions can be divided in two categories:

- Navier–Stokes Characteristic Boundary Conditions $NSCBC$, proposed by Poinsot and Lele [71] to control the wave crossing the computational boundaries by preventing the appearance of numerical instabilities. The formulation uses the characteristic wave decomposition derived for the Euler equations and generalized to the Navier-Stokes equations with detailed chemistry but also with tabulated chemistry by Vicquelin and al. in [85][1].

- Newman - Dirichlet BC, $\mathcal{R} = -1$, the acoustic disturbance is completely reflected at the boundary $p'_+ = -p'_-$ and therefore no pressure fluctuations are allowed at the boundary. This type of boundary is compatible with wall enclosed combustion computations. Notice that, wave decomposition is not required, the conserved variables being directly used and therefore is relatively easy to implement in compressible solvers. This type of BC has been used for the RCM LES simulations performed henceforth and is described in the following.

[1] Although the $NSCBC$ is not addressed in this work, Appendix C can yield a major contribution to their development as it presents the wave decomposition for the conservative variables transported under the (ρ^*, e^*, c^*) tabulated chemistry approach

An isothermal boundary condition should be able to transmit to the near-wall cells the presence of a wall with an imposed target temperature.
The target values that a solution needs to take on the boundary of the domain can be directly assigned by *Dirichlet* or *Newman BC* type. Imposing directly the target value without any other model implies a high number of points in the near wall region[2].

For industrial applications that use relatively coarse meshes an adequate wall model is to be used to correctly predict the parietal fluxes throughout the adjacent wall cells. The purpose of model is to estimate the gradient of the transported variables in the first near-wall cell based on the local physical considerations given by the Navier-Stokes variables. A classical boundary layer model is briefly presented in this paper, for additional knowledge concerning the implementation in cell-vertex numerical solvers as $AVBP$ address to [1,11] or find general information on parietal models in [46].
In a boundary layer, two characteristic regions Fig. 5.5 can be distinguished: an outer layer mainly controlled by large scale turbulent structures and an inner layer, $\approx 20\%$ of its length δ where the flow behavior is governed by both molecular and turbulent diffusion.
The analysis of a turbulent boundary layer flow over a flat plate has revealed that the inner layer has a self similar solution for the mean axial velocity . The self-similar behavior is assured by considering dimensionless parietal units for the axial velocity $u^+ = \bar{u}/u_\tau$ and for the wall length $y^+ = y/y_\tau$. The characteristics of the thiner inner boundary layer used are the friction length y_τ and the friction velocity u_τ, defined as: $u_\tau = \sqrt{\frac{\tau_w}{\rho_w}}$ and respectively $y_\tau = \frac{\mu_w}{\rho_w u_\tau}$ using the wall-friction which corresponds to the viscous wall shear stress τ_w and the thermodynamical characteristics as its density ρ_w and its dynamical viscosity μ_w.

- In the inertial sub-layer the turbulent transport is predominant $\mu_t^+ >> \mu^+$ and a possible model is the Prandtl mixing length:

[2]the number of points needed to correctly capture the inner zone of a boundary layer of size δ is estimated by Chapman [12] to be $Re_\delta^{1.8}$

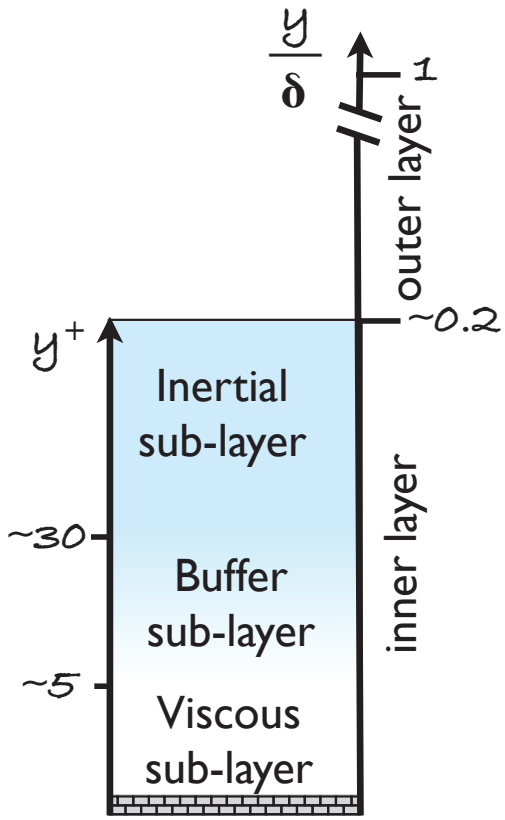

Figure 5.5 : *Boundary layer structure*

$$\mu_t^+ = (ky^+)^2 \frac{du^+}{dy^+} \tag{5.1}$$

with von Karman constant k commonly value 0.41. By using these assumptions, it is shown, see the demonstration in [11], that the average velocity of the turbulent flow u^+ is proportional to the logarithm of the distance from that point to the wall y^+, eq. 5.2.

$$u^+ = \frac{1}{k} ln(y^+) + C \tag{5.2}$$

- In the closed vicinity of the wall the viscous effects are predominant and the velocity is linear to the wall distance 5.3. In the buffer

layer, between 5 wall units and 30 wall units, neither law holds .

$$u^+ = y^+ \tag{5.3}$$

- In $AVBP$ code the value $y^+ = 11.445$ where the two equations intercept is used as a delimitation value: before 11 wall units the linear approximation is more accurate and after 11 wall units the logarithmic approximation is used.

The parietal thermal boundary layer features the same behavior as the dynamic boundary layer but they rarely grow at the same rate.

$$T^+ = \frac{Pr_t}{k} ln(y^+) + C_T(Pr) \tag{5.4}$$

$$T^+ = Pry^+ \tag{5.5}$$

This BC imposes constraints on the viscous fluxes before applying the numerical scheme and no special precautions were needed for the tabulated approach. Note that when needed the variables e.g. the temperature, are to be read by interpolation in the thermo-chemical database (ρ^*, e^*, c^*).

Newman - Dirichlet BCs were used to imposed the isothermal walls of the MCR, argued by the following criteria:

- adapted to wall enclosed combustion as the acoustic disturbance is completely reflected at the boundary
- easily to implement in compressible solvers by directly using the conservative variables
- straightforward to couple to tabulated chemistry approach

5.4 *LES* results analysis

Two simulations of the *RCM* will be presented in the following: a non-reactive case in which the machine is filled with a $N_2/Ar/CO_2$ mixture and a reactive case in which the machine is filled with a lean $n-neptane/air/EGR$ mixture.
The parameters of the simulations are presented in Table 5.3.

Flow Features	
Governing equations	**unsteady Navier-Stokes**
Turbulence	**standard Smagorinsky model**
Kinetics	**Tabulated chemistry**
Numerical parameters	
Numerical scheme	*TTGC*
Boundary condition	**Non-characteristic with parietal model**
CFL	**0.7 (phase1-14) /0.05 (phase 15)**
Artificial viscosity	**based on Colin Sensor [1]**

Table 5.3 : *RCM simulation parameters*

5.4.1 Non-reactive case

One of the primary objective of the study will be addressed in this section, namely the investigation of the initial turbulent flow prior to combustion. As indicated by theoretical bases [88, 89], the instantaneous temperature distribution is the relevant criteria in distinguishing between combustion regimes. Hence, accurately describing the fluid motion inside the combustion chamber is crucial both for the ignition process and for the combustion propagation phenomenology.

5.4.1.1 Piston movement validation

The *RCM* experimental set-up developed at *UPMC* has a high compression ratio CR =16 which is achieved within a short compression time $\tau = 31.5\ ms$. Following the experimental data, the piston motion has

been simulated using 15 successive meshes as described in section 5.2.2. As shown in Fig. 5.6 the chamber volume decrease is well reproduced by the simulation. The meshes are capable to reproduce the piston motion without significant volume lost and thus mass variation which is below 1%. This approves that the 15 CAD geometries were correctly build and the sequential connection between them is accurately performed.

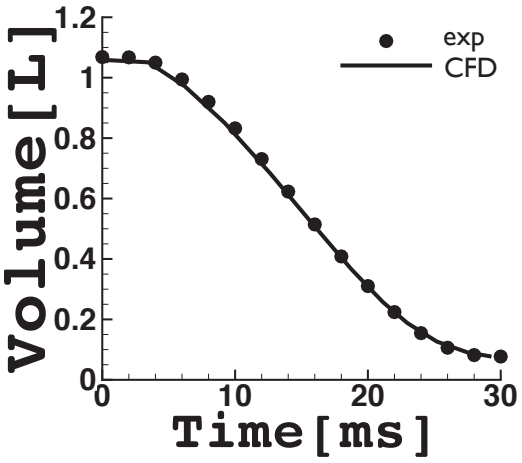

Figure 5.6 : *Comparison between RCM volume evolution experimental (UPMC) and numerical simulation (EM2C)*

In the case of the given RCM there is no algebraic law for the piston motion contrary to a classical engine case exposed in chapter 4. An experimental volume law evolution is discretized and at each time step the piston position is found by interpolation. Figure 5.7 shows a comparison between the experimental imposed piston speed and the maximum grid speed. Small differences between the two evolutions are expected due to the linear interpolations between the meshes.

5.4.1.2 Pressure time evolution

The chamber is initially fielld with inert mixture and depressurized at $p_0 = 0.35\ bar$. The volume is diminished as explained above and the pressure is increased while the mixture is put into motion towards the clearance volume.

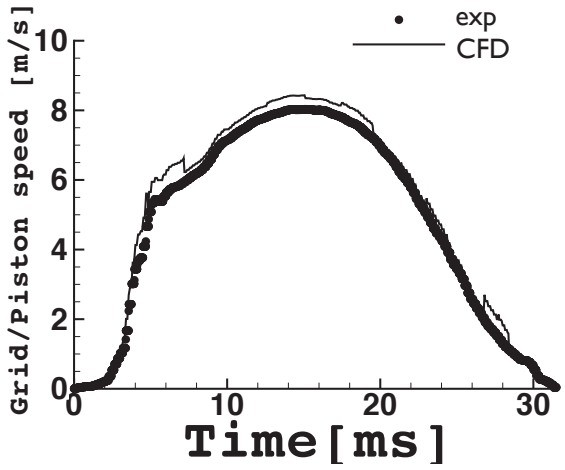

Figure 5.7 : *Comparison between RCM piston speed(UPMC) and maximum grid speed (EM2C)*

In order to reproduce the cold flow measurements, non-reactive 3-D simulations with tabulated chemistry were performed. For this purpose, a non-reactive thermo-chemical table with the same composition as the one used in experiments was conceived. The initial mass fractions are given in Table 5.4 and they were chosen as to have a mean heat capacity as close as possible to the reactive $n - C_7H_{16}$/air mixture used in the next section. The progress variable is zero during all the computation $c = 0$ being a dummy coordinate.

Species	**Molar fraction**
C_7H_{16}	0
H_2	0
O_2	0
N_2	0.5014
Ar	0.4248
CO_2	0.0738

Table 5.4 : *Inert mixture composition*

The pressure varies inside the inert thermo-chemical table and thus is able to cover the entire range of pressure delivered by the piston motion. The mean pressure evolution inside the RCM is given in Figure 5.8 normalized by $p_0 = 0.35\ bar$. Both the evolution of the pressure during the compression stage $\tau < 31.5\ ms$ and after the TDC is reached, are well predicted by the simulation. In an RCM the piston is kept steady after the TDC and the slight decrease in the pressure value is due to the wall heat losses.

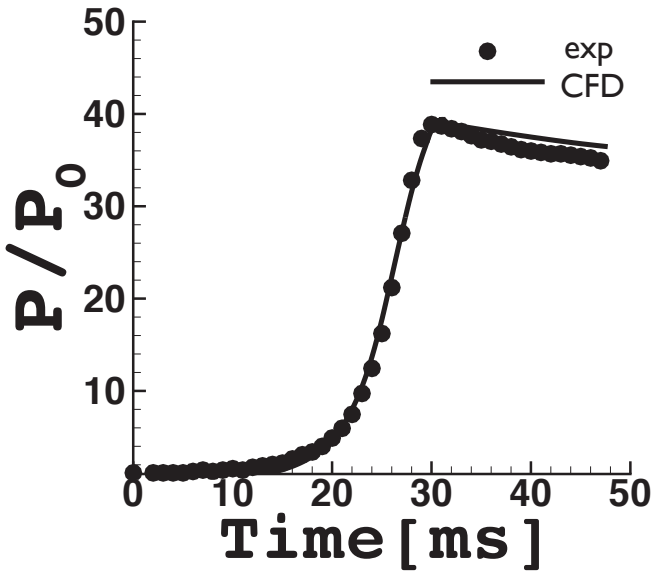

Figure 5.8 : *Comparison between RCM pressure evolution experimental (UPMC) and numerical simulation (EM2C)*

5.4.1.3 Velocity field time evolution

As the entire, full-scale RCM was simulated, the velocity field is available both in the pre-compression and in the compression chamber. Figure 5.9 shows the velocity field in a 2-D cut in the central axis of the RCM, 13 ms after the BDC.

Fig. 5.10 focusses on the compression chamber and shows the velocity field obtained by the simulation at different instances during compression and in the post-compression period.

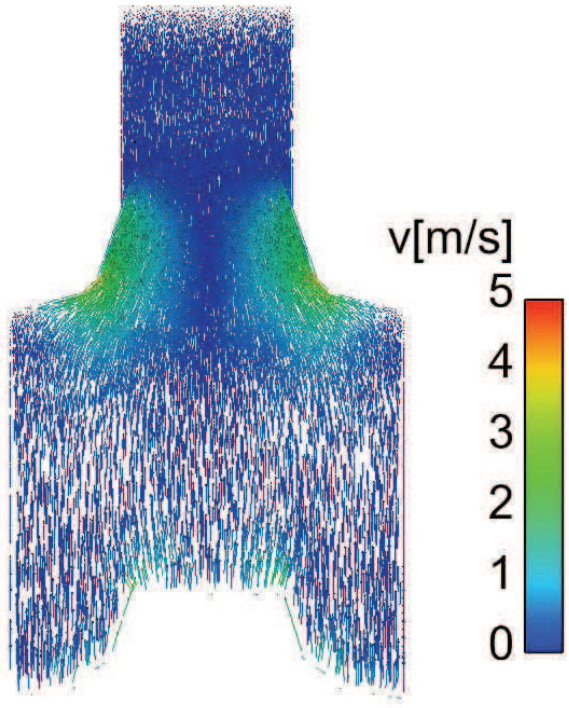

Figure 5.9 : *$AVBP - TTC$: 2-D velocity field time evolution in the RCM chamber* 13 *ms after the BDC*

Due to the piston motion, the fluid in the chamber is put into motion in the same direction. Near the TDC, two upper and two lower symmetrical recirculation zones are created near the wall. The speed is of order of 10 to 20 m/s in these zones and of approximately 5 m/s in the middle of the chamber. After the piston stop Fig. 5.10(e), the two vortices continue moving upwards and they are broken in contact with the top cylinder head, at about 25 ms after the TDC.

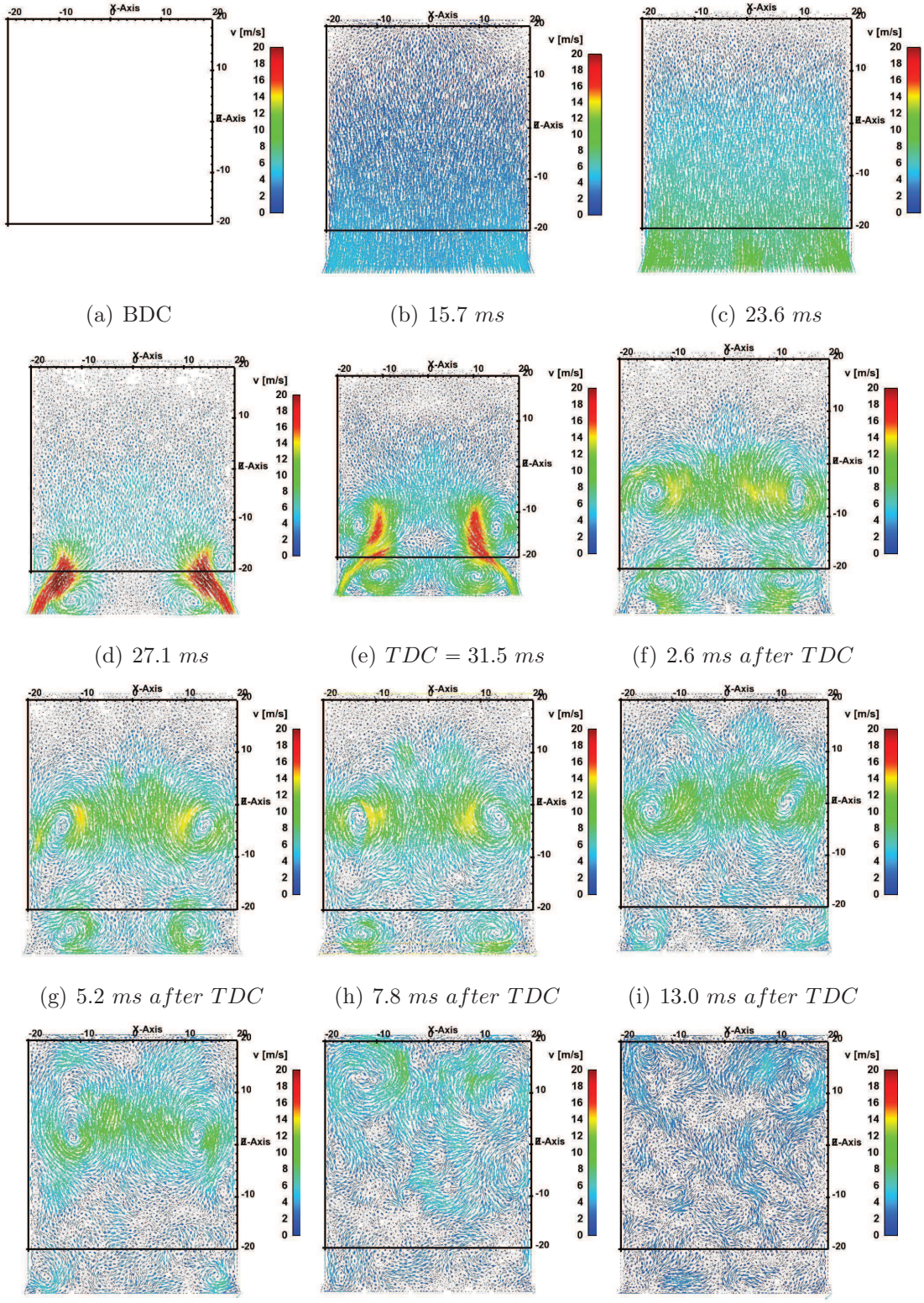

(a) BDC (b) 15.7 *ms* (c) 23.6 *ms*

(d) 27.1 *ms* (e) $TDC = 31.5$ *ms* (f) 2.6 *ms after TDC*

(g) 5.2 *ms after TDC* (h) 7.8 *ms after TDC* (i) 13.0 *ms after TDC*

(j) 18.2 *ms after TDC* (k) 23.4 *ms after TDC* (l) 46.8 *ms after TDC*

Figure 5.10 : *$AVBP - TTC$: Velocity field time evolution in a 2-D cut in the central axis of the RCM chamber*

5.4.1.4 Comparison with experiments

Experimentally the chamber was filled with an inert mixture. The instantaneous flow field was measured by PIV system by [42].
The comparison between the velocity field measured by PIV and the calculated using the $AVBP-TTC$ solver is shown in the Figs. 5.11, 5.12 and 5.13, at the TDC so just after the piston reaches the combustion chamber head, 5 ms after TDC and 10 ms after TDC, respectively.

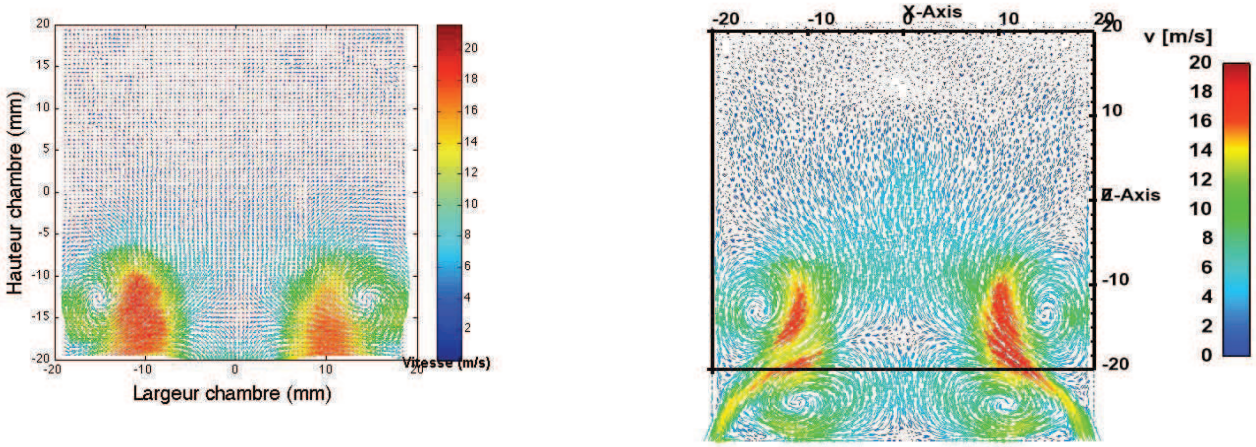

Figure 5.11 : *Velocity field validation at TDC: PIV measurements (left figure), LES simulation using AVBP-TTC code (right figure).*

The PIV field and the tangential numerical velocity vectors were colored by the speed. The two upper vortices can be observed both in the experiments and in the simulation. Due to optical impediments, the two lower contra-rotating vortices are not visible by PIV measurements.
Computed results closely match with experimental observation at all three instances. The presence of the symmetrical vortices, the magnitude of the speed in the recirculation zone and the temporal evolution of the vortices are accurately reproduced by the numerical simulation. This validates the coupling between the thermo-chemical tables (ρ, e, c) and the LES compressible solver and its ability to predict the fluid dynamics inside a variable volume engine.

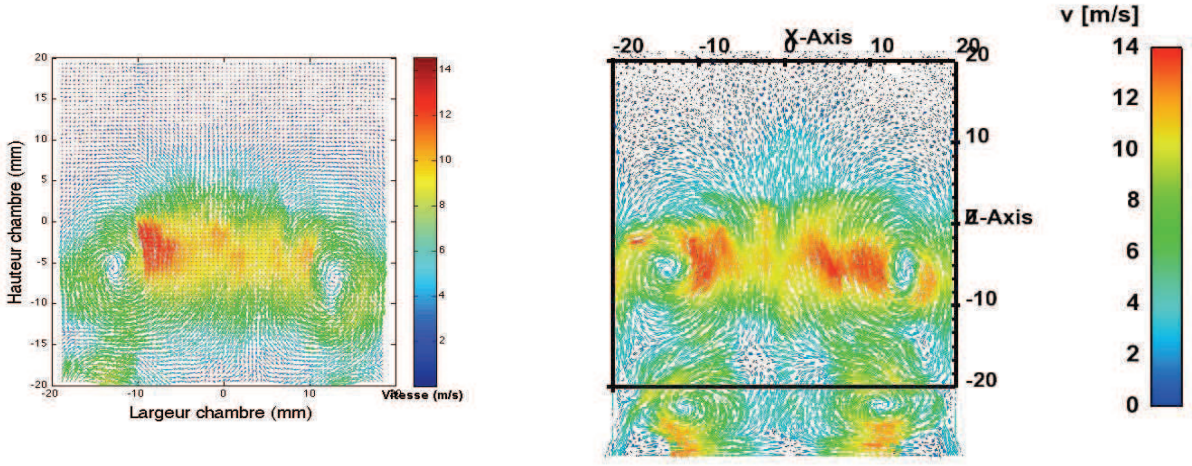

Figure 5.12 : *Velocity field validation 5 ms after the TDC: PIV measurements (left figure), LES simulation using AVBP-TTC code (right figure).*

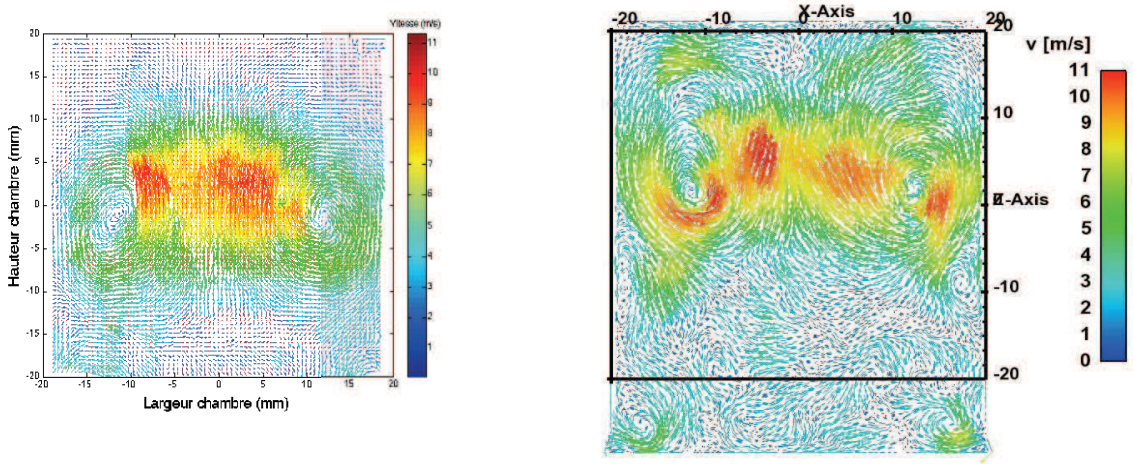

Figure 5.13 : *Velocity field validation 10 ms after the TDC: PIV measurements (left figure), LES simulation using AVBP-TTC code (right figure).*

5.4.1.5 Temperature field time evolution

Figure 5.14 shows the temperature evolution on a slice situated in the middle of the RCM chamber. Initially, at BDC, the gas mixture at rest is specified with uniform temperature $T = 343K$. At the end of compression the piston comes to rest and remains there for the subsequent time steps. The temperature evolution during the first 46.8 ms of the post-compression period is shown. As it is a non-reactive mixture simulation, the temperature inhomogeneities created during the compression are entirely related to the heat transfer between the fluid and the cold external walls. Unable to have access to the experimental temperature field, the numerical simulation gives an additional information inside the chamber.

Notice that the temperature field varies significantly after the TDC, therefore the thermal field of the mixture is in continuous motion and depending on the moment of auto-ignition, i.e. for two fuels with different ignition-delays, various combustion modes would be possible. This highlights a possible way of controlling the combustion propagation and thus controlling a $SCCI$ engine by choosing the optimum conditions for which the pressure rise spreads over several crank angle degrees.

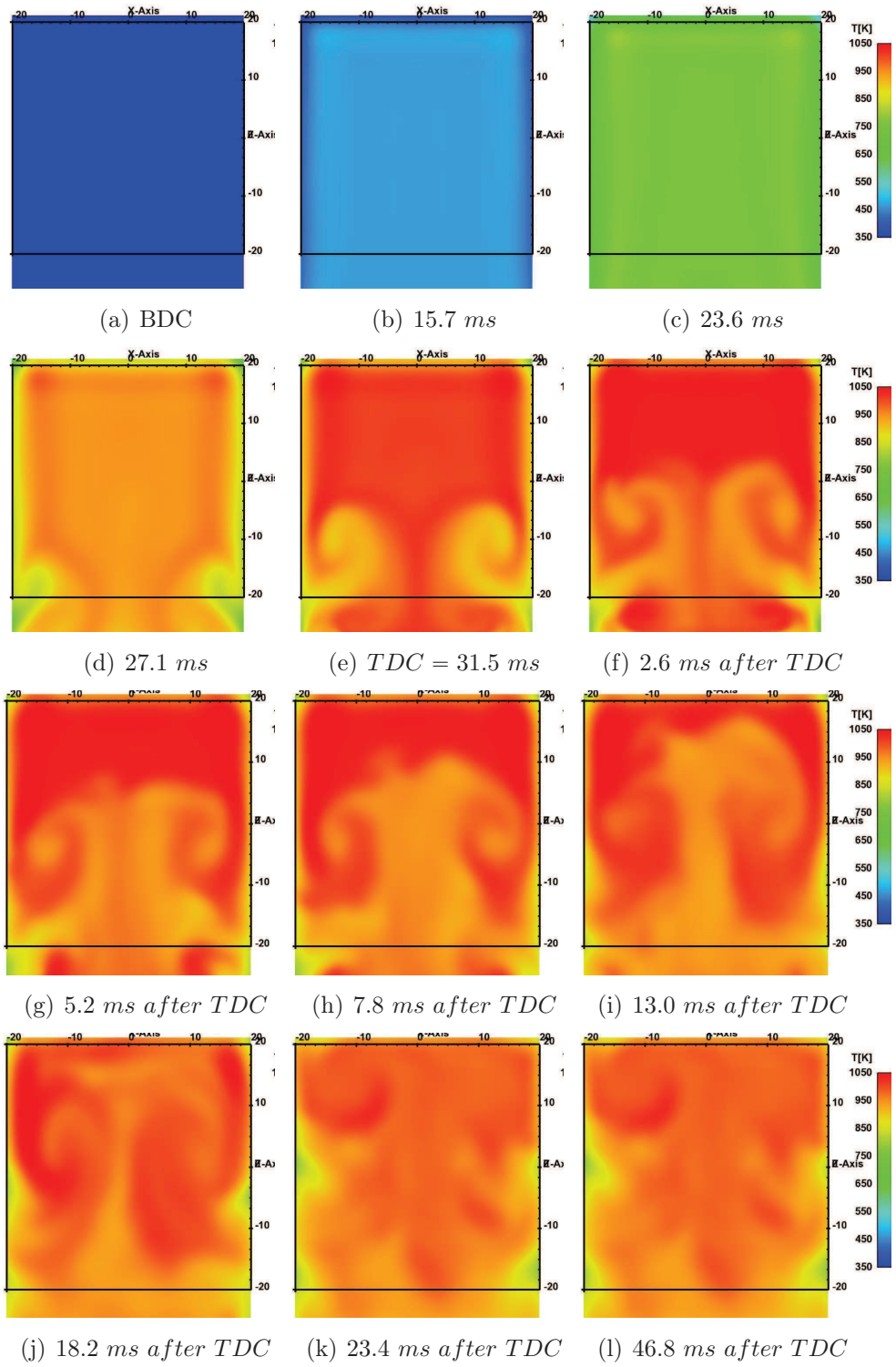

(a) BDC (b) 15.7 ms (c) 23.6 ms

(d) 27.1 ms (e) $TDC = 31.5$ ms (f) 2.6 ms $after$ TDC

(g) 5.2 ms $after$ TDC (h) 7.8 ms $after$ TDC (i) 13.0 ms $after$ TDC

(j) 18.2 ms $after$ TDC (k) 23.4 ms $after$ TDC (l) 46.8 ms $after$ TDC

Figure 5.14 : *$AVBP-TTC$: Temperature time evolution in the RCM chamber*

5.4.2 Reactive case

As previously discussed, the walls of the entire RMC facility are cooled down during the entire process. In a first step, the thermo-chemical table must consider the heat losses to accurately capture the localization of the ignition kernels. Secondly, the thermo-chemical table must accurately follow the chemical reaction when the RCM is filled with a reactive mixture. For these purposes, a reactive thermo-chemical table with a lean mixture of $n-C_7H_{16}$/air/EGR with the equivalence ratio of $\phi = 0.8$ and 79% diluted by a N_2-CO_2 (30%-70% respectively) mixture was conceived. This composition had been chosen to be representative to a $HCCI$ engine fuel.

5.4.2.1 Velocity field time evolution

In reactive mixtures, the tracer particles seem to have different concentrations with and without the flame front and it makes difficult the analysis of the velocity vectors [66]. Thus, the PIV was only set-up for inert mixtures. Figure 5.14 presents the time evolution of the velocity field in the chamber. Although no comparison is possible with the experimental velocity field, the aerodynamic behavior of the reactive mixture before the ignition takes place is similar to the inert mixture as they were chosen to have the same heat capacity.
Computed results provide insights into the nature of the fluid dynamics and of the temperature distribution inside the RCM chamber. The fluid dynamics inside a rapid compression machine depends strongly on its geometrical characteristics. At TDC Fig. 5.15(e), two symmetrical vortices span the lower part of the chamber, which shear cold gases from the boundary and brings them inside. As in the non-reactive case, along with the main vortices, two corner vortices are formed near the cylinder wall.The regime near the lower head cylinder is greatly affected by the flow of the cold gases from the boundary. At the end of compression Fig. 5.15(e), the maximum velocity in the chamber is about 20 m/s. As the vortices move forward to the top header of the cylinder, the regime in the chamber is strongly modified. At about 45 ms after compression Fig. 5.14(l), the maximum velocity has reduced to about 2 m/s and the velocity pattern is almost uniform.

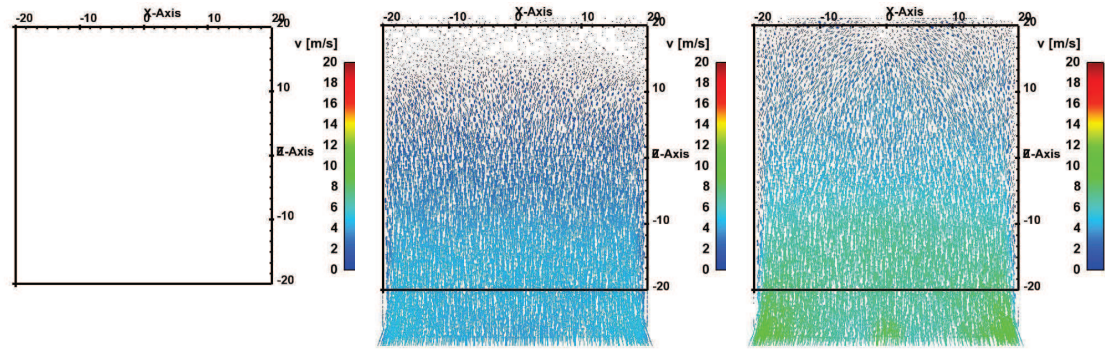

(a) *BDC* (b) 15.7 *ms* (c) 23.6 *ms*

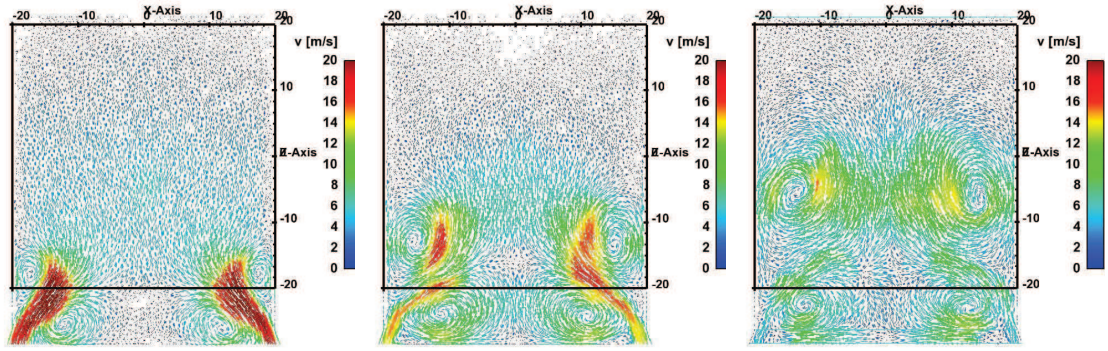

(d) 27.1 *ms* (e) $TDC = 31.5$ *ms* (f) 2.6 *ms after TDC*

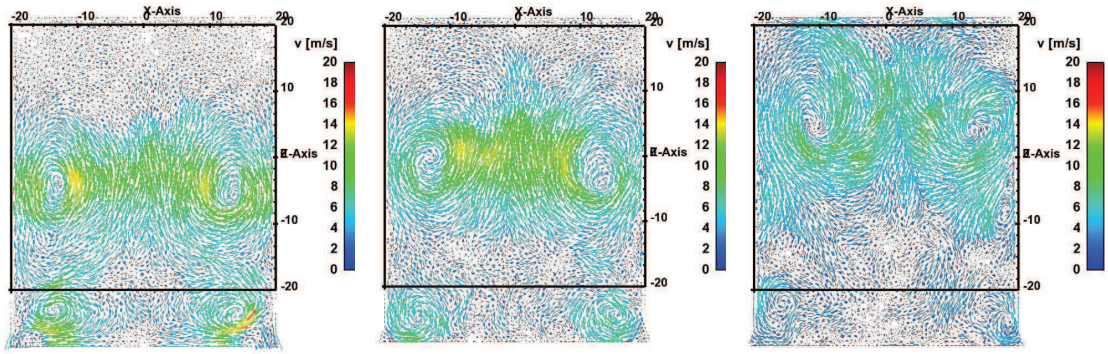

(g) 5.2 *ms after TDC* (h) 7.8 *ms after TDC* (i) 13.0 *ms after TDC*

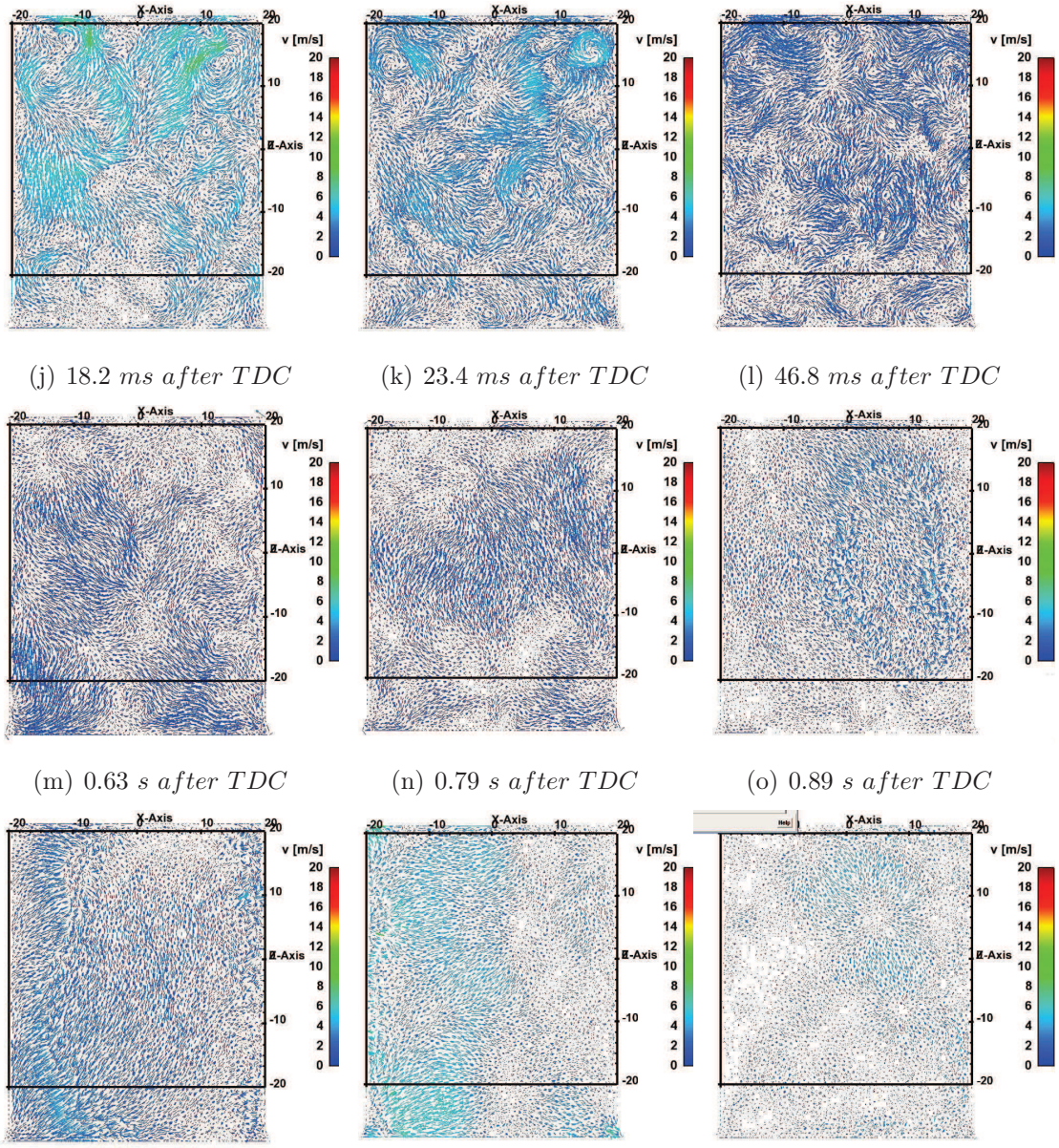

(j) 18.2 *ms after TDC* (k) 23.4 *ms after TDC* (l) 46.8 *ms after TDC*

(m) 0.63 *s after TDC* (n) 0.79 *s after TDC* (o) 0.89 *s after TDC*

(p) 0.90 *s after TDC* (q) 0.91 *s after TDC* (r) 0.93 *s after TDC*

Figure 5.14 : *AVBP – TTC: 2-D velocity field time evolution in the RCM chamber*

5.4.2.2 Temperature field time evolution

Figure 5.15 shows the instantaneous temperature evolution during the compression and just after the beginning of auto-ignition of the mixture. The temperature is initially uniform in the chamber and increases gradually until the pair of vortices enter in the chamber. These results indicate that with this specific $UPMC$ piston design, the gas velocity after compression is relatively high and the core region shrinks relatively quickly due to rapid dragging of cold gases.

The adiabatic core assumption is found to be valid after about 45 ms, Fig. 5.14(l). For the $n-C_7H_{16}$ mixture chosen in this study, the propagation of the flame front can be seen at 130 ms, Fig. 5.14(o), and therefore the design of the RCM is well-adapted.

For fuels with very short auto-ignition delays, the complex aerodynamic features affect the state of the reacting core and alter the measurement of the auto-ignition delay time.

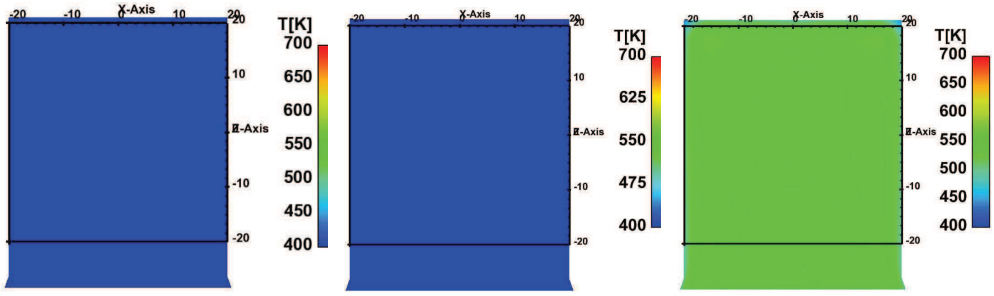

(a) BDC (b) 15.7 ms (c) 23.6 ms

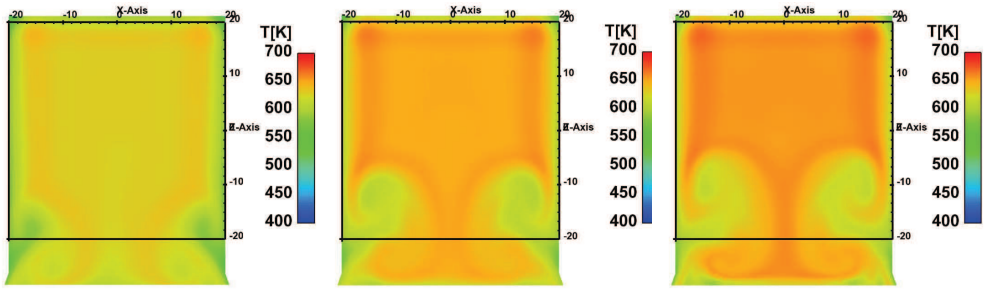

(d) 27.1 ms (e) $TDC = 31.5$ ms (f) 2.6 ms $after$ TDC

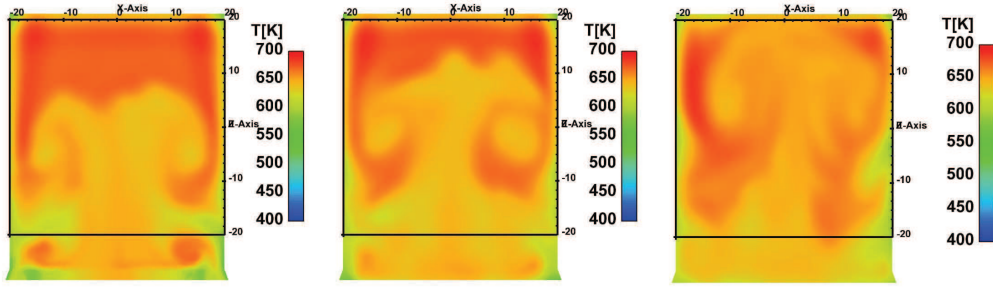

(g) 5.2 *ms after TDC* (h) 7.8 *ms after TDC* (i) 13.0 *ms after TDC*

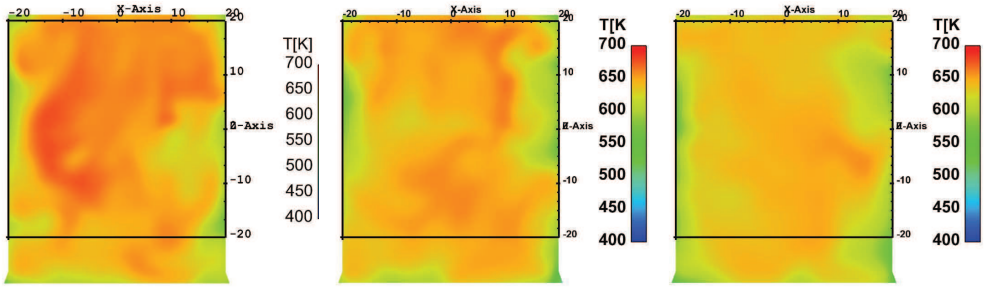

(j) 18.2 *ms after TDC* (k) 23.4 *ms after TDC* (l) 46.8 *ms after TDC*

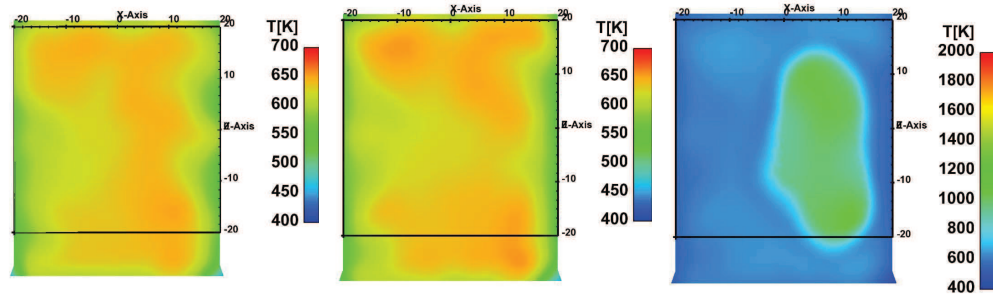

(m) 0.63 *s after TDC* (n) 0.79 *s after TDC* (o) 0.89 *s after TDC*

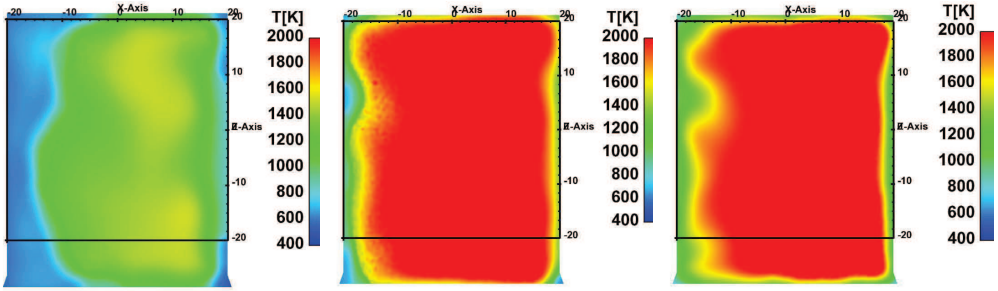

(p) 0.90 *s after TDC* (q) 0.91 *s after TDC* (r) 0.93 *s after TDC*

Figure 5.15 : *AVBP – TTC: Temperature field time evolution in the RCM chamber*

5.4.2.3 Species field time evolution

This section gives a view on the chemical species evolution in the rapid compression machine.
Figure 5.16 shows the progress variable time evolution in the RCM chamber. During the compression, the reaction is initiated in the near wall region; 10 ms after the TDC, due to the cold gases brought by the two vortices from the bottom, the progress variable has a higher value in the upper region of the chamber. The vortices continue to move the mixture and finally the reaction takes place in the middle of the chamber.

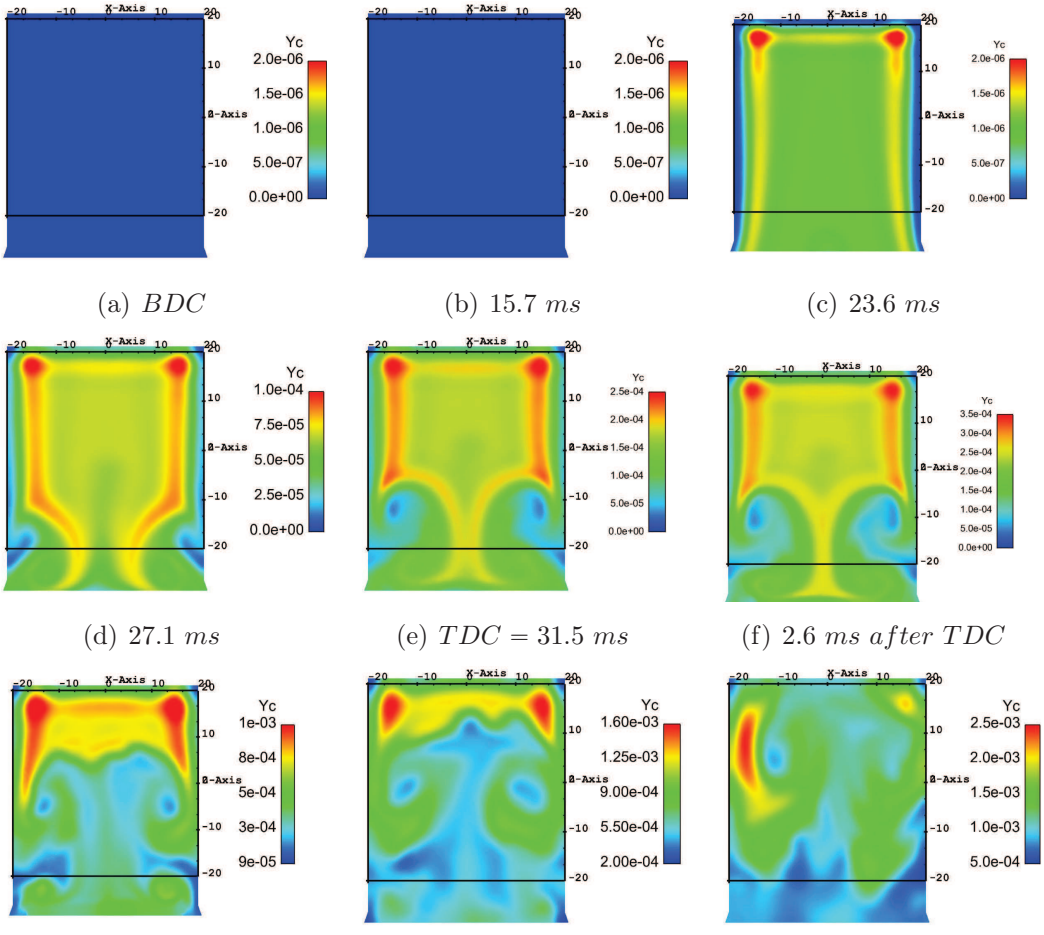

(a) BDC (b) 15.7 ms (c) 23.6 ms

(d) 27.1 ms (e) $TDC = 31.5$ ms (f) 2.6 ms $after$ TDC

(g) 5.2 ms $after$ TDC (h) 7.8 ms $after$ TDC (i) 13.0 ms $after$ TDC

Figure 5.17 shows the normalized progress variable time evolution in the RCM chamber, which is a transported variable.

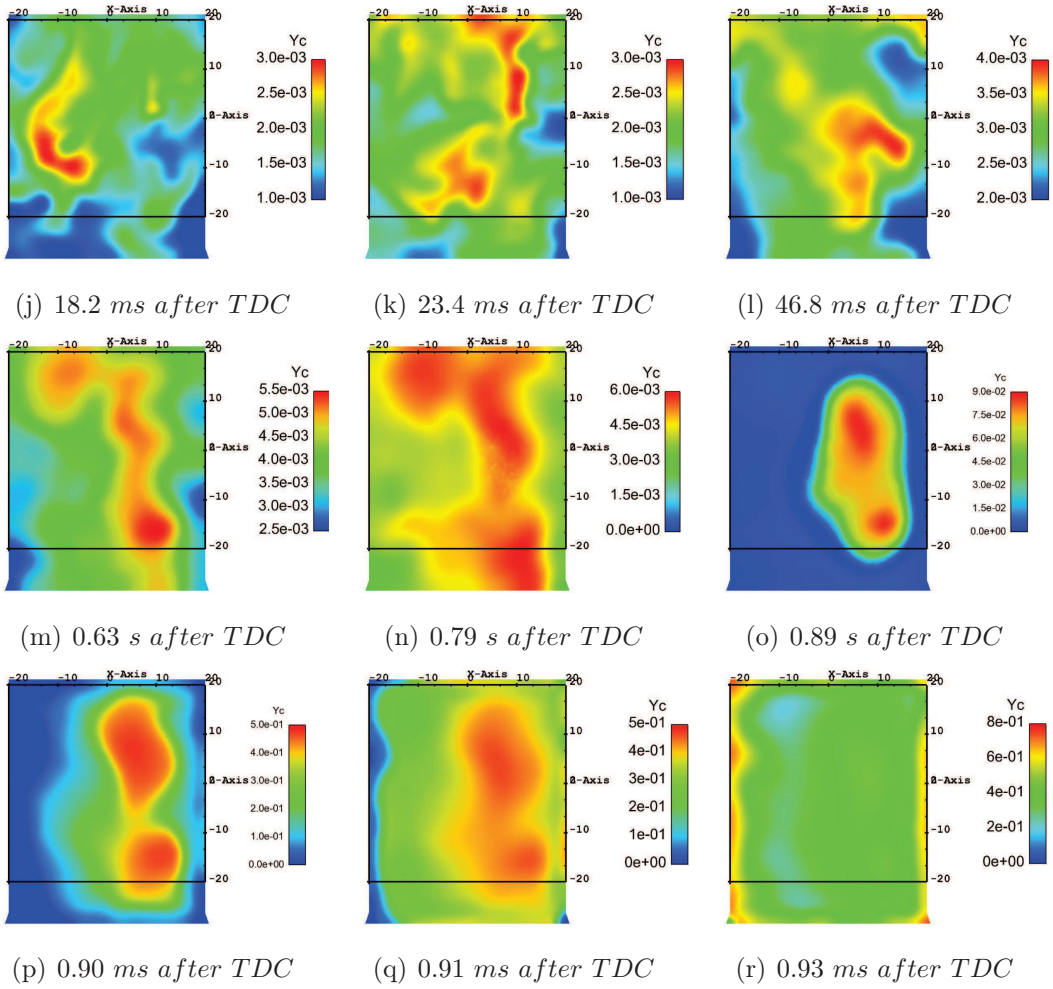

(j) 18.2 *ms after TDC* (k) 23.4 *ms after TDC* (l) 46.8 *ms after TDC*

(m) 0.63 *s after TDC* (n) 0.79 *s after TDC* (o) 0.89 *s after TDC*

(p) 0.90 *ms after TDC* (q) 0.91 *ms after TDC* (r) 0.93 *ms after TDC*

Figure 5.16 : *$AVBP - TTC$: Progress variable time evolution in the RCM chamber*

Figure 5.18 shows the evolution of the pollutant species CO in the RCM chamber.
Figures 5.19 and 5.20 show the hydroxyl radical evolution in the chamber in two different $2-D$ sections in the RCM chamber. It can be observed that the profile changes from one section to the other, highlighting that only a $3-D$ simulation is able to localize the auto-ignition kernels.
Numerical simulations give further knowledge on the chemical features that experiments can not provide today and thus improve the control of specific pollutants.

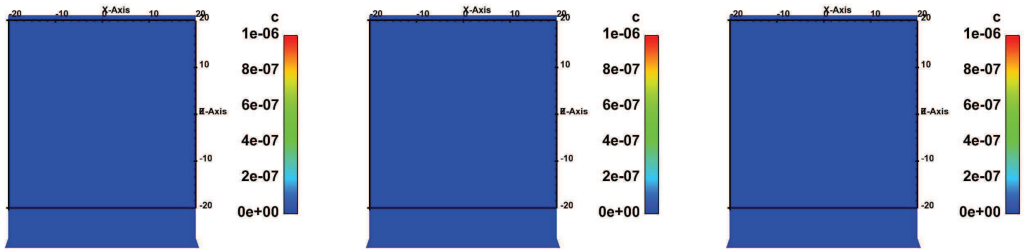

(a) *BDC* (b) 15.7 *ms* (c) 23.6 *ms*

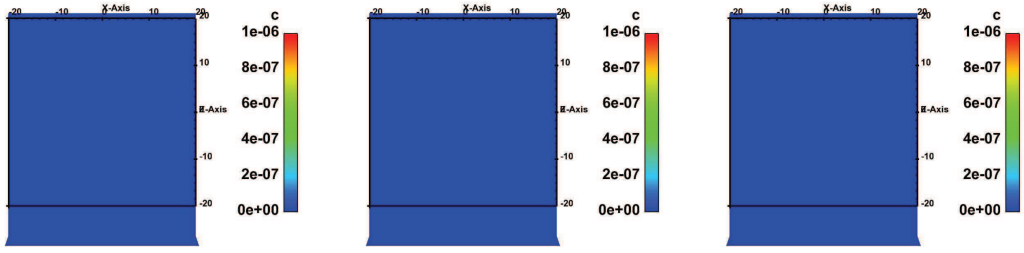

(d) 27.1 *ms* (e) *TDC* = 31.5 *ms* (f) +2.6 *ms after TDC*

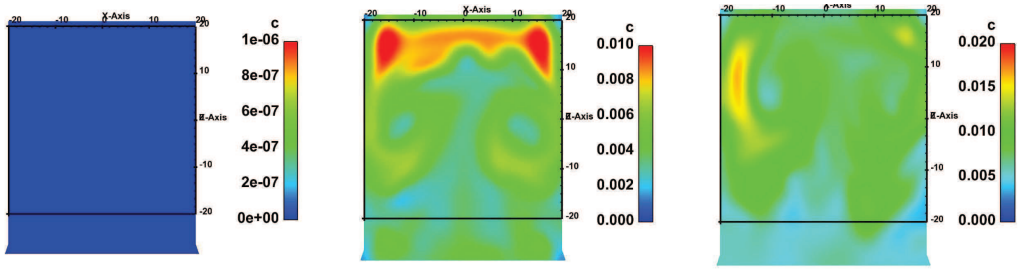

(g) 5.2 *ms after TDC* (h) 7.8 *ms after TDC* (i) 13.0 *ms after TDC*

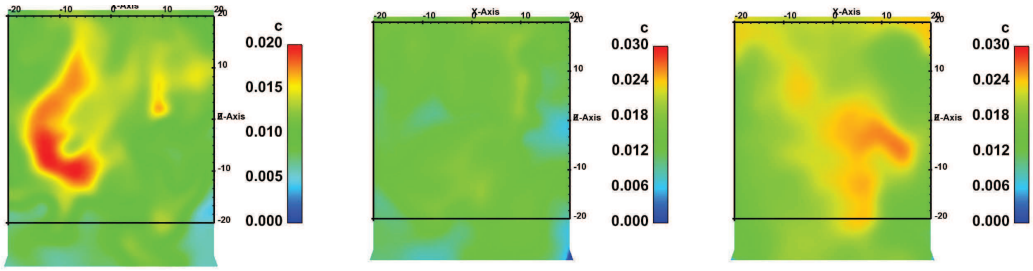

(j) 18.2 *ms after TDC* (k) 23.4 *ms after TDC* (l) 46.8 *ms after TDC*

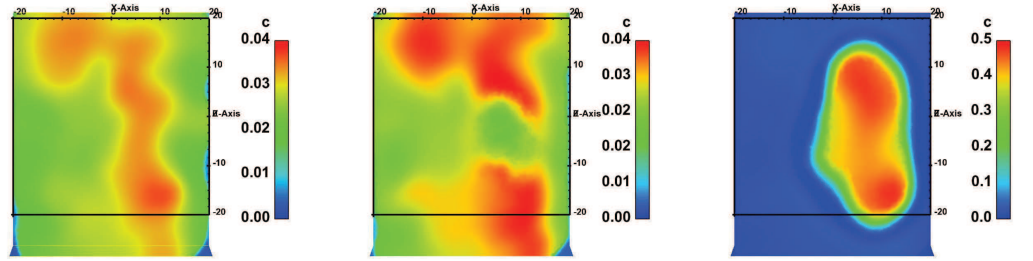

(m) 0.63 *s after TDC* (n) 0.79 *s after TDC* (o) 0.89 *s after TDC*

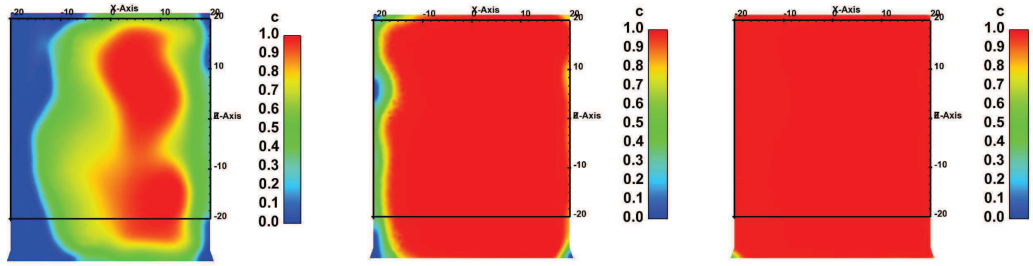

(p) 0.90 *s after TDC* (q) 0.91 *s after TDC* (r) 0.93 *s after TDC*

Figure 5.17 : *AVBP – TTC: Normalized progress variable time evolution in the RCM chamber*

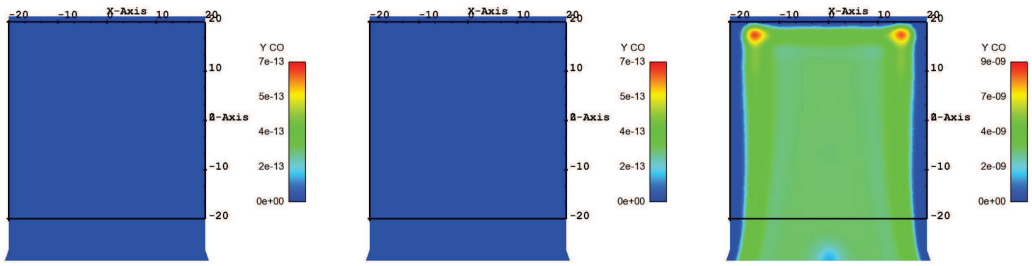

(a) *BDC*

(b) 15.7 *ms*

(c) 23.6 *ms*

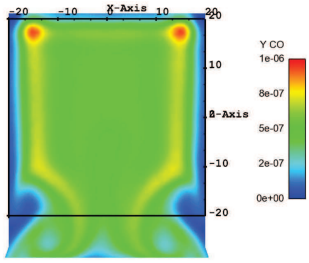

(d) 27.1 *ms*

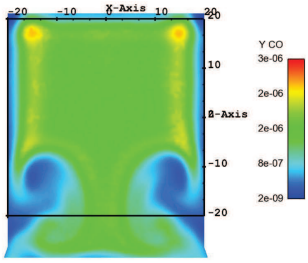

(e) $TDC = 31.5$ *ms*

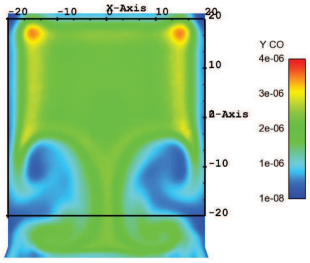

(f) 2.6 *ms after TDC*

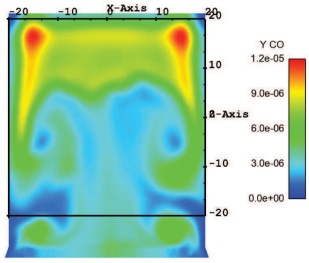

(g) 5.2 *ms after TDC*

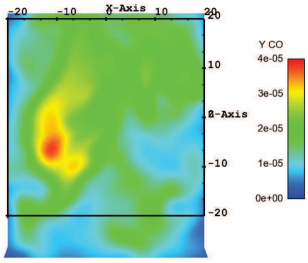

(h) 7.8 *ms after TDC*

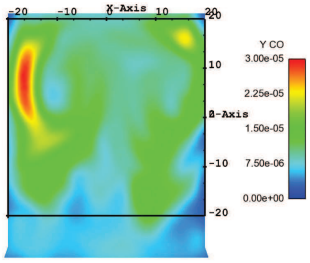

(i) 13.0 *ms after TDC*

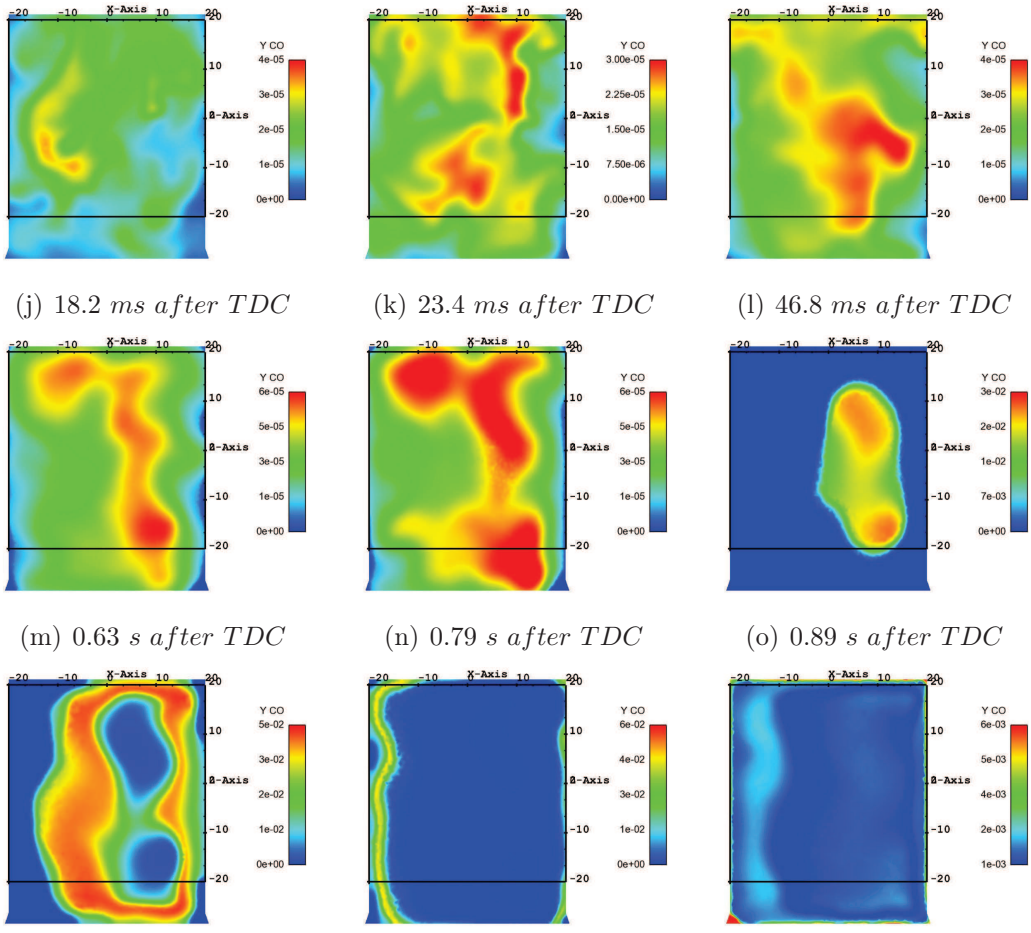

(j) 18.2 *ms after TDC* (k) 23.4 *ms after TDC* (l) 46.8 *ms after TDC*

(m) 0.63 *s after TDC* (n) 0.79 *s after TDC* (o) 0.89 *s after TDC*

(p) 0.90 *s after TDC* (q) 0.91 *s after TDC* (r) 0.93 *s after TDC*

Figure 5.18 : *AVBP − TTC: Carbon monoxyde radical time evolution in the RCM chamber*

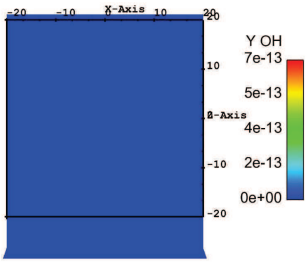

(a) *BDC*

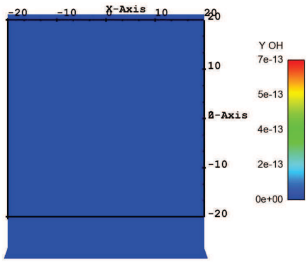

(b) 15.7 *ms*

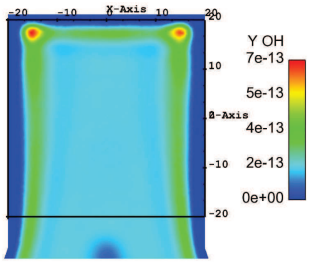

(c) 23.6 *ms*

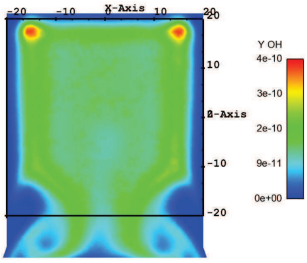

(d) 27.1 *ms*

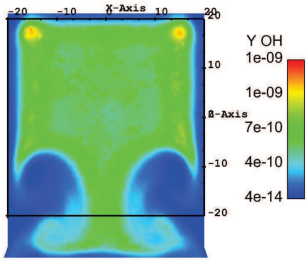

(e) *TDC* = 31.5 *ms*

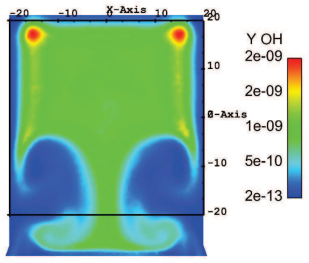

(f) +2.6 *ms after TDC*

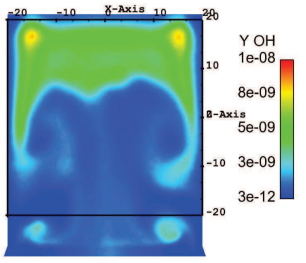

(g) 5.2 *ms after TDC*

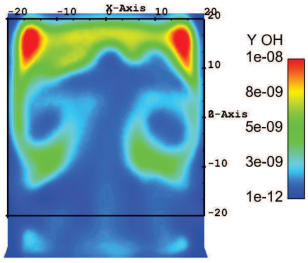

(h) 7.8 *ms after TDC*

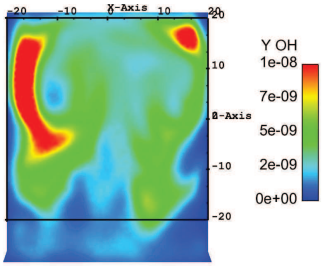

(i) 13.0 *ms after TDC*

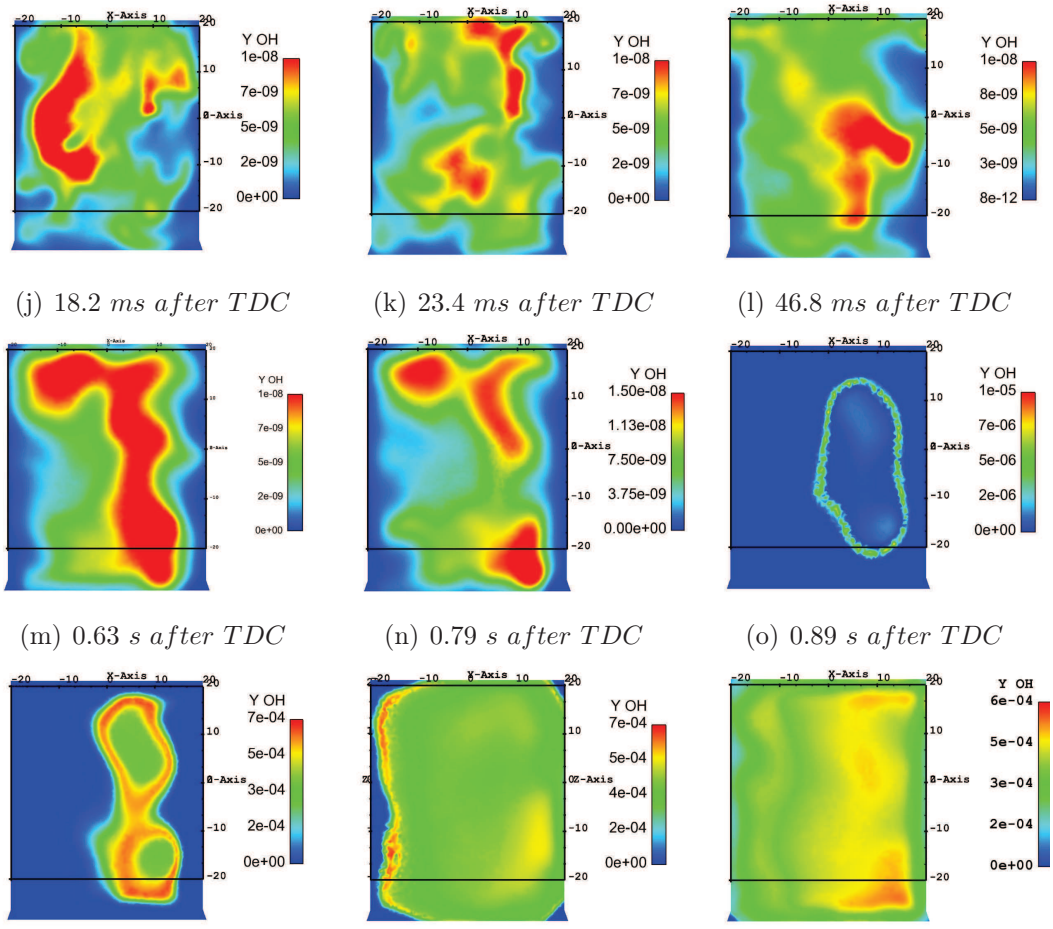

(j) 18.2 *ms after TDC* (k) 23.4 *ms after TDC* (l) 46.8 *ms after TDC*

(m) 0.63 *s after TDC* (n) 0.79 *s after TDC* (o) 0.89 *s after TDC*

(p) 0.90 *s after TDC* (q) 0.91 *s after TDC* (r) 0.93 *s after TDC*

Figure 5.19 : *AVBP−TTC: Hydroxyl radical time evolution in the RCM chamber in the y=0 plane*

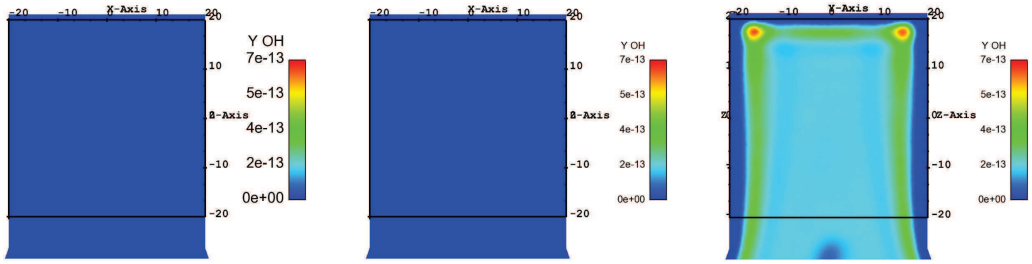

(a) *BDC* (b) 15.7 *ms* (c) 23.6 *ms*

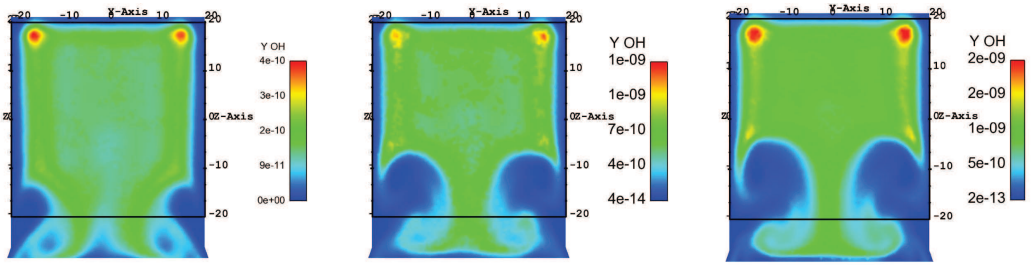

(d) 27.1 *ms* (e) *TDC* = 31.5 *ms* (f) 2.6 *ms after TDC*

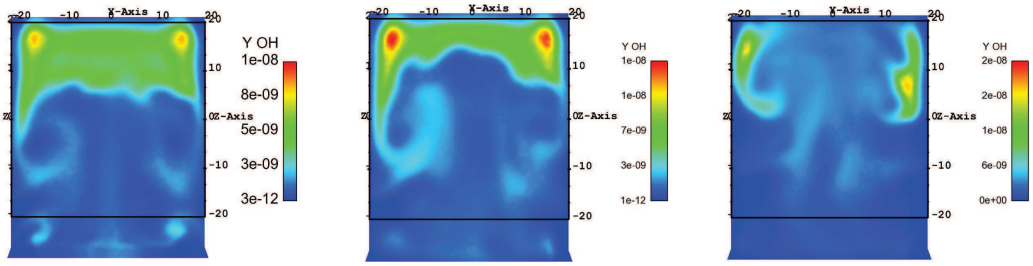

(g) 5.2 *ms after TDC* (h) 7.8 *ms after TDC* (i) 13.0 *ms after TDC*

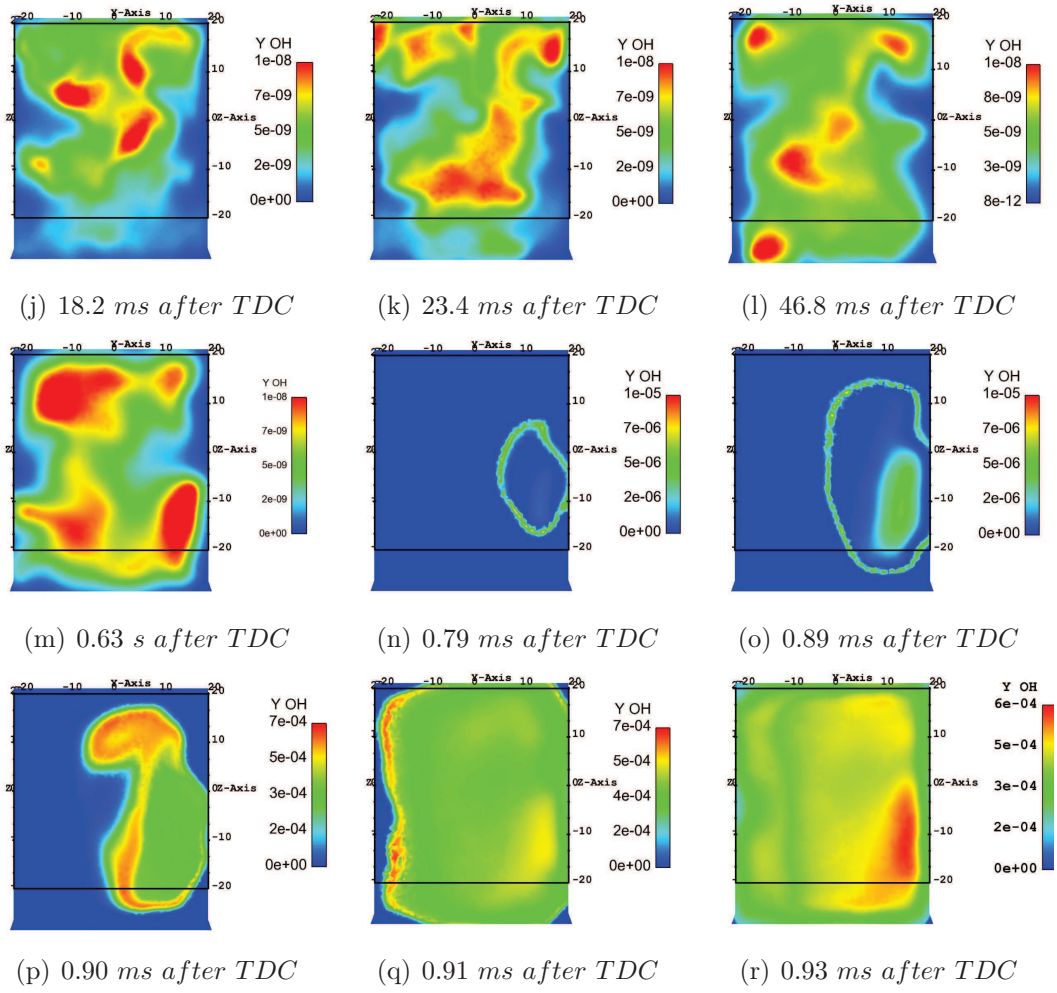

(j) 18.2 *ms after TDC* (k) 23.4 *ms after TDC* (l) 46.8 *ms after TDC*

(m) 0.63 *s after TDC* (n) 0.79 *ms after TDC* (o) 0.89 *ms after TDC*

(p) 0.90 *ms after TDC* (q) 0.91 *ms after TDC* (r) 0.93 *ms after TDC*

Figure 5.20 : *AVBP−TTC: Hydroxyl radical time evolution in the RCM chamber in the x=0 plane*

5.4.2.4 Local analyses of auto-ignition

In order to analyze the auto-ignition, we consider four points in a horizontal section located in the middle of chamber $z = 0\ mm$, Fig. 5.21(a) and we observe the temperature time evolution. The observation was repeated at two other levels, $z = 10\ mm$, Fig. 5.21(b) and $z = -10\ mm$, Fig. 5.21(c). As thermal stratifications are present in the chamber, the auto-ignition does not take place simultaneously throughout the volume but is situated in preferential regions in the combustion chamber. In some regions ignition is almost over and in other regions it has not started yet. Further more, the combustion regimes can be different, both main and cool flame coexist.

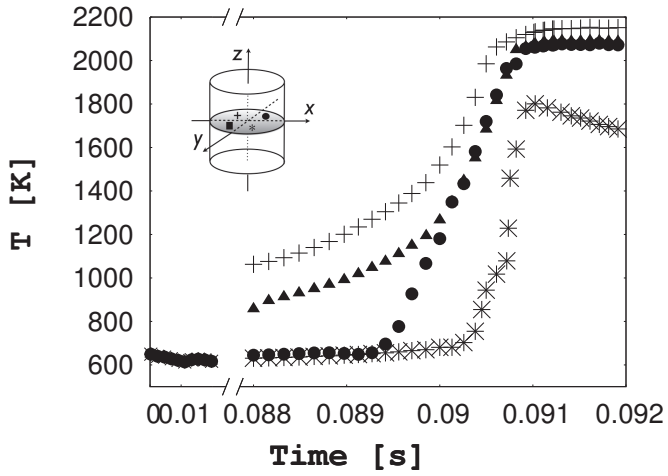

(a) z= 0 mm, R=10 mm, θ= 45°, 135°, 225°, 315°

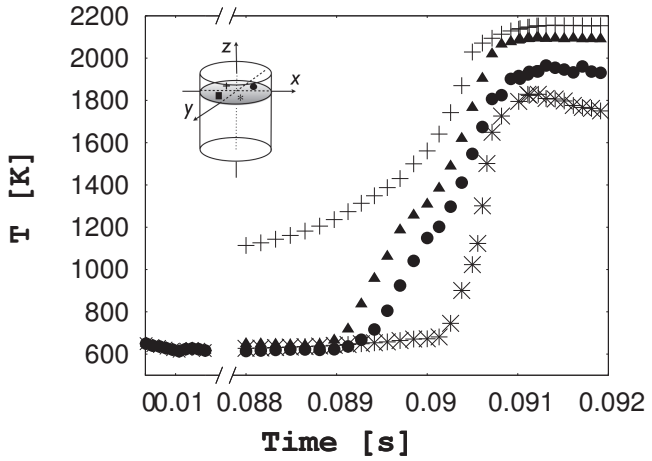

(b) z= + 10mm, R=10 mm, θ= 45°, 135°, 225°, 315°

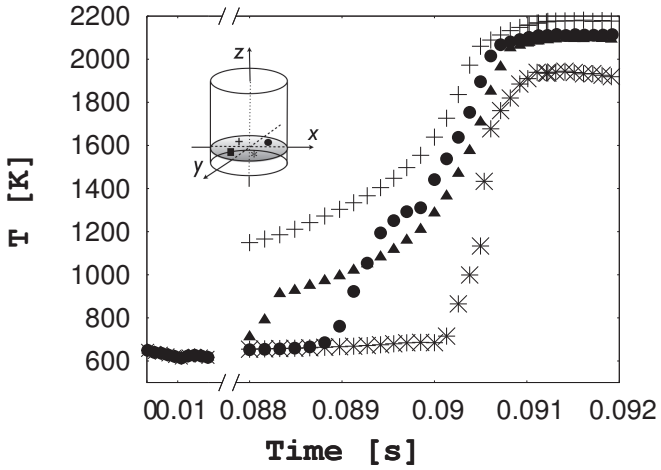

(c) z= - 10mm, R=10 mm, θ= 45°, 135°, 225°, 315°

Figure 5.21 : *Locally temperature time evolution in the RCM chamber in three horizontal positions*

Figure 5.22 gives the temperature time evolution of three points located vertically in the chamber for different regions depicted in the label. The evolutions shows that the flame propagation takes place in the horizontal direction.

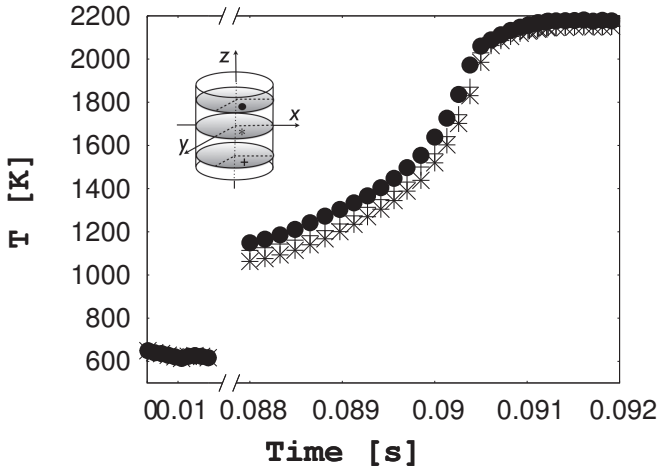

(a) right: $R = 10\ mm$, $\theta = 45°$, $z = -10\ mm$, $z = 0\ mm$, $z = +10\ mm$

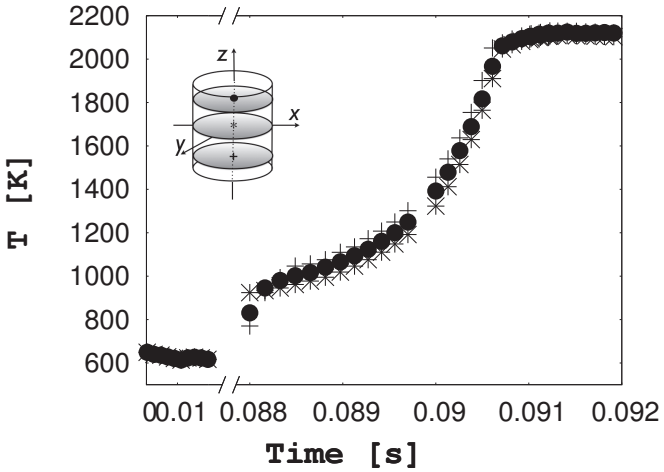

(b) middle: $R = 0\ mm$, $z = -10\ mm$, $z = 0\ mm$, $z = +10\ mm$

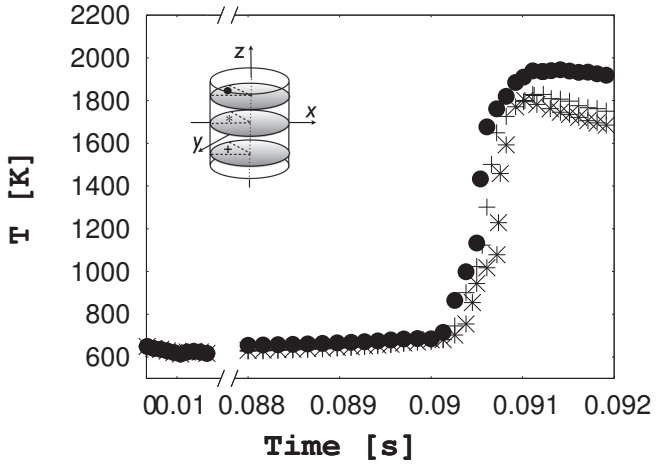

(c) left: $R = 10\ mm$, $\theta = 225°$, $z = -10\ mm$, $z = 0\ mm$, $z = +10\ mm$

Figure 5.22 : *Temperature time evolution in the RCM chamber of three points located vertically at three radial positions*

Conclusion

In this thesis auto-ignition of internal combustion engines has been studied using a LES compressible solver. Chemical kinetics was introduced by tabulation method. The coupled solver was applied to an adiabatic homogeneous compression ignition engine and a rapid compression machine with heat losses.

The first part of this study proposes a methodology that enables the development of an efficient thermo-chemical table for ICE applications. Although the FPI method was largely used to model chemistry in stationary combustors, variable volume configurations have specific issues that have been addressed in this work. In order to account for auto-ignition, the flamelet features of classical FPI approach is replaced by an auto-igniting homogeneous mixture approach. Thus the proposed method assumes that the chemistry of an ICE with a premixed charge can be mapped by a collection of 0-D reactor computation data using as coordinates: the progress variable (c), the energy (e) and the density (ρ). As memory size needed for the thermo-chemical table can limit the use of the tabulation approach when used in parallel codes, a benchmark discretization for each of the chosen coordinates has been given. Constant volume, variable pressure simulations were performed to test the accuracy of the auto-ignition delay estimation when using the tabulation method compared with the detailed chemistry approach. The validation was performed using two mechanisms for n-heptane fuel showing once again that the thermo-chemical table building does not depend upon the chosen detailed chemical. Then, the crossing interpolation in the table was checked by performing 0-D variable volume computations with the tabulated and detailed chemistry approach. The power stroke behavior was accurately predicted for all the test, both for stoichiometric with no-dilution mixture

as for lean diluted mixture. The efficiency in terms of CPU time is at least of the order of 10.

The second part of the study demonstrates the feasibility of the coupling tabulated approach with compressible LES solvers used to variable volume configurations. Usually, perturbations due to compressible effects are not considered during the generation of the database. This yields no-straight forward the introduction of the tabulated chemistry in compressible solvers, as the transported energy value e will not coincide with the energy for which the table was conceived e^{tab}. Due to strongly compressible effects in ICE, energy was considered as database coordinate. The created (ρ,e,c) thermo-chemical table has been implemented in the AVBP LES code - TTC version. The consistency of the coupling between the thermo-chemical table and the CFD solver has been ensured through analysis of the compressible effects and of the auto-ignition delay predictions. Acoustic and entropic waves behavior through the computational domain was analyzed. The chemical prediction capability of this technique was in a first step validated in a homogeneous HCCI configuration. Finally, the influence of the thermal stratification on auto-ignition was studied by large eddy simulation using tabulated chemistry for better understanding the combustion process in rapid compression machines. The numerical solutions obtained using the $AVBP$ compressible LES solver coupled with the thermo-chemical tables (ρ^*,e^*,c^*) was verified and validated in comparison with experimental techniques based on digital image analysis.

Perspectives

In the case of stratified mixtures, concerning the development of the thermo-chemical table, one should consider variations in the mixture fractions. Thus it is necessary a coordinate for the mixture fraction and also a coordinate for the dilution by the exhaust gas recirculation EGR. This will enable the use of the table in partially premixed configurations inside the flammability domain. Outside the flammability domain the progress variable reaction rate should be corrected in order to account for the interaction between iso-mixture fraction surfaces.

Also more realistic interaction between the chemistry and turbulence should be taken into account. The statistic approach seems a promising technique and can easily be used in the tabulated-chemistry approach.

For the thermo-chemical table used in this work, the mean progress variable reaction rate should be calculated using the Probability Density Function (PDF) of the progress variable by a β-function and that of the energy and density by a Dirac-function.

References

[1] *http://www.cerfacs.fr/4-26334-The-AVBP-code.php/.*

[2] *http://www.ansa-usa.com/.*

[3] *http://www.centaursoftware.com.au/.*

[4] *https://inle.cerfacs.fr/projects/hip/.*

[5] G. Albouze, T. Poinsot, and L. Gicquel. Chemical kinetics modeling and les combustion model effects on a perfectly premixed burner. *Comptes Rendus Mecanique*, 337(6 - 7):318 – 328, 2009.

[6] P. Auzillon. Modélisation de la structure et de la dynamique des flammes pour la simulation aux grandes échelles., 2011.

[7] C. Bekdemir, L. Somers, and L. de Goey. Modeling diesel engine combustion using pressure dependent flamelet generated manifolds. *Proceedings of the Combustion Institute*, 33(2):2887 – 2894, 2011.

[8] M. Belhi, P. Domingo, and P. Vervisch. Direct numerical simulation of the effect of an electric field on flame stability. *Combustion and Flame*, 157(12):2286 – 2297, 2010.

[9] R. Bird, W. Stewart, and E. Lightfoot. *Transport Phenomena*. 1960.

[10] D. Bradley, L. K. Kwa, A. K. C. Lau, M. Missaghi, and S. B. Chin. Laminar flamelet modeling of recirculating premixed methane and propane-air combustion. *Combustion and flame*, 71(2):109–122, 1988.

[11] O. Cabrit. Modelisation des flux parietaux sur les tuyeres des moteurs a propergol solide, 2009.

[12] D. Chapman. Computational aerodynamics development and outlook. *AIAA journal*, 17:1293–1313, 1979.

[13] H. Ciezki and G. Adomeit. Shock-tube investigation of self-ignition of n-heptane-air mixtures under engine relevant conditions. *Combustion and Flame*, 93(4):421 – 433, 1993.

[14] O. Colin and A. Benkenida. The 3-Zones Extended Coherent Flame Model (ECMFM3Z) for computing premixed/diffusion combustion. *Oil & Gas Science and Technology - Rev. IFP*, 59(6):593–609, 2004.

[15] O. Colin, A. P. da Cruz, and S. Jay. Detailed chemistry-based auto-ignition model including low temperature phenomena applied to 3-D engine calculations. *Proceedings of the Combustion Institute*, 30(2):2649 – 2656, 2005.

[16] O. Colin, F. Ducros, D. Veynante, and T. Poinsot. A thickened flame model for large eddy simulations of turbulent premixed combustion. *Physics of Fluids*, 12(7):1843–1863, 2000.

[17] C. Correa, H. Niemann, B. Schramm, and J. Warnatz. Reaction mechanism reduction for higher hydrocarbons by the ILDM method. *Proceedings of the Combustion Institute*, 28(2):1607 – 1614, 2000.

[18] H. Curran, P. Gaffuri, W. Pitz, and C. Westbrook. A comprehensive modeling study of n-heptane oxidation. *Combustion and Flame*, 114(1-2):149 – 177, 1998.

[19] C. Curtiss and J. Hirschfelder. Transport properties of multi-component gas mixtures. *The Journal of Chemical Physics*, (3):2124 – 2134, 1949.

[20] A. P. da Cruz. Three-dimensional modeling of self-ignition in HCCI and conventional diesel engines. *Combustion Science and Technology*, 176(5-6):867–887, 2004.

[21] G. De Soete. *Kinetics of Combustion and Combustion Related Nitrogen Chemistry*. 1997.

[22] K. R. Dinesh, X. Jiang, and J. van Oijen. Numerical simulation of hydrogen impinging jet flame using flamelet generated manifold reduction. *International Journal of Hydrogen Energy*, 37(5):4502 – 4515, 2012.

[23] P. Domingo, L. Vervisch, S. Payet, and R. Hauguel. Dns of a premixed turbulent v flame and les of a ducted flame using a fsd-pdf subgrid scale closure with fpi-tabulated chemistry. *Combustion and Flame*, 143(4):566 – 586, 2005.

[24] F. Ducros, P. Comte, and M. Lesieur. Large-eddy Simulation of transition to turbulence in a boundary layer developing spatially over a flat plate. *Journal of Fluids Mechanics*, 1996.

[25] F. Ducros, F. Nicoud, and T. Poinsot. Wall-adapting local eddy-viscosity models for simulations in complex geometries. pages 293–300, 1998.

[26] G. N. Dugue, V. and D. Veynante. Applicability of large eddy simulation to the fluid mechanics in a real engine configuration by means of an industrial code. *SAE international*, page 1194, 2006.

[27] C. Duwig. Study of a filtered flamelet formulation for large eddy simulation of premixed turbulent flames. *Flow, Turbulence and Combustion*, 79(4):433 – 454, 2007.

[28] M. Embouazza. Etude de l'auto-allumage par réduction des schémas cinétiques chimiques. application à la combustion homogène diesel., 2005.

[29] B. Enaux, V. Granet, O. Vermorel, C. Lacour, C. Pera, C. Angelberger, and T. Poinsot. LES study of cycle-to-cycle variations in a spark ignition engine. *Proceedings of the Combustion Institute*, 33(2):3115 – 3122, 2011.

[30] K. Epping, S. Aceves, R. Bechtold, and J. Dec. The potential of HCCI combustion for high efficiency and low emissions. *SAE international*, page 1923, 2002.

[31] B. Fiorina. Modélisation de la combustion turbulent pour l'amélioration de la prédiction des polluants dans un brûleur industriel, 2004.

[32] B. Fiorina. Tabulation de la cin'etique chimique pour la mod'elisation de la combustion turbulente, 2012.

[33] B. Fiorina, R. Baron, O. Gicquel, D. Thevenin, S. Carpentier, and N. Darabiha. Modelling non-adiabatic partially premixed flames

using flame-prolongation of ILDM. *Combustion Theory and Modelling*, (3):449–470, 2003.

[34] B. Fiorina, O. Gicquel, L. Vervisch, S. Carpentier, and N. Darabiha. Approximating the chemical structure of partially premixed and diffusion counterflow flames using FPI flamelet tabulation. *Combustion and Flame*, 140(3):147 – 160, 2005.

[35] B. Fiorina, O. Gicquel, L. Vervisch, S. Carpentier, and N. Darabiha. Premixed turbulent combustion modeling using tabulated detailed chemistry and PDF. *Proceedings of the Combustion Institute*, 30(1):867 – 874, 2005.

[36] B. Fiorina, R. Vicquelin, P. Auzillon, N. Darabiha, O. Gicquel, and D. Veynante. A filtered tabulated chemistry model for LES of premixed combustion. *Combustion and Flame*, 157(3):465–475, Mar. 2010.

[37] M. Germano, U. Piomelli, P. Moin, and W. H. Cabot. A dynamic subgrid-scale eddy viscosity model. *Physics of Fluids A: Fluid Dynamics*, 3(7):1760–1765, July 1991.

[38] O. Gicquel, N. Darabiha, and D. Thévenin. Laminar premixed hydrogen/air counterflow flame simulations using flame prolongation of ILDM with differential diffusion. *Proceedings of the Combustion Institute*, 28(2):1901 – 1908, 2000.

[39] V. Giovangigli. Structure et extinction de flammes laminaires premelangees, 1988.

[40] D. Goryntsev, A. Sadiki, M. Klein, and J. Janicka. Large eddy simulation based analysis of the effects of cycle-to-cycle variations on air-fuel mixing in realistic DISI IC-engines. *Proceedings of the Combustion Institute*, 32(2):2759 – 2766, 2009.

[41] A. Guibert, P.and Keromnes and G. Legros. Development of a turbulence controlled rapid compression machine for HCCI combustion. *SAE international*, page 1869, 2007.

[42] P. Guibert, A. Keromnes, and G. Legros. An experimental investigation of the turbulence effect on the combustion propagation in a rapid compression machine. *Flow, Turbulence and Combustion*, 84:79–95, 2010.

[43] J. Herzler, L. Jerig, and P. Roth. Shock tube study of the ignition of lean n-heptane/air mixtures at intermediate temperatures and high pressures. *Proceedings of the Combustion Institute*, 30(1):1147 – 1153, 2005.

[44] J. Heywood. *Internal Combustion Engine Fundamentals*. 1988.

[45] K. J. Hughes, M. Fairweather, J. F. Griffiths, R. Porter, and A. S. Tomlin. The application of the QSSA via reaction lumping for the reduction of complex hydrocarbon oxidation mechanisms. *Proceedings of the Combustion Institute*, 32(1):543 – 551, 2009.

[46] F. Jaegle, O. Cabrit, S. Mendez, and T. Poinsot. Implementation methods of wall functions in cell-vertex numerical solvers. *Flow, Turbulence and Combustion*, 85:245–272, 2010. 10.1007/s10494-010-9276-1.

[47] S. Jay and O. Colin. A variable volume approach of tabulated detailed chemistry and its applications to multidimensional engine simulations. *Proceedings of the Combustion Institute*, 2010.

[48] S. Jay and O. Colin. A variable volume approach of tabulated detailed chemistry and its applications to multidimensional engine simulations. *Proceedings of the Combustion Institute*, 33(2):3065 – 3072, 2011.

[49] G. Karim and H. Li. Knock in Gas Fueled S.I.Engines. *International Conference on Automotive Technologies*, 2004.

[50] R. J. Kee, F. M. Rupley, E. Meeks, and J. A. Miller. CHEMKIN-III: A fortran chemical kinetics package for the analysis of gas-phase chemical and plasma kinetics. Technical report, Sandia National Laboratories, May 1996.

[51] D. I. Kolaitis and M. A. Founti. On the assumption of using n-heptane as a surrogate fuel for the description of the cool flame oxidation of diesel oil. *Proceedings of the Combustion Institute*, 32(2):3197 – 3205, 2009.

[52] G. Kuenne, A. Ketelheun, and J. Janicka. LES modeling of premixed combustion using a thickened flame approach coupled with FGM tabulated chemistry. *Combustion and Flame*, 158(9):1750 – 1767, 2011.

[53] F. Lafossas, M. Castagne, J. Dumas, and S. Henriot. Development and validation of a knock model in spark ignition engines using a CFD code. *SAE international*, page 2701, 2002.

[54] G. Lecocq, S. Richard, J.-B. Michel, and L. Vervisch. A new LES model coupling flame surface density and tabulated kinetics approaches to investigate knock and pre-ignition in piston engines. *Proceedings of the Combustion Institute*, 33(2):3105 – 3114, 2011.

[55] T. Lu and C. K. Law. Toward accommodating realistic fuel chemistry in large-scale computations. *Progress in Energy and Combustion Science*, 35(2):192 – 215, 2009.

[56] U. Maas and S. Pope. Implementation of simplified chemical kinetics based on intrinsic low-dimensional manifolds. *International Symposium on Combustion*, 24(1):103 – 112, 1992.

[57] E. Meeks, J. M. Deur, D. Hodgson, M. V. Petrova, K. V. Puduppakkam, C. Wang, C. K. Westbrook, A. M. Dean, W. H. Green, M. Koshi, and U. Maas. Application of model fuels to engine simulation. *SAE international*, page 1843, 2007.

[58] J.-B. Michel, O. Colin, and C. Angelberger. On the formulation of species reaction rates in the context of multi-species cfd codes using complex chemistry tabulation techniques. *Combustion and Flame*, 157(4):701 – 714, 2010.

[59] J.-B. Michel, O. Colin, and D. Veynante. Modeling ignition and chemical structure of partially premixed turbulent flames using tabulated chemistry. *Combustion and Flame*, 152(1-2):80 – 99, 2008.

[60] A. Miyoshi. *http://www.frad.t.u-tokyo.ac.jp/ miyoshi/KUCRS/.*

[61] A. Najafi-Yazdi, B. Cuenot, and L. Mongeau. Systematic definition of progress variables and intrinsically low-dimensional, flamelet generated manifolds for chemistry tabulation. *Combustion and Flame*, 159(3):1197 – 1204, 2012.

[62] P. Nguyen, L. Vervisch, V. Subramanian, and P. Domingo. Multidimensional flamelet-generated manifolds for partially premixed combustion. *Combustion and Flame*, 157(1):43 – 61, 2010.

[63] P.-D. Nguyen, L. Vervisch, V. Subramanian, and P. Domingo. Multidimensional flamelet-generated manifolds for partially premixed combustion. *Combustion and Flame*, 157(1):43 – 61, 2010.

[64] J. Oijen. Flamelet-generated manifolds: Development and application to premixed laminar flames, 2002.

[65] J. A. V. Oijen and L. P. H. D. Goey. Modelling of premixed counterflow flames using the flamelet-generated manifold method. *Combustion Theory and Modelling*, 6(3):463–478, 2002.

[66] T. Otsuka and P. Wolanski. Particle image velocimetry (PIV) analysis of flame structure. *Journal of Loss Prevention in the Process Industries*, 14(6):503 – 507, 2001.

[67] Pera, C., Colin, O., and Jay, S. Development of a fpi detailed chemistry tabulation methodology for internal combustion enginess. *Oil & Gas Science and Technology - Rev. IFP*, 64(3):243–258, 2009.

[68] N. Peters. Laminar diffusion flamelet models in non-premixed turbulent combustion. *Progress in Energy and Combustion Science*, 10(3):319–339, 1984.

[69] U. Piomelli. Large-eddy simulation: achievements and challenges. *Progress in Aerospace Sciences*, 35(4):335–362, May 1999.

[70] W. J. Pitz and C. J. Mueller. Recent progress in the development of Diesel surrogate fuels. *Progress in Energy and Combustion Science*, 37(3):330 – 350, 2011.

[71] T. Poinsot and S. Lelef. Boundary conditions for direct simulations of compressible viscous flows. *Journal of Computational Physics*, 101(1):104 – 129, 1992.

[72] T. Poinsot and D. Veynante. *Theoretical and Numerical Combustion, Second Edition*. 2000.

[73] G. Ribert, O. Gicquel, N. Darabiha, and D. Veynante. Tabulation of complex chemistry based on self-similar behavior of laminar premixed flames. *Combustion and Flame*, 146(4):649 – 664, 2006.

[74] G. Ribert, K. Wang, and L. Vervisch. A multi-zone self-similar chemistry tabulation with application to auto-ignition including cool-

flames effects. *Fuel*, 91(1):87 – 92, 2012.

[75] S. Richard, O. Colin, O. Vermorel, A. Benkenida, C. Angelberger, and D. Veynante. Towards large eddy simulation of combustion in spark ignition engines. *Proceedings of the Combustion Institute*, 31(2):3059 – 3066, 2007.

[76] T. W. Ryan and T. J. Callahan. Homogeneous charge compression ignition of Diesel fuel. *SAE international*, 1996.

[77] S. Singh, M. P. Musculus, and R. D. Reitz. Mixing and flame structures inferred from oh-plif for conventional and low-temperature diesel engine combustion. *Combustion and Flame*, 156(10):1898 – 1908, 2009.

[78] J. Smagorinsky. General circulation experiments with the primitive equations. *American Meteorological Society*, 1963.

[79] W. Sutherland. *The viscosity of gases and molecular force, Philosophical Magazine Series 5*, volume 36. 1893.

[80] F. Tao, V. I. Golovitchev, and J. Chomiak. Self-ignition and early combustion process of n-heptane sprays under diluted air conditions: Numerical studies based on detailed chemistry. *SAE international*, page 2931, 2000.

[81] L. Thobois. Aerodynamics in internal combustion engines, turbulent combustion modeling in spark ignition engines, combustion instabilities, 2006.

[82] J. van Oijen, F. Lammers, and L. de Goey. Modeling of complex premixed burner systems by using flamelet-generated manifolds. *Combustion and Flame*, 127(3):2124 – 2134, 2001.

[83] L. Verhoeven, W. Ramaekers, J. van Oijen, and L. de Goey. Modeling non-premixed laminar co-flow flames using flamelet-generated manifolds. *Combustion and Flame*, 159(1):230 – 241, 2012.

[84] O. Vermorel, S. Richard, O. Colin, C. Angelberger, A. Benkenida, and D. Veynante. Towards the understanding of cyclic variability in a spark ignited engine using multi-cycle les. *Combustion and Flame*, 156(8):1525 – 1541, 2009.

[85] R. Vicquelin, B. Fiorina, S. Payet, N. Darabiha, and O. Gicquel. Coupling tabulated chemistry with compressible CFD solvers. *Proceedings of the Combustion Institute*, 2010.

[86] G. Wang, M. Boileau, D. Veynante, and K. Truffin. Large eddy simulation of a growing turbulent premixed flame kernel using a dynamic flame surface density model. *Combustion and Flame*, 159(8):2742 – 2754, 2012.

[87] K. Wang, G. Ribert, P. Domingo, and L. Vervisch. Self-similar behavior and chemistry tabulation of burnt-gas diluted premixed flamelets including heat-loss. *Combustion Theory and Modelling*, 14(4):541–570, 2010.

[88] B. Ya. and Zeldovich. Regime classification of an exothermic reaction with nonuniform initial conditions. *Combustion and Flame*, 39(2):211 – 214, 1980.

[89] C. S. Yoo, T. Lu, J. H. Chen, and C. K. Law. Direct numerical simulations of ignition of a lean n-heptane/air mixture with temperature inhomogeneities at constant volume: Parametric study. *Combustion and Flame*, 158(9):1727 – 1741, 2011.

Appendix A

N-heptane kinetical mechanisme

A 89-species skeletal n-heptane kinetic mechanism [89]. ELEMENTS
H C O N Ar
END
SPECIES

h h2 o o2 oh h2o n2 co hco co2 ch3 ch4 ho2 h2o2 ch2o ch3o c2h6 c2h4 c2h5 ch2 ch c2h c2h2 c2h3 ch3oh ch2oh ch2co hcco c2h5oh pc2h4oh sc2h4oh ch3co ch2cho ch3cho c3h4-a c3h4-p c3h6 c4h6 nc3h7 ic3h7 c3h8 ic4h7 ic4h8 c4h7 c4h8-2 c4h8-1 sc4h9 pc4h9 tc4h9 ic4h9 ic4h10 c4h10 ch3coch3 ch3coch2 c2h5cho c2h5co c5h9 c5h10-1 c5h10-2 ic5h12 ac5h11 bc5h11 cc5h11 dc5h11 ac5h10 bc5h10 cc5h10 ic5h9 nc5h12 c5h11-1 c5h11-2 c5h11-3 neoc5h12 neoc5h11 c2h5o ch3o2 c2h5o2 ch3o2h c2h5o2h c2h3o1-2 ch3co2 c2h4o1-2 c2h4o2h o2c2h4oh ch3co3 ch3co3h c2h3co c2h3cho c3h5o c3h6ooh1-2 c3h6ooh1-3 c3h6ooh2-1 nc3h7o ic3h7o nc3h7o2h ic3h7o2h nc3h7o2 ic3h7o2 c3h6o1-3 ic4h8o ic4h8oh io2c4h8oh ic4h7o c4h7o c4h8oh-1 c4h8oh-2 c4h8oh-1o2 c4h8oh-2o2 tc4h8ooh-io2 ic4h8ooh-io2 ic4h8ooh-to2 c4h8ooh1-2 c4h8ooh1-3 c4h8ooh1-4 c4h8ooh2-1 c4h8ooh2-3 c4h8ooh2-4 ic4h8o2h-i ic4h8o2h-t tc4h8o2h-i c4h8o1-2 c4h8o1-3 c4h8o1-4 c4h8o2-3 cc4h8o pc4h9o sc4h9o ic4h9o tc4h9o pc4h9o2h sc4h9o2h ic4h9o2h tc4h9o2h tc4h9o2 ic4h9o2 sc4h9o2 pc4h9o2 ch3coch2o2 ch3coch2o2h ch3coch2o neoc5ketox neoc5kejol ac5h11o2 bc5h11o2 cc5h11o2 dc5h11o2 ac5h11o2h bc5h11o2h cc5h11o2h dc5h11o2h ac5h11o cc5h11o dc5h11o ac5h10ooh-a ac5h10ooh-b ac5h10ooh-c ac5h10ooh-d bc5h10ooh-a bc5h10ooh-c bc5h10ooh-d cc5h10ooh-a cc5h10ooh-b cc5h10ooh-d dc5h10ooh-a dc5h10ooh-b dc5h10ooh-c a-ac5h10o a-bc5h10o a-cc5h10o a-dc5h10o b-cc5h10o b-dc5h10o c5h11o-1 c5h11o-2 c5h11o-3 neoc5h11o neo-c5h10o c3h5-a c3h5-s c3h5-t c3h3 c3h2 c3h6o1-2 ho2cho o2cho ocho ch2(s) ic4h7-i1 c3h6oh hoc3h6o2 o2c2h4o2h ch2o2hcho ic4h7ooh ic3h5cho tc3h6ocho tc3h6cho ic3h7cho ic4h7oh ic3h6co ic4h6oh ic3h5co ic3h7co tc3h6o2cho tc3h6o2hco ic3h5o2hcho tc3h6ohcho tc3h6oh ic3h5oh tc4h8cho o2c4h8cho o2hc4h8co c3h5oh ch2cch2oh nc3h7cho nc3h7co ch2ch2coch3 c2h5coch2 c2h5coch3 ch2choohcoch3 ch3choococh3 ch3chcoch3 c2h3coch3 ch3chco ch2ch2cho c3h6cho-3 c3h6cho-2 c2h5chco ic3h5coch3 ic3h5coch2 ac3h4coch3 sc3h5coch2 ch3chocho ch3chcho sc3h5cho sc3h5co ic3h6cho c3h6cho-1 c2h5coc2h5 c2h5coc2h4p c2h5coc2h4s c2h5coc2h3 pc2h4coc2h3 sc2h4coc2h3 ic3h6chcoch3 ac3h5chcoch3 ic3h6chcoch2 nc3h7coch3 nc3h7coch2 c3h6coch3-1 c3h6coch3-2 c3h6coch3-3 ic3h7coch3 ic3h7coch2 ic3h6coch3 tc3h6coch3 nc3h7coc2h5 c3h6coc2h5-1 c3h6coc2h5-2 c3h6coc2h5-3 nc3h7coc2h4p nc3h7coc2h4s ic3h7coc2h5 ic3h6coc2h5 tc3h6coc2h5 ic3h7coc2h4p ic3h7coc2h4s ic3h7coc2h3 ic3h6coc2h3 tc3h6coc2h3 ic3h5coc2h5 ac3h4coc2h5 ic3h5coc2h4p ic3h5coc2h4s nc4h9cho nc4h9co ac3h5cho ac3h5co c2h3chcho c4h8cho-1 c4h8cho-2 c4h8cho-3 c4h8cho-4 neoc5h9q2 neoc5h9q2-n ic4h6q2-ii hoch2o hocho nc6h14 c6h13-1 c6h13-2 c6h13-3 c6h12-1 c6h12-2 c6h12-3 c6h11 c6h13o-1 c6h13o-2 c6h13o-3 nc7h16 c7h15-1 c7h15-2 c7h15-3 c7h15-4 c7h14-1 c7h14-2 c7h14-3 c7h13 c7h15o-1 c7h15o-2 c7h15o-3 c7h15o-4 ar
END

REACTIONS cal/mole

c2h5+o2=ch3cho+oh	8.680000e+14	-1.121000	10610.000000
c2h5+o2=c2h4+ho2	1.730000e+26	-4.423000	10438.000000
c2h5+o2=c2h4o1-2+oh	3.520000e+27	-5.005000	15249.000000
c2h5+o2=c2h5o2	9.890000e+55	-13.55100	15110.000000
c2h5+o2=c2h4o2h	7.840000e+40	-9.739000	14966.000000
c2h5o2=c2h4+ho2	7.530000e+55	-13.50400	46652.000000
c2h5o2=c2h4o2h	4.140000e+65	-17.02900	52310.000000
c2h5o2=c2h4o1-2+oh	1.070000e+65	-16.47500	57170.000000
c2h4o2h=c2h4+ho2	2.920000e+38	-8.269000	23756.000000
c2h4o2h=c2h4o1-2+oh	4.840000e+38	-8.348000	23736.000000
c2h5o2+ho2=c2h5o2h+o2	4.100000e+11	0.000000	-1390.000000
ch3o2+ho2=ch3o2h+o2	2.500000e+11	0.000000	-1570.000000
nc3h7o+o2=c2h5cho+ho2	8.430000e+9	0.000000	-300.000000
ch3+o2=ch3o+o	1.375000e+13	0.000000	30520.000000
REV /	8.506000e+14	-4.500000e-1	2.479000e+3 /
ch3+o2=ch2o+oh	5.870000e+11	0.000000	14240.000000
REV /	1.175000e+11	1.900000e-1	6.606000e+4 /
ch3+o2(+M)=ch3o2(+M)	1.006000e+8	1.630000	0.000000
LOW/	3.816E+31	-4.89 3432/	
TROE/ 0.045	880.1	2500000000	1786000000/
ch3o2+ch3=2ch3o	9.000000e+12	0.000000	-1200.000000
REV /	3.484000e+12	1.800000e-1	2.828000e+4 /
ch3+ho2=ch3o+oh	1.500000e+13	0.000000	0.000000
REV /	9.284000e+13	-1.200000e-1	2.524000e+4 /
ch3+ho2=ch4+o2	3.610000e+12	0.000000	0.000000
REV /	6.281000e+14	-1.000000e-1	5.623000e+4 /
ch3o(+M)=ch2o+h(+M)	6.800000e+13	0.000000	26170.000000
h2/ 2.000/			
h2o/ 6.000/			
co/ 1.500/			
co2/ 2.000/			
ch4/ 2.000/			
c2h6/ 3.000/			
LOW/	1.867E+25	-3 24307/	
TROE/0.9	2500	1300	1.0E+99/
hco+M=h+co+M	4.750000e+11	0.700000	14900.000000
h2/ 2.500/			
h2o/ 6.000/			
co/ 1.900/			
co2/ 3.800/			
co+o2=co2+o	2.530000e+12	0.000000	47700.000000
co+oh=co2+h	2.230000e+5	1.900000	-1160.000000
hco+oh=co+h2o	3.020000e+13	0.000000	0.000000
co+ho2=co2+oh	3.010000e+13	0.000000	23000.000000
hco+ho2=ch2o+o2	2.970000e+10	0.330000	-3861.000000
h+o2=o+oh	1.970000e+14	0.000000	16540.000000
o+h2=h+oh	5.080000e+4	2.670000	6292.000000
o+h2o=2oh	2.970000e+6	2.020000	13400.000000
oh+h2=h+h2o	2.160000e+8	1.510000	3430.000000
h2o2+oh=h2o+ho2	1.000000e+12	0.000000	0.000000
DUP			

h2o2+oh=h2o+ho2	5.800000e+14	0.000000	9560.000000
DUP			
h+o2(+M)=ho2(+M)	1.480000e+12	0.600000	0.000000
h2/ 1.300/			
h2o/ 14.000/			
co/ 1.900/			
co2/ 3.800/			
ar/ 0.670/			
LOW/	3.5E+16	-0.41	-1116/
TROE/0.5	1.0E-30	1.0E+30	1.0E+100/
ho2+o=oh+o2	3.250000e+13	0.000000	0.000000
ho2+h=2oh	7.080000e+13	0.000000	300.000000
ho2+h=h2+o2	1.660000e+13	0.000000	820.000000
ho2+oh=h2o+o2	2.890000e+13	0.000000	-500.000000
h2o2+h=h2o+oh	2.410000e+13	0.000000	3970.000000
o+h+M=oh+M	4.720000e+18	-1.000000	0.000000
h2/ 2.500/			
h2o/ 12.000/			
co/ 1.900/			
co2/ 3.800/			
ar/ 0.750/			
2o+M=o2+M	6.170000e+15	-0.500000	0.000000
h2/ 2.500/			
h2o/ 12.000/			
co/ 1.900/			
co2/ 3.800/			
ar/ 0.830/			
h2+M=2h+M	4.570000e+19	-1.400000	104400.000000
h2/ 2.500/			
h2o/ 12.000/			
co/ 1.900/			
co2/ 3.800/			
h2o2+o=oh+ho2	9.550000e+6	2.000000	3970.000000
h+oh+M=h2o+M	4.500000e+22	-2.000000	0.000000
h2/ 0.730/			
h2o/ 12.000/			
co/ 1.900/			
co2/ 3.800/			
ar/ 0.380/			
2ho2=h2o2+o2	4.200000e+14	0.000000	11980.000000
DUP			
2ho2=h2o2+o2	1.300000e+11	0.000000	-1629.000000
DUP			
h2o2(+M)=2oh(+M)	2.950000e+14	0.000000	48400.000000
h2/ 2.500/			
h2o/ 12.000/			
co/ 1.900/			
co2/ 3.800/			
ar/ 0.640/			
LOW/	1.27E+17	0 45500/	
TROE/	0.5	1.0E-30	1.0E+30/

h2o2+h=h2+ho2	6.030000e+13	0.000000	7950.000000
c3h5o=c2h3cho+h	5.800000e+13	0.000000	13600.000000
c3h5o=c2h3+ch2o	5.000000e+9	1.418000	30500.000000
REV /	1.000000e+12	0.000000e+0	1.000000e+4 /
c3h5o+o2=c2h3cho+ho2	8.430000e+9	0.000000	-300.000000
nc3h7+o2=c3h6+ho2	1.710000e+42	-9.211000	19790.000000
nc3h7+o2=>nc3h7o2	5.530000e+62	-15.669000	17788.000000
nc3h7o2=>nc3h7+o2	1.260000e+62	-14.626000	50279.000000
nc3h7+o2=c3h6ooh1-3	3.690000e+54	-13.096000	23483.000000
REV /	6.350000e+53	-1.255500e+1	3.795500e+4 /
nc3h7o2=c3h6+ho2	3.250000e+56	-13.822000	45661.000000
nc3h7o2=c3h6ooh1-3	3.530000e+50	-12.185000	39545.000000
REV /	1.130000e+52	-1.321400e+1	2.253400e+4 /
c3h6ooh1-3=c2h4+ch2o+oh	1.080000e+32	-5.673000	34099.000000
ic3h7+o2=c3h6+ho2	3.900000e+48	-11.002000	21249.000000
ic3h7+o2=>ic3h7o2	4.160000e+73	-18.952000	21998.000000
ic3h7o2=>ic3h7+o2	3.490000e+71	-17.307000	56609.000000
ic3h7o2=c3h6+ho2	8.460000e+65	-16.450000	50010.000000
ch3+h(+M)=ch4(+M)	2.138000e+15	-0.400000	0.000000
h2/ 2.000/			
h2o/ 5.000/			
co/ 2.000/			
co2/ 3.000/			
LOW/	3.31E+30	-4 2108/	
TROE/0	1.0E-15	1.0E-15	40/
ch4+h=ch3+h2	1.727000e+4	3.000000	8224.000000
REV /	6.610000e+2	3.000000e+0	7.744000e+3 /
ch4+oh=ch3+h2o	1.930000e+5	2.400000	2106.000000
REV /	3.199000e+4	2.400000e+0	1.678000e+4 /
ch4+o=ch3+oh	3.150000e+12	0.500000	10290.000000
REV /	5.296000e+10	5.000000e-1	7.715000e+3 /
c2h6+ch3=c2h5+ch4	1.510000e-7	6.000000	6047.000000
REV /	9.649000e-10	6.560000e+0	1.022000e+4 /
h2o2+oh=h2o+ho2	1.000000e+12	0.000000	0.000000
REV /	1.685000e+11	3.300000e-1	3.146000e+4 /
DUP			
.			
.			
.			
.			
.			
.			
c7h13=c3h5-a+c4h8-1	2.500000e+13	0.000000	45000.000000
REV /	1.000000e+13	0.000000e+0	9.600000e+3 /
c7h13=c4h7+c3h6	2.500000e+13	0.000000	45000.000000
REV /	1.000000e+13	0.000000e+0	9.600000e+3 /
c7h14-1=pc4h9+c3h5-a	1.000000e+16	0.000000	71000.000000
REV /	1.000000e+13	0.000000e+0	0.000000e+0 /
c7h14-2=c4h7+nc3h7	1.000000e+16	0.000000	71000.000000
REV /	1.000000e+13	0.000000e+0	0.000000e+0 /
c7h14-3=c4h7+nc3h7	1.000000e+16	0.000000	71000.000000
REV /	1.000000e+13	0.000000e+0	0.000000e+0 /
c7h15o-1=ch2o+c6h13-1	4.683000e+17	-1.340000	20260.000000
REV /	1.000000e+11	0.000000e+0	1.190000e+4 /
c7h15o-2=ch3cho+c5h11-1	8.660000e+21	-2.390000	21880.000000
REV /	1.000000e+11	0.000000e+0	1.290000e+4 /

c7h15o-3=c2h5cho+pc4h9	5.600000e+21	-2.330000	21360.000000
REV /	1.000000e+11	0.000000e+0	1.290000e+4 /
c7h15o-4=nc3h7cho+nc3h7	6.684000e+21	-2.290000	21620.000000
REV /	1.000000e+11	0.000000e+0	1.290000e+4 /
nc7h16+o2cho=c7h15-1+ho2cho	1.680000e+13	0.000000	20440.000000
REV /	1.170000e+3	2.250000e+0	3.057000e+3 /
nc7h16+o2cho=c7h15-2+ho2cho	1.120000e+13	0.000000	17690.000000
REV /	2.482000e+1	2.640000e+0	2.823000e+3 /
nc7h16+o2cho=c7h15-3+ho2cho	1.120000e+13	0.000000	17690.000000
REV /	2.482000e+1	2.640000e+0	2.823000e+3 /
nc7h16+o2cho=c7h15-4+ho2cho	5.600000e+12	0.000000	17690.000000
REV /	2.472000e+1	2.640000e+0	2.823000e+3 /
15-1+ho2=c7h15o-1+oh	7.000000e+12	0.000000	-1000.000000
REV /	1.129000e+16	-7.500000e-1	2.698000e+4 /
15-2+ho2=c7h15o-2+oh	7.000000e+12	0.000000	-1000.000000
REV /	1.967000e+18	-1.370000e+0	2.889000e+4 /
15-3+ho2=c7h15o-3+oh	7.000000e+12	0.000000	-1000.000000
REV /	1.967000e+18	-1.370000e+0	2.889000e+4 /
15-4+ho2=c7h15o-4+oh	7.000000e+12	0.000000	-1000.000000
REV /	1.967000e+18	-1.370000e+0	2.889000e+4 /
15-1+ch3o2=c7h15o-1+ch3o	7.000000e+12	0.000000	-1000.000000
REV /	1.103000e+18	-1.330000e+0	3.175000e+4 /
15-2+ch3o2=c7h15o-2+ch3o	7.000000e+12	0.000000	-1000.000000
REV /	1.921000e+20	-1.950000e+0	3.366000e+4 /
15-3+ch3o2=c7h15o-3+ch3o	7.000000e+12	0.000000	-1000.000000
REV /	1.921000e+20	-1.950000e+0	3.366000e+4 /
15-4+ch3o2=c7h15o-4+ch3o	7.000000e+12	0.000000	-1000.000000
REV /	1.921000e+20	-1.950000e+0	3.366000e+4 /
ch3o2+h2o2=ch3o2h+ho2	1.320000e+4	2.500000	9560.000000
c2h5o2+h2o2=c2h5o2h+ho2	1.320000e+4	2.500000	9560.000000
nc3h7o2+h2o2=nc3h7o2h+ho2	1.320000e+4	2.500000	9560.000000
ic3h7o2+h2o2=ic3h7o2h+ho2	1.320000e+4	2.500000	9560.000000
END			

Appendix B

Linear acoustic equations

The objective of this part is to recast the classical linear acoustic equations for a one-component isentropic flow. Mass, momentum and energy conservation equations are written in 1-D under zero viscosity and no heat conduction assumption. This leads to the 1-D Euler equation system (B.1).

$$\frac{\partial \boldsymbol{\rho}}{\partial t} + \frac{\partial \boldsymbol{\rho u}}{\partial x} = 0 \tag{B.1a}$$

$$\frac{\partial \boldsymbol{\rho u}}{\partial t} + \frac{\partial \boldsymbol{\rho u^2}}{\partial x} = -\frac{\partial p}{\partial x} \tag{B.1b}$$

$$\frac{\partial \boldsymbol{\rho E}}{\partial t} + \frac{\partial \boldsymbol{\rho u E}}{\partial x} = -\frac{\partial up}{\partial x} \tag{B.1c}$$

In order to assess the acoustic wave equations it is commonly considered that the flow undergoes reversible processes. From the consideration of the second law of thermodynamics, the flow maintains a constant value of entropy, thus under this restriction, the pressure and the density are related as follows:

$$p\rho^{-\gamma} = e^{s_0 C_v} \tag{B.2}$$

where $\gamma = \frac{C_p}{C_v}$ is the specific heat ratio. Consequently, it is preferred to replace the energy equation (B.1c) by the equation (B.2) .
The acoustic perturbations are amplitude disturbances p', ρ', T' and u', to the mean field variable $\overline{p}$, $\overline{\rho}$, $\overline{T}$ and $\overline{u}$, here $\overline{u} = 0$:

$$p = \overline{p} + p', \quad \rho = \overline{\rho} + \rho', \quad T = \overline{T} + T', \quad u = \overline{u} + u' \tag{B.3}$$

For a one-component system, only two intensive variables are required for its description, i.e. in an isentropic flow of entropy $\overline{s}$, one may write $p(\overline{\rho} + \rho', \overline{s}) = \overline{p}(\overline{\rho}, \overline{s}) + p'$. Performing the formal Taylor series expansion of the pressure $p(\overline{\rho} + \rho', \overline{s})$ in powers of the density fluctuations ρ', the following equations are obtained:

$$p' = \sum_{k=1}^{+\infty} (\rho')^k \left(\frac{\partial p(\overline{\rho}, \overline{s})}{\partial \overline{\rho}}\right)_{\overline{s}} \tag{B.4a}$$

$$at\ 1^{st} order: \quad p' = \rho' \left(\frac{\partial p(\overline{\rho}, \overline{s})}{\partial \overline{\rho}}\right)_{\overline{s}} \tag{B.4b}$$

The pressure rate of change to respect of the mean density, at constant entropy is actually the square of the speed of sound:

$$c^2 = \left(\frac{\partial p(\overline{\rho}, \overline{s})}{\partial \overline{\rho}}\right)_{\overline{s}} \tag{B.5}$$

which leads to:

$$c = \sqrt{\gamma r \overline{T}} \tag{B.6}$$

If the induced variations in pressure p', density ρ' and velocity u' are small compared to the reference values of these quantities $\overline{p}$, $\overline{\rho}$ and $\overline{u}$, the first order approximation is reasonably used by neglecting the higher order terms. Likewise the terms of zero order vanish as the mean field variables are independent of time and of position. So, the system of equations (B.1) is checked by the first order perturbations:

$$p' = c^2 \rho' \tag{B.7a}$$

$$\frac{1}{c^2}\frac{\partial \boldsymbol{p}'}{\partial t} + \overline{\rho}\frac{\partial \boldsymbol{u}'}{\partial x} = 0 \tag{B.7b}$$

$$\overline{\rho}\frac{\partial \boldsymbol{u}'}{\partial t} + \frac{\partial p'}{\partial x} = 0 \tag{B.7c}$$

The last two terms can be compacted by eliminating the velocity perturbations leading to the wave equations for pressure or velocity disturbance:

$$\frac{\partial^2 p'}{\partial x^2} - \frac{1}{c^2}\frac{\partial^2 p'}{\partial t^2} = 0 \tag{B.8a}$$

$$\frac{\partial^2 u'}{\partial x^2} - \frac{1}{c^2}\frac{\partial^2 u'}{\partial t^2} = 0 \tag{B.8b}$$

Any single-valued and second order differentiable function of the form $\phi(x \pm ct)$ is able to satisfy the wave equations (B.8) as it can be proven by direct substitution. Physically, the solution function $\phi(x \pm ct)$ is stationary to the observer who moves at steady speed c along the $x - axis$ in both directions. The signal described initially by $\phi(x, t = 0)$ remains unchanged in form. Hence, the solution is two traveling waves: one traveling to the right $\phi_+(x - ct)$ and the other one traveling to the left $\phi_-(x + ct)$.
Therefore, the general solution of *1-D* linear acoustic equations B.7 describing the propagation of the acoustic disturbance functions $\rho'(x,t)$, $p'(x,t)$ and $u'(x,t)$ in a medium at a constant entropy is:

$$\rho'(x,t) = \frac{1}{c^2}p'(x,t) \tag{B.9a}$$

$$p'(x,t) = p'_+(x - ct) + p'_-(x + ct) \tag{B.9b}$$

$$u'(x,t) = u'_+(x - ct) + u'_-(x + ct) \tag{B.9c}$$

In the favorable event that the linearized momentum is conserved, the equation B.7c is satisfied, the pressure and the velocity traveling waves are joint through the relations:

$$p'_+ = \overline{\rho}\, c u'_+ \tag{B.10a}$$

$$p'_- = -\overline{\rho}\, c u'_- \tag{B.10b}$$

In conclusion, with given initial and boundary conditions, the system of equations (B.7) traces the acoustic perturbations p', ρ' and u' that arise in one-component isentropic fluids and exhibits the analytical solution (B.9).
Note that the pressure and the velocity perturbations are related by the factor $\overline{\rho}c$ called the *impedence*, a characteristic of the medium through which the disturbance propagates.

Appendix C

1-D characteristic wave

The objective of this part is to recast the $1-D$ Euler equations from the conservative to non-conservative followed by the characteristic wave decomposition. A general mathematical formulation for tabulated and detailed chemistry representations is outlined and the differences are analyzed. Also the discrepancy of the new tabulation method with respect to other tabulation methods will be addressed .

C.1 From conservative variables to non-conservative variables

The model equations for solving acoustics are the compressible $1-D$ Euler equations carrying the hypothesis of a uniform mean field, with linear acoustics, no source term, no viscosity or heat conductivity.

$$\frac{\partial \boldsymbol{\rho}}{\partial t} + \frac{\partial \boldsymbol{\rho u}}{\partial x} = 0 \tag{C.1a}$$

$$\frac{\partial \boldsymbol{\rho u}}{\partial t} + \frac{\partial \boldsymbol{\rho u^2}}{\partial x} = -\frac{\partial p}{\partial x} \tag{C.1b}$$

$$\frac{\partial \boldsymbol{\rho E}}{\partial t} + \frac{\partial \boldsymbol{\rho u E}}{\partial x} = -\frac{\partial up}{\partial x} \tag{C.1c}$$

$$\frac{\partial \boldsymbol{\rho \psi_l}}{\partial t} + \frac{\partial \boldsymbol{\rho u \psi_l}}{\partial x} = 0 \qquad , l = 1, ..., N \tag{C.1d}$$

In detailed chemistry formulation, $\psi_l = Y_k$ stands for the k^{th} chemical species, $N = N_{sp}$ being the number of the species participating in the kinetic mechanism.
In tabulated chemistry ψ_l stands for one of the reduced set of variables used in the tabulation process, $N \ll N_{sp}$ is then the number of dimensions of the database, in the particular case of this work $\psi = (\rho^*, e^*, c^*)$.
In the vectorial form, the balance equations for conservative variables become:

$$\frac{\partial \vec{\boldsymbol{U}}}{\partial t} + \frac{\partial \vec{\boldsymbol{F}}_{\boldsymbol{U}}}{\partial x} = 0 \tag{C.2}$$

where $\overrightarrow{U}$ is the conservative variable vector:

$$\overrightarrow{U} = \begin{pmatrix} \rho \\ \rho u \\ \rho E \\ \vdots \\ \rho\psi_l \\ \vdots \end{pmatrix} \tag{C.3}$$

and $\overrightarrow{F}_U$ is the vector of *Eulerian* non-viscous fluxes.

$$\overrightarrow{F}_U = \begin{pmatrix} \rho u \\ \rho u^2 + p \\ \rho u E + up \\ \vdots \\ \rho u \psi_l \\ \vdots \end{pmatrix} \tag{C.4}$$

Using the non-viscous fluxes' *Jacobian* matrix: $\overline{\overline{J_U}} = \frac{\partial \overrightarrow{F}_U}{\partial \overrightarrow{U}}$, the relation C.2 becomes:

$$\frac{\partial \overrightarrow{U}}{\partial t} + \overline{\overline{J_U}} \frac{\partial \overrightarrow{U}}{\partial x} = 0 \tag{C.5}$$

with

$$\begin{aligned} \overline{\overline{J_U}} &= \begin{pmatrix} \frac{\partial \rho u}{\partial \rho} & \frac{\partial \rho u}{\partial \rho u} & \frac{\partial \rho u}{\partial \rho E} & \cdots & \frac{\partial \rho u}{\partial \rho Y_k} & \cdots \\ \frac{\partial (\rho u^2 + p)}{\partial \rho} & \frac{\partial (\rho u^2 + p)}{\partial \rho u} & \frac{\partial (\rho u^2 + p)}{\partial \rho E} & \cdots & \frac{\partial (\rho u^2 + p)}{\partial \rho \psi_l} & \cdots \\ \frac{\partial (\rho u E + up)}{\partial \rho} & \frac{\partial (\rho u E + up)}{\partial \rho u} & \frac{\partial (\rho u E + up)}{\partial \rho E} & \cdots & \frac{\partial (\rho u E + up)}{\partial \rho \psi_l} & \cdots \\ \vdots & \vdots & \vdots & \ddots & \vdots & \ddots \\ \frac{\partial \rho u \psi_l}{\partial \rho} & \frac{\partial \rho u \psi_l}{\partial \rho u} & \frac{\partial \rho u \psi_l}{\partial \rho E} & \cdots & \frac{\partial \rho u \psi_l}{\partial \rho \psi_l} & \cdots \\ \vdots & \vdots & \vdots & \ddots & \vdots & \ddots \end{pmatrix} \\ &= \begin{pmatrix} 0 & 1 & 0 & \dots & 0 & \dots \\ \beta e_c - u^2 - \mathcal{X} + \sum_{l=1}^{N} \chi_l & 2u - \beta u & \beta & \dots & \chi_l & \dots \\ -uH + u\beta e_c & H - \beta u^2 & (\beta+1)u & \dots & u\chi_l & \dots \\ \vdots & \vdots & \vdots & \ddots & \vdots & \ddots \\ -u\psi_l & \psi_l & 0 & \dots & u & \dots \\ \vdots & \vdots & \vdots & \ddots & \vdots & \ddots \end{pmatrix} \end{aligned} \tag{C.6}$$

For this compact form, the following definitions were used:

$$\begin{aligned} &\beta = \gamma - 1 \\ &H = E - \frac{p}{\rho} \\ &E = e_c + e \qquad e_c = \frac{u^2}{2} \qquad e = \sum_{k=1}^{N_{sp}} e_{s,k} Y_k \\ &\mathcal{X} = rT - \beta e \\ &\chi_l = \sum_{k=1}^{N_{sp}} (r_k T - \beta e_{s,k}) \frac{\partial Y_k}{\partial \psi_l}, \qquad l = 1, N \end{aligned} \tag{C.7}$$

Notice a multi-species formulation particularity, that the term of the matrix $\mathcal{X}$ cancels mutually with $\sum_{k=1}^{N_{sp}} \chi_l$ as $\frac{\partial Y_k}{\partial \psi_l} = \frac{\partial Y_k}{\partial Y_k} = 1$.

This is not the case for the tabulated chemistry formulation as the reduced variables sum $\sum_{k=1}^{N_{fic}} \psi_l \subset [0, N]$ is not equal to one, except for some singularities.

In order to rewrite the equations in primitive variables $\overrightarrow{V}$:

$$\overrightarrow{V} = \begin{pmatrix} \rho \\ u \\ p \\ \vdots \\ \rho\psi_l \\ \vdots \end{pmatrix} \tag{C.8}$$

the *Jacobian* matrix between the conservatives and non-conservatives variables $\overline{\overline{M}} = \frac{\partial \overrightarrow{U}}{\partial \overrightarrow{V}}$ is needed, leading to the following expression:

$$\overline{\overline{M}} \frac{\partial \overrightarrow{\boldsymbol{V}}}{\partial t} + \overline{\overline{J}}\, \overline{\overline{M}} \frac{\partial \overrightarrow{\boldsymbol{V}}}{\partial x} = 0 \tag{C.9}$$

with the matrix $\overline{\overline{M}}$ calculated as:

$$\overline{\overline{M}} = \begin{pmatrix} \frac{\partial \rho}{\partial \rho} & \frac{\partial \rho}{\partial u} & \frac{\partial \rho}{\partial P} & \cdots & \frac{\partial \rho}{\partial \psi_l} & \cdots \\ \frac{\partial \rho u}{\partial \rho} & \frac{\partial \rho u}{\partial u} & \frac{\partial \rho u}{\partial P} & \cdots & \frac{\partial \rho u}{\partial \psi_l} & \cdots \\ \frac{\partial \rho E}{\partial \rho} & \frac{\partial \rho E}{\partial u} & \frac{\partial \rho E}{\partial P} & \cdots & \frac{\partial \rho E}{\partial \psi_l} & \cdots \\ \vdots & \vdots & \vdots & \ddots & \vdots & \ddots \\ \frac{\partial \rho \chi_l}{\partial \rho} & \frac{\partial \rho \chi_l}{\partial u} & \frac{\partial \rho \chi_l}{\partial P} & \cdots & \frac{\partial \rho \chi_l}{\partial \psi_l} & \cdots \\ \vdots & \vdots & \vdots & \ddots & \vdots & \ddots \end{pmatrix} = \begin{pmatrix} 1 & 0 & 0 & \ldots & 0 & \ldots \\ u & \rho & 0 & \ldots & 0 & \ldots \\ e_c - \frac{1}{\beta}\mathcal{X} & \rho u & \frac{1}{\beta} & \ldots & -\frac{\rho}{\beta}\chi_l & \ldots \\ \vdots & \vdots & \vdots & \ddots & \vdots & \ddots \\ \chi_l & 0 & 0 & \ldots & \rho & \ldots \\ \vdots & \vdots & \vdots & \ddots & \vdots & \ddots \end{pmatrix} \tag{C.10}$$

and the product of the two matrices gives:

$$\overline{\overline{J_U}}\, \overline{\overline{M}} = \begin{pmatrix} u & \rho & 0 & \ldots & 0 & \ldots \\ u^2 & 2\rho u & 1 & \ldots & 0 & \ldots \\ u e_c - \frac{u}{\beta}\mathcal{X} & \rho H + \rho u^2 & \frac{\beta+1}{\beta} u & \ldots & -\frac{\rho u}{\beta}\chi_l & \ldots \\ \vdots & \vdots & \vdots & \ddots & \vdots & \ddots \\ u\chi_l & \rho\psi_l & 0 & \ldots & \rho u & \ldots \\ \vdots & \vdots & \vdots & \ddots & \vdots & \ddots \end{pmatrix} \tag{C.11}$$

Then, when C.8 is left multiplied by $\overline{\overline{M}}^{-1} = \frac{\partial \overrightarrow{V}}{\partial \overrightarrow{U}}$ leads to the evolution of the non-conservatives variables:

$$\frac{\partial \overrightarrow{\boldsymbol{V}}}{\partial t} + \overline{\overline{M}}^{-1} \overline{\overline{J}}\, \overline{\overline{M}} \frac{\partial \overrightarrow{\boldsymbol{V}}}{\partial x} = 0 \tag{C.12}$$

the inverse of the $\overline{\overline{M}}$ matrix reads:

$$\overline{\overline{M}}^{-1} = \begin{pmatrix} \frac{\partial \rho}{\partial \rho} & \frac{\partial u}{\partial \rho} & \frac{\partial P}{\partial \rho} & \cdots & \frac{\partial \psi_l}{\partial \rho} & \cdots \\ \frac{\partial \rho}{\partial \rho u} & \frac{\partial u}{\partial \rho u} & \frac{\partial P}{\partial \rho u} & \cdots & \frac{\partial \psi_l}{\partial \rho u} & \cdots \\ \frac{\partial \rho}{\partial \rho E} & \frac{\partial u}{\partial \rho E} & \frac{\partial P}{\partial \rho E} & \cdots & \frac{\partial \psi_l}{\partial \rho E} & \cdots \\ \vdots & \vdots & \vdots & \ddots & \vdots & \ddots \\ \frac{\partial \rho}{\partial \rho \psi_l} & \frac{\partial u}{\partial \rho \psi_l} & \frac{\partial P}{\partial \rho \psi_l} & \cdots & \frac{\partial \psi_l}{\partial \rho \psi_l} & \cdots \\ \vdots & \vdots & \vdots & \ddots & \vdots & \ddots \end{pmatrix} = \begin{pmatrix} 1 & 0 & 0 & \ldots & 0 & \ldots \\ -\frac{u}{\rho} & \frac{1}{\rho} & 0 & \ldots & 0 & \ldots \\ \beta e_c & \rho u & -\beta & \ldots & \chi_l & \ldots \\ \vdots & \vdots & \vdots & \ddots & \vdots & \ddots \\ -\frac{1}{\rho}\psi_l & 0 & 0 & \ldots & \frac{1}{\rho} & \ldots \\ \vdots & \vdots & \vdots & \ddots & \vdots & \ddots \end{pmatrix} \tag{C.13}$$

The primitive variables transport equation can be also written as:

$$\frac{\partial \vec{\boldsymbol{V}}}{\partial t} + \overline{\overline{J_V}} \frac{\partial \vec{\boldsymbol{V}}}{\partial x} = 0 \tag{C.14}$$

with the product $\overline{\overline{J_V}} = \overline{\overline{M^{-1}}}\ \overline{\overline{J_U}}\ \overline{\overline{M}}$ being:

$$\overline{\overline{J_V}} = \begin{pmatrix} u & \rho & 0 & \dots & 0 & \dots \\ 0 & u & \frac{1}{\rho} & \dots & 0 & \dots \\ 0 & \rho c^2 & u & \dots & 0 & \dots \\ \vdots & \vdots & \vdots & \ddots & \vdots & \ddots \\ 0 & 0 & 0 & \dots & u & \dots \\ \vdots & \vdots & \vdots & \ddots & \vdots & \ddots \end{pmatrix} \tag{C.15}$$

The projection of the primitive variable is not necessary for this *1-D* case but for a boundary condition problem a change to a base orthogonal to the boundary is required.

C.2 Characteristic wave decomposition

In order to decompose the system into characteristic waves $\vec{W}$, the matrix $\overline{\overline{J_V}}$ must be diagonalized. This is equivalent to find the eigenvalues of the matrix.
The vector r_m will be one eigenvector of the matrix $\overline{\overline{J_V}}$ with an eigenvalue λ^m if the following equation holds:

$$\overline{\overline{J_V}} r_m = \lambda^m r_m \tag{C.16}$$

As to determine the set of eigenvalues λ^m of the $\overline{\overline{J_V}}$ matrix, the roots of the characteristic polynomial have to be found.

$$det(\overline{\overline{J_V}} - \lambda I_3) = 0 \tag{C.17}$$

Using the relation C.15 this leads to:

$$det(\overline{\overline{J_V}} - \lambda I_3) = \begin{pmatrix} u-\lambda & \rho & 0 & \dots & 0 & \dots \\ 0 & u-\lambda & \frac{1}{\rho} & \dots & 0 & \dots \\ 0 & \rho c^2 & u-\lambda & \dots & 0 & \dots \\ \vdots & \vdots & \vdots & \ddots & \vdots & \ddots \\ 0 & 0 & 0 & \dots & u-\lambda & \dots \\ \vdots & \vdots & \vdots & \ddots & \vdots & \ddots \end{pmatrix} = (u-\lambda)^N [(u-\lambda)^2 - c^2] = 0 \tag{C.18}$$

So the spectrum of the $\overline{\overline{J_V}}$ matrix is (u, $u+c$, $u-c$, ..., u, ...). Using the mathematical expression C.16, the eigenspace of $\overline{\overline{J_V}}$ is accessible as well. One of the eigenvectors corresponding to each eigenvalue are given bellow:

$$\lambda^1 = u,\ r_1 = \begin{pmatrix} 1 \\ 0 \\ 0 \\ \vdots \\ 0 \\ \vdots \end{pmatrix}; \lambda^2 = u+c, r_2 = \begin{pmatrix} \frac{\rho}{2c} \\ \frac{1}{2} \\ \frac{\rho c}{2} \\ \vdots \\ 0 \\ \vdots \end{pmatrix}; \lambda^3 = u-c, r_3 = \begin{pmatrix} \frac{\rho}{2c} \\ -\frac{1}{2} \\ \frac{\rho c}{2} \\ \vdots \\ 0 \\ \vdots \end{pmatrix}; \dots; \lambda^l = u, r_l = \begin{pmatrix} 0 \\ 0 \\ 0 \\ \vdots \\ 1 \\ \vdots \end{pmatrix}; \dots \tag{C.19}$$

As the eigenvectors of the $(N+3)$x$(N+3)$ matrix $\overline{\overline{J_V}}$ are linearly independent one can conclude that the $\overline{\overline{J_V}}$ matrix is diagonalizable, therefore an orthogonal matrix $\overline{\overline{P}}$ exists, such as:

$$\overline{\overline{J_V}} = \overline{\overline{P}}\,\overline{\overline{\Lambda}}\,\overline{\overline{P}}^{-1} \tag{C.20}$$

where $\overline{\overline{\Lambda}}$ is a diagonal matrix with diagonal entries being the eigenvalues of $\overline{\overline{J_V}}$:

$$\overline{\overline{\Lambda}} = \begin{pmatrix} u & 0 & 0 & \dots & 0 & \dots \\ 0 & u+c & 0 & \dots & 0 & \dots \\ 0 & 0 & u-c & \dots & 0 & \dots \\ \vdots & \vdots & \vdots & \ddots & \vdots & \ddots \\ 0 & 0 & 0 & \dots & u & \dots \\ \vdots & \vdots & \vdots & \ddots & \vdots & \ddots \end{pmatrix} \tag{C.21}$$

The column vectors of $\overline{\overline{P}}$ are the eigenvectors corresponding to the eigenvalues of $\overline{\overline{J_V}}$:

$$\overline{\overline{P}} = \begin{pmatrix} 1 & \frac{\rho}{2c} & \frac{\rho}{2c} & \dots & 0 & \dots \\ 0 & \frac{1}{2} & -\frac{1}{2} & \dots & 0 & \dots \\ 0 & \frac{\rho c}{2} & \frac{\rho c}{2} & \dots & 0 & \dots \\ \vdots & \vdots & \vdots & \ddots & \vdots & \ddots \\ 0 & 0 & 0 & \dots & 1 & \dots \\ \vdots & \vdots & \vdots & \ddots & \vdots & \ddots \end{pmatrix} \tag{C.22}$$

and the inverse matrix of $\overline{\overline{P}}$ is:

$$\overline{\overline{P}}^{-1} = \begin{pmatrix} 1 & 0 & -\frac{1}{c^2} & \dots & 0 & \dots \\ 0 & 1 & \frac{1}{\rho c} & \dots & 0 & \dots \\ 0 & -1 & \frac{1}{\rho c} & \dots & 0 & \dots \\ \vdots & \vdots & \vdots & \ddots & \vdots & \ddots \\ 0 & 0 & 0 & \dots & 1 & \dots \\ \vdots & \vdots & \vdots & \ddots & \vdots & \ddots \end{pmatrix} \tag{C.23}$$

The equation C.12 describing the primitive variables evolution becomes :

$$\frac{\partial \overrightarrow{\boldsymbol{V}}}{\partial t} + \overline{\overline{P}}\,\overline{\overline{\Lambda}}\,\overline{\overline{P}}^{-1}\frac{\partial \overrightarrow{\boldsymbol{V}}}{\partial x} = 0 \tag{C.24}$$

Variations of the characteristic variables are defined as $\partial\overrightarrow{W} = \overline{\overline{P}}^{-1}\partial\overrightarrow{V}$. This enables to express the characteristic variables in terms of primitive variables:

$$\partial\overrightarrow{W} = \begin{pmatrix} \partial w_s \\ \partial w_+ \\ \partial w_- \\ \vdots \\ \partial w_{\chi_k} \\ \vdots \end{pmatrix} = \begin{pmatrix} \partial\rho - \frac{1}{c^2}\partial p \\ \partial u + \frac{1}{\rho c}\partial p \\ -\partial u + \frac{1}{\rho c}\partial p \\ \\ \vdots \\ \partial\chi_l \\ \vdots \end{pmatrix} \tag{C.25}$$

Finally the use of this definition in equation C.23 which is then multiplied at left by $\overline{\overline{P}}^{-1}$ leads to the *1-D* Euler conservation equations in terms of characteristic waves:

$$\frac{\partial \overrightarrow{\boldsymbol{W}}}{\partial t} + \begin{pmatrix} u & 0 & 0 & \dots & 0 & \dots \\ 0 & u+c & 0 & \dots & 0 & \dots \\ 0 & 0 & u-c & \dots & 0 & \dots \\ \vdots & \vdots & \vdots & \ddots & \vdots & \ddots \\ 0 & 0 & 0 & \dots & u & \dots \\ \vdots & \vdots & \vdots & \ddots & \vdots & \ddots \end{pmatrix} \frac{\partial \overrightarrow{\boldsymbol{W}}}{\partial x} = 0 \tag{C.26}$$

or in the compact form:

$$\frac{\partial \overrightarrow{\boldsymbol{W}}}{\partial t} + \overline{\overline{\Lambda}} \frac{\partial \overrightarrow{\boldsymbol{W}}}{\partial x} = 0 \tag{C.27}$$

The passage from the characteristic variable to the conservatives variables $\partial \overrightarrow{U} = \overline{\overline{R_U}} \partial \overrightarrow{W}$ is performed by applying the matrix multiplication $\overline{\overline{R_U}} = \overline{\overline{M}}\ \overline{\overline{P}}$:

$$\overline{\overline{R_U}} = \begin{pmatrix} 1 & \frac{\rho}{2c} & \frac{\rho}{2c} & \dots & 0 & \dots \\ u & \frac{\rho}{2c}(u+c) & \frac{\rho}{2c}(u-c) & \dots & 0 & \dots \\ e_c - \frac{\mathcal{X}}{\beta} & \frac{\rho}{2c}(e_c - \frac{\mathcal{X}}{\beta} + cu + \frac{c^2}{\beta}) & \frac{\rho}{2c}(e_c - \frac{\mathcal{X}}{\beta} - cu + \frac{c^2}{\beta}) & \dots & -\frac{\rho}{\beta}\chi_l & \dots \\ \vdots & \vdots & \vdots & \ddots & \vdots & \ddots \\ \psi_l & \frac{\rho}{2c}\psi_l & \frac{\rho}{2c}\psi_l & \dots & \rho & \dots \\ \vdots & \vdots & \vdots & \ddots & \vdots & \ddots \end{pmatrix} \tag{C.28}$$

Vice versa, the passage matrix $\overline{\overline{L_U}} = \overline{\overline{P}}^{-1}\ \overline{\overline{U}}^{-1}$ will enable the transformation of the conservative variables into the characteristic variables following the relation $\partial \overrightarrow{W} = \overline{\overline{L_U}} \partial \overrightarrow{U}$.

$$\overline{\overline{L_U}} = \begin{pmatrix} -\frac{1}{c^2}(\beta e_c - \mathcal{X} + \sum_{l=1}^{N} \chi_l - c^2) & -\frac{1}{c^2}\beta u & -\frac{1}{c^2}\beta & \dots & -\frac{1}{c^2}\beta\chi_l & \dots \\ \frac{1}{\rho c}(\beta e_c - \mathcal{X} + \sum_{l=1}^{N} \chi_l - uc) & -\frac{1}{\rho c}(u\beta - c) & \frac{1}{\rho c}\beta & \dots & \frac{1}{\rho c}\chi_l & \dots \\ \frac{1}{\rho c}(\beta e_c - \mathcal{X} + \sum_{l=1}^{N} \chi_l + uc) & -\frac{1}{\rho c}(u\beta + c) & \frac{1}{\rho c}\beta & \dots & \frac{1}{\rho c}\chi_l & \dots \\ \vdots & \vdots & \vdots & \ddots & \vdots & \ddots \\ -\frac{1}{\rho}\psi_l & \frac{\rho}{2c}\psi_l & \frac{\rho}{2c}\psi_l & \dots & \frac{1}{\rho} & \dots \\ \vdots & \vdots & \vdots & \ddots & \vdots & \ddots \end{pmatrix} \tag{C.29}$$

As mentioned before the tabulated chemistry formulation particularity is: $\mathcal{X} \neq \sum_{l=1}^{N} \chi_l$.
In the here presented particular case of the non-adiabatic database (ρ*, e*, c*) the transformation matrix are:

$$\overline{\overline{R_U}}_{\rho*,e*,c*} = \begin{pmatrix} 1 & \frac{\rho}{2c} & \frac{\rho}{2c} & 0 & 0 & 0 \\ u & \frac{\rho}{2c}(u+c) & \frac{\rho}{2c}(u-c) & 0 & 0 & 0 \\ e_c - \frac{\mathcal{X}}{\beta} & \frac{\rho}{2c}(e_c - \frac{\mathcal{X}}{\beta} + cu + \frac{c^2}{\beta}) & \frac{\rho}{2c}(e_c - \frac{\mathcal{X}}{\beta} - cu + \frac{c^2}{\beta}) & -\frac{\rho}{\beta}\chi_{\rho*} & -\frac{\rho}{\beta}\chi_{e*} & -\frac{\rho}{\beta}\chi_{c*} \\ \rho* & \frac{\rho}{2c}\rho* & \frac{\rho}{2c}\rho* & \rho & 0 & 0 \\ e* & \frac{\rho}{2c}e* & \frac{\rho}{2c}e* & 0 & \rho & 0 \\ c* & \frac{\rho}{2c}c* & \frac{\rho}{2c}c* & 0 & 0 & \rho \end{pmatrix} \tag{C.30}$$

$$\overline{\overline{L_U}}_{\rho*,e*,c*} = \begin{pmatrix} -\frac{1}{c^2}(\beta e_c - \mathcal{X} + \sum_{l=1}^{N}\chi_l - c^2) & -\frac{1}{c^2}\beta u & -\frac{1}{c^2}\beta & -\frac{1}{c^2}\beta\chi_{\rho*} & -\frac{1}{c^2}\beta\chi_{e*} & -\frac{1}{c^2}\beta\chi_{c*} \\ \frac{1}{\rho c}(\beta e_c - \mathcal{X} + \sum_{l=1}^{N}\chi_l - uc) & -\frac{1}{\rho c}(u\beta - c) & \frac{1}{\rho c}\beta & \frac{1}{\rho c}\chi_{\rho*} & \frac{1}{\rho c}\chi_{e*} & \frac{1}{\rho c}\chi_{c*} \\ \frac{1}{\rho c}(\beta e_c - \mathcal{X} + \sum_{l=1}^{N}\chi_l + uc) & -\frac{1}{\rho c}(u\beta + c) & \frac{1}{\rho c}\beta & \frac{1}{\rho c}\chi_{\rho*} & \frac{1}{\rho c}\chi_{e*} & \frac{1}{\rho c}\chi_{c*} \\ -\frac{1}{\rho}\rho* & \frac{\rho}{2c}\rho* & \frac{\rho}{2c}\rho* & \frac{1}{\rho} & 0 & 0 \\ -\frac{1}{\rho}e* & \frac{\rho}{2c}e* & \frac{\rho}{2c}e* & 0 & \frac{1}{\rho} & 0 \\ -\frac{1}{\rho}c* & \frac{\rho}{2c}c* & \frac{\rho}{2c}c* & 0 & 0 & \frac{1}{\rho} \end{pmatrix} \tag{C.31}$$

In comparison to other tabulation methods [85] new terms appear specific to the non-adiabatic tabulation strategy

$$\begin{aligned} \chi_{c*} &= \sum_{k=1}^{N_{sp}}(r_k T - \beta e_{s,k})\frac{\partial Y_k}{\partial c*} \\ \chi_{\rho*} &= \sum_{k=1}^{N_{sp}}(r_k T - \beta e_{s,k})\frac{\partial Y_k}{\partial \rho*} = \chi_{c*}\frac{\partial c*}{\partial \rho*} \\ \chi_{e*} &= \sum_{k=1}^{N_{sp}}(r_k T - \beta e_{s,k})\frac{\partial Y_k}{\partial e*} = \chi_{c*}\frac{\partial c*}{\partial e*} \end{aligned} \tag{C.32}$$

Two of the variables that are used for tabulation, namely the normalized density $\rho*$ and the normalized energy $e*$, can be recovered from the transported variables ρ, ρu and ρE by applying the forrmula C.33

$$\begin{aligned} e* &= \frac{(E - e_c) - e^-}{e^+ - e^-} \\ \rho* &= \frac{\rho - \rho^-}{\rho^+ - \rho^-} \end{aligned} \tag{C.33}$$

These definitions reduce the matrices by two dimensions:

$$\overline{\overline{R_U}}_{c*} = \begin{pmatrix} 1 & \frac{\rho}{2c} & \frac{\rho}{2c} & 0 \\ u & \frac{\rho}{2c}(u + c) & \frac{\rho}{2c}(u - c) & 0 \\ e_c - \frac{\mathcal{X}}{\beta} & \frac{\rho}{2c}(e_c - \frac{\mathcal{X}}{\beta} + cu + \frac{c^2}{\beta}) & \frac{\rho}{2c}(e_c - \frac{\mathcal{X}}{\beta} - cu + \frac{c^2}{\beta}) & -\frac{\rho}{\beta}\chi_{c*} \\ c* & \frac{\rho}{2c}c* & \frac{\rho}{2c}c* & \rho \end{pmatrix} \tag{C.34}$$

$$\overline{\overline{L_U}}_{c*} = \begin{pmatrix} -\frac{1}{c^2}(\beta e_c - \mathcal{X} + \sum_{l=1}^{N}\chi_l - c^2) & -\frac{1}{c^2}\beta u & -\frac{1}{c^2}\beta & -\frac{1}{c^2}\beta\chi_{c*} \\ \frac{1}{\rho c}(\beta e_c - \mathcal{X} + \sum_{l=1}^{N}\chi_l - uc) & -\frac{1}{\rho c}(u\beta - c) & \frac{1}{\rho c}\beta & \frac{1}{\rho c}\chi_{c*} \\ \frac{1}{\rho c}(\beta e_c - \mathcal{X} + \sum_{l=1}^{N}\chi_l + uc) & -\frac{1}{\rho c}(u\beta - c) & -\frac{1}{\rho c}(u\beta + c) & \frac{1}{\rho c}\chi_{c*} \\ -\frac{1}{\rho}c* & \frac{\rho}{2c}c* & \frac{\rho}{2c}c* & \frac{1}{\rho} \end{pmatrix} \tag{C.35}$$

So only the term χ_{c*} should be tabulated, implying that only the species' derivatives by the progress variable must be known during the tabulation process, and $\chi_{\rho*}$ and χ_{e*} turn to be unnecessary.
The presented wave decomposition can be easily extended into a more complex *3-D* geometry but in some situations, i.e. for characteristic boundary conditions treatment, a rotation to another reference system can be necessary.